The Evolution of Nuclear Structure in Odd-*A* Zinc Isotopes

Thesis submitted in accordance with the requirements of

the University of Liverpool for the degree of Doctor in Philosophy

by

Calvin Wraith

Oliver Lodge Laboratory

September 2018

Abstract

The hyperfine spectra of odd-A Zn ($Z = 30$) isotopes from $N = 33 - 49$ have been measured using collinear laser spectroscopy at the COLLAPS (COLlinear LAser sPectroScopy) experiment at ISOLDE, CERN. From the hyperfine spectra, nuclear spins I, magnetic dipole moments μ and spectroscopic quadrupole moments Q_s were determined across the Zn isotope chain, with isotopes ranging from stability to neutron-rich nuclei approaching $N = 50$. The $4s4p\ ^3P_2^o \rightarrow 4s5s\ ^3S_1$ atomic transition was probed using a CW laser tuned to 481.1873 nm wavelength, and allowed for maximal sensitivity to the nuclear spin in order to unambiguously confirm the ground and isomeric state spins of $^{73-79}$Zn. The nuclear moments of Zn isotopes were determined using the reference isotope ^{67}Zn and the hyperfine coefficients $A(^3P_2) = +531.987(5)$ MHz and $B(^3P_2) = +35.806(5)$ MHz, and reference moments $\mu = +0.875479(9)\mu_N$ and $Q_s = +0.122(10)$ b, the latter of which is introduced in this work based on new electric field gradient (EFG) calculations.

The nuclear moments are compared to predictions from large-scale shell model calculations in the f_5pg_9 (JUN45 and jj44b) and pfg_9d_5 (A3DA-m and LNPS-m) model spaces. The improvement of magnetic dipole moment predictions from JUN45 over those from A3DA-m and LNPS-m as $N = 50$ is approached points to the persistence of the $N = 50$ shell gap in neutron-rich Zn isotopes. Regarding quadrupole moments, the close agreement between measured Q_s values and A3DA-m predictions beyond $N = 40$ highlights the importance of the $\nu d_{5/2}$ orbital for characterising quadrupole deformation.

The hyperfine structure of the newly-discovered isomer in ^{79}Zn with tentatively assigned

spin-parity of $I^{\pi} = 1/2^{+}$ has been directly observed for the first time in this work. In order to reproduce its measured nuclear properties, a novel interaction with an extended model space, PFSDG-U, is developed to understand the contributions to the nuclear wave function from np-mh excitations across the $N = 50$ shell closure.

Contents

Abstract **i**

Contents **iii**

List of Figures **vii**

List of Tables **xiv**

List of Publications **xvii**

Glossary **xxi**

Acknowledgements **xxii**

1 Nuclear Structure from Laser Spectroscopy **1**

1.1 This Work 4

1.2 Physics Motivation 6

2 Atomic Spectra **9**

2.1 Fine Structure 9

2.2 Hyperfine Structure 12

2.2.1 Magnetic Dipole Moment 14

2.2.2 Hyperfine Anomaly 17

2.2.3 Electric Quadrupole Moment 17

2.2.4 Hyperfine Spectrum . . . 19
2.3 Extracting Nuclear Properties . . . 21
2.3.1 Determining Nuclear Spin . . . 22
2.3.2 Nuclear Electromagnetic Moments . . . 24
2.4 Isotope Shift . . . 26
2.4.1 Mass Shift . . . 26
2.4.2 Field Shift . . . 27
2.4.3 Isotope Shift from Atomic Factors . . . 28
2.4.4 King-Plot Analysis . . . 29
2.5 This Work . . . 30

3 Nuclear Theory **31**
3.1 Evidence for Nuclear Shell Structure . . . 32
3.2 The Nuclear Shell Model . . . 33
3.2.1 The Independent Particle Model . . . 34
3.2.2 Magnetic Dipole Moments . . . 36
3.2.3 Electric Quadrupole Moments . . . 39
3.2.4 Interacting Shell Model . . . 41
3.3 Large-Scale Shell-Model Interactions . . . 44
3.3.1 JUN45 and jj44b Interactions . . . 45
3.3.2 A3DA and LNPS Interactions . . . 47

4 Collinear Laser Spectroscopy at ISOLDE **50**
4.1 Isotope Production . . . 51
4.2 Ion Beam Production . . . 53
4.3 Beam Cooling and Bunching . . . 55
4.4 The Collinear Laser Spectroscopy Method . . . 57
4.5 The COLLAPS Experiment . . . 60
4.5.1 Accelerating Potential . . . 60

4.5.2 Charge-Exchange Cell 63
4.5.3 Atomic Transition 65
4.5.4 The COLLAPS Laser Setup 66
4.5.5 Detection Region 69

5 Analysis of Zinc Hyperfine Spectra **73**
5.1 χ^2-minimisation Method 73
5.1.1 Spectral Line Shape 75
5.1.2 Peak Asymmetry 76
5.2 Nuclear Spin Determination 77
5.2.1 ^{73}Zn ($N = 43$) 79
5.2.2 ^{75}Zn ($N = 45$) 84
5.2.3 ^{77}Zn ($N = 47$) 88
5.2.4 ^{79}Zn ($N = 49$) 91
5.3 Collated Fitting Results 95

6 Discussion **98**
6.1 Comparison to Shell Model Interactions 98
6.2 JUN45 and jj44b Interactions 99
6.2.1 Energy Level Systematics 100
6.2.2 Magnetic Dipole Moments 103
6.2.3 Spectroscopic Quadrupole Moments 110
6.3 Modified LNPS and A3DA Interactions 114
6.3.1 Energy Level Systematics 115
6.3.2 Magnetic Dipole Moments 118
6.3.3 Spectroscopic Quadrupole Moments 124
6.4 PFSDG-U Interaction 126
6.4.1 Model Space and Parameters 126
6.4.2 Energy Level Systematics in $N = 49$ Isotones 128

6.4.3 Magnetic Dipole Moment of ^{79g,m}Zn 130
6.4.4 Spectroscopic Quadrupole Moment of ^{79}Zn 133

7 Conclusion **135**
7.1 Recommendations for Future Work 140

Bibliography **152**

A Spin Assignments of $^{63-71g,69-71m}$Zn **153**
A.1 ^{63}Zn ($N = 33$) 153
A.2 ^{65}Zn ($N = 35$) 155
A.3 ^{67}Zn ($N = 37$) 157
A.4 ^{69}Zn ($N = 39$) 159
A.4.1 Ground State Spin 160
A.4.2 Isomeric State Spin 161
A.5 ^{71}Zn ($N = 41$) 163
A.5.1 Ground State Spin 163
A.5.2 Isomeric State Spin 164

B χ^2-minimisation Fit Parameters with Free Intensities **166**

List of Figures

2.1 The precession of the nuclear spin I and the total electron angular momentum J around the total angular momentum F. The J component is formed by the coupling of the orbital angular momentum L and the electron spin angular momentum S. 13

2.2 Scale representation of the observed hyperfine level splitting of the $3d^{10}4s4p\ ^3P_2^o$ level in the $I = 3/2$ ground state of ^{63}Zn due to the magnetic dipole component of the hyperfine interaction. 16

2.3 Visualisation of the nuclear charge distribution and its relation to the electric quadrupole moment Q. The axis of symmetry is labelled by z. 18

2.4 Final splitting of the $3d^{10}4s4p\ ^3P_2^o$ level in the $I = 3/2$ ground state of ^{63}Zn after the perturbations due to the electric quadrupole component of the hyperfine interaction are considered in addition to contributions from the magnetic dipole component. 19

2.5 Hyperfine structure of the $I = 3/2$ ground state of ^{63}Zn measured via the $4s4p\ ^3P_2^o \rightarrow 4s5s\ ^3S_1$ atomic transition using collinear laser spectroscopy. The splitting of atomic J levels into hyperfine F states is shown here, with the F quantum number of each state and its frequency splitting from the unperturbed J state given on the right hand side. Allowed transitions between F states based on selection rules denoted by arrows. 21

3.1 Single-particle energy levels calculated from the independent particle model using the harmonic oscillator potential, and then adding the l^2 term and the spin-orbit interaction term $l \cdot s$. The magic numbers from the harmonic oscillator potential with and without the spin-orbit interaction are shown in the circles. Single-particle levels are labelled on the right-hand side with their Nl_j values and multiplicity $(2l + 1)$. 37

3.2 Example of a model space and core used in the interacting shell model. The valence space denotes the active nucleon orbitals, which extend from the inert core to the model space truncation. 42

3.3 The f_5pg_9 model space and inert ^{56}Ni core of the JUN45 and jj44b effective interactions. The two interactions differ in their parametrisation (see text for details). 46

3.4 The model spaces of the LNPS-m (green dashed line) and A3DA-m (blue dashed line) effective interactions on top of a ^{48}Ca and ^{40}Ca core, respectively. 48

4.1 Overview of the ISOLDE experimental hall at CERN, Geneva, with a focus on the COLLAPS experiment. Some notable beam line components are labelled. Image adapted from Ref. [67]. 51

4.2 Target configuration at ISOLDE. Image taken from Ref [70]. 52

4.3 Three-step laser ionisation scheme for the production of singly charged Zn ions. The types of laser used and the operating wavelengths for Zn shown here are obtained from the Ref. [72]. 54

4.4 Potential experienced by ions V_z as a function of distance travelled within the ISCOOL structure z. 56

4.5 Schematic representation of the collinear laser spectroscopy method at the laser-atom/ion interaction point. 58

4.6 Visual representation of the longitudinal velocity spread in the ion beam Δv_z without without the application of an accelerating voltage V, and the longitudinal velocity spread after accelerating voltage is applied $\Delta v_z'$. 59
4.7 The COLLAPS beam line from ISCOOL to the detection region. Image taken from [79]. 61
4.8 A simplified circuit diagram of the electrical components that combine to produce the scanning voltage applied across the CEC. 62
4.9 Graphical representation of a scanning cycle at COLLAPS. The scanning range of the accelerating potential, V_{scan}, is scanned over in N steps, with Δt being the time between each scanning step. Once the final step is reached, the system cycles back to the first step to repeat the scanning process. 63
4.10 Simplified atomic level orientation for Zn showing the atomic transition selected for spectroscopy from the metastable $4s4p\ ^3P_2^o$ state to $4s5s\ ^3S_1$. . . . 66
4.11 Schematic diagram of the cavity elements in the Matisse tunable laser (not to scale). Optical elements labelled in the image include mirrors (M), folding mirrors (FM), tuning mirror (TM), piezo-mount (PM), fast piezo-mount (FPM), Ti:Sa crystal, thick etalon (TE), unidirectional device (UD), birefringent filters (BF) and output coupler (OC). The OC directs a portion of the output laser light to a reference cavity. 67
4.12 Schematic diagram of the cavity elements in the Wavetrain frequency doubler cavity (not to scale). Optical elements labelled in the image (not already referenced in Figure 4.11) include electro-optical modulator (EOM), lens (L), beam shifter (BS), nonlinear crystal lithium triborate (LBO) and Brewster prism (BP). 68
4.13 Measured hyperfine spectra of ^{73}Zn from this work with no photon gating (top) and an MCP triggered 5μs photon gate (bottom). 70
4.14 The fast release of Zn from a UC_x target compared to the release of Ga. Image taken from [86]. 71

4.15 Hyperfine spectrum of ^{73}Zn measured with a 2×10 ms proton triggered ISCOOL cycle. The enhancement of the isomeric structure relative to the ground state due to the shortened cycle length is clear when comparing this spectrum to the 4×100 ms cycle spectrum in the lower panel of Figure 4.13. 72

5.1 χ^2-minimisation fits with satellite peaks (blue) and without satellite peaks (red) included compared to the measured spectrum of ^{68}Zn. The blue and red dashed lines represent the respective peak centroids from the two fits with $\Delta\nu_0 \approx 6$ MHz. 78

5.2 Plot of the fitted spectrum for different spin assignments of the ground state in ^{73}Zn. 81

5.3 Plot of the fitted spectrum for different spin assignments of the isomeric state in ^{73}Zn. 82

5.4 Plot of the fitted spectrum for different spin assignments of the ground state of ^{75}Zn. 85

5.5 Plot of the fitted spectrum for different spin assignments of the isomeric state in ^{75}Zn. 87

5.6 Plot of the fitted spectrum for different spin assignments of the ground state of ^{77}Zn. 89

5.7 Plot of the fitted spectrum for different spin assignments of the isomeric state in ^{77}Zn. 91

5.8 Plot of the fitted spectrum for different spin assignments of the ground state of ^{79}Zn. 93

5.9 χ^2-minimisation fits to the measured spectrum of ^{79}Zn with the $I = 1/2$ (top) and 3/2 (bottom) isomeric state spin assignments. The inset graphs show the fits to the 3$^{\text{rd}}$ isomer peak measured in a focused scan away from the main structure. In order to observe the 3$^{\text{rd}}$ isomer peak, a greater number of scans was required than for the main structure. Thus the intensity of the third peak is normalised to the number of scans performed across the main structure. . . 94

5.10 Ratio of the hyperfine A coefficients of Zn isotopes for the upper and lower states, $A(^3P_2)/A(^3S_1)$, of the atomic transition $4s4p\ ^3P_2^{\text{o}} \rightarrow 4s5s\ ^3S_1$ measured in this work are shown with fitting errors. Values are compared to the expected ratio, $R_{\text{exp}} = 0.4197(3)$, obtained from the literature values $A(^3P_2) = +531.987(5)$ [89] MHz and $A(^3S_1) = +1267.5(1.0)$ MHz [90]. 97

6.1 Measured low-energy spectra of Zn isotopes from $N = 41-49$ are compared to predictions from the JUN45 and jj44b shell-model interactions. Dotted lines represent the change in energy of the ground and isomeric states, while the vertical dashed line at ^{79}Zn shows the error on the measured energy. 101

6.2 Experimental g-factors across the isotope chain in comparison to single-particle estimates and predictions from the JUN45 and jj44b interactions. The measured g-factor of ^{79m}Zn is not shown here due to scaling, as $g_{\text{expt}} = -2.036$. Errors on measured g-factors are smaller than the size of the symbols. 105

6.3 Comparison of measured high-spin state g-factors for isotopes from $N = 39-49$ and the predictions from the JUN45 and jj44b shell-model interactions. . . . 107

6.4 Proton (top) and neutron occupation (bottom) in the f_5pg_9 model space normalised to the maximum number of nucleons per orbital, as predicted by the JUN45 interaction. 109

6.5 Spectroscopic quadrupole moments, Q_{s}, of $^{69-79}$Zn measured in this work compared to predictions from the JUN45 and jj44b shell model interactions. . . . 112

6.6 Proton and neutron occupation in the f_5pg_9 model space normalised to the maximum number of nucleons per orbital, as predicted by the JUN45 interaction. 115

6.7 Measured low-energy spectra of Zn isotopes from $N = 41-49$ are compared to predictions from the A3DA-m and LNPS-m shell-model interactions. Dotted lines represent the change in energy of the ground and isomeric states, while the vertical dashed line at ^{79}Zn shows the error on the measured energy. . . . 117

6.8 Experimental g-factors across the isotope chain in comparison to single-particle estimates and predictions from the A3DA-m and LNPS-m interactions. The measured g-factor of ^{79m}Zn and predictions from the interactions are not shown here due to scaling, as $g_{\mathrm{expt}} = -2.036$, $g_{\mathrm{LNPS-m}} = -1.48$ and $g_{\mathrm{A3DA-m}} = -1.21$. Errors on measured g-factors are smaller than the size of the symbols. 120

6.9 Comparison of measured high-spin state g-factors for isotopes from $N = 39-49$ and the predictions from the LNPS-m and A3DA-m shell-model interactions. 121

6.10 Proton and neutron occupation from $N = 39 - 49$ in the fpg_9d_5 model space normalised to the maximum number of nucleons per orbital, as predicted by the A3DA-m interaction. Data for the $\pi f_{7/2}$ orbital are not shown here to focus on the systematics of higher lying levels, as the normalised occupancy remains at ≈1 across the range. 123

6.11 Spectroscopic quadrupole moments, Q_{s}, of $^{69-79}$Zn measured in this work compared to predictions from the A3DA-m and LNPS-m shell model interactions. 125

6.12 The nucleon configuration of ^{75}Zn with the model space of the PFSDG-U interaction. The valence space consists of a full pf-shell for protons and sdg-shell for neutrons on top of a virtual ^{60}Ca core. 127

6.13 Measured low energy spectra of $N = 49$ isotones are compared to predictions from the PFSDG-U shell-model interaction (values for ^{79}Zn from [19], other isotopes adapted from [109, 110]). Dotted lines represent the change in energy for low-lying states while the vertical dashed line at ^{79}Zn shows the error on the measured energy. 129

6.14 Experimental g-factors of the $9/2^+$ ground and isomeric $1/2^+$ states of ^{79}Zn in comparison to single-particle estimates and predictions from the A3DA-m, LNPS-m and PFSDG-U interactions. 131

6.15 Normalised neutron occupancies for orbitals in the *sdg*-shell for the ground and isomeric states in ^{79}Zn as predicted by the PFSDG-U interaction. Occupancies are normalised to the maximum number of neutrons in the orbital. 132

A.1 Plot of the fitted spectrum for different spin assignments of the ground state in ^{63}Zn. The corresponding χ^2_r are displayed in Table A.1, along with the hyperfine coefficients. 154

A.2 Plot of the fitted spectrum for different spin assignments of the ground state in ^{65}Zn. 156

A.3 Plot of the fitted spectrum for different spin assignments of the ground state in ^{67}Zn. 158

A.4 Plot of the fitted spectrum for different spin assignments of the ground state in ^{69}Zn. 160

A.5 Plot of the fitted spectrum for different spin assignments of the isomeric state in ^{69}Zn. The first hyperfine transition peak of the isomeric state lies outside the scan range shown here. 162

A.6 Plot of the fitted spectrum for different spin assignments of the ground state in ^{71}Zn. 164

A.7 Plot of the fitted spectrum for different spin assignments of the isomeric state in ^{71}Zn. 165

List of Tables

1.1 Literature values of μ, Q_s and I for the ground and isomeric states from $^{63-79}$Zn. Tentatively assigned nuclear spins are shown in parentheses along with the references they are taken from, while all μ and Q_s values are taken from [14]. 5

2.1 Atomic energy levels in neutral Zn nuclei in terms of their electron configuration, total angular momentum quantum numbers, and energy relative to the ground state [33]. 11

5.1 Results from the χ^2-minimisation fitting of the ground state structures for ^{73}Zn. 81

5.2 Results from the χ^2-minimisation fitting of the isomeric state structures for ^{73}Zn. 83

5.3 Results from the χ^2-minimisation fitting of the ground state structures for ^{75}Zn. 86

5.4 Results from the χ^2-minimisation fitting of the isomeric state structures for ^{75}Zn. 87

5.5 Results from the χ^2-minimisation fitting of the ground state structures for ^{77}Zn. 90

5.6 Results from the χ^2-minimisation fitting of the isomeric state structures for ^{77}Zn. 91

5.7 Results from the χ^2-minimisation fitting of the ground state structures for ^{79}Zn. 93

5.8 Results from the χ^2-minimisation fitting of the isomeric state structures for ^{79}Zn. 95

5.9 Final values of I, $A(^3S_1)$, $A(^3P_2)$ and $B(^3P_2)$ obtained from the χ^2-minimisation fitting in this work and by X. F. Yang. The moments μ_{expt} and $Q_{\text{s,expt}}$ are calculated from the hyperfine coefficients shown and the reference isotope ^{67}Zn with reference values of $A(^3P_2) = +531.987(5)$ MHz and $B(^3P_2) = +35.806(5)$ MHz from [89], $\mu = +0.875479(9)\mu_N$ from [14] and $Q_s = +0.122(10)$ b from this work and [94]. 96

6.1 Nuclear magnetic dipole moments, μ (μ_N) calculated from experimental data are compared to JUN45 and jj44b shell-model calculations. †To calibrate across the isotope chain the magnetic dipole moment of ^{67}Zn is used as reference, with $\mu = +0.875479(9)$ μ_N taken from [14]. The precise hyperfine coefficient $A(^3P_2) = +531.987(5)$ MHz [89] is used as the reference for calculations. . . . 104

6.2 Spectroscopic quadrupole moments, Q_{s} (b), calculated from experimental data are compared to JUN45 and jj44b shell-model calculations. †To calibrate $Q_{\text{s,expt}}$ across the isotope chain, the quadrupole moment of ^{67}Zn is used as reference, with $Q_{\text{s}} = +0.122(10)$ b calculated for this work (details given in [94]). The precise hyperfine coefficient $B(^3P_2) = +35.806(5)$ MHz [89] is used as the reference in calculations. 111

6.3 Nuclear magnetic dipole moments, μ (μ_N) calculated from experimental data are compared to A3DA-m and LNPS-m shell-model calculations. †To calibrate across the isotope chain the magnetic dipole moment of ^{67}Zn is used as reference, with μ taken from [14]. The precise hyperfine coefficient $A(^3P_2) = +531.987(5)$ MHz [89] is used. 119

6.4 Spectroscopic quadrupole moments, Q_s (b), calculated from experimental data are compared to A3DA-m and LNPS-m shell-model calculations. †To calibrate across the isotope chain the quadrupole moment of ^{67}Zn is used as reference, with $Q_s = +0.122(10)$ b calculated for this work (details given in [94]). The precise hyperfine coefficient $B(^3P_2) = +35.806(5)$ MHz [89] is used as the reference in calculations. 124

6.5 Calculated magnetic dipole moments μ for low-lying states in ^{79}Zn and ^{81}Ge from the PFSDG-U interaction. 131

6.6 Calculated energies (MeV) and quadrupole moments Q_s for low-lying levels in ^{79}Zn and ^{81}Ge from the PFSDG-U interaction. 133

A.1 Results from the χ^2-minimisation fitting of the ground state structures for ^{63}Zn. 155

A.2 Results from the χ^2-minimisation fitting of the ground state structures for ^{65}Zn. 157

A.3 Results from the χ^2-minimisation fitting of the ground state structures for ^{67}Zn. 159

A.4 Results from the χ^2-minimisation fitting of the ground state structures for ^{69}Zn. 161

A.5 Results from the χ^2-minimisation fitting of the isomeric state structures for ^{69}Zn. 162

A.6 Results from the χ^2-minimisation fitting of the ground state structures for ^{71}Zn. 164

A.7 Results from the χ^2-minimisation fitting of the isomeric state structures for ^{71}Zn. 165

B.1 The hyperfine structure coefficients $A(^3P_2)$, $A(^3S_1)$ and $B(^3P_2)$ and their errors from the χ^2-minimisation fitting process in this work (details in Chapter 5) and from the complementary analysis by X. F. Yang. The simple average of these values provides the final hfs coefficients used to calculate magnetic dipole moments, μ, and electric quadrupole moments, Q_s, by means of a reference isotope. The commonly agreed upon nuclear spins, I, are also shown. 167

List of Publications

Peer Reviewed Journals: Part of This Work

C. Wraith, X. F. Yang, L. Xie, C. Babcock, J. Bieroń, J. Billowes, M. L. Bissell, K. Blaum, B. Cheal, L. Filippin, R. F. Garcia Ruiz, W. Gins, L. K. Grob, G. Gaigalas, M. Godefroid, C. Gorges, H. Heylen, M. Honma, P. Jönsson, S. Kaufmann, M. Kowalska, J. Krämer, S. Malbrunot-Ettenauer, R. Neugart, G. Neyens, W. Nörtershäuser, F. Nowacki, T. Otsuka, J. Papuga, R. Sánchez, Y. Tsunoda, and D. T. Yordanov. Evolution of nuclear structure in neutron-rich odd-Zn isotopes and isomers. *Phys. Lett. B*, 771: 385 391, 2017.

X. F. Yang, **C. Wraith**, L. Xie, C. Babcock, J. Billowes, M. L. Bissell, K. Blaum, B. Cheal, K. T. Flanagan, R. F. Garcia Ruiz, W. Gins, C. Gorges, L. K. Grob, H. Heylen, S. Kaufmann, M. Kowalska, J. Kraemer, S. Malbrunot-Ettenauer, R. Neugart, G. Neyens, W. Nörtershäuser, J. Papuga, R. Sánchez, and D. T. Yordanov. Isomer Shift and Magnetic Moment of the Long-Lived $1/2^+$ Isomer in $^{79}_{30}Zn_{49}$: Signature of Shape Coexistence near ^{78}Ni. *Phys. Rev. Lett.*, 116:182502, 30 May 2016.

L. Xie, X. F. Yang, **C. Wraith**, C. Babcock, J. Billowes, M. L. Bissell, K. Blaum, B. Cheal, K. T. Flanagan, R. F. Garcia Ruiz, W. Gins, C. Gorges, L. K. Grob, H. Heylen, S. Kaufmann, M. Kowalska, J. Kraemer, S. Malbrunot-Ettenauer, R. Neugart, G. Neyens, W. Nörtershäuser, J. Papuga, R. Sánchez, and D. T. Yordanov. Nuclear charge radii of $^{62-80}$Zn: Investigation of nuclear deformation and correlations. To be published.

X. F. Yang, Y. Tsunoda, C. Babcock, J. Billowes, M. L. Bissell, K. Blaum, B. Cheal, R. F. Garcia Ruiz, W. Gins, C. Gorges, L. K. Grob, H. Heylen, S. Kaufmann, M. Kowalska, J. Kraemer, S. Malbrunot-Ettenauer, R. Neugart, G. Neyens, W. Nörtershäuser, T. Otsuka, J. Papuga, R. Sánchez, **C. Wraith**, L. Xie, and D. T. Yordanov. Investigating the abnormal deformation of the $5/2^+$ isomeric state in ^{73}Zn: indicator for triaxiality and shape coexistence? *Phys. Rev. C*, 97:044324, Apr 2018.

Peer Reviewed Journals: Other Contributions

C. Babcock, H. Heylen, M. L. Bissell, K. Blaum, P. Campbell, B. Cheal, D. Fedorov, R. F. Garcia Ruiz, W. Geithner, W. Gins, T. Day Goodacre, L. K. Grob, M. Kowalska, S. M. Lenzi, B. Maass, S. Malbrunot-Ettenauer, B. Marsh, R. Neugart, G. Neyens, W. Nörtershäuser, T. Otsuka, R. Rossel, S. Rothe, R. Sánchez, Y. Tsunoda, **C. Wraith**, L. Xie, and X. F. Yang. Quadrupole moments of odd-A $^{53-63}$Mn: Onset of collectivity towards $N = 40$. *Phys. Lett. B*, 760:387 392, 2016.

P. Chhetri, D. Ackermann, H. Backe, M. Block, B. Cheal, Christoph E. Düllmann, J. Even, R. Ferrer, F. Giacoppo, S. Göotz, F. P. Heßberger, O. Kaleja, J. Khuyagbaatar, P. Kunz, M. Laatiaoui, F. Lautenschläger, W. Lauth, E. M. Ramirez, A. K. Mistry, S. Raeder, **C. Wraith**, T. Walther, and A. Yakushev. Impact of buffer gas quenching on the $^1S_0 \longrightarrow {}^1P_1$ ground-state atomic transition in nobelium. *Eur. Phys. J. D*, 71(7):195, Jul 2017.

H. Heylen, C. Babcock, R. Beerwerth, J. Billowes, M. L. Bissell, K. Blaum, J. Bonnard, P. Campbell, B. Cheal, T. Day Goodacre, D. Fedorov, S. Fritzsche, R. F. Garcia Ruiz, W. Geithner, Ch. Geppert, W. Gins, L. K. Grob, M. Kowalska, K. Kreim, S. M. Lenzi, I. D. Moore, B. Maass, S. Malbrunot-Ettenauer, B. Marsh, R. Neugart, G. Neyens, W. Nörtershäuser, T. Otsuka, J. Papuga, R. Rossel, S. Rothe, R. Sánchez, Y. Tsunoda, **C. Wraith**, L. Xie, X. F. Yang, and D. T. Yordanov. Changes in nuclear structure along the Mn isotopic chain studied via charge radii. *Phys. Rev. C*, 94:054321, Nov 2016.

M. Laatiaoui, W. Lauth, H. Backe, M. Block, D. Ackermann, B. Cheal, P. Chhetri, Christoph E. Düllmann, P. van Duppen, J. Even, R. Ferrer, F. Giacoppo, S. Götz, F. P. Heßberger, M. Huyse, O. Kaleja, J. Khuyagbaatar, P. Kunz, F. Lautenschläger, A. Kishor Mistry, S. Raeder, E. M. Ramirez, T. Walther, **C. Wraith**, and A. Yakushev. Atom-at-a-time laser resonance ionization spectroscopy of nobelium. *Nature*, 538(7626):495498, Oct 2016.

F. Lautenschläger, P. Chhetri, D. Ackermann, H. Backe, M. Block, B. Cheal, A. Clark, C. Droese, R. Ferrer, F. Giacoppo, S. Götz, F. P. Heßberger, O. Kaleja, J. Khuyagbaatar, P. Kunz, A. K. Mistry, M. Laatiaoui, W. Lauth, S. Raeder, Th. Walther, and **C. Wraith**. Developments for resonance ionization laser spectroscopy of the heaviest elements at SHIP. *Nucl. Instrum. Methods Phys. Res., Sect. B*, 383:115 122, 2016.

S. Raeder, D. Ackermann, H. Backe, R. Beerwerth, J. Berengut, M. Block, A. Borschevsky, B. Cheal, P. Chhetri, Ch.E. Düllmann, V.A. Dzuba, E. Eliav, J. Even, R. Ferrer, V.V. Flambaum, S. Fritzsche, F. Giacoppo, S. Götz, F. P. Heßberger, M. Huyse, U. Kaldor, O. Kaleja, J. Khuyagbaatar, P. Kunz, M. Laatiaoui, F. Lautenschläger, W. Lauth, E. Minaya Ramirez, A. K. Mistry, W. Nazarewicz, S.G. Porsev, M.S. Safronova, U.I. Safronova, B. Schuetrumpf, P. Van Duppen, T. Walther, **C. Wraith**, and A. Yakushev. Probing sizes and shapes of nobelium isotopes by laser spectroscopy. *Phys. Rev. Lett.*, 120:232503, Jun 2018.

Glossary

Collinear Laser Spectroscopy The experimental method by which electronic transitions within atoms or ions are probed by a continuous wave laser beam that is parallel (or collinear) to a fast atom/ion beam.

Fluke High-voltage power supply used at COLLAPS with a voltage range of -10kV to $+10$kV.

Hyperfine structure The splitting of atomic energy levels due to the interaction of nuclear electromagnetic moments with the magnetic and electric fields generated by electrons.

ISOLDE The Isotope Separator On Line DEvice (ISOLDE) at CERN is radioactive ion beam facility that is dedicated to the production, study and research of exotic nuclei.

Isomeric state Long-lived ($>$ 10 ms for laser spectroscopy) metastable state from which the de-excitation to the ground state is hindered e.g. if the isomeric state spin differs greatly from the ground state spin.

Kepco High-voltage power supply (Kepco Model BOP 500M) used to provide linear amplification to the digital-to-analog (DAC) converter voltage output of $\pm$10V.

MCP The 'measurement and control program' (MCP) used at COLLAPS for the collection and processing of experimental data.

Radioactive Ion Beam (RIB) A beam of radioactive nuclei that is produced by impinging particles upon a target material. Reaction products are then ionised in order to produce an ion beam which can be focused and guided by magnets and electrostatic beam line components.

Acknowledgements

To Mum, Dad and Maxine, for their continued love and support.

To Lucy, for being my rock.

Thanks to my supervisor Bradley for his advice, encouragement and guidance. It has been a privilege to work with such a respected figure in the field of laser spectroscopy during the last four years.

Thanks to all the collaborators I worked with on experiments at ISOLDE, GSI and University of Jyväskylä. In particular, thanks to the local team at COLLAPS for ensuring this experiment ran smoothly.

Thanks to everyone in the office for providing plenty of distractions throughout the last four years. Without trips to the AJ, 5-a-side football games, Guardian crosswords and chess tournaments, my thesis would have been finished a hell of a lot quicker, although it would have been a lot more boring.

Thanks to the Science & Technology Facilities Council (STFC) for providing the funding that made this all possible.

Chapter 1

Nuclear Structure from Laser Spectroscopy

In the early 19th century, John Dalton coined the term "atom" to describe the "indivisible" particle that formed each chemical element. It wasn't until the late 1890's that physicists confirmed atoms were in fact made up of smaller constituent particles, or subatomic particles, after the discovery of the negatively-charged electron by J.J. Thomson [1]. Attention then switched to producing a model that could describe the internal structure of the atom. This search gave rise to the field of nuclear physics. The "plum pudding model" of the atom, proposed by J.J. Thomson in 1904 [2], hypothesised that electrons were distributed within a positively charged region of space, thus producing neutral atoms. The work of Ernest Rutherford, who had earlier been under the supervision of J.J. Thomson in 1904, and his students in 1911 on the eponymous Geiger-Marsden experiments [3] revealed a different picture. By firing α-particles at a gold foil and detecting the scattering angle, it was determined that most α-particles passed straight through the foil while a tiny fraction were deflected back at angles $> 90°$. This lead to the conclusion that small volumes of positive charge existed within the gold foil that were separated largely by empty space. These findings formed the basis of the Rutherford model of the atom which placed a positively charged nucleus at the

centre, where the majority of the atomic mass was concentrated, with the surrounding area consisting of a "cloud" of electrons. A couple of years later Niels Bohr would refine this model, with his Bohr model of the atom [4] stating that electrons must orbit the nucleus in discrete energy levels as opposed to existing in within an energy continuum around the nucleus. In the following decades, intense interest in solving the puzzle of the atomic nucleus lead to further fundamental discoveries, including the existence of the proton in 1919 [5] and neutron in 1932 [6], collectively referred to as nucleons, as constituent particles of the nucleus.

In 1914, the Bohr model received experimental justification from the Franck-Hertz experiment [7, 8]. Here energetic electrons that passed through a mercury vapour lost a specific energy ($\sim$ 4.9 eV) corresponding to an electron excitation, while light detected from the vapour had a wavelength corresponding to the $\sim$ 4.9 eV lost from the initial electron (by $E = hc/\lambda$). This confirmed the discrete nature of electron orbits in atoms and one of the first measured spectral lines for an individual atomic transition. However, around the time of the discovery of the neutron, physicists were attempting to describe the phenomenon of the "splitting" of its spectral line into multiple components. This was discovered in 1892 by Albert A. Michelson [9] in the spectra of mercury and thallium. The first physical interpretation of this phenomenon was not published until 1924 [10] when Wolfgang Pauli suggested that hyperfine structure arises due to the coupling of a nuclear angular momentum with the angular momentum of electrons to form a resultant angular momentum. By 1935 the understanding of hyperfine structure had improved greatly due to the the work of Enrico Fermi [11] and Hermann Schüler. They stated that the hyperfine interaction consisted of magnetic and electric components, leading to the splitting of single energy levels into multiple levels that each have different couplings of nuclear and electron angular momenta. It is transitions between these shifted levels that produce the additional spectral lines observed experimentally. Our understanding of hyperfine structure has continued to improve; the measurement of hyperfine spectra is an important tool for determining the isotope shifts, nuclear moments and nuclear spins of nuclei. The development of an experimental technique to probe the hyperfine structure of atoms therefore became a priority.

One experimental method that allows the nature of atomic energy levels to be understood is optical spectroscopy. The technique is based on the detection of electromagnetic radiation absorbed by or emitted from atoms that have resonantly interacted with light. Perhaps the most notable advance in optical spectroscopy occurred in the early 1970's when the tunable laser was first introduced. The ability to finely tune the output wavelength of laser light facilitated the identification and study of atomic transitions via laser spectroscopy. As laser technology advanced, the power of lasers increased, tunable wavelength ranges increased and, most importantly for the study of hyperfine structure, laser linewidths decreased. The combination of these properties of modern lasers meant that laser spectroscopy provided an ideal method by which the small perturbations to atomic energy levels could be probed. In the context of nuclear physics, laser spectroscopy provides model-independent measurements of the nuclear moments, nuclear spins and isotope shifts for the ground and long-lived isomeric states of nuclei. Additionally, the technique can be used to discover long-lived isomeric states.

The measurement of nuclear properties of stable (or long-lived) nuclei have long been accessible by a wide variety of experimental techniques, meaning these properties are well understood. However, given that the majority of nuclei lie far from stability and have unknown properties, there was great interest in developing facilities to study more exotic nuclei. This lead to the emergence of Radioactive Ion Beam (RIB) facilities for the production of radioactive nuclei in large quantities. In order to study these short-lived nuclei effectively, RIB facilities have been developed to produce nuclei in reactions, extract them efficiently and electrostatically transport them in a sufficient quantity before they decay. As a result, laser spectroscopy at RIB facilities can probe short-lived states directly, with measurable state lifetimes at the order of milliseconds. Continual developments at these facilities have increased the sensitivity of the laser spectroscopy technique, with the ion cooler-buncher providing bunched ion beams to experiments being the most notable modern advancement. By increasing the number of isotopes measurable via laser spectroscopy experiments, the evolution of nuclear structure with changing neutron number can be understood over a greater uninterrupted range. By measuring more and more isotope chains, whole regions of the

nuclear chart can be mapped and regions of interest for future studies can be uncovered.

1.1 This Work

The main body of this thesis will focus on the analysis of experimental data in the form of hyperfine spectra of Zn ($Z = 30$) isotopes obtained from the COLlinear LAser sPectroScopy experiment COLLAPS at ISOLDE, CERN. By analysing the hyperfine spectrum of an isotope, its nuclear spin I, magnetic dipole moment μ and spectroscopic quadrupole moment Q_s can be determined. The measurement of these quantities across the Zn isotope chain will provide information on the evolution of nuclear structure as N changes. The Zn isotope chain so far remains incomplete with regards to these quantities, with the values of μ, Q_s and I determined from other experiments prior to this work shown in Table 1.1. Regarding nuclear electromagnetic moments, μ remains unknown for the ground states of $^{69-79}$Zn and the isomeric states of $^{73-79}$Zn, while Q_s is yet to be determined for $^{71-79}$Zn. The nuclear spin I for the ground and isomeric states of $^{73-79}$Zn have only been tentatively assigned based on inferences from decay spectroscopy experiments. Since laser spectroscopy provides an *absolute measurement* of the nuclear spin, this work will unambiguously assign spins to these states and therefore also higher lying states based on nuclear decay data.

To collect all the relevant data for these isotopes, we adopt the collinear laser spectroscopy technique (see Chapter 4 for more information) at the COLLAPS beam line at ISOLDE, CERN. The already successful collinear laser method and its application at ISOLDE has advanced in the past decade with the addition of the ISCOOL radio frequency quadrupole (RFQ) cooler and buncher [12]. The delivery of temporally well-defined ion bunches to the COLLAPS setup is the primary advantage of ISCOOL, with bunched beams leading to background suppression in hyperfine spectra of the order of $\sim 10^4$. A reacceleration voltage is applied to the cooled ion bunches to reduce longitudinal velocity spread induced by kinetic energy spread, thus reducing the broadening of spectral lines [13] and increasing the resolution of peaks in the spectrum. The combination of ion beam cooling and acceleration

Table 1.1: Literature values of μ, Q_s and I for the ground and isomeric states from $^{63-79}$Zn. Tentatively assigned nuclear spins are shown in parentheses along with the references they are taken from, while all μ and Q_s values are taken from [14].

A	I	$\mu_{\text{lit}}(\mu_N)$	$Q_{\text{s,lit}}$(b)
63	3/2	−0.28164(5)	+0.29(3)
65	5/2	+0.7690(2)	−0.023(2)
67	5/2	+0.875479(9)	+0.150(15)
		+0.8752049(11)	
69	1/2	—	—
69^m	9/2	1.157(2)	−0.51(5)
71	1/2	—	—
71^m	9/2	1.052(6)	—
73	(1/2) [15]	—	—
73^m	(5/2) [15]	—	—
75	(7/2) [16]	—	—
75^m	(1/2) [17]	—	—
77	(7/2) [18]	—	—
77^m	(1/2) [18]	—	—
79	(9/2) [19]	—	—
79^m	(1/2) [19]	—	—

voltage means collinear laser spectroscopy provides a high-resolution method with excellent background suppression for the measurement of hyperfine structure.

In short, this work will aim to extend the known values of μ, Q_s and I in odd-A Zn isotopes to ^{79}Zn. These values for the ground and isomeric states of $^{73-79}$Zn will be measured for the first time, while the values for $^{63-71}$Zn will be also measured in order to assess the accuracy of literature values and our analysis process. The general structure of this thesis will outline the background theory, the experimental techniques and results in the following order:

- Chapter 2 - description of how the hyperfine splitting of atomic levels occurs and how the resulting hyperfine structure can be observed via atomic spectra. The way in which the nuclear spin I, magnetic dipole moment μ, spectroscopic quadrupole moment Q_s and mean-square charge-radius $\langle r^2 \rangle$ are extracted from a hyperfine spectrum is explained.

- Chapter 3 - explanation of the nuclear shell model and how it can be used to pro-

vide estimates of observable nuclear properties. A number of large-scale shell model interactions are also introduced that will be used in the discussion section in Chapter 6.

- Chapter 4 - detailed outline of RIB production at the ISOLDE facility (CERN) and the collinear laser spectroscopy experiment COLLAPS at ISOLDE.

- Chapter 5 - explanation of the data analysis process used to determine nuclear properties from hyperfine spectra of Zn isotopes. In this chapter the ground and isomeric state nuclear spins of $^{73-79}$Zn will be confirmed, and the final electromagnetic moments for $^{63-79}$Zn stated.

- Chapter 6 - the measured low-lying spin states and electromagnetic moments for $^{63-79}$Zn will be compared to large-scale shell model interaction predictions.

- Chapter 7 - summary of the experimental work completed, the nuclear properties extracted from spectra and the implications of the results.

1.2 Physics Motivation

In terms of its position in the nuclear chart, Zn proves an appealing prospect for further examination due to its proximity to the $Z = 28$ shell closure. As the first even-Z element after Ni ($Z = 28$), the odd-N isotopes provide the first glimpse of neutron dominated nuclear structure beyond the shell closure and how quickly it develops from stability. The broad range of isotopes available for study in the Zn chain, particularly on the neutron-rich side, also provides a chance to investigate the $N = 50$ shell gap. The Zn chain is rare in this aspect as the stability of the $Z = 28$ and $N = 50$ shell closures can be simultaneously tested. Experimental results can be compared to predictions from shell-model interactions with varying model spaces, ranging from those with excitations limited to orbitals between $N, Z = 28 - 50$ to those extending beyond these shell closures. This variation in model space will allow informed conclusions to be reached regarding the stability of the $Z = 28$ and $N = 50$ closures, and hence the potentially doubly magic nature of the neutron-rich nucleus

^{78}Ni [20, 21]. This nucleus is the most exotic proposed doubly magic nucleus (in terms of N/Z ratio) and presents a challenge experimentally as it is difficult to produce at RIB facilities. This isotope has garnered great interest from numerous branches of physics, including nuclear theorists due to the challenging model space required to describe its nuclear properties, and astrophysicists as ^{78}Ni is an important waiting point in the astrophysical r-process [22].

It is predicted that the filling of the $\nu g_{9/2}$ orbit will reduce the spin-orbit splitting between the $\pi f_{7/2}$ and $\pi f_{5/2}$ levels and hence the $Z = 28$ shell gap by means of the tensor interaction [23]. Collinear laser spectroscopy experiments on Cu [24, 25] ($Z = 29$) and Ga [26] ($Z = 31$) revealed a ground state spin change beyond the $N = 40$ sub-shell closure as neutron number increases. This effect is attributed to the tensor interaction which causes the lowering of the $\pi f_{5/2}$ orbital below $\pi p_{3/2}$ as $\nu g_{9/2}$ is filled, resulting in a ground state spin change from $3/2^-$ to $5/2^-$ between $^{73}_{29}$Cu$_{44}$ and $^{75}_{29}$Cu$_{46}$ and also between $^{79}_{31}$Ga$_{48}$ and $^{81}_{31}$Ga$_{50}$. Since Zn lies between Cu and Ga in terms of proton number, the determination of this level inversion in Zn will reveal the Z-dependence of this effect, although the fact that Zn is an even-Z nucleus means the inversion will have to be inferred from shell-model predictions as the effect on measurable quantities will be extremely subtle.

An isomeric state in ^{79}Zn with a tentatively assigned spin-parity of $1/2^+$ has recently been discovered [19]. The spin-parity assigned to this state suggests the unpaired neutron must occupy an orbital that lies beyond the $N = 50$ shell closure, hence the isomer is expected to be intruder in its nature. The lowering of the $1/2^+$ intruder level has be tracked through $N = 49$ isotones from $^{87}_{38}$Sr to $^{81}_{32}$Ge [27], and has since been measured in ^{79}Zn along with the $5/2^+$ intruder level [19]. By measuring its hyperfine structure, the nuclear spin and magnetic dipole moments of the isomer can be determined, while comparisons to shell model calculations can shed light on the dominant wave function configurations and hence the orbital in which the unpaired neutron lies. A recently developed interaction, named PFSDG-U [28], will be adopted here as its neutron valence space extends beyond the aforementioned interactions to include the full *sdg*-shell ($N = 40$ to $N = 70$). The interaction can also be utilised further to provide a theoretical estimate of the $N = 50$ shell gap, and hence an insight into its much

studied robustness in ^{78}Ni and in surrounding nuclei [28, 29, 30, 31].

Chapter 2

Atomic Spectra

The measurement of nuclear properties is required for understanding how nuclear structure develops across the chart of nuclides. Laser spectroscopy provides one such method by which these properties can be obtained experimentally. These properties, including nuclear spin, magnetic dipole moments, spectroscopic quadrupole moments, and isotope shifts, and how they relate to the hyperfine structure of spectral lines will be outlined in this chapter.

2.1 Fine Structure

Prior to discussing the splitting of spectral lines into fine and hyperfine levels, we must first look at the gross structure of an atomic transition. The gross structure of atomic energy levels consists of discrete states of different principal quantum number, n, as described by the Bohr model of the atom. The excitation of an electron, assumed to have no spin, between two such energy states and its subsequent de-excitation reveals this structure through the detection of an emitted photon, whose energy corresponds to the difference in energy between the two electronic states and is characteristic of a given transition in the atom. The discrete energy of this excitation is referred to as a spectral line. Fine structure manifests as the splitting of these spectral lines due to the different couplings of the individual electron spin, s, and its subsequent coupling with the orbital angular momentum, l, to form the total electron angular

momentum, j. In the LS coupling scheme the individual electron spins, s_i, are summed over the number of electrons in the atom i to form the total electron spin S, and similarly the individual orbital angular momenta, l_i, is summed over i to give the total orbital angular momentum L. The coupling of L and S then gives the total angular momentum J of the atom. Alternatively, in the jj coupling scheme l_i and s_i couple to give an individual total angular momentum j_i. These then couple together to form the total angular momentum J of the atom. These couplings along with the inclusion of the spin-orbit interaction leads to the difference between the fine structure and the gross structure, and work to lift the degeneracy of orbital angular momentum states into levels with total angular momentum J. The resulting level structure can be probed with laser spectroscopy, whereby monochromatic photons from the laser are tuned to the specific excitation frequency of a transition between two states within the atom, hereafter referred to as the resonant frequency. After excitation, the atom de-excites to a lower energy state and emits a photon as a result of spontaneous emission, which can be counted.

Since the energy levels within multi-electron atoms are not only dependent upon the electron configuration but also the total angular momentum, they are commonly denoted by a shorthand description of the total angular momentum quantum numbers (which are capitalised when there are contributions from many electrons) when referred to in spectroscopy. This simplified notation is widely used to characterise the levels involved in atomic transitions in both neutral atoms and charged ions.

In the LS coupling scheme each level is described by its electron configuration (starting from the previous inert gas), a term symbol and its total angular momentum J, all of which are isotope independent for a given element. The term symbol portrays the total spin quantum number S and the total orbital quantum number L followed by the total angular momentum quantum number J in the form $^{2S+1}L_J$, where L is written as the letter corresponding to the electron orbital (S,P,D,F...). For a given L and S the number of possible states of J is given by the spin multiplicity of $2S+1$ when $L > S$. For $L < S$, the number of J states is $2L+1$. In either case, J can take on any value within the range of $J = L+S, L+S-1, ..., |L-S|$.

The lowest-lying energy levels in neutral Zn atoms are shown in Table 2.1. Taking the excited state $3d^{10}4s4p\ ^3P_2^o$ as an example, the electron configuration beyond that of the inert gas Ar is displayed as $3d^{10}4s4p$ while for the ground state it is $3d^{10}4s^2$. Hence the excited state is dominated by an electron excitation from a $4s$ orbit to the $4p$. The spin state is a triplet as denoted by the superscript '3', and so $S = 1$ ($2S + 1 = 3$), the atomic orbital P indicates that $L = 1$ and its subscript '2' represents the J value. The secondary superscript 'o' signifies an odd-parity term symbol due to an odd number of electrons in an odd-parity orbital (i.e. $p, f, h, ...$). The energy of these levels is given in units of cm^{-1} and the difference between these quantities represents the frequency to which the laser must be tuned to probe a transition between two atomic levels, referred to as the wavenumber. Quantum states are subject to selection rules that constrain the allowed transitions in an atom based on the transition multipolarity (Eλ/Mλ corresponding to either electric or magnetic transitions). In the case of electric dipole transitions (E1) between atomic states, the selection rules of $\Delta J = 0, 1$ and $J = 0 \nrightarrow J = 0$ apply and so must be considered when selecting the upper and lower levels for spectroscopy. These transitions can be found for a range of elements in datasets compiled from experimental results, such as the Kurucz [32] or NIST [33] databases.

Table 2.1: Atomic energy levels in neutral Zn nuclei in terms of their electron configuration, total angular momentum quantum numbers, and energy relative to the ground state [33].

Configuration	Term	J	Level (cm^{-1})
$3d^{10}4s^2$	^1S	0	0.000
$3d^{10}4s4p$	$^3P^o$	0	32 311.350
		1	32 501.421
		2	32 890.352
$3d^{10}4s4p$	$^1P^o$	1	46 745.413
$3d^{10}4s5s$	^3S	1	53 672.280
$3d^{10}4s5s$	^1S	0	55 789.228
$3d^{10}4s5p$	$^3P^o$	0	61 247.904
		1	61 274.455
		2	61 330.891

2.2 Hyperfine Structure

Beyond the scale of fine structure, a phenomenon occurs due to the electromagnetic field generated by atomic electrons at the site of the nucleus and its interaction with the nuclear spin and moments. This effect produces small shifts in the energy of electron states, the scale of which is $\sim 10^3$ smaller than that of fine structure, and is therefore referred to as hyperfine structure. In terms of quantum numbers, the interaction is defined as the coupling of the nuclear spin, I, and the total electron angular momentum, J, to form the total (electronic plus nuclear) angular momentum, F, that would otherwise be degenerate without any perturbative effects. Analogous to the case discussed earlier for J, the number of F states is dictated by the values of I and J, both of which must be greater than zero. If $I > J$, there are $2J + 1$ possible F values, while the reverse produces $2I + 1$ values. The range of possible F values is analogous to those discussed earlier for J, with $F = I + J, I + J - 1, ..., |I - J|$. In the instance that $I = 0$ for a given state, as is seen in, for example, the ground states of all even-even nuclei due to the tendency of nucleons to couple pairwise to zero, there will only be one observable transition between the single hyperfine states of the upper and lower levels. This produces a distinct hyperfine spectrum with only a single transition peak.

Atomic electrons experience a potential generated by the nucleus, which is comprised of numerous components

$$V = V_{\text{monopole}} + V_{\text{dipole}} + V_{\text{quadrupole}} + V_{\text{octupole}} + ..., \tag{2.1}$$

where the monopole term represents the Coulomb-like potential that determines the electron energy levels. The additional components, referred to as 'multipoles', are responsible for smaller perturbations to the hyperfine energy levels produced by the monopole term, the effects of which decrease with increasing term order (as $1/r^n$, where n depends on the term). The combination of these perturbations leads to the splitting of J states into hyperfine F states with an energetic separation of ΔE_{HFS}. Dipole transitions from one of the lower orbital

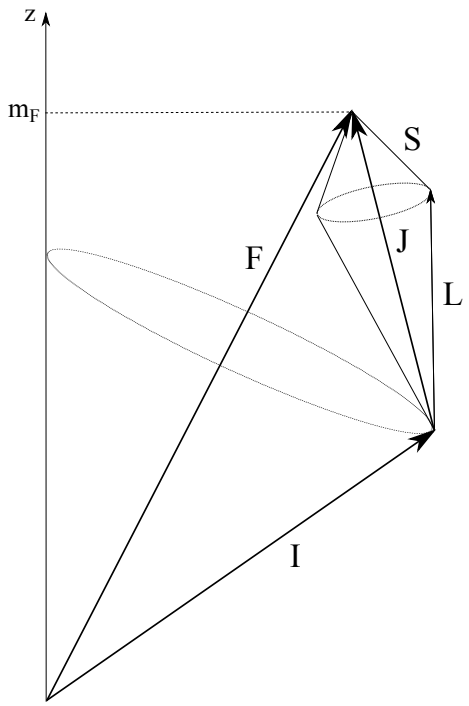

Figure 2.1: The precession of the nuclear spin I and the total electron angular momentum J around the total angular momentum F. The J component is formed by the coupling of the orbital angular momentum L and the electron spin angular momentum S.

F states to an F state in the higher orbital follow the selection rules:

$$\Delta F = 0, \pm 1 \qquad F = 0 \nrightarrow F = 0. \tag{2.2}$$

Through the use of a laser tuned to the frequency region of a transition between the two selected J states, the energy of atomic F state transitions can be measured from the resulting hyperfine spectrum. The scale of perturbations to F states created from the interaction of the nucleus and orbital electrons can be quantified by the nuclear electromagnetic multipole moments. These moments have parity of $(-1)^L$ for electric moments and $(-1)^{L+1}$ for magnetic moments (where $L = 0$ for monopole, $L = 1$ for dipole, $L = 2$ for quadrupole, and so on). The number of multipole moments are reduced due to the fact that all odd-parity static multipole moments vanish during the computation of their expectation values [34], and so the electric monopole, magnetic dipole, electric quadrupole, etc., are the non-vanishing moments.

Of the remaining moments, the magnetic dipole moment and electric quadrupole moment are of particular interest for the purpose of understanding nuclear structure through hyperfine structure. The electric monopole moment does not contribute to hyperfine splitting, while the effects of higher order moments are beyond the capabilities of laser spectroscopy and are therefore considered negligible. The remainder of this thesis will focus on the magnetic dipole moments and electric quadrupole moments of nuclei, both of which are highlighted in more detail in the following sections.

2.2.1 Magnetic Dipole Moment

Classically, the magnetic dipole moment $\boldsymbol{\mu}$ vector occurs perpendicular to the orbit of charged particles that in turn create currents. The magnetic dipole moment can be used to describe the distribution and effect of these currents on other moving charges, which is analogous to the orbit of electrons around a nucleus. By considering a distribution of currents over a volume in space, it can be shown that the corresponding z-component of the magnetic dipole moment μ_z in the quantum realm is

$$\mu_z = \frac{e\hbar}{2m} m_l, \tag{2.3}$$

where e is the electric charge, m is the mass of the particle and m_l is the projection of the orbital angular momentum l. In the presence of an externally applied magnetic field B, the magnetic moment will adopt its lowest energy configuration and align with the direction of the applied field (z-axis). The quantity measured experimentally represents the maximum projection of the magnetic moment on the z-axis, where the maximum value of m_l is $+l$, resulting in the magnetic moment μ

$$\mu = \frac{e\hbar}{2m} l. \tag{2.4}$$

By using the the proton mass m_p in Equation 2.4 we obtain the physical constant of the magnetic moment from the quantity $e\hbar/2m$, called the nuclear magneton μ_N, which is equal

to 3.15245×10^{-8}eV/T. To consider all contributions to the magnetic moment, an addition is made to Equation 2.4 to account for the intrinsic spin of the nucleon s, for which there is no classical analogue. We can then state that

$$\boldsymbol{\mu} = (g_l \boldsymbol{l} + g_s \boldsymbol{s})\mu_N/\hbar, \tag{2.5}$$

where g_l and g_s represent the g-factors for the orbital and intrinsic spin contributions to the magnetic moment, respectively. These g-factors vary for each nucleon, with $g_l = 1$ and $g_s = 5.5856912$ for protons and $g_l = 0$ and $g_s = -3.8260837$ for neutrons. To apply this principle to a real nucleus, we must consider the sum of both the orbital and spin angular momenta of all nucleons, such that $\sum_{i=1}^{A}(\boldsymbol{l}_i + \boldsymbol{s}_i)$, which produces the total nuclear angular momentum vector $\boldsymbol{I}$. This allows us to rewrite Equation 2.5 as

$$\mu_I = g_I I \mu_N, \tag{2.6}$$

where μ_I is the nuclear magnetic dipole moment and I is the nuclear spin quantum number, the maximum projection of the vector $\boldsymbol{I}$ on the quantisation axis. The interaction of the nuclear magnetic dipole moment with the magnetic field generated by the motion of electrons $\boldsymbol{B}_e$ results in the magnetic dipole contribution to the hyperfine splitting. For an atomic nucleus, the energy of this interaction, E_μ, is given by [34]

$$E_\mu = \frac{A}{\hbar^2}(\boldsymbol{I} \cdot \boldsymbol{J}), \tag{2.7}$$

where

$$A = \frac{\mu B_e(0)}{IJ}, \tag{2.8}$$

where $B_e(0)$ is the magnetic field at the site of the nucleus due to orbiting electrons and A is the magnetic hyperfine coefficient. The latter of these can be measured directly from a hyperfine spectrum and will be referenced again later in this chapter.

The quantity $\boldsymbol{I} \cdot \boldsymbol{J}$ can be evaluated by taking the vector sum of $\boldsymbol{I}$ and $\boldsymbol{J}$ $(= \boldsymbol{F})$ and squaring, giving

$$\boldsymbol{F}^2 = \boldsymbol{I}^2 + 2(\boldsymbol{I} \cdot \boldsymbol{J}) + \boldsymbol{J}^2, \tag{2.9}$$

which, when rearranged to make $\boldsymbol{I} \cdot \boldsymbol{J}$ the subject gives

$$\boldsymbol{I} \cdot \boldsymbol{J} = \frac{1}{2}\Big[\boldsymbol{F}^2 - \boldsymbol{I}^2 - \boldsymbol{J}^2\Big], \tag{2.10}$$

$$\langle \boldsymbol{I} \cdot \boldsymbol{J} \rangle = \frac{\hbar^2}{2}\Big[F(F+1) - I(I+1) - J(J+1)]. \tag{2.11}$$

Therefore, the magnetic dipole contribution to the splitting of an atomic level into hyperfine F states is

$$\frac{\Delta E_\mu}{h} = \frac{1}{2}AK, \tag{2.12}$$

where $K = F(F+1) - I(I+1) - J(J+1)$ is used to simplify the expression. The interaction energy is divided by h since the hyperfine splitting is typically evaluated as a frequency and given in units of MHz. An example of this level splitting is shown in Figure 2.2 for the $I = 3/2$ nuclear ground state of ^{63}Zn for the $3d^{10}4s4p\ ^3\mathrm{P}^\mathrm{o}_2$ level in neutral Zn.

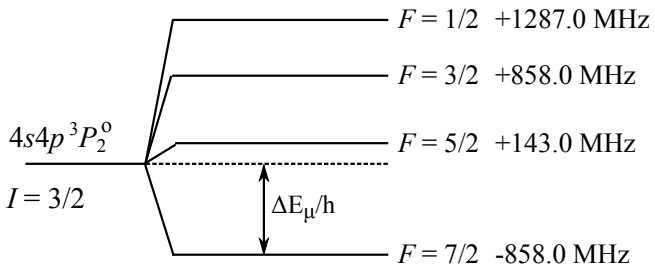

Figure 2.2: Scale representation of the observed hyperfine level splitting of the $3d^{10}4s4p\ ^3P^\mathrm{o}_2$ level in the $I = 3/2$ ground state of ^{63}Zn due to the magnetic dipole component of the hyperfine interaction.

2.2.2 Hyperfine Anomaly

The assumption of a point-like nucleus underpins the method of extracting the magnetic dipole moment from the previous section. While this simplifies the expressions, the reality is that a nucleus occupies a finite volume in space. This has an effect on how the magnetic dipole moment μ and the hyperfine interaction energy E_M are considered, since the interaction is sensitive to the distribution of magnetisation over the nuclear volume. This sensitivity effects the magnetic hyperfine coefficient A such that

$$A = A_{\text{point}}(1 - \epsilon), \tag{2.13}$$

where ϵ is the hyperfine anomaly. This leads to a reduction of the A coefficient and subsequently the magnetic dipole moment as derived from Equation 2.8.

2.2.3 Electric Quadrupole Moment

An atomic nucleus can possess an electric quadrupole moment that reflects the shape of its charge distribution based on the sign and magnitude of the moment. A classical description of the charge distribution and how it couples to the quadrupole moment in the rest frame of the nucleus is represented by the intrinsic quadrupole moment Q_0

$$Q_0 = \frac{1}{e}\int (3z^2 - r^2)\rho d\nu, \tag{2.14}$$

where e is the electric charge, ρ is the charge density, $r^2 = x^2 + y^2 + z^2$, z represents the axis of symmetry and $d\nu$ is the volume element of the charged nucleus that is integrated over. For a positive quadrupole moment, we assign the nucleus a prolate shape due to an extended charge distribution in the z-axis, while a negative Q_0 has an extended distribution in the x-y plane, called oblate. These shapes are often assigned to nuclei with an odd number of protons or neutrons, whereas a zero moment corresponds to a spherical nucleus with all paired nucleons. These nuclear shapes are shown in Figure 2.3.

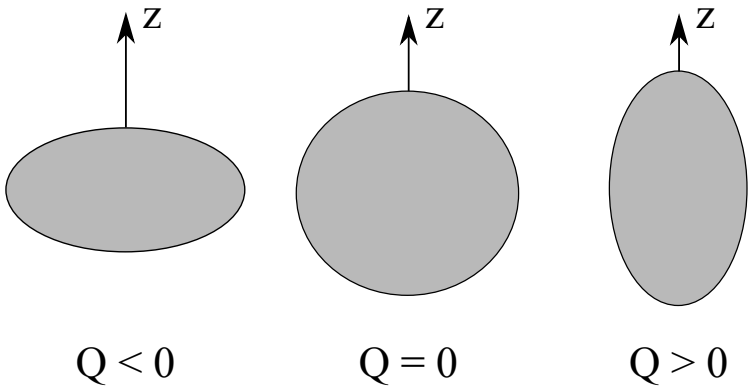

Figure 2.3: Visualisation of the nuclear charge distribution and its relation to the electric quadrupole moment Q. The axis of symmetry is labelled by z.

The intrinsic quadrupole moment cannot be measured directly by means of laser spectroscopy due to the time-averaged appearance in the laboratory frame of the nucleus. The measured quantity instead gives the projection of Q_0 on the quantisation axis, referred to as the spectroscopic quadrupole moment, Q_s. For a well-deformed nucleus with $I > 1/2$, the two quantities can be related by

$$Q_s = Q_0 \left(\frac{I(2I-1)}{(I+1)(2I+3)} \right), \tag{2.15}$$

where I is the nuclear spin quantum number. The electric quadrupole contribution to the hyperfine splitting, E_Q, arises as a result of the quadrupole moment interacting with the electric field gradient produced by orbiting electrons, $\langle \partial^2 V / \partial z^2 \rangle$. This quantity is contained within the electric hyperfine coefficient B, which is given as

$$B = eQ_s \left\langle \frac{\partial^2 V_e}{\partial z^2} \right\rangle. \tag{2.16}$$

As for the magnetic hyperfine coefficient A mentioned earlier, B can be measured directly from a hyperfine spectrum. For a nucleus with $I > 1/2$ and $J > 1/2$, the electric quadrupole contribution to the observable hyperfine splitting (again given as a frequency) is

$$\frac{\Delta E_Q}{h} = \frac{3K(K+1) - 4I(I+1)J(J+1)}{8I(2I-1)J(2J-1)}B. \tag{2.17}$$

A combination of the splitting due to the magnetic dipole and electric quadrupole components of the hyperfine interaction gives the total hyperfine splitting, ΔE_{HFS}, for a given atomic J level

$$\frac{\Delta E_{\mathrm{HFS}}}{h} = \frac{\Delta E_\mu}{h} + \frac{\Delta E_Q}{h} = \frac{1}{2}AK + \frac{3K(K+1) - 4I(I+1)J(J+1)}{8I(2I-1)J(2J-1)}B. \tag{2.18}$$

This splitting is shown for the $3d^{10}4s4p\ {}^3P_2^{\mathrm{o}}$ level in the $I = 3/2$ ground state of ^{63}Zn in Figure 2.4, with the splitting due to the electric component displayed as a perturbation to the magnetic splitting (shown previously in Figure 2.2).

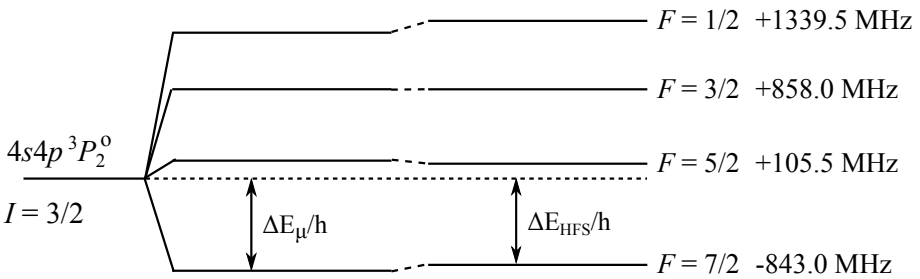

Figure 2.4: Final splitting of the $3d^{10}4s4p\ {}^3P_2^{\mathrm{o}}$ level in the $I = 3/2$ ground state of ^{63}Zn after the perturbations due to the electric quadrupole component of the hyperfine interaction are considered in addition to contributions from the magnetic dipole component.

2.2.4 Hyperfine Spectrum

As mentioned earlier in Section 2.2, laser light tuned to the frequency region of a transition between two atomic states, J_{lower} and J_{upper}, can be used to probe the splitting of J states into hyperfine F states. In the resulting hyperfine spectrum, peaks correspond to transitions between F states in the lower and upper atomic levels (F_{lower} and F_{upper}), which in terms of frequency, are given as

$$\gamma = \nu + \alpha_{\mathrm{u}} A_{\mathrm{u}} + \beta_{\mathrm{u}} B_{\mathrm{u}} - \alpha_{\mathrm{l}} A_{\mathrm{l}} - \beta_{\mathrm{l}} B_{\mathrm{l}}, \tag{2.19}$$

$$\alpha = \frac{K}{2}, \tag{2.20}$$

$$\beta = \frac{3K(K+1) - 4I(I+1)J(J+1)}{8I(2I-1)J(2J-1)}, \tag{2.21}$$

where ν is the centroid of the spectrum, A and B are the hyperfine coefficients, and the subscripts 'u' and 'l' denote the upper and lower transition states, respectively. The factors α and β will vary based on the quantum numbers corresponding to the each state in the transition. An example of this is shown in Figure 2.5. This figure shows the complete hyperfine structure of the $I = 3/2$ ground state of ^{63}Zn obtained from the $4s4p\ ^3P_2^{\mathrm{o}} \rightarrow 4s5s\ ^3S_1$ atomic transition.

A reference frequency is subtracted from the spectrum to reduce frequency values from the order of THz to MHz, since it is only the hyperfine spacings that are of interest. This is shown in Figure 2.5 where the x-axis is labelled as "relative frequency". The reference frequency used in this work corresponds to the wavenumber of the $4s4p\ ^3P_2^{\mathrm{o}} \rightarrow 4s5s\ ^3S_1$ transition (20781.928 cm^{-1} [32]). The subtraction of a reference frequency will not affect the hyperfine A and B parameters extracted from the spectrum since they are only dependent on the *relative* spacing of peaks.

There are four F_{lower} states ($2I + 1$, $I = 3/2$) since $I < J$ for the lower state $4s4p\ ^3P_2^{\mathrm{o}}$. For the upper state $4s5s\ ^3S_1$, there are three F states as $I > J$ ($2J + 1$, $J = 1$). Using the selection rules outlined in Equation 2.2, there are eight permitted transitions between F_{upper} and F_{lower} (highlighted by arrows in Figure 2.5) and therefore eight observable hyperfine transition peaks in this spectrum.

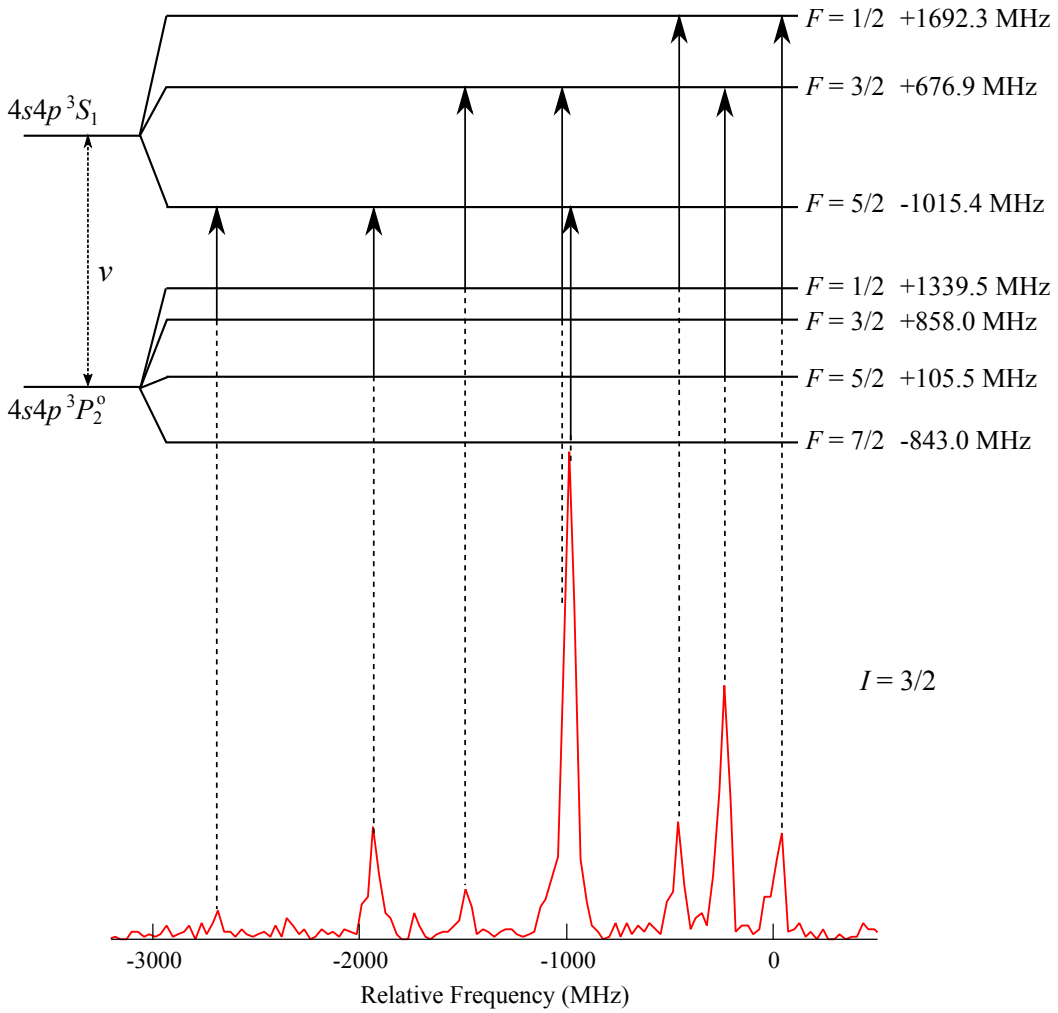

Figure 2.5: Hyperfine structure of the $I = 3/2$ ground state of ^{63}Zn measured via the $4s4p\ ^3P_2^o \rightarrow 4s5s\ ^3S_1$ atomic transition using collinear laser spectroscopy. The splitting of atomic J levels into hyperfine F states is shown here, with the F quantum number of each state and its frequency splitting from the unperturbed J state given on the right hand side. Allowed transitions between F states based on selection rules denoted by arrows.

2.3 Extracting Nuclear Properties

From a measured hyperfine spectrum it is possible to determine the nuclear spin I, magnetic dipole moment μ and spectroscopic quadrupole moment Q_s. The nuclear spin can sometimes be determined simply by the number of peaks in the spectrum, although more versatile techniques are often required to determine I reliably. This quantity is vital for our understanding

of level systematics within nuclei and for the correct evaluation of nuclear properties.

The relative spacing of peaks provides information on the hyperfine A and B parameters required to calculate μ and Q_s via Equations 2.8 and 2.16, respectively. However, values of B_e and $\langle \partial^2 V / \partial z^2 \rangle$ in these equations are difficult to determine reliably with atomic physics calculations, and hence alternative methods are required to calculate electromagnetic moments. Some of the techniques used to determine μ, Q_s and I from hyperfine spectra are highlighted in the following sections.

2.3.1 Determining Nuclear Spin

The correct value of nuclear spin is required to calculate the hyperfine A and B parameters in Equations 2.12 and 2.17. Further to this, the *absolute measurement* of ground and isomeric state spins via laser spectroscopy can underpin the spin assignments of excited states based on the relative spin assignments from decay spectroscopy experiments.

A method for reliably determining the nuclear spin of a state is therefore imperative, and for many hyperfine structures this can be as simple as counting the number of transition peaks in the spectrum. However, at higher values of nuclear spin (i.e. $I > J_{\mathrm{u,l}}$) their hyperfine structures will be represented by the same number of peaks, meaning this technique is no longer applicable. More stringent methods are required in this instance, and the following sections outline some alternative methods for determining the nuclear spin, which are listed in order of applicability.

Relative Peak Spacing

Each nuclear spin value produces a characteristic hyperfine structure that can be recognised not only by the number of transition peaks but also their relative frequency spacing. A comparison of experimental data to the model hyperfine spectrum of a given spin value can determine the correct spin assignment. Even if the model spectrum has the correct number of peaks, it may not be able to fit to all simultaneously due to the spin dependent hyperfine coefficients in Equations 2.19. This process can be repeated until a satisfactory match is

found between the two hyperfine structures and a spin assignment is confirmed. In this sense, the spectrum provides a fingerprint unique to the nuclear spin.

Hyperfine Coefficient Ratio

If the above is not conclusive, another such method that will be used in the analysis outlined in Chapter 5, takes the ratio of the hyperfine A coefficients of the upper and lower states of each isotope measured with an atomic transition, given in Equation 2.8, to show that

$$\frac{A_{\text{lower}}}{A_{\text{upper}}} = \frac{B_{\text{e,lower}}}{B_{\text{e,upper}}} \frac{J_{\text{upper}}}{J_{\text{lower}}}, \tag{2.22}$$

where the subscripts 'lower' and 'upper' denote the different atomic states. In this relation the μ and I values cancel out as they are independent of atomic configuration. Given the assumption that the magnetic field from electrons B_e remains constant for both states across the isotope chain and that J_{upper} and J_{lower} are constant for each isotope, the ratio of the hyperfine A coefficients should also remain constant. By comparing measured A coefficients to the known ratio for another isotope in the chain, it can be determined whether the nuclear spin corresponding to the A values is correct. A very small deviation ($< 1\%$) from the known ratio can be indicative of the presence of a hyperfine anomaly, but a more significant deviation points to an incorrect spin assignment. Likewise, the ratio of the electric hyperfine parameters, $\frac{B_{\text{lower}}}{B_{\text{upper}}}$, will also be constant along an isotope chain, if the correct nuclear spin has been used in the analysis.

Intensity of Transition Peaks

The intensity of observed transitions between hyperfine states of different atomic levels is dependent upon the angular momentum of the involved hyperfine states and the line strength of the unperturbed atomic transition, $S_{J_{\text{lower}}J_{\text{upper}}}$. As such, without external contributions, the absolute intensity of hyperfine transition peaks in the spectrum are given by

$$S_{F_{\text{lower}}F_{\text{upper}}} = (2F_{\text{lower}}+1)(2F_{\text{upper}}+1)\begin{Bmatrix} F_{\text{lower}} & F_{\text{upper}} & 1 \\ J_{\text{upper}} & J_{\text{lower}} & I \end{Bmatrix}^2 S_{J_{\text{lower}}J_{\text{upper}}} \tag{2.23}$$

where $\{...\}$ is a Wigner 6-j symbol. The normalisation of the calculated intensities to produce relative values that can be compared to the observed hyperfine spectrum can allow the nuclear spin to be determined.

2.3.2 Nuclear Electromagnetic Moments

The magnetic and electric hyperfine coefficients, A and B, are directly related to the observed splitting of atomic energy levels into hyperfine states of quantum number F. The coefficients are different for each of the two states involved in the atomic transition and can be assessed based on the separation of transition peaks between F states in a hyperfine spectrum. The calculation of the magnetic dipole moment μ and spectroscopic quadrupole moment Q_s from Equations 2.8 and 2.16, respectively are dependent on a precise knowledge of the electromagnetic fields induced by electrons in the form of the the magnetic field at the site of the nucleus B_e and the electric field gradient $\langle \partial^2 V/\partial z^2 \rangle$.

To overcome this, the dependence of μ and Q_s on B_e and $\langle \partial^2 V/\partial z^2 \rangle$ can be removed under the assumption that they remain constant across the isotope chain. This allows measured values to be calibrated to an isotope (usually stable) with known nuclear properties, referred to as a reference isotope. For the magnetic dipole moment, a reference isotope must have a known μ and I, as well as an A value obtained for the selected atomic level while the spectroscopic quadrupole moment requires a reference with a known Q_s and B value from the same atomic level. Equations 2.8 and 2.16 can therefore be rearranged to provide the measured moments

$$\mu = \mu_{\text{ref}} \frac{IA}{I_{\text{ref}} A_{\text{ref}}}, \tag{2.24}$$

$$Q_s = Q_{\mathrm{s,ref}} \frac{B}{B_{\mathrm{ref}}}, \tag{2.25}$$

where the subscript 'ref' denotes the nuclear properties of the reference isotope, and the measured and reference hyperfine coefficients used in an equation must be from the same state, i.e. either the upper or lower state. Taking the ratio of the measured properties and the reference isotope, the dependence of the moment upon B_e is removed, as is the dependence of the quadrupole moment upon the electric field gradient. This leaves equations only dependent on experimental observables and previously determined quantities. The uncertainties on reference values from experiment and hyperfine coefficients determined in this work must be considered due to their effect on the moments extracted from Equations 2.24 and 2.25. The errors on μ and Q_s are calculated by adding fractional errors in quadrature, such that

$$\Delta\mu = \mu \times \sqrt{\left(\frac{\Delta\mu_{\mathrm{ref}}}{\mu_{\mathrm{ref}}}\right)^2 + \left(\frac{\Delta A}{A}\right)^2 + \left(\frac{\Delta A_{\mathrm{ref}}}{A_{\mathrm{ref}}}\right)^2}, \tag{2.26}$$

$$\Delta Q_s = Q_s \times \sqrt{\left(\frac{\Delta Q_{\mathrm{s,ref}}}{Q_{\mathrm{s,ref}}}\right)^2 + \left(\frac{\Delta B}{B}\right)^2 + \left(\frac{\Delta B_{\mathrm{ref}}}{B_{\mathrm{ref}}}\right)^2}. \tag{2.27}$$

Hyperfine Anomaly

The reduction in the hyperfine A coefficient has an effect on the calculation of the magnetic dipole moment by means of the reference isotope. Consideration of the hyperfine anomaly changes Equation 2.24 such that

$$\mu = \mu_{\mathrm{ref}} \frac{IA}{I_{\mathrm{ref}} A_{\mathrm{ref}}} (1 + \Delta), \tag{2.28}$$

where $\Delta = \epsilon - \epsilon_{\mathrm{ref}}$. Any electronic state that is not subject to a hyperfine anomaly can be used to extract nuclear moments otherwise a potential hyperfine anomaly must be factored into the quoted error. A method that was discussed in Section 2.3.1 involving the ratio of upper and lower state A coefficients can be used to determine the presence of the hyperfine anomaly. If this quantity remains constant for all isotopes, the presence of a hyperfine anomaly can be

ruled out or considered to be accounted for within the statistical errors of the experiment.

2.4 Isotope Shift

As we move across the isotope chain, the composition of the nucleus changes in such a way that the atomic states experience a small shift in energy, referred to as the isotope shift. The hyperfine structure of an isotope is centred around a centroid frequency ν^A, which will have experienced some shift from the frequency of the unperturbed atomic transition. The isotope shift can be shown in relative terms between two isotopes for the same atomic transition

$$\delta\nu_{\mathrm{IS}}^{AA'} = \nu^{A'} - \nu^{A}, \tag{2.29}$$

where $\nu^{A'}$ and ν^{A} are the centroid frequencies of isotopes A' and A. The physical basis of the frequency shift is attributed to two different contributions between the isotopes A' and A

$$\delta\nu_{\mathrm{IS}}^{AA'} = \delta\nu_{\mathrm{MS}}^{AA'} + \delta\nu_{\mathrm{FS}}^{AA'}, \tag{2.30}$$

where $\delta\nu_{\mathrm{MS}}^{AA'}$ is the mass shift contribution and $\delta\nu_{\mathrm{FS}}^{AA'}$ is the field shift contribution.

2.4.1 Mass Shift

The first component to consider in the isotope shift, the mass shift, accounts for the recoil kinetic energy of the nucleus with a finite mass. The energy difference of an atomic state between two isotopes A' and A is given by

$$\delta E_{\mathrm{MS}} = \frac{1}{2m_u}\frac{A'-A}{AA'}\left(\sum_i \boldsymbol{p}_i^2 + 2\sum_{i>j}\boldsymbol{p}_i\cdot\boldsymbol{p}_j\right), \tag{2.31}$$

where m_u is the atomic mass unit and $\boldsymbol{p}_i$ is the individual electron momentum, which is summed over the total number of electrons in the atom. The momentum terms $\boldsymbol{p}_i^2$ and $\boldsymbol{p}_i\cdot\boldsymbol{p}_j$ represent the normal mass shift (NMS) and the specific mass shift (SMS) contributions to

the mass shift, respectively. The mass shift can therefore be written as

$$\delta\nu_{\mathrm{MS}}^{AA'} = \delta\nu_{\mathrm{NMS}}^{AA'} + \delta\nu_{\mathrm{SMS}}^{AA'} = N\left(\frac{A'-A}{AA'}\right) + S\left(\frac{A'-A}{AA'}\right), \tag{2.32}$$

where N is the atomic factor relating the normal mass shift and S is that for the specific mass shift, which when summed form the mass shift factor M. The first atomic factor N can be easily calculated by

$$N = \nu_0 \cdot \frac{m_e}{m_u}, \tag{2.33}$$

where ν_0 is the transition frequency and m_e is the mass of an electron. The second atomic factor S meanwhile is reliant upon theoretical calculations to provide an estimate of its effect and tends to be smaller than that of N. The magnitude of the mass shift decreases with increasing nuclear mass and is negligible when assessing the isomer shift between nuclear states with the same A [35], both due to the multiplicative factor $(A'-A)/(AA')$.

2.4.2 Field Shift

The field shift between two isotopes arises due to the spatial overlap of the electron charge distribution and the changing nuclear volume as the number of neutrons increases or decreases. A nucleus in a constant electronic charge density generated by atomic electrons $|\psi_e(0)|$ (i.e. equal to the value at $r = 0$) over its volume has an energy given by

$$E = \frac{Ze^2}{6\epsilon_0}|\psi_e(0)|^2\langle r^2\rangle, \tag{2.34}$$

where the mean-square charge radius $\langle r^2\rangle$ is described in terms of the nuclear charge distribution $\rho(r)$

$$\langle r^2\rangle = \frac{\int_0^\infty \rho(\boldsymbol{r})r^2 dV}{\int_0^\infty \rho(\boldsymbol{r})dV}. \tag{2.35}$$

The field shift component between two different isotopes is related to the small energy shift of the atomic electrons, an effect that manifests itself in the observable shifting of a spectral line by

$$\delta\nu_{\mathrm{FS}}^{AA'} = \frac{Ze^2}{6h\epsilon_0}\Delta|\psi_e(0)|^2\delta\langle r^2\rangle^{AA'}, \tag{2.36}$$

where $\Delta|\psi_e(0)|^2$ is the change in the electron density at the nucleus between the upper and lower atomic states. The expression for the field shift is generally displayed more simply as

$$\delta\nu_{\mathrm{FS}}^{AA'} = F\delta\langle r^2\rangle^{AA'}, \tag{2.37}$$

where F is the field shift factor, which is dependent on the electronic configuration and is unique for each atomic transition. An estimate of F can be deduced from non-optical $\delta\langle r^2\rangle$ data [36] or via theoretical calculations. Any observable centroid shift between two nuclear states of the same isotope, referred to as the isomer shift, are solely attributed to the field shift, as the mass shift is zero.

2.4.3 Isotope Shift from Atomic Factors

As shown above, the contributing factors to the isotope shift can be shown in terms of the mass shift and field shift atomic factors, which leads to the relation

$$\delta\nu_{IS}^{AA'} = M\frac{A'-A}{AA'} + F\delta\langle r^2\rangle^{AA'}, \tag{2.38}$$

where the atomic factors M and F contain the optical transition dependence, while $(A'-A)/(AA')$ and $\delta\langle r^2\rangle^{AA'}$ contain the nuclear properties. In the situation where M and F are unknown for a transition, the King plot method can be used calculate their values if they are already known for a different transition within the same element, and will be outlined in the next section. For any cases where there is insufficient experimental data to perform a King plot analysis, theoretical calculations are called upon to provide further insight.

2.4.4 King-Plot Analysis

The King plot method for extracting atomic factors can be applied to an optical transition for which there have been at least three measured isotope shifts of a given element. Starting from Equation 2.38 and applying the modification factor $\mu^{A,A'}$

$$\mu^{A,A'} = \frac{AA'}{A' - A}, \tag{2.39}$$

gives the following relations:

$$\mu^{A,A'}\delta\nu_{IS,i}^{AA'} = M_i + \mu^{A,A'}F_i\delta\langle r^2\rangle^{AA'}, \tag{2.40}$$

$$\mu^{A,A'}\delta\nu_{IS,j}^{AA'} = M_j + \mu^{A,A'}F_j\delta\langle r^2\rangle^{AA'}, \tag{2.41}$$

where the subscripts 'i' and 'j' denote the two optical transitions. Since $\mu^{A,A'}\delta\langle r^2\rangle^{AA'}$ is the same for both transitions, Equations 2.40 and 2.41 can be combined to form a straight line equation

$$\mu^{A,A'}\delta\nu_{IS,j}^{AA'} = \frac{F_j}{F_i}\mu^{A,A'}\delta\nu_{IS,i}^{AA'} + M_j - \frac{F_j}{F_i}M_i, \tag{2.42}$$

with the two axes represented by $\mu^{A,A'}\delta\nu_{IS,i}^{AA'}$ and $\mu^{A,A'}\delta\nu_{IS,j}^{AA'}$. The straight line, once plotted, will have a gradient of

$$\text{gradient} = \frac{F_j}{F_i}, \tag{2.43}$$

and a y-intercept of

$$\text{intercept} = M_j - \frac{F_j}{F_i}M_i. \tag{2.44}$$

The properties derived from the subsequent straight line plot can therefore reveal the atomic factors of the transition under investigation when the same values are known for the

secondary transition. If non-optical values of $\delta\langle r^2\rangle$ are known, these factors can be treated in the above as a transition where $F = 1$ and $M = 0$.

2.5 This Work

This thesis will be focused on the extraction and analysis of nuclear spins and electromagnetic moments from the hyperfine spectra of odd-A Zn isotopes. The extraction of these properties will use the methods outlined earlier in Section 2.3, and the analysed results will be discussed in detail in Chapters 5 and 6. The mean-square charge-radii will not be addressed any further in this document, although the results of this are soon to be published [37]. The experimental spins and moments will be interpreted in-line with the predictions of state-of-the-art shell-model interactions. A number of these interactions will be introduced in the next chapter.

Chapter 3

Nuclear Theory

In the previous chapter, we showed how certain properties of nuclei can be determined from an atomic spectrum. In order to gain an insight into the properties of nuclei that have not been measured experimentally, a predictive model of the nucleus is required. The shell model is one such example that has been proven successful for predicting the shell structure observed in atomic physics. This success provided the motivation to create an analogous shell model for nuclear physics. The basic principle of the shell model says that the properties of a nucleus are determined by valence particle(s) above an inert core of paired particles. Therefore, based on the observation of a nuclear shell structure, this principle provides an excellent basis from which a predictive model for nuclear physics can be developed.

Due to the breadth of the nuclear chart, a single generic shell model cannot be applied to all nuclides. Instead, we can use many different shell-model interactions that are specifically tailored to certain regions of the nuclear chart. For the purposes of laser spectroscopy experiments in nuclear structure physics, a shell model must be able to correctly associate the ground state with at least a level with the measured nuclear spin, and the electromagnetic moments, which are very sensitive to the calculated nuclear wave function, in order to be deemed "successful". Such models can thereafter be used with confidence to predict these properties in unmeasured isotopes to provide a roadmap for areas of interest for future studies.

This chapter will outline some the experimental evidence for nuclear shell structure before introducing the basic principles of the non-interacting and interacting shell models, and the nuclear properties they can be used to predict. Finally, a set of more sophisticated shell model interactions will be introduced and their relevance to Zn discussed.

3.1 Evidence for Nuclear Shell Structure

Nuclear shell structure is a term used to describe the clustering of nucleon orbitals separated by large energy gaps [38]. The presence of this underlying shell structure has long been observed as discontinuities in the systematic trends of nuclear properties with varying N or Z. For example, the measured values of the single-nucleon separation energy for both protons and neutrons, $S_{\mathrm{p,n}}$, exhibit maxima at $N, Z = 8, 20, 28, 50, 82$ and 126 [39, 40]. For nuclei with just one nucleon beyond these maxima, a sharp drop is observed. The inference is that the maxima of $S_{\mathrm{p,n}}$ correspond to the closing of nuclear shells where all nucleons are paired in orbitals that are filled up to a shell gap, meaning the energy required to remove a single nucleon is high. For closed shell +1 nuclei the unpaired nucleon is easier to separate, hence the sharp drop in $S_{\mathrm{p,n}}$. The result is analogous to the trend in ionisation potential of atomic nuclei at atomic shell closures. Further evidence of increased stability at these N, Z values is observed in the systematics of 2_1^+ excited state energies as a notable increase in 2_1^+ at $N, Z = 8, 20, 28, 50, 82$ and 126 relative to other nuclei [41, 40]. These N and Z values are commonly referred to as "magic numbers". For nuclei with magic numbers of both protons and neutrons simultaneously, the 2_1^+ states are observed at even higher energies than in singly magic nuclei, suggesting these "doubly magic" nuclei are even more bound.

Theoretical calculations have pointed to the existence of new magic numbers in the superheavy region of the nuclear chart [42], although the practical limits of producing such elements currently prevents the measurement of such systems [43]. For now, the universally accepted magic numbers of $N, Z = 8, 20, 28, 50, 82$ and 126 provide the starting point for mapping nuclear structure across the nuclear chart. Therefore, in order for any model of the

nucleus to be deemed successful, first and foremost it must be able to reproduce these magic numbers. Away from the valley of stability in the nuclear chart, determining the potential evolution of these N and Z magic numbers as N and/or Z change is one of the major experimental goals of nuclear physics. Due to the improvement in production of exotic isotopes at RIB facilities, the data required to probe the robustness of magic numbers is now much more accessible.

3.2 The Nuclear Shell Model

A shell model for nuclear physics can, to some extent, adopt the fundamental principles of the atomic shell model. For instance, both models are based on the filling of orbitals with fermions in accordance with the Pauli exclusion principle. However, certain differences between electrons and nucleons prevent the exact same ideology being directly applied to the nuclear realm with the potential they experience being one key example. In the atomic shell model electrons experience an external potential generated by the nucleus, while for nucleons the potential is not independent, it is instead self-generated and dictated in part by the number of nucleons in the nucleus. The detail in which the nuclear potential is modelled will therefore determine the accuracy and complexity of the shell model.

The successful reproduction of the known nucleon magic numbers using the shell model approach was first shown in the independent works of Goeppert-Mayer [44, 45] and Haxel, *et al.* [46]. In both instances, a central mean-field potential with spin-orbit corrections was used. This section will discuss the construction of an independent particle shell model for nuclear physics, based on the principles outlined by Goeppert-Mayer and Haxel, *et al.*, and how the model can be used to estimate the properties of nuclei. An extension of this model that uses a more complex potential based on nucleon-nucleon interactions is also introduced.

3.2.1 The Independent Particle Model

The shell structure observed within nuclei is based on the clustering of orbitals separated by energy gaps that corresponding to the known magic numbers. The energy of these orbitals correspond to eigenvalues of the Schrödinger equation for a many-body system

$$\hat{H}\Psi_k = E_k\Psi_k, \tag{3.1}$$

where $\hat{H}$ is the Hamiltonian operator and Ψ_k is the wave function of nucleons in a given orbital k, and E_k is the eigenvalue of the Hamiltonian operator for Ψ_k that corresponds to the energy of the orbital k. The Hamiltonian describes the total energy of the system and is equal to the kinetic energy K plus the potential energy V. Initially, the potential can be simplified somewhat by removing the Coulomb interaction between protons and considering only the strong force between nucleons. This allows the Hamiltonian to be given in terms of the many-body interaction terms [47]

$$\begin{aligned} H &= K + V, \\ &= \sum_{i}^{A} \frac{p_i^2}{2m_i} + \sum_{i<j}^{A} V_{ij} + \sum_{i<j<k}^{A} V_{ijk} + ..., \end{aligned} \tag{3.2}$$

where A is the atomic number of the nucleus, m_i is the nucleon mass, p is the momentum and $V_{ij}, V_{ijk}...$ are the many-body terms for interactions between nucleons $i, j, k....$ The complexity of the nuclear potential is evident from Equation 3.2 when interactions between an increasing number of nucleons are considered. Therefore it becomes desirable to simplify our model of the potential. The mean-field approximation provides one such method in which we assume each nucleon only exists in an external field that is generated by the remaining $A - 1$ nucleons. The potential is now reduced to a one-body problem where each nucleon is independent and only bound by an effective central potential $U(r)$ that originates from the centre of the nucleus and is included in the independent particle Hamiltonian term

$$H_0 = \sum_i^A \frac{p_i^2}{2m} + \sum_i^A U_i(\boldsymbol{r_i}), \tag{3.3}$$

where i is the number of non-interacting nucleons. This "independent particle model" of the nucleus provides a reasonable approximation of nuclei close to magic numbers. However, as the number of neutrons and protons depart from magicity it becomes impossible to ignore contributions from interacting nucleons. The presence of two-body "residual" interactions between nucleons, V_{ij}, is accounted for by adding a residual interaction term H_{res} to H_0 to give [47]

$$\begin{aligned} H &= \left[\sum_i^A \frac{p_i^2}{2m} + \sum_i^A U_i(\boldsymbol{r_i})\right] + \left[\sum_{i<j}^A V_{ij}(\boldsymbol{r_i}, \boldsymbol{r_j}) - \sum_i^A U_i(\boldsymbol{r_i})\right], \\ &= H_0 + H_{\text{res}}. \end{aligned} \tag{3.4}$$

The mean-field potential can be modelled by a number of mathematical models, including the finite-square well, harmonic oscillator or the Woods-Saxon potential, amongst others. Taking the harmonic oscillator model, the energy eigenvalues $E = \hbar\omega(N + \frac{3}{2})$, where N is the major oscillator quantum number, yield shell closures at $N, Z = 2, 8, 20, 40, 70, ...$ that are only in agreement with known magic numbers up to 20. In order to reproduce the magic numbers above 20, it was shown by Goeppert-Mayer [44, 45] and Haxel, *et al.* [46] that the addition of a strong spin-orbit potential was required. The inclusion of the spin-orbit potential accounts for the interaction of a nucleon's spin angular momentum, s, with its orbital angular momentum, l. By also including an l^2 term to flatten the potential well as l increases, the harmonic oscillator potential becomes

$$U(r) = \frac{1}{2}m\omega^2 r^2 + D\boldsymbol{l}^2 + C\boldsymbol{l}\cdot\boldsymbol{s}, \tag{3.5}$$

where $\frac{1}{2}m\omega^2 r^2$ is the unperturbed harmonic oscillator potential, and C and D are constants. The effect of each component on the derived single-particle energies is shown in Figure 3.1 from left to right. The l degeneracy of the harmonic oscillator levels are lifted by the inclusion

of the l^2 term, while the spin-orbit term $l \cdot s$ splits l states into two separate states with total angular momentum $j = l \pm \frac{1}{2}$ (for the s-state where $l = 0$, only $j = l + \frac{1}{2}$ is formed). As a result of the spin-orbit interaction, spin-orbit partners are now separated by energy

$$E_{l+\frac{1}{2}} - E_{l-\frac{1}{2}} = \frac{V_{\mathrm{SO}}\hbar^2}{2}(2l+1). \tag{3.6}$$

The modification of the nuclear potential to include the spin-orbit potential reproduces a number of key features of nuclear shell structure, including the increase in energy splitting between $l \pm \frac{1}{2}$ states with increasing l and the reduction of $l + \frac{1}{2}$ states below their spin-orbit partners (if V_{SO} is chosen to be negative) [34].

The independent particle model of the nucleus provides an excellent starting point for understanding the nuclear properties of nuclei. The model, based upon the filling of single-particle orbits in accordance with the Pauli exclusion principle up to a maximum of $2j + 1$ nucleons per orbital, assumes that nucleons in filled orbitals do not contribute to the measurable properties of a nucleus. The spin-parity and electromagnetic moments of closed shell ± 1 nuclei are therefore well approximated by this model. However for nuclei further from magic numbers, the increased number of nucleons above the "inert core" of paired particles leads to an increase in particle-particle and particle-core interactions. These interactions mean that the low-lying states of such nuclei can be formed by many nucleons acting together, and are hence referred to as *collective effects*. The independent particle model can still be used to estimate the nuclear properties of odd-A nuclei far from magic numbers, albeit somewhat crudely, through the use of effective parameters. The calculation of electromagnetic moments using the independent particle model will be discussed in the following sections, along with the additional parameters required to account for collective effects in mid-shell regions.

3.2.2 Magnetic Dipole Moments

The independent particle model can be used to estimate the magnetic dipole moment of odd-A isotopes close to magic numbers. For a nucleon ($s = 1/2$) with total angular momentum j

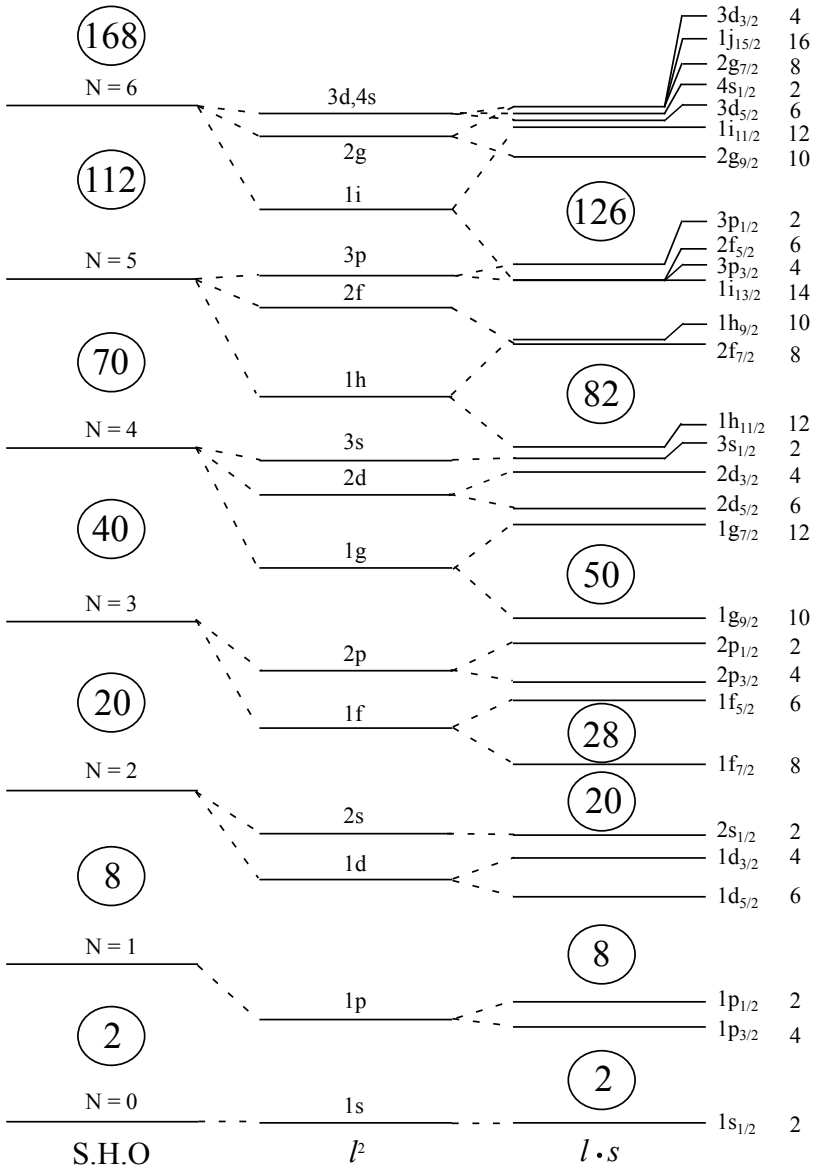

Figure 3.1: Single-particle energy levels calculated from the independent particle model using the harmonic oscillator potential, and then adding the l^2 term and the spin-orbit interaction term $l \cdot s$. The magic numbers from the harmonic oscillator potential with and without the spin-orbit interaction are shown in the circles. Single-particle levels are labelled on the right-hand side with their Nl_j values and multiplicity $(2l + 1)$.

and orbital angular momentum l, the single particle moment, μ_{SP}, is quantified by [34]

$$\begin{aligned} \text{for} \quad \mathrm{j} = l + \frac{1}{2} \qquad & \mu_{\mathrm{SP}} = \left[g_l \left(j - \frac{1}{2} \right) + \frac{1}{2} g_s \right] \mu_N, \\ \text{for} \quad \mathrm{j} = l - \frac{1}{2} \qquad & \mu_{\mathrm{SP}} = \left[g_l \frac{j(j+\frac{3}{2})}{(j+1)} - \frac{1}{2} \frac{1}{j+1} g_s \right] \mu_N, \end{aligned} \tag{3.7}$$

where $g_{l,s}$ are the free orbital and spin g-factors, respectively, with values of $g_l = 1$ and $g_s = 5.5856912$ for protons, and $g_l = 0$ and $g_s = -3.8260837$ for neutrons. The resulting moments represent the values of free nucleons and are often referred to as Schmidt moments. They represent the upper and lower limits within which the large majority of experimental magnetic dipole moments lie.

In reality, the magnetic moments of free nucleons do not accurately reflect the behaviour of a nucleon in the nuclear medium since a nucleus can rarely be described by a sole particle acting independently outside a doubly magic core. It is more realistic to consider that this single-particle interacts with other valence nucleons and paired particles in the "inert" core [48], the effects of which lead to the deviation of experimental magnetic dipole moments from Schmidt moments. Therefore it is more common to use 'effective' g-factors to calculate single-particle moments. This reduces the magnitude of the Schmidt moment with a quenching factor, q_s, such that $g_s^{\mathrm{eff}} = q_s g_s^{\mathrm{free}}$ to produce a more realistic estimate of the magnetic moment although the scatter of experimental moments around the effective moments suggest the model is still too general and simplistic.

The effective magnetic moment can provide an extremely sensitive insight into the orbital occupied by a single-nucleon in a nucleus. For an orbital with angular momentum l, a single-nucleon occupying that orbital will have a g-factor approaching

$$g = g_l \pm \frac{1}{2l+1}(g_s - g_l), \tag{3.8}$$

where '+' corresponds to $l + 1/2$ orbitals and '$-$' to $l - 1/2$ orbitals. These values can be spin-quenched, as mentioned above for moments, for a more realistic representation of the g-factor of a single-nucleon in an orbital within the nuclear medium.

In order to compare the effective g-factor to that from experiment, we remove the nuclear

spin dependence, I, of the magnetic dipole moment from Equation 2.6 (and negate the nuclear magneton, μ_N) to give

$$g = \frac{\mu}{I}. \tag{3.9}$$

The g-factor is very sensitive to the orbital occupied by an unpaired nucleon, while having little sensitivity to orbitals in which paired particles are coupled to spin zero. Therefore the close proximity of the measured g-factor to the effective g-factor of a given orbital, even if it has a different nuclear spin, strongly indicates that the wave function of the state is dominated by an unpaired nucleon in that orbital. In the process of filling a subshell (with l_j) with nucleons, the g-factor of these isotopes should be roughly the same providing they each have a leading wave function contribution from an $(Nl_j)^1$ odd-particle configuration. Any notable deviation from this linear trend in g-factor can be indicative of configuration mixing and hence a reduction in the purity of the $(Nl_j)^i$ configuration.

3.2.3 Electric Quadrupole Moments

The independent particle model estimate of the electric quadrupole moment, Q_{sp}, outside an inert core of nucleons is dependent on the total angular momentum of the orbital it occupies, j. The moment is calculated via the relation

$$Q_{\text{sp}} = -e_j \frac{2j-1}{2(j+1)} \langle r_j^2 \rangle, \tag{3.10}$$

where e_j is the free-nucleon charge, given as $e_\pi = 1$ and $e_\nu = 0$, and $\langle r_j^2 \rangle$ is the mean square charge radius of the orbital j. Beyond the first unpaired nucleon in a subshell, each additional nucleon added to the same subshell contributes to the quadrupole moment. For an isotope with n nucleons in a subshell of maximum capacity $2j+1$, the quadrupole moment can be calculated from the single-particle moment Q_{sp} via Equation 3.11

$$Q = Q_{\text{sp}}\left[1 - 2\frac{n-1}{2j-1}\right]. \tag{3.11}$$

For the first nucleon in the subshell ($n = 1$), the equation shows that $Q = Q_{\text{sp}}$, while for a subshell one nucleon from full capacity ($n = 2j$), i.e. a 'hole' state, $Q = -Q_{\text{sp}}$. This gives us the basic approximation that single-particle and single-hole state quadrupole moments in a subshell will be equal and opposite, with the deformation of the nucleus evolving from oblate (negative Q) to prolate (positive Q) with increasing N or Z. In the process of filling the subshell, the quadrupole moments of odd-A nuclei are expected to follow a linear trend between Q_{particle} and Q_{hole} that crosses zero at mid-shell [48], providing no collective effects are present.

These moments are based on for free-nucleon charges of $e_\pi = 1$ and $e_\nu = 0$. However, modifications to e_π, e_ν are required to more accurately reflect the behaviour of nucleons in a nucleus. Deviations of measured quadrupole moments from the independent particle model estimates with free-nucleon charges arise due to, firstly, the non-zero quadrupole moment measurements of odd-N, even-A isotopes (meaning $e_\nu \neq 0$), and secondly from the influence of two-body residual interactions involving nucleons and the core. As such, free-nucleon charges $e_{\pi,\nu}$ are replaced by the effective charges e^{π}_{eff} and e^{ν}_{eff} to account for these effects to some degree.

Seniority States

For an isotope with n nucleons in a valence orbital, its quadrupole moment can be estimated from Equation 3.11 as a function of the single-particle moment. However, for nuclei with $n > 1$, multi-valence particle configurations and residual interactions can have a measurable effect on its nuclear properties. In these nuclei it becomes possible for valence nucleons pairs (coupled to spin zero) to break and contribute to the measured quadrupole moment. Here, the number of unpaired nucleons in orbit j not coupled to spin zero that instead couple to a total spin I is denoted by the seniority ν [48]. These are referred to as seniority-ν

states. The resulting moment deviates from the linear trend of single-particle values from Q_{particle} and Q_{hole} (calculated from Equation 3.11), and instead follows a separate linear trend corresponding to the ν and I of the state that crosses zero at the midpoint of the subshell. The quadrupole moment of a seniority state with $\nu > 1$ can be estimated from the effective single-particle moment (seniority-1), $Q_{\text{sp}} = \langle j|\hat{Q}|j\rangle$, the applicable coefficients of fractional parentage (cfp) [49] and the relation [50, 51]

$$\langle J^n(I) \mid \widehat{Q} \mid J^n(I)\rangle = \frac{2J+1-2n}{2J+1-2\nu}\nu \sum_{J_1}(-1)^{J_1+J+I}(\text{cfp})^2 \times (2\text{I}+1) \begin{Bmatrix} J & I & J_1 \\ I & J & 2 \end{Bmatrix} \langle \text{J}|\widehat{\text{Q}}|\text{J}\rangle, \tag{3.12}$$

in which the quadrupole moment of a state with n particles in an orbit and seniority ν is linked to the Q_{sp} via cfp $= [J^{n-1}(\nu_1, J_1), J; I|\}J^n\nu I]$ [50], where J_1 is an intermediate total angular momentum coupling of $\nu - 1$ particles (required for $\nu \geq 3$ configurations). The alignment of measured moments with the calculated values of seniority-ν states is therefore indicative of a deviation from single-particle behaviour.

3.2.4 Interacting Shell Model

Modern advancements at RIB facilities (discussed in more detail in Chapter 4) have made the more exotic reaches of the nuclear chart more widely accessible, and hence increased our understanding of nuclear structure in exotic systems. The measured nuclear properties of these isotopes reveal striking changes in the shell structure with the appearance of new magic numbers and disappearance of typical shell closures [52, 53, 54, 55] and the discovery of new nuclear structure phenomena, including the halo nuclei in very neutron-rich systems [56]. These features are beyond the reach of the simplistic independent particle model, even with the inclusion of effective parameters. A more sophisticated model of the nucleus is required in order to understand how these features occur and to predict other new phenomena.

The interacting shell model description of the nucleus extends beyond the independent

particle model by considering interactions between nucleons across a number of orbitals, referred to as the "model space". This model space lies on top of a core of fully occupied orbitals. In order to limit contributions to the model space from the core, doubly magic nuclei are commonly selected as the inert core in such models. Ideally, the model space would be large in order to obtain the most accurate model of the nucleus possible, however, the scale of such calculations are too computationally demanding. The interacting shell model overcomes this problem by applying a truncation to the model space, which defines an upper limit for nucleon excitations, to reduce its size. This leaves a "valence space" of active nucleon orbitals that are only partially occupied or empty between which nucleons can be excited. A schematic diagram of a model space and core is shown in Figure 3.2. Orbitals between magic numbers (i.e. a major shell) present an ideal valence space as the large energy gaps restrict cross-shell mixing.

The orbitals selected for the model space and core can have a direct effect on the accuracy of predictions for the electromagnetic moments of nuclei. For instance, interacting shell model estimates of magnetic moments are improved when all spin-orbit partners are included in the

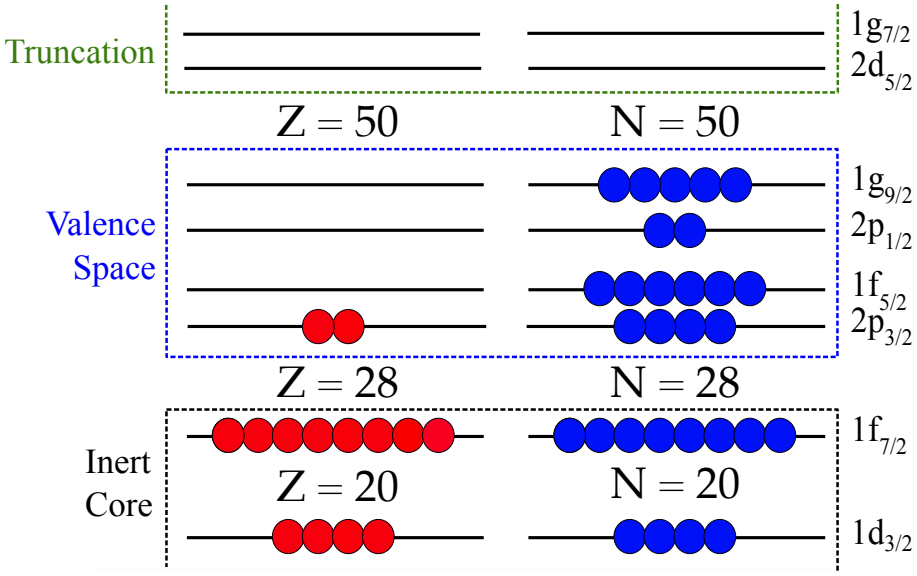

Figure 3.2: Example of a model space and core used in the interacting shell model. The valence space denotes the active nucleon orbitals, which extend from the inert core to the model space truncation.

valence space, while for quadrupole moments the influence of $\Delta l = 2$ and $\Delta j = 2$ transitions are vital. In the event that these orbitals are not included in the valence space, effective parameters are used (as discussed earlier in Sections 3.2.2 and 3.2.3).

The occupancy pattern of nucleons across the valence orbitals is described by the configuration ϕ. For a given spin and parity, the summation of all possible configurations and each of their associated probability amplitudes, c_i, gives the overall wave function [57]

$$\Psi = \sum c_i \phi_i. \tag{3.13}$$

From the resulting wave function, nuclear properties of interest can be calculated. The summation of multiple configurations to form the wave function accounts for the fact that the wave functions of many nuclei are not pure but involve a great deal of configuration mixing. This is generally observed in nuclei between shell closures and occurs due to the presence of residual interactions.

In order to determine the wave function, the Schrödinger equation $H\Psi = E\Psi$ must be solved. We construct the interacting shell model Hamiltonian H with the single-particle energies (SPEs), ϵ_i, and two-body matrix elements (TBMEs) of the nucleon-nucleon interaction V, $\langle j_i j_j J|V|j_k j_l J\rangle$, where j_i is the single-particle state of a nucleon and J is the total angular momentum that two nucleons in j_i and j_j are coupled to. Regarding the latter, it is assumed that higher-body nucleon interactions (i.e. > 2) are either not influential on the energy scale of interest or their effects are renormalised into the two-body interactions [57]. The diagonal elements of the Hamiltonian matrix correspond to the SPEs of states and the off-diagonal elements the TBMEs.

Based on the reduced model space of the interacting shell model, an effective nucleon-nucleon interaction is used. This effective interaction is specifically tailored to the selected valence orbitals. This will take into account, to some extent, the excitation of nucleons from the core to valence orbitals (core polarisation) and the scattering of nucleons with high-lying intermediate states [57]. The Schrödinger equation therefore becomes $H_{\text{eff}}\Psi_{\text{eff}} = E\Psi_{\text{eff}}$,

where the subscript 'eff' denotes the effective components of the equation. The effective interaction can be derived using the phenomenological approach where TBMEs are left as free parameters that are fit to experimental data, or by the microscopic approach where the bare nucleon-nucleon interaction is tuned empirically to align with experiment. Since the effective interaction is directly related to the experimental data it is fitted to, the selected data must be appropriate for the predictive scope of the interaction.

The selection of the model space and the complementary effective interaction provide only the basis for the interacting shell model. The process of diagonalising the Hamiltonian matrix to extract the information of interest presents a greater problem even for a limited model space and is traditionally achieved through the use of complex computer codes. Different approaches to this have lead to the development of many different large-scale shell model interactions that are tailored to certain regions of the nuclear chart.

3.3 Large-Scale Shell-Model Interactions

The size of the shell model Hamiltonian increases with the size of the model space, and therefore the Hamiltonian matrix becomes more and more difficult to diagonalise as the model space increases. Since modern day computer programs approach the diagonalisation problem by storing matrix elements, their effective range and the size of Hamiltonian matrices are limited by the available computational power. Currently large-scale shell model calculations are carried out by theoretical groups across the world, often with the use of supercomputers to maximise the computational power at their disposal that maximise the amount of matrix dimensions that can be considered. Such shell model codes include ANTOINE and MSHELL, although these programs reach a practical limit around the 1 billion dimension scale [57]. This limit can be overcome by the Monte-Carlo Shell Model (MCSM) [58], a method that selects only the basis states important to the eigenstate of interest. Therefore, while traditional shell model interactions may need to truncate their model space to describe nuclei over broad ranges (leading to discontinuities in the comparison of their results), the MCSM approach

can be applied across whole isotope chains from β-stability to exotic nuclei with more orbitals in play.

A number of large-scale shell model interactions and their relevance to Zn are discussed here. Effective interactions used in these calculations are typically derived by an empirical fitting to experimental values of binding energies and excitation energies that results in modifications to TBMEs and SPEs. For each interaction, the assumed core and active orbitals will dictate the range of isotopes from which experimental energies can be used. When necessary, the experimental energies used for in the fitting process will be given below. Predictions from these interactions will be compared to the measured nuclear properties of Zn from this work in Chapter 6.

3.3.1 JUN45 and jj44b Interactions

The JUN45 [59] and jj44b [26] interactions both aim to provide a systematic description of upper pf-shell nuclei. The interactions therefore adopt a valence space consisting of the SP orbits $1p_{3/2}$, $0f_{5/2}$, $1p_{1/2}$, and $0g_{9/2}$ on top of an inert ^{56}Ni core, as shown in Fig. 3.3, representing the nucleon orbits between the $N, Z = 28$ and $N, Z = 50$ shell closures, i.e. the f_5pg_9 model space. The relatively limited model space leads to the exclusion of the spin-orbit partners of $0f_{5/2}$ and $0g_{9/2}$, and so calculations of the magnetic moment require a significantly quenched spin g-factor. The realistic JUN45 interaction is constructed by modifying 133 TBMEs and 4 SPEs to fit to 400 experimental energies across 69 nuclei with $Z = 30 - 33$ and $N = 46 - 50$ [59]. While the process is similar for the jj44b interaction, it is fitted to $\sim$600 binding and excitation energies for nuclei with $Z = 28 - 30$ and $N = 48 - 50$ [26]. The rms deviation between the energies from experiment and theory is 250 keV for jj44b [26], while JUN45 shows a minor improvement of 185 keV [59].

To compensate for the exclusion of the $f_{5/2}$ and $g_{9/2}$ LS partners, the free spin g-factor, g_s^{free}, is quenched to provide the effective spin g-factor, g_s^{eff}. The comparison of experimental magnetic dipole moments to calculated values for ^{57}Ni to ^{96}Pd reveals an improvement with a quenching factor of $q_s = 0.7$ and an effective orbital g-factor, $g_l^{\text{eff}} = g_l^{\text{free}} \pm \delta g_l$, with $\delta g_l = 0$.

In a similar manner, the effective charges are obtained as $e_{\mathrm{p}}^{\mathrm{eff}} = 1.5e$ and $e_{\mathrm{n}}^{\mathrm{eff}} = 1.1e$ from a least squares fit to experimental quadrupole moments [59]. Since both the JUN45 and jj44b interactions use the same f_5pg_9 model space, both interactions adopt the same effective parameters.

The creators of the JUN45 interaction acknowledge the potential softness of the ^{56}Ni core suggested in [60], and hence refer to the model space as an interesting test of the $\pi f_{7/2}$ orbit's influence over the description of upper pf-shell nuclei. The JUN45 interaction has already exhibited a poor agreement with the electromagnetic moments and excitation energies of Ni ($Z = 28$) for this very reason, although a marginal improvement in predictions for Cu ($Z = 29$) isotopes is asserted in [59]. This is disputed however in [25] where an overestimation of the magnetic moments of odd-A Cu isotopes by JUN45 and jj44b indicates the need for cross $Z, N = 28$ excitations from the $f_{7/2}$ orbital. This is also noted in light Zn isotopes where the $3/2^-$ doublets in ^{65}Zn are well described by pf-shell calculations [59]. The suitability of the JUN45 and jj44b interactions to Zn is therefore up for debate, meaning the comparison

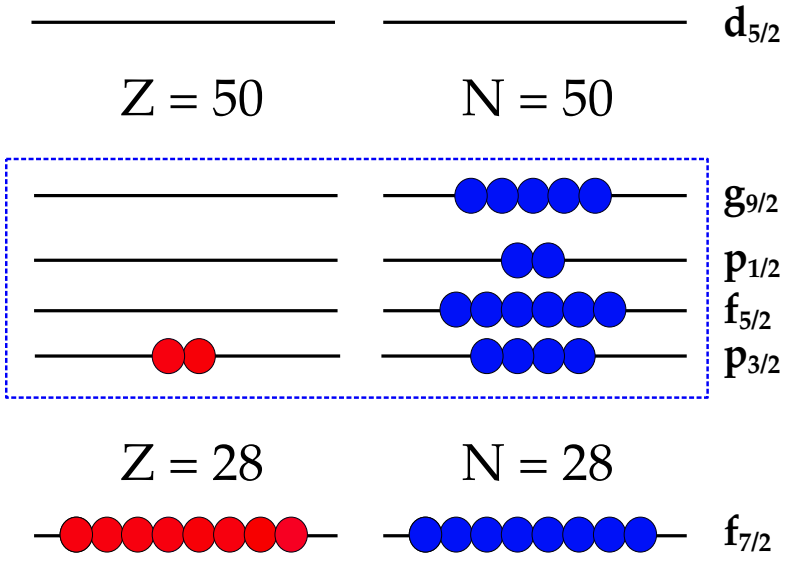

Figure 3.3: The f_5pg_9 model space and inert ^{56}Ni core of the JUN45 and jj44b effective interactions. The two interactions differ in their parametrisation (see text for details).

of results from this work to their predictions will provide a more thorough conclusion on the matter.

The correction of two-body matrix elements (TBMEs) between the upper pf-shell and $g_{9/2}$ is also a motivation for the selection of the f_5pg_9 model space. The monopole matrix elements between $\pi f_{5/2}$ and $\nu g_{9/2}$ are of particular interest due to their effect on shell structure in neutron-rich nuclei. This manifests as the attractive monopole interaction from the tensor force that lowers the $\pi f_{5/2}$ ($j = l - 1/2$) as the $\nu g_{9/2}$ ($j = l + 1/2$) is filled [23], and has been directly observed in Cu ($Z = 29$) [25] and Ga ($Z = 31$) [26] isotopes as a ground state spin change from $I^\pi = 3/2^-$ to $I^\pi = 5/2^-$ due to the inversion of $\pi p_{3/2}$ and $\pi f_{5/2}$. This level reordering will only have a subtle effect on the ground state properties of even-Z, odd-A Zn isotopes, but may be probed through the occupation numbers of f_5pg_9 orbitals. The repulsive counterpart interaction of $\nu g_{9/2}$ with $\pi f_{7/2}$ ($j = l + 1/2$) that works to raise the orbital is expected to lead to a reduction of the $Z = 28$ shell gap, although this is beyond the current model space and will not be reproduced by the JUN45 and jj44b interactions.

The small model space of the JUN45 and jj44b interactions present an interesting opportunity to probe the potentially doubly magic neutron-rich nucleus ^{78}Ni. A good agreement between the predicted ground state nuclear spin and magnetic dipole moment of ^{79}Zn ($N = 49$) and measured values could signal a lack of excitations across $Z = 28$ and $N = 50$ in neutron-rich nuclei only two protons from ^{78}Ni. The comparison of JUN45 and jj44b predictions to large-scale shell model calculations with extended model spaces will provide evidence to either support or dispute this claim.

3.3.2 A3DA and LNPS Interactions

For nuclei with $Z \sim 28$, the $\pi f_{7/2}$ orbit has proved to be pivotal for describing the evolution of nuclear structure. One such example, the inability of predictions in the fpg model space to recreate the low-lying 2_1^+ level in ^{66}Fe ($Z = 25$) that points to collective behaviour around $N = 40$ proved to be the motivation for the development of the LNPS interaction [61]. This interaction therefore adopts the full pf-shell for protons and the $\nu d_{5/2}$ orbit added on to

the aforementioned f_5pg_9 space for neutrons in order to account for contributions from $\pi f_{7/2}$ in neutron-rich isotopes. The valence space lies above a doubly magic ^{48}Ca core, as shown in Figure 3.4, that is reported to be more stable than ^{56}Ni [60]. The effective interaction is constructed with several sets of realistic TBMEs and monopole corrections in order for effective SPEs to reproduce experiment.

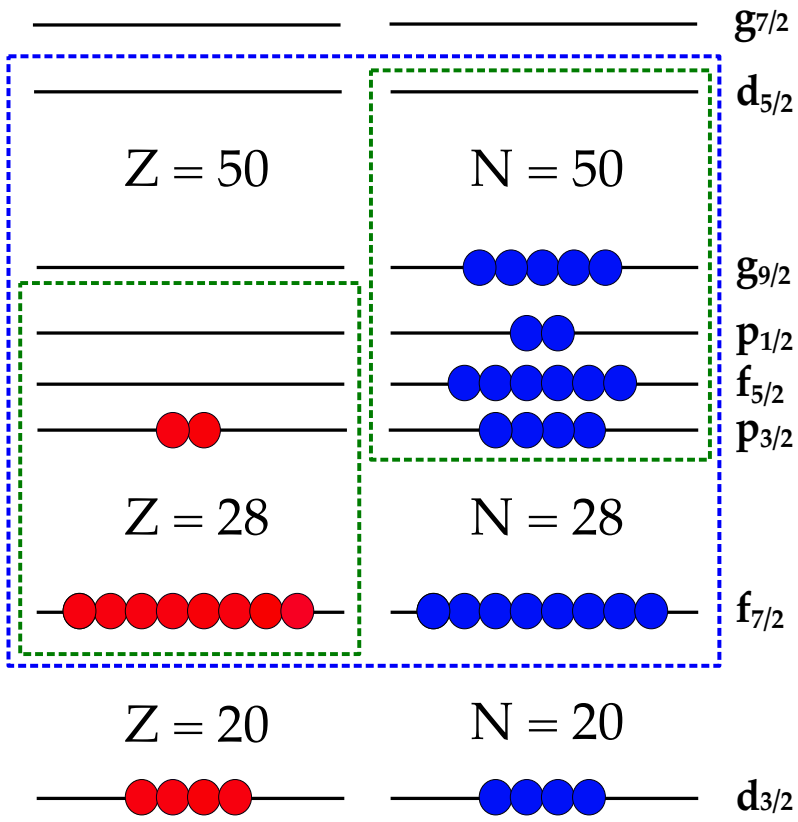

Figure 3.4: The model spaces of the LNPS-m (green dashed line) and A3DA-m (blue dashed line) effective interactions on top of a ^{48}Ca and ^{40}Ca core, respectively.

The A3DA interaction [62] is constructed somewhat differently to other interactions based on conventional shell model calculations. The calculations for A3DA are instead performed by the Monte-Carlo Shell Model (MCSM), which refers to the application of the Quantum Monte-Carlo Diagonalisation (QMCD) method to the nuclear shell model. The QMCD method selects only the basis states important to the eigenstate of interest, with the diagonalisation of the corresponding Hamiltonian matrix providing a good approximation of the

exact diagonalisation over the entire Hilbert space [58]. The MCSM method can therefore be applied to larger valence spaces than conventional shell model calculations without the need for truncation, making it ideal for studying isotope chains from *beta*-stability to exotic nuclei. The A3DA interaction is able to adopt a large model space consisting of the full pf-shell plus the $g_{9/2}$ and $d_{5/2}$ orbits for both protons and neutrons on top of a ^{40}Ca core (LS closed shell). In this work, a modified version of the A3DA interaction (A3DA-m) with corrections to SPEs and monopole components related to $g_{9/2}$ is used due to the inability of the original A3DA interaction to describe nuclei with $N \approx 40$ [63].

The extension of the LNPS and A3DA-m interaction model spaces beyond the f_5pg_9 provides an opportunity to determine how vital the inclusion of orbitals beyond this model space are for characterising the evolution of nuclear structure in the mass region of Zn. The $\nu d_{5/2}$ and $\nu f_{7/2}$ orbitals have previously been highlighted as important for describing quadrupole collectivity in the f_5pg_9 shell [59]. The development of collectivity beyond $N = 40$ has been observed in Ga isotopes ($Z = 31$) [26], although no increase in collectivity has been measured in Cu isotopes ($Z = 29$) [25] in the same region. Therefore the quadrupole moments of Zn ($Z = 30$) will provide an interesting probe of the Z-dependence of this collectivity beyond $N = 40$. In the event that there is evidence of collectivity, the comparison of predictions from A3DA-m and LNPS to those from JUN45 and jj44b will signal how influential $\nu d_{5/2}$ and $\pi f_{7/2}$ are in describing it.

As mentioned previously in Section 3.3.1, the nuclear properties of ^{79}Zn ($N = 49$) will shed light on the potentially doubly magic nucleus ^{78}Ni, the magicity of which is dependent on the robustness of the $Z = 28$ and $N = 50$ shell closures in neutron-rich nuclei. The close agreement of A3DA-m and LNPS predictions and the measured ground state nuclear spin and magnetic dipole moment of ^{79}Zn would signal the presence of excitations across $Z = 28$ and $N = 50$, and hence the weakening of these shell closures only two protons away from Ni.

Chapter 4

Collinear Laser Spectroscopy at ISOLDE

The measurement of nuclear structure properties across an isotope chain provides an opportunity to investigate how nuclear structure evolves across the nuclear chart. The production of nuclei with proton-to-neutron ratios very different from stable isotopes (exotic nuclei) is therefore imperative for obtaining a full picture of this behaviour. Radioactive ion beam (RIB) facilities commonly utilise either in-flight separation or isotope separation on-line (ISOL) techniques to produce exotic ion beams on a large scale. The ISOLDE facility at CERN adopts the latter technique to supply radioactive beams to a range of experimental setups, as shown in Figure 4.1. The use of selective laser ionisation [64], high-resolution mass separation [65] and beam bunching and cooling [66] at ISOLDE facilitates the production of high isotopic and isobaric purity radioactive beams. The Collinear Laser Spectroscopy experiment (COLLAPS) at ISOLDE benefits greatly from the improved beam purity and quality and provides high-resolution measurements of hyperfine spectra.

This section will outline the RIB production process at ISOLDE and how it is utilised by the COLLAPS experiment to produce hyperfine spectra. Where necessary, details of how the experiment is optimised specifically for Zn isotopes will be given.

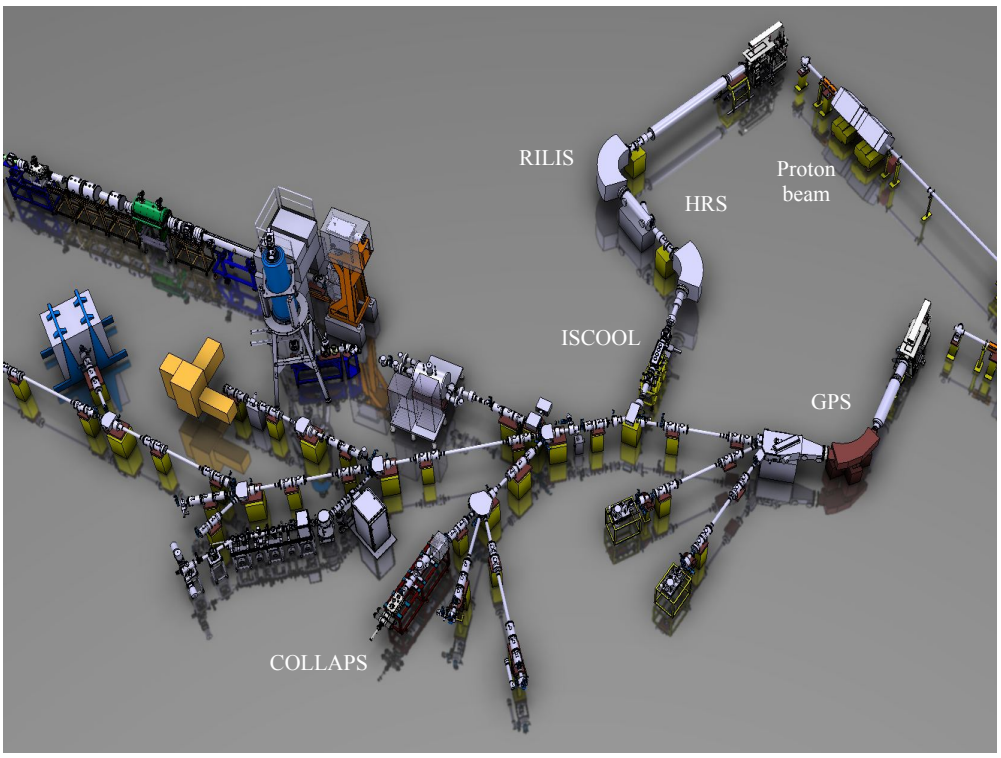

Figure 4.1: Overview of the ISOLDE experimental hall at CERN, Geneva, with a focus on the COLLAPS experiment. Some notable beam line components are labelled. Image adapted from Ref. [67].

4.1 Isotope Production

The ISOLDE facility produces isotopes by bombarding a thick target with protons. Proton bunches from the Proton Synchrotron Booster (PSB) arrive every 1.2 s with 1.4 GeV-per proton (2μA beam current) and impinge upon the target, producing radioactive nuclei through spallation, fragmentation and fission reactions. Actinide elements prove to be a desirable material for targets at ISOL facilities due to their large fission cross sections upon interaction with high-energy particles. One of the most common actinides used in targets is ^{238}U in the form of uranium mixed carbide with an excess of graphite, UC_x, that can be produced with commercially available uranium dioxide powder and graphite. The combination of the target thickness ($\approx$45 g/cm^2) and the beam energy and current at ISOLDE is capable of producing radioactive isotopes over the majority of the nuclear chart (as evidenced in Fig. 2a in [68]),

with particularly high fission production yields for neutron-rich isotopes with $70 < A < 160$ highlighting the suitability of UC_x for studying Zn.

Further improvements on neutron-rich isotope production can be obtained through the use of a neutron-converter [69]. The target and converter configuration at ISOLDE are given in Figure 4.2. In the direct beam configuration, 1.4 GeV protons impinge upon the UC_x target. This deposits a great deal of energy within the target and increases background through the production of neutron-deficient isobars. Conversely, the interaction of the 1.4 GeV proton beam with a high-Z metal converter (e.g. Ta, W), i.e. the converter configuration, isotropically produces MeV energy spallation neutrons that induce fission reactions within the target. This improves the ratio of neutron-rich isotope to neutron-deficient isobar production from the target. The reduction of beam power deposited in the target due to the converter also works to prolong the use of targets.

UC_x targets are heated to temperatures $> 2000°$C to promote the fast diffusion of reaction products through the target material from which point a temperature-controlled transfer line transports atoms to the ion source.

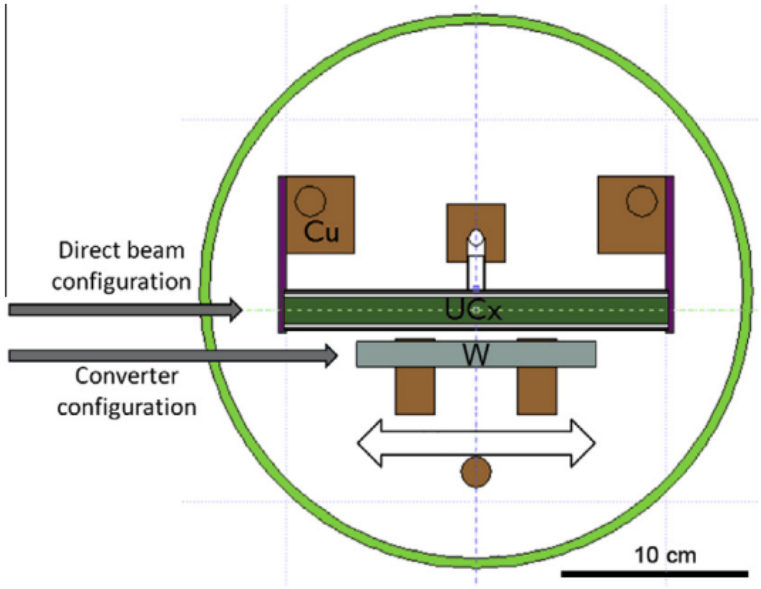

Figure 4.2: Target configuration at ISOLDE. Image taken from Ref [70].

4.2 Ion Beam Production

There are three primary ion sources available at the ISOLDE facility, they include surface ion sources, plasma ion sources and laser ion sources. The surface ion source consists of a single heated metal tube with a work function greater than that of the atom to be ionised, which ionises the atom of interest upon contact. The plasma ion source produces ions through the interaction of atoms and a plasma. The plasma is created by accelerating electrons through a gas mixture that is ionised and then confined and condensed within a magnetic field. The laser ion source is used in this work for the ionisation of Zn atoms, and so will be discussed in more detail here.

The ISOLDE Resonance Ionisation Laser Ion Source (RILIS) [71] uses laser beams with precisely tuned wavelengths to selectively ionise reaction products. The RILIS setup consists of a hot metal cavity ($T \sim 2000$ K) that spatially confines the atomic vapour from the transfer line to provide a reliable laser-atom interaction region. This volume is then irradiated by multiple laser beams (three at most), with each laser frequency, $h\nu$, tuned to one part of a multi-step photo-ionisation scheme such that $h\nu_1 + h\nu_2 + h\nu_3 \geq \text{IP}$. Three lasers are typically used in a RILIS ionisation scheme in order to ensure the selective ionisation of the element of interest and greatly increase the isobaric purity of the subsequent ion beam (as this cannot be guaranteed by mass separation alone). The laser light is produced by any of three Nd:YAG pumped tunable dye lasers and three Nd:YAG pumped tunable Titanium:Sapphire (Ti:Sa) lasers that are all operational simultaneously. This range of lasers provides RILIS users with a continuous wavelength range of 210 nm to 950 nm from fundamental beams and the generation of multiple harmonics. This wavelength range affords great adaptability for producing multi-step ionisation schemes, with the RILIS group having determined such schemes for more than 35 of the elements produced at ISOLDE (as of 2016 [72]).

The three-step ionisation process for Zn isotopes used in this work consists of two resonant photo-excitations and a third non-resonant step. Wavelengths of the first two steps, $\lambda_{1,2}$, are provided by dye lasers pumped by a frequency doubled Nd:YAG laser (with $\lambda = 532$ nm)

with power around 40 W, with the laser light for step one frequency converted to the third harmonic such that $\lambda_1 = 213.92$ nm (at ~ 0.2 W) and $\lambda_2 = 636.41$ nm (~ 10 W). High-power frequency-doubled light (40 W) from the Nd:YVO_4 laser at $\lambda = 532$ nm is used for the non-resonant final step. This ionisation scheme for Zn is shown in Figure 4.3. While the yield of Zn will be selectively enhanced during this process, contamination from elements that are easily surface ionised (e.g. neutron-deficient Rb) can still be produced in the hot metal cavity.

Post-ionisation, ions are extracted from the ion source and experience an acceleration

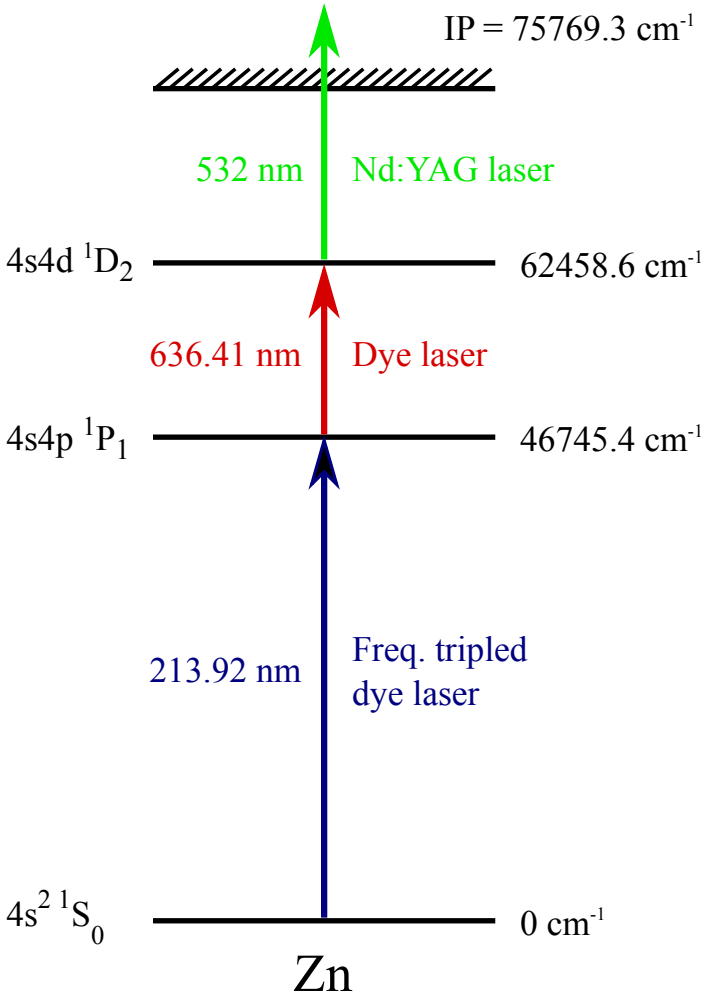

Figure 4.3: Three-step laser ionisation scheme for the production of singly charged Zn ions. The types of laser used and the operating wavelengths for Zn shown here are obtained from the Ref. [72].

voltage due to the high-voltage platform on which the target region is floated (between $30-60$ kV). The resulting ion beam is transported to one of two ion separators on-line at ISOLDE, the general purpose separator (GPS) [73] or the high-resolution separator (HRS) [65]. The GPS consists of a single 70° bending magnet, while the HRS consists of a 90° bending magnet followed by a 60° bending magnet. Within the dipole fields from the bending magnets, particles within the beam with different charge-to-mass ratios (q/m) will follow different paths. The specific tuning of the dipole magnetic field for the isotope (A) of interest coupled with the Z selectivity of RILIS leads to a high degree of isotope selectivity for ion beam production at ISOLDE. Due to the superior mass resolving power ($R = m/dm$) of HRS ($R > 5000$) over GPS ($R > 1000$), and its coupling to the ion cooler buncher (introduced in Section 4.3), the former is used in this work. A series of electrostatic optical elements within the HRS work to guide and focus the beam through the large dipole magnets. Beam diagnostics are monitored throughout the HRS section by wire scanners and Faraday cups that provide feedback regarding beam profile/shape, intensity and electrostatic tuning. The output beams from GPS and HRS both feed a common beam line system that connects to experiments in the ISOLDE hall.

4.3 Beam Cooling and Bunching

Prior to the delivery of the ion beam to the separate experimental beam lines, it first arrives at the ion cooler buncher, ISCOOL [12], in the focal plane of the HRS after the 60° magnet. ISCOOL is a gas-filled linear Paul trap, the purpose of which is to deliver pulsed ion beams with reduced transverse emittance and energy spread.

The ISCOOL structure is maintained on a high-voltage platform ($30-60$ kV) that coupled with a series of injection electrodes of increasing voltage work to decelerate the incoming ion beam to a few hundred eV [74]. The main quadrupole structure is formed by four rods, with a radiofrequency (RF) field applied to each rod and adjacent rods out of phase in order to confine ions in the radial direction. The ion cloud is slowed and cooled by helium gas at

$\sim$ 0.1 mbar through thermal collisions. A series of ring electrodes create a small potential gradient to guide ions through the structure and to extraction electrodes where they are re-accelerated approximately to the energy they entered the structure with, but with reduced energy spread. The ion beam from ISCOOL can be released in the continuous mode or bunched mode depending on the needs of the experiment being supplied with beam. For bunched beams, a trapping potential is applied to the end-plate electrode to close the trap and accumulate ions as shown in Figure 4.4. After a sufficient period, the potential is dropped and an ion bunch is released. The period of accumulation within ISCOOL and the subsequent release, t_{ISCOOL}, can be manipulated based on the elements and isotope under study.

For its application to collinear laser spectroscopy, the bunched beam mode presents significant practical advantages over the continuous mode largely due to its ability to suppress non-resonant scattered photon counts associated with laser spectroscopy experiments. This leads to hyperfine spectra with an enhanced signal-to-noise ratio from which nuclear properties can be extracted more accurately and reliably. This background reduction is primarily achieved as a result of the temporal coordination of ion bunches from ISCOOL with photon

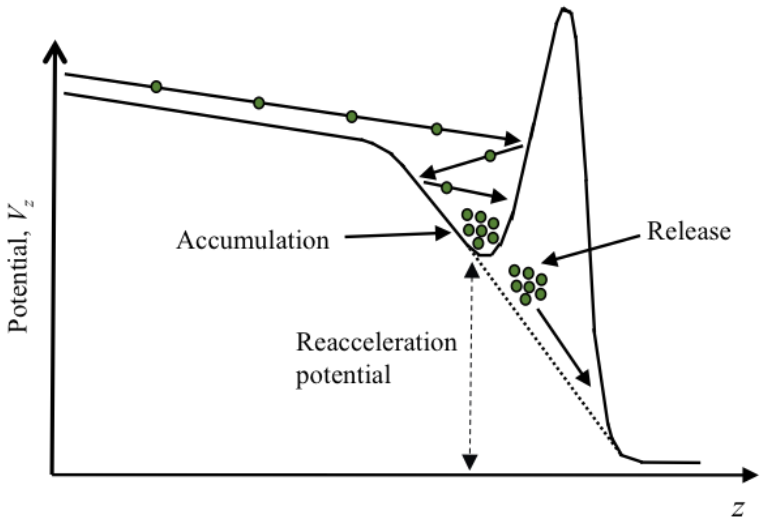

Figure 4.4: Potential experienced by ions V_z as a function of distance travelled within the ISCOOL structure z.

counting in the detection region. This will be discussed in more detail in Section 4.5.5.

4.4 The Collinear Laser Spectroscopy Method

Two experimental techniques, crossed beam and collinear laser spectroscopy, are typically used to perform Doppler-free optical spectroscopy. The crossed beam technique involves the interaction of an atom/ion beam (or ensemble) and a perpendicular laser beam. However, this technique is largely inefficient due to the short interaction time and low crossover region between the laser beam and the ensemble, hence preventing its application to beams of exotic nuclei where production yields are already low. The collinear laser spectroscopy technique [75, 76], on the other hand, is based on the parallel alignment of a fast ion beam and a co-propagating laser beam. A simplified representation of the laser-atom/ion interaction region is shown in Figure 4.5. This geometry allows for maximal spatial overlap of the laser beam and ensemble in the axial direction and a significant increase in their interaction time. Collinear laser spectroscopy therefore offers a number of practical advantages over the crossed beam method for spectroscopy of fast beams.

In the process of producing radioactive isotopes and performing laser spectroscopy, broadening of spectral lines occurs. As a result the overall clarity of the hyperfine spectrum can be greatly reduced, with broadening of the scale of GHz [77] capable of completely masking the hyperfine structure. A number of different mechanisms contribute to spectral line broadening, including collisional broadening, power broadening and Doppler broadening [78]. The latter of these mechanisms occurs due to the distribution of velocities in the ensemble that originates from thermal motion within hot cavities. Atoms in the ensemble, each travelling at different velocities v, will absorb radiation from the laser in their own rest frame, thus leading to a larger range of frequencies being absorbed by atoms in the ensemble. While the use of cooled beams nowadays partially mitigates this problem, the reduction of velocity spread within the ion beam is key to reduce broadening effects on hyperfine spectra.

The collinear geometry is able to reduce the longitudinal spread in velocity by utilising

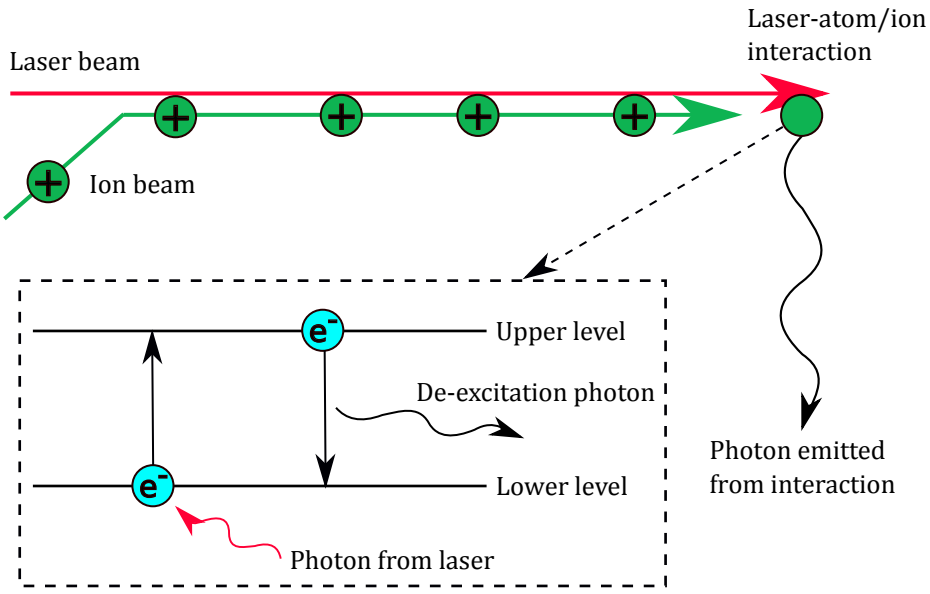

Figure 4.5: Schematic representation of the collinear laser spectroscopy method at the laser-atom/ion interaction point.

the electrostatic potential V used to accelerate the ion beam. Since all ions experience the same accelerating potential, the initial energy spread of the beam ΔE is conserved. So using the relation

$$\Delta E = m\bar{v}\Delta v, \tag{4.1}$$

it can be seen that the product of average velocity and velocity spread, $\bar{v} \times \Delta v$, must also remain constant in the direction of travel. Therefore, increasing the velocity of ions through the application of an accelerating potential works to reduce the longitudinal velocity spread. This is shown visually in Figure 4.6. For a typical accelerating potential of 40 kV, the aforementioned broadening effects can be reduced by three orders of magnitude to the scale of natural line width [13].

In addition to the reduction of broadening, the accelerating potential allows the laser frequency, ν_L, to be kept constant (to provide the approximate frequency of an atomic transition in the element of interest) while an additional accelerating voltage applied to the ensemble

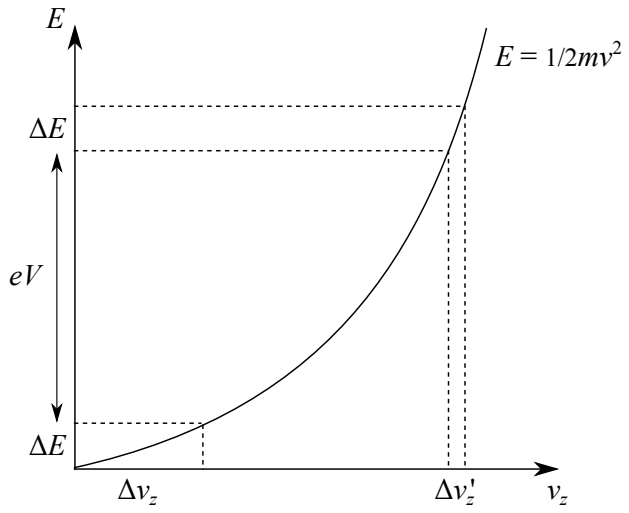

Figure 4.6: Visual representation of the longitudinal velocity spread in the ion beam Δv_z without without the application of an accelerating voltage V, and the longitudinal velocity spread after accelerating voltage is applied $\Delta v_z'$.

is scanned across the hyperfine splitting. This process, referred to as Doppler tuning, also overcomes the issues associated with scanning the laser frequency itself. Each voltage step in the scanning process is converted to the frequency seen in the rest frame of the atom, ν, by the Doppler effect

$$\nu = \nu_{\mathrm{L}}(1 + \alpha \pm \sqrt{2\alpha + \alpha^2}), \tag{4.2}$$

with

$$\alpha = \frac{eV}{mc^2}, \tag{4.3}$$

where e is the electric charge, V is the total accelerating voltage applied to the ensemble (contributing factors covered in Section 4.5), m is the isotope mass in eV/c^2, and c is the speed of light. The use of $\pm$ is dictated by the orientation of the ion and laser beams, with $'-'$ used for a collinear (parallel laser and ion beams, as used in this work) arrangement and $+$ for anti-collinear. The fluorescence detected from the subsequent atomic de-excitation will correspond to a single step in the voltage (and frequency) scan, thus producing the overall

hyperfine spectrum. Collinear laser spectroscopy is therefore a high-resolution means of providing measurements of nuclear spin, electromagnetic moments and mean-square charge-radii of isotopes via their hyperfine structure. These results are also obtained in a model-independent way.

4.5 The COLLAPS Experiment

COLLAPS is a permanent installation at ISOLDE, CERN, that utilises the collinear laser spectroscopy technique. The experiment takes ion beams from ISCOOL with electrostatic deflectors diverting ions down the main beam line parallel to the collinear laser beam. For neutral atom spectroscopy, the ion beam is guided by a series of injection electrodes with increasing magnitude of potential into the charge-exchange cell (CEC) in order to neutralise the ions. A post acceleration potential is applied to the CEC, after which the collinear laser and atoms interact, that allows for scanning over the hyperfine splitting. The fluorescence produced by the atomic decay from its excited state is then measured in photomultiplier tubes (PMTs) in the detection region at the end of the beam line. For ionic spectroscopy, the CEC is removed from the beam line and the post acceleration voltage is instead applied to the detection region. A schematic diagram of COLLAPS is given in Figure 4.7, with some of its main components discussed in the following sections.

4.5.1 Accelerating Potential

Conversion of a measured hyperfine spectrum as a function of accelerating voltage to frequency is required to determine the hyperfine A and B coefficients (in units of MHz) needed for the electromagnetic moments. The total accelerating voltage, V_{total}, that dictates the frequency seen by ions in their rest frame (Equation 4.2) at COLLAPS is understood quantitatively by

$$V_{\text{total}} = V_{\text{ISCOOL}} - [V_{\text{DAQ}} \times k + V_{\text{offset}}], \tag{4.4}$$

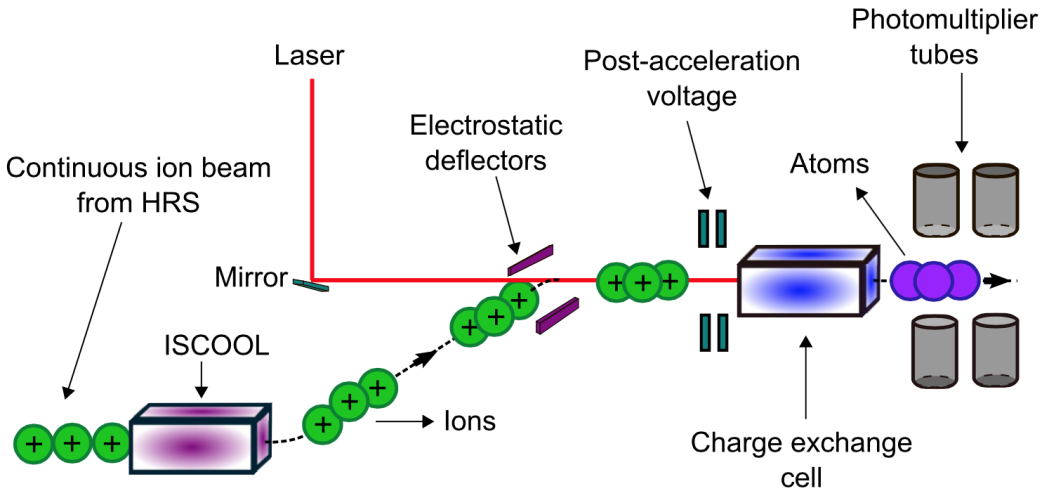

Figure 4.7: The COLLAPS beam line from ISCOOL to the detection region. Image taken from [79].

where V_{ISCOOL} is the high-voltage platform of ISCOOL with an operational range of $30 - 60$ kV that determines the energy of the ion beam approaching COLLAPS. The remaining factors combine to form the post acceleration voltage that is applied to the charge-exchange cell (CEC), as shown in Figure 4.8. The CEC will be described in detail in the following section. The combination of the data acquisition (DAQ) voltage, $V_{\mathrm{DAQ}} = \pm 10$ V, from an 18-bit digital-to-analog converter (DAC) and a linear amplification factor, $k \approx 50$, from the "Kepco" unit provides a maximum scanning range of $V_{\mathrm{scan}} = \pm 500$ V over which the full hyperfine structure is measured. The k factor is monitored frequently during the beam time to ensure its consistency. The other component of the post acceleration voltage, V_{offset}, corresponds to the high-voltage from one of three separate "Fluke" power supplies, and takes a value within ± 10 kV. The Flukes float on top of the "Kepco" unit to provide an "offset" to V_{scan} that can be tuned to account for isotopes of different masses.

Traditionally, one Fluke is permanently set for a reference isotope scan, and the other two set to different polarities. The voltages V_{scan} and V_{offset} pass through a 1000:1 voltage divider, are read-out by a precision voltmeter and recorded by the 'measurement and control program' (MCP).

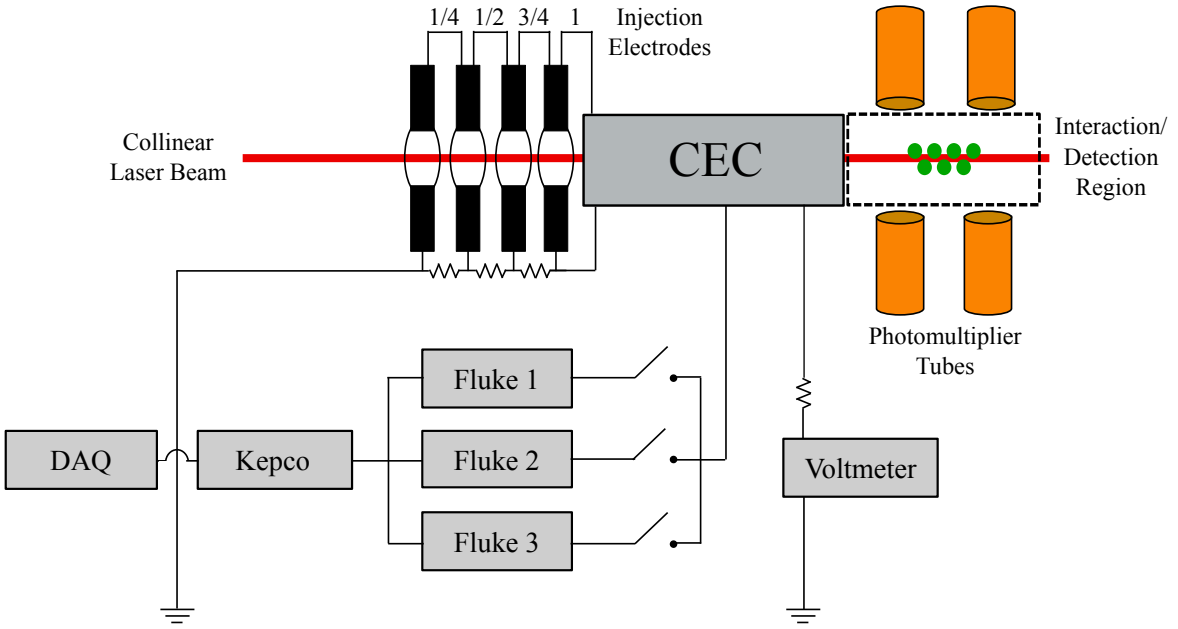

Figure 4.8: A simplified circuit diagram of the electrical components that combine to produce the scanning voltage applied across the CEC.

The scanning range of the accelerating potential is divided up into N channels, with photon counts collected for each voltage step over a period Δt. For each step in the voltage scan a single ion bunch will typically be released from ISCOOL to the beam line. The amount of bunches released from ISCOOL for each voltage step and the duration of their accumulation/release cycles can be varied to improve background reduction in the detection region (more details in Section 4.5.5). The value of N must be chosen such that individual components of the hyperfine structure can be resolved. The voltage change from one channel to the next, $V_{\text{scan}}/(N-1)$, is controlled and recorded by the MCP. Repetition of this cycle is necessary to increases statistics and hence the clarity of the hyperfine spectrum. This process is shown visually in Figure 4.9.

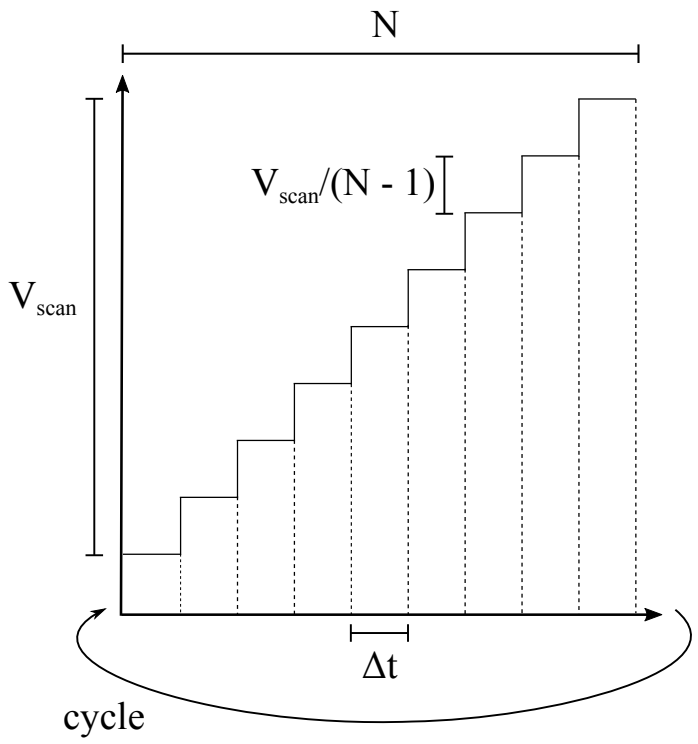

Figure 4.9: Graphical representation of a scanning cycle at COLLAPS. The scanning range of the accelerating potential, V_{scan}, is scanned over in N steps, with Δt being the time between each scanning step. Once the final step is reached, the system cycles back to the first step to repeat the scanning process.

4.5.2 Charge-Exchange Cell

Wavelengths required for spectroscopy of neutral atom beams are often easier to access than those of their ionic counterparts [80]. The neutralisation of low-energy ion beams therefore provides a practical advantage for collinear laser spectroscopy experiments. One such method by which this can be achieved is through a CEC located within the vacuum beam line.

At COLLAPS, the CEC [81] consists of a central horizontal metal tube located within a larger chamber. The inner tube is heated so that when a solid alkali-metal is placed inside, an alkali vapour is produced. Blocks at either end of the tube are cooled by oil circulation in order to condense the vapour within the path of the ion beam. In-flight neutralisation occurs in the CEC as a result of ion-atom charge-exchange interactions between the ion beam and

neutral alkali vapour. Electrostatic ion deflectors at the end of the CEC can deflect non-neutralised ions. As mentioned earlier, for spectroscopy of neutral atoms the Doppler tuning potential is applied to the CEC. However, for spectroscopy of ions, the CEC is simply removed from the beam line. The tuning potential is instead applied to the detection region where the collinear laser interacts with the ion beam.

The neutralisation efficiency of the CEC, N_{eff}, is given by the attenuation model of a particle beam moving through a medium [80]

$$N_{\text{eff}} = (1 - e^{-n\sigma l}) \times 100\%, \tag{4.5}$$

where n is the alkali vapour density in cm^{-3}, σ is the cross section of the neutralisation process in cm^2 and l is the effective interaction length in cm. This quantity is monitored regularly by measuring ion beam current before the CEC with a Faraday cup and the current after the CEC with ions having been deflected away. Since the alkali vapour density n and effective interaction length l are dependent on the temperature in the horizontal tube, a measured change in N_{eff} can be counteracted by changing the heater temperature. The charge exchange process between an incident fast ion $\underline{\text{X(a)}}^+$ in state a and an alkali atom of the charge exchange vapour Y(c) in state c is described by

$$\underline{\text{X(a)}}^+ + \text{Y(c)} \rightarrow \underline{\text{X(b)}} + \text{Y(d)}^+ + \Delta\text{E}_{\text{a,b,c,d}}, \tag{4.6}$$

where $\underline{\text{X(b)}}$ is an outgoing fast atom in state b, Y(d)^+ is an alkali ion in state d, and $\Delta E_{a,b,c,d}$ corresponds to the energy between states a, b, c, d. For resonant collisions, $\Delta E = 0$. Non-resonant collisions however have a non-zero energy difference, $\Delta E \neq 0$, that results in the loss of kinetic energy from the outgoing fast atom beam. As a result, atoms neutralised via the non-resonant channel will have a lower velocity than those neutralised via the resonant channel [82] and hence the resonance will be measured at a seemingly higher beam energy than the resonant frequency in the Doppler-shifted spectrum. In hyperfine spectra, this can lead to an observable asymmetry in the measured line shape. The effect of this on the

hyperfine spectrum of Zn isotopes will be discussed in Section 5.1.2.

For laser spectroscopy of Zn atoms, the incident Zn ion beam is neutralised in a charge-exchange vapour of Na atoms. The energy excess in this charge-exchange interaction can be understood as the difference in their ionisation potentials (IP), with the IP of Zn (= 9.39 eV) [83] and the IP of Na (= 5.14 eV) [84] producing an energy excess of $\Delta E = 4.25$ eV. As a result, atomic levels with $E \gtrapprox 4.25$ eV will be preferentially populated as a result of this CEC interaction. The metastable $4s4p\ ^3P_\mathrm{J}$ triplet of states in Zn ($\Delta E \approx 4.02$ eV) is one such set of states that is quasi-resonantly populated. This is advantageous for laser spectroscopy of Zn since there are a number of strong transitions to higher-lying states from $4s4p\ ^3P_{0,1,2}$. This triplet will therefore form the lower level of the atomic transition used to study Zn.

4.5.3 Atomic Transition

The selection of an atomic transition for spectroscopy is vital for the efficient determination of nuclear properties from hyperfine spectra. For studying Zn, the decision is made somewhat simpler by the aforementioned neutralisation process in the CEC with the Na atomic vapour where the small energy excess from the charge-exchange collisions quasi-resonantly populates the long-lived metastable $4s4p\ ^3P^\mathrm{o}_\mathrm{J}$ triplet state in Zn. The ground state transition to or from the $^3P^\mathrm{o}_1$ level in this triplet (the only allowed ground state to $^3P^\mathrm{o}_\mathrm{J}$ triplet transition based on selection rules) is too weak for efficient spectroscopy and so the energy excess from the CEC process helps to avoid this problem.

The $4s4p\ ^3P^\mathrm{o}_\mathrm{J}$ triplet state presents an ideal lower atomic level for spectroscopy as there are numerous strong transitions to higher lying states [85]. Additionally, de-excitations from the $^3P^\mathrm{o}_{0,2}$ states to the $4s^2\ ^1S_0$ ground state are forbidden by selection rules and the $^3P^\mathrm{o}_1$ level has a 20μs lifetime, which means there is sufficient time to perform spectroscopy. From this triplet, the transition from the $4s4p\ ^3P^\mathrm{o}_2$ level at 32890.22cm^{-1} to the $4s5s\ ^3S_1$ at 53672.24cm^{-1} is selected for spectroscopy of neutral Zn atoms. This corresponds to a wavelength of 481.1873 nm. The $J = 2 \rightarrow 1$ transition provides a greater sensitivity to the nuclear spin than the alternative $J = 0, 1 \rightarrow 1$ transitions due to the increased number of observable hyperfine

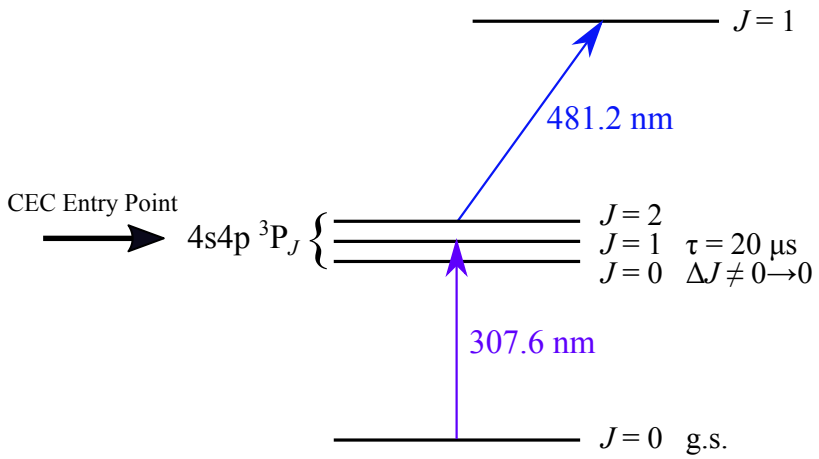

Figure 4.10: Simplified atomic level orientation for Zn showing the atomic transition selected for spectroscopy from the metastable $4s4p\ ^3P_2^o$ state to $4s5s\ ^3S_1$.

transition peaks between the upper and lower F states (using $F = I + m_J$).

4.5.4 The COLLAPS Laser Setup

Production of the 481.1873 nm wavelength light for the $4s4p\ ^3P_2^o \rightarrow 4s5s\ ^3S_1$ transition is achieved via the Matisse 2 Titanium:Sapphire (Ti:Sa) tunable laser and Wavetrain 2 external cavity frequency doubler at COLLAPS. The following sections will outline the basic principles of these devices.

Matisse Ti:Sa Laser

The Matisse system, shown in Figure 4.11, is pumped by a continuous wave (CW) frequency doubled Nd:YVO_4 laser at 532 nm with 15 W power in order to produce a laser output in CW mode, as required for collinear laser spectroscopy. Pump radiation excites electrons in the titanium-doped sapphire crystal (Ti^{3+}:Al_2O_3) from the ground state band to an excited state band. Here the electrons de-excite due to collisional relaxation to the bottom of the band, meaning the population inversion condition of the laser gain medium is achieved. Stimulated emission of these excited state electrons to the ground state band amplifies the laser light across the tunable wavelength range. Ti:Sa crystals provide a broad tunable wavelength

output, $\lambda = 650 - 1100$ nm, which, in addition to the narrow linewidth of its output light makes them ideal for high-resolution spectroscopy. The output laser wavelength is tuned by a combination of thick etalons (TE), tuning mirrors (TM), folding mirrors (FM) and a Lyot filter (three motor-driven birefringent filters (BF)), with counter-clockwise circulation around the ring cavity maintained by a unidirectional device (UD). The final folding mirror (bottom right) is partially reflective, allowing some light to escape the cavity and the remainder to continue to circulate the Matisse cavity to increase the intra-cavity optical power. A portion of the output laser light, dictated by the transmission of the output coupler (OC), is redirected to a temperature controlled reference cavity for active stabilisation of the laser frequency. This produces an error signal that is sent to the fast piezo-mounted folding mirror in order to apply fast cavity length corrections. The light that is transmitted through the output goes to the frequency doubler cavity. To ensure long-term stabilisation of the Ti:Sa, the tunable laser frequency is locked to a Fabry-Pérot interferometer (FPI) that is itself locked to a stabilised helium:neon (He:Ne) laser.

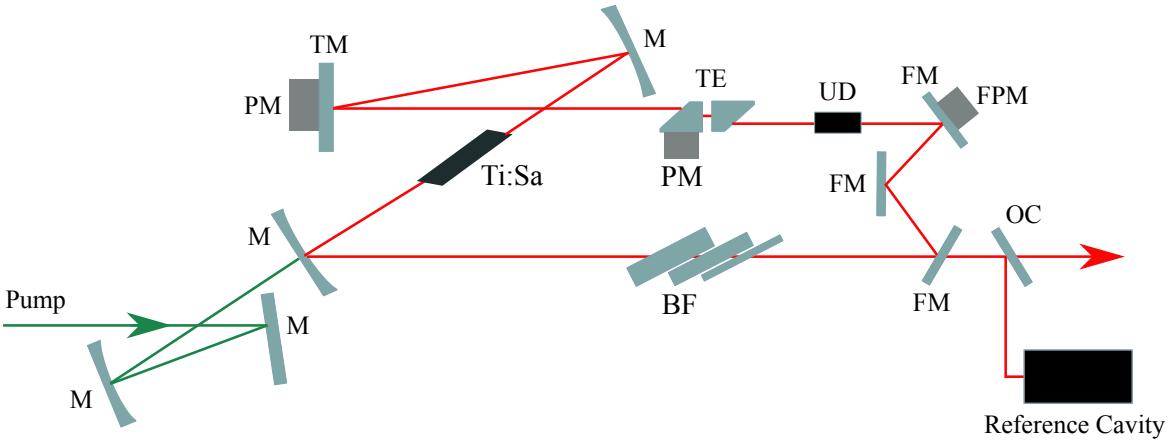

Figure 4.11: Schematic diagram of the cavity elements in the Matisse tunable laser (not to scale). Optical elements labelled in the image include mirrors (M), folding mirrors (FM), tuning mirror (TM), piezo-mount (PM), fast piezo-mount (FPM), Ti:Sa crystal, thick etalon (TE), unidirectional device (UD), birefringent filters (BF) and output coupler (OC). The OC directs a portion of the output laser light to a reference cavity.

Wavetrain Frequency Doubler

The 481.1873 nm wavelength light required for spectroscopy of Zn is produced by frequency doubling laser light from the Matisse within the WaveTrain external frequency doubler cavity. A schematic diagram of the Wavetrain is given in Figure 4.12. Upon entering the Wavetrain, the fundamental beam passes through an electro-optical modulator (EOM) to add sidebands to the fundamental beam for the active stabilisation of the ring cavity length. The fundamental is then focused through a series of lenses (L), directed to the central ring cavity by folding mirrors (FM) and mode matched with the cavity by a beam shifter (BS). In this triangle cavity, the fundamental passes through a nonlinear lithium triborate (LBO) crystal to produce frequency doubled laser light that passes through a mirror (M), is focused by a lens and directed to the ISOLDE hall by a series of folding mirrors. The fundamental beam that is not frequency doubled by the crystal is reflected back into the triangle cavity by a mirror and continues its circulation to increase the laser power. A Brewster prism (BP) ensures only fundamental light passes through the doubling crystal to increase the frequency conversion

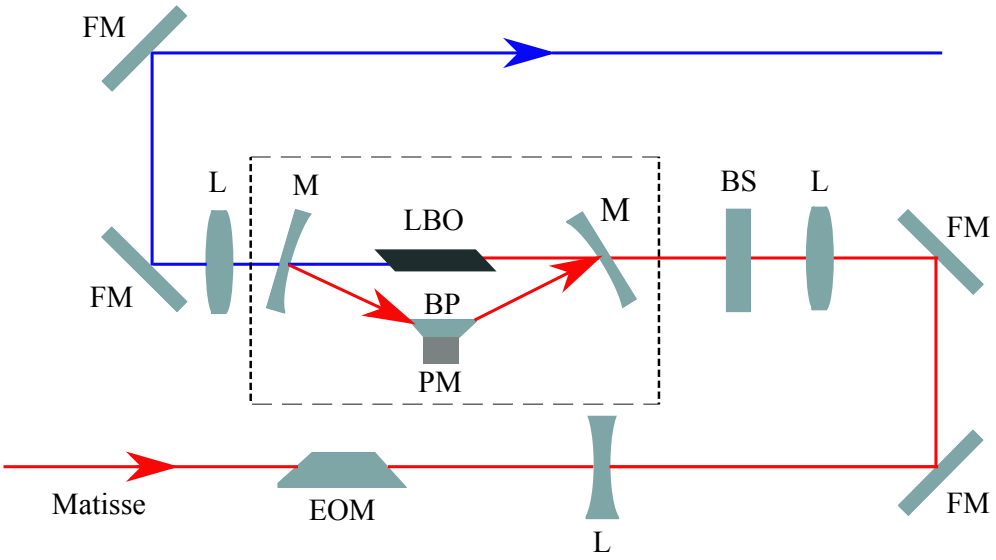

Figure 4.12: Schematic diagram of the cavity elements in the Wavetrain frequency doubler cavity (not to scale). Optical elements labelled in the image (not already referenced in Figure 4.11) include electro-optical modulator (EOM), lens (L), beam shifter (BS), nonlinear crystal lithium triborate (LBO) and Brewster prism (BP).

process. Prior to entering the beam line, the laser power can be managed by neutral density filters.

4.5.5 Detection Region

Fluorescence emitted due to the atomic de-excitation of particles in the bunched beam is detected by a set of four PMTs at the end of the COLLAPS beam line, oriented in two rows perpendicular to the beam path as shown in Figure 4.8. The corresponding signals are amplified, passed through a discriminator and, if greater than the threshold defined on the unit, the signal is counted by MCP. The addition of a Brewster window at the end of the beam line reduces internal laser reflections that are a source of background.

For each step in the voltage scan, the total number of counts is recorded by the MCP before moving on to the next step in the scan. The number of steps taken across the scan region must be sufficient to resolve the hyperfine splitting. This process produces a hyperfine spectrum initially as a function of scanning voltage, V_{DAQ}, that is then converted to frequency by Equations 4.2 and 4.4.

Background Reduction

The reduction of background counts in the detection region is required to produce hyperfine spectra for low radioactive yields, with the dominant contribution to background in collinear laser spectroscopy experiments coming from continuous non-resonant scattered photons due to the laser beam. The suppression of such background can be achieved through the temporal coordination of ion-bunch release from ISCOOL with the counting of photons by the MCP. At COLLAPS, users can select a photon "gate" to place on the photon signal recorded by the MCP, t_{MCP}, that defines the period in which photons are accepted. By calculating the time-of-flight of an individual isotope, the photon gate can be applied so that photons are only counted while the ion bunch containing the isotope-of-interest is in front of the PMTs.

The data acquisition software allows collection of data with a user defined photon gate

(and one without photon gating) across all four PMTs simultaneously[1]. For a given photon gate in the MCP, t_{MCP}, the background reduction is given by:

$$\text{background reduction} \approx \frac{\mathrm{t_{ISCOOL}}}{\mathrm{t_{MCP}}} \tag{4.7}$$

where t_{ISCOOL} is the length of a single accumulation and release cycle of ISCOOL. For the study of Zn, suitable photon gates from ToF measurements range from $t_{\mathrm{MCP}} = 3 -$

[1]The gate applied to the back row of PMTs is slightly delayed to account for the extra distance travelled by the ion bunch.

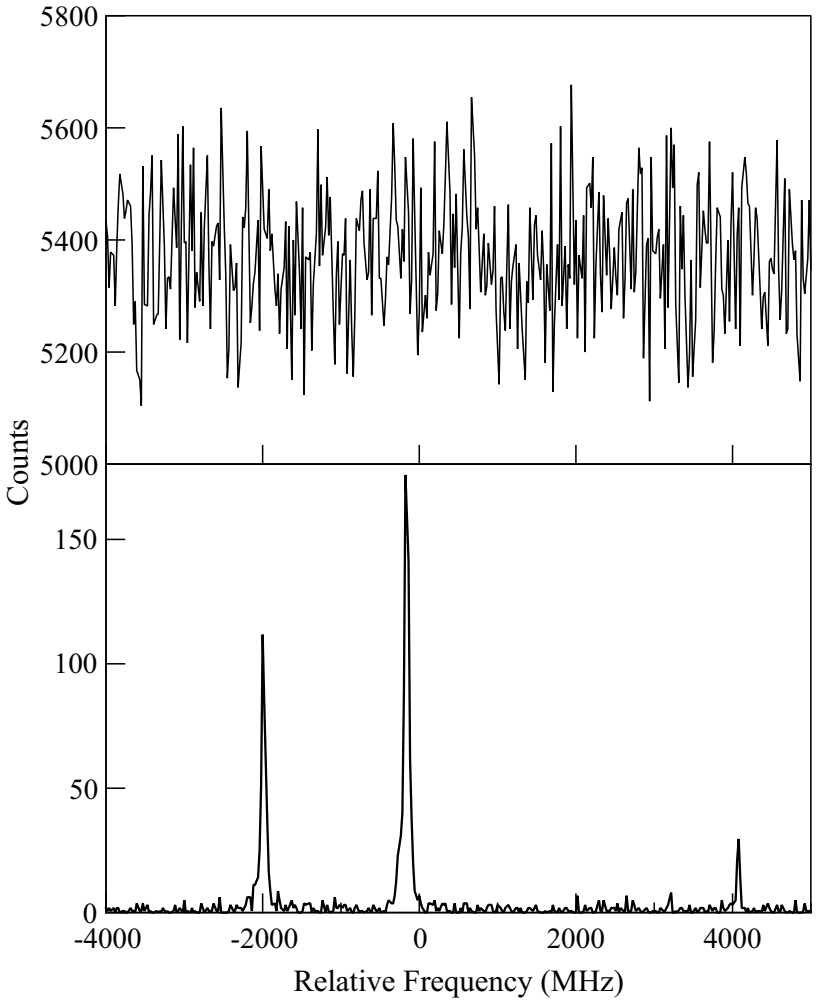

Figure 4.13: Measured hyperfine spectra of ^{73}Zn from this work with no photon gating (top) and an MCP triggered 5μs photon gate (bottom).

10μs. Taking the 5μs gate as an example with an ISCOOL cycle of $t_{\mathrm{ISCOOL}} = 100$ ms, the background seen in ungated spectra can be reduced by a factor of $\sim 4\times10^4$ with this method. This improvement is shown in Figure 4.13 for the hyperfine spectrum of ^{73}Zn.

Further suppression of background is achieved through proton triggering, where the data acquisition program is triggered by the impact of a proton pulse on the target. This method means the release of ions from ISCOOL and photon counting in the MCP can be initiated at a specified time after proton impact to maximise release from the target. The relatively fast release of Zn from the UC_x target at ISOLDE dominates over the slower release of Ga until $\approx$ 800 ms after protons impact upon the target, as shown in Figure 4.14. Therefore we select the first 600 ms after proton impact to accept bunched beam from ISCOOL to maximise the yield of Zn from the target relative to the Ga isobar. This also presents a distinct advantage for the measurement of short-lived isotopes.

In order to avoid overfilling of the buncher, and maintain the well-defined temporal structure of the ion bunch, the individual accumulation and release cycle of ISCOOL is often divided into multiple shorter cycles. For the 600 ms window of maximum Zn release from

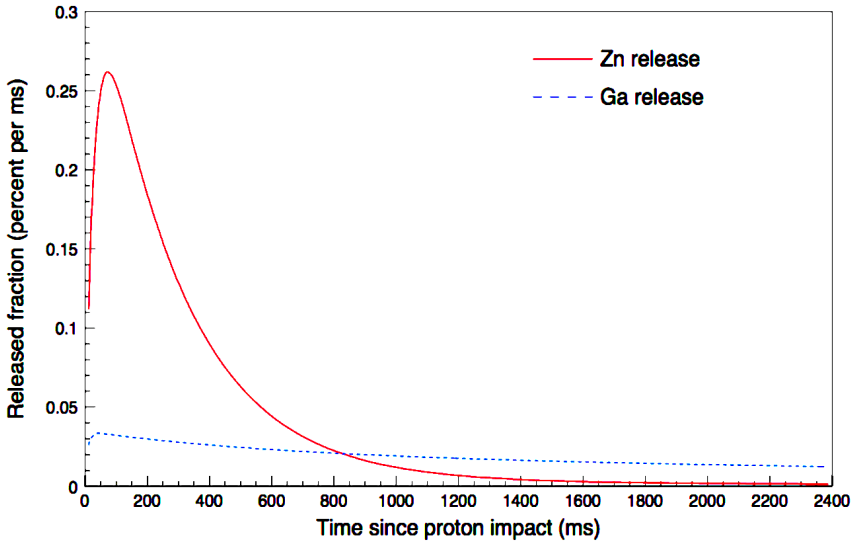

Figure 4.14: The fast release of Zn from a UC_x target compared to the release of Ga. Image taken from [86].

the target, ISCOOL cycles of 3×200 ms or 4×100 ms after proton impact on target will be applied to most isotopes across the Zn chain in this work. The only notable exception to this will be the cycle used for the 13 ms state in ^{73}Zn. Instead, the accumulation and release cycles are reduced to 10×10 ms or 2×10 ms in order to ensure data is collected while a significant fraction of the short-lived isomer still exists after the interaction of protons and the target. The clear enhancement of the isomeric state structure in ^{73}Zn relative to the ground state (lower panel of Figure 4.13) when using the 2×10 ms proton triggered ISCOOL cycle is shown in Figure 4.15. Proton triggering therefore provides a significant advantage for the study of isotopes with relatively short-lived states.

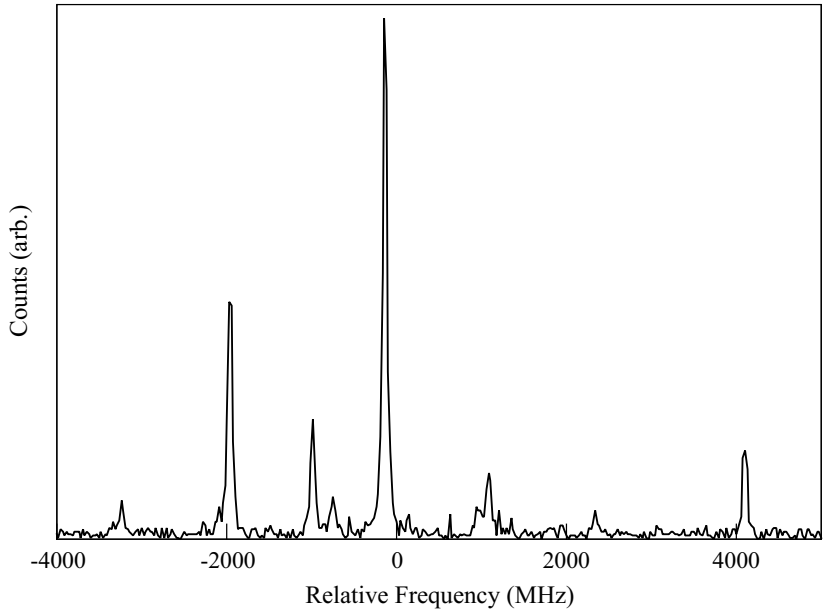

Figure 4.15: Hyperfine spectrum of ^{73}Zn measured with a 2×10 ms proton triggered ISCOOL cycle. The enhancement of the isomeric structure relative to the ground state due to the shortened cycle length is clear when comparing this spectrum to the 4×100 ms cycle spectrum in the lower panel of Figure 4.13.

Chapter 5

Analysis of Zinc Hyperfine Spectra

The collinear laser spectroscopy method allows for the unambiguous assignment of ground and isomeric state nuclear spins, I. In principle, the results from laser spectroscopy can be used in conjunction with decay spectroscopy data to make definitive spin assignments of higher lying levels due to measured transition multipolarities. Confirmed spins can then be used in the analysis to determine magnetic dipole moments, μ, spectroscopic quadrupole moments, Q_s, and mean-square charge radii, $\langle r^2 \rangle$, in a model-independent way from measured hyperfine spectra (using equations previously stated in Chapter 2). These nuclear properties provide information about nucleon configurations in nuclei, and the shape and size of the nucleus. The accurate extraction of nuclear properties from a hyperfine spectrum is therefore paramount for us to understand the development of nuclear structure across an isotope chain.

5.1 χ^2-minimisation Method

The nuclear properties from a hyperfine spectrum can be obtained by producing a model hyperfine structure, that is dependent on the centroid ν_0, nuclear spin, I, and the hyperfine coefficients (A_u, A_l, B_u, B_l), and comparing it to the initial measured spectrum. Estimates of these hyperfine parameters are initially obtained by superimposing a model hyperfine spectrum on to the experimental spectrum and altering the model parameters until a close

agreement between the two structures is seen. These parameters can then be used as a starting point for a more thorough comparison.

For the extraction of nuclear properties from hyperfine spectra, χ^2-minimisation is a widely adopted technique. The χ^2-minimisation process involves the fitting of a model to experimental data by varying individual fitting parameters until the χ^2 statistic is minimised. The χ^2 value is defined as

$$\chi^2 = \sum_i^n \frac{(x_i - x_i')^2}{\sigma_i^2}, \tag{5.1}$$

where n is the number of bins, x_i is the fitted counts in the ith bin, x_i' is the experimentally measured counts and σ_i is the error on the measured counts in each bin, $\sigma_i = \sqrt{x_i' + 1}$. From the χ^2 value, a quantitative *goodness-of-fit* between the model and experiment can be calculated. This quantity, referred to as the reduced χ^2, χ_r^2, is defined as

$$\chi_r^2 = \frac{\chi^2}{\nu}, \tag{5.2}$$

where ν is the number of degrees of freedom, with $\nu = n - N$, where n is the number of bins and N is the number of fitting parameters. The χ_r^2 is also used to determine errors on the nuclear properties extracted from the χ^2-minimisation test. Fitting errors are obtained by calculating the covariance matrix for each parameter and taking the square root of its diagonal elements. Then, factoring in the quantitative goodness of fit to the data, χ_r^2, the error on a single fitting parameter is given by

$$Error = \sigma \times \sqrt{\chi_r^2}. \tag{5.3}$$

The errors provided by the fitting for A_u, A_l, B_u and B_l are carried forward through the analysis and therefore contribute to errors on the calculated magnetic dipole moments and spectroscopic quadrupole moments. During this analysis, χ^2-minimisation fits to ground and isomeric state structures are completed simultaneously where necessary, with the quantities

ν_0[1], A_u, A_l, B_u, B_l for each nuclear state left as free parameters throughout.

5.1.1 Spectral Line Shape

Prior to performing the χ^2-minimisation fitting to data, we must first select the line shape of the fitted spectrum. The absorption spectrum is measured as a frequency distribution around the resonant transition frequency, with the natural line shape for an atomic transition closely following that of a Lorentzian distribution (in the case where no thermal or Doppler broadening effects are present) [78]. Therefore, the non-normalised Lorentzian distribution, L, is used here for the fitting process to hyperfine spectra, and is given by:

$$L(x) = I\frac{\Gamma^2}{4[(x-x_0)^2 + (\Gamma/2)^2]} \tag{5.4}$$

where x is the frequency, I is the peak intensity, x_0 is the peak centroid and Γ is the full-width at half maximum (FWHM) of the resonance peak. The Voigt line shape (a convolution of Gaussian and Lorentzian line shapes) was also considered for this work due to its ability to account for broadening effects, however, comparison of the extracted properties from each line shape revealed minimal differences. Intensities of resonance peaks in the fit are initially constrained to Racah relative intensity values [88] at 90°, a method which forces peaks in the fitted spectrum to have a proportion of the overall intensity based on angular momentum coupling rules. This proves useful for determining nuclear spin assignments. Firstly, the intensity distribution depends on the nuclear spin. Secondly, if an incorrect spin is assigned and tested, when fitting with free intensity parameters, the intensity of unmatched fitting peaks can collapse to ≈ 0 to reduce the error of the fit. Racah intensities therefore more clearly highlight incorrect spin assignments both statistically and visually. Once a spin is unambiguously determined, the fit is repeated with free intensity parameters for each peak, which should produce A and B values that are within errors of those obtained from fits with Racah relative intensities.

[1]The extracted centroids (used to determine the mean-square charge radii, $\langle r^2 \rangle$) will not be referenced in this work, but will be covered in a future publication from the COLLAPS collaboration by L. Xie [87].

5.1.2 Peak Asymmetry

The influence of non-resonant charge exchange interactions on collinear laser spectroscopy has been discussed in Section 4.5.2. These types of inelastic interactions between the ion beam and charge exchange vapour leave a number atoms in higher energy states, the energy of which corresponds to the kinetic energy lost from the beam during a single collision, ΔE. As a result, the fluorescence from these atoms is detected at a seemingly lower frequency than the resonance peak. The frequency offset of these photons from the resonance is given by the product of ΔE (in eV) and the mass-dependent linear approximation. This can lead to an asymmetry of the measured resonance peaks, which, if unaccounted for leads to incorrect values of hyperfine structure coefficients and the centroid obtained from the χ^2-minimisation fitting.

For Zn, the dominant CEC interaction between fast Zn ions and Na vapour is only quasi-resonantly populating the $4s4p\ ^3P_2$ triplet. The $J = 2$ state in this triplet is the lower level of the atomic transition selected for this work, $4s4p\ ^3P_2^{\mathrm{o}} \rightarrow 4s5s\ ^3S_1$, meaning population of this state is required for any resonances to be detected. Therefore, any observed asymmetry in hyperfine transition peaks of Zn isotopes will occur as a result of additional non-resonant collisions in the CEC that populate other excited states, which subsequently decay to the $J = 2$ state.

In order to account for this asymmetry in the χ^2-minimisation fitting, a series of Lorentzian "satellite peaks" separated by a constant energy offset from the resonance peak are added to the model. The decreasing probability of each additional non-resonant CEC collision means the intensity of these satellite peaks must decrease as n increases. Therefore, satellite peak intensities are best described by the Poisson distribution [82]

$$P(n, b) = \frac{b^n}{n!} e^{-b}, \tag{5.5}$$

where n is the satellite peak number (with $n = 0$ being the resonance peak) that corresponds to the number of successive inelastic collisions, and b is a factor that depends on the length

and density of the Na charge exchange vapour. The latter is left as a free parameter to account for any changes to CEC conditions during the experiment. Minor modifications are made to the Lorentzian line shape described in Equation 5.4 to produce a skewed Lorentzian profile that accounts for n satellite peaks,

$$L_{\text{skew}}(x) = \sum_{n} P(n,b) \times I \frac{\Gamma^2}{4[(x - (x_0 + n \times x_{\text{offset}}))^2 + (\Gamma/2)^2]} \tag{5.6}$$

where x_{offset} is the frequency offset due to an inelastic collision in the CEC that varies with isotope mass. The energy offset (and hence frequency offset) and number of collisions are initially left as free parameters that are evaluated during the initial fitting process.

Final values of $n \leq 5$ and $\Delta E \approx 2.6$ eV are obtained from the fitting and are then fixed for all isotopes. The fitted energy offset of ≈ 2.6 eV is in agreement with the average energy between the $4s4p\ ^3P_{0,1,2}$ triplet of states and the $4s5s\ ^3S_1$ level in Zn ($\Delta E \approx 2.625$ eV). This confirms that the peak asymmetry occurs as a result of multiple CEC collisions that lead to population of the ^3P_J triplet involved in the atomic transition used in this work. The effect of this skewed Lorentzian line shape on fitting parameters is shown in Figure 5.1, where the difference between the centroid of ^{68}Zn from the pure Lorentzian line shape to the skewed Lorentzian is ≈ 6 MHz. While it is possible that other high-lying states may be populated during CEC collisions, the lack of a fast transition to the $^3P_2^{\text{o}}$ state means they will not contribute to any peak asymmetry measured via the $4s4p\ ^3P_2^{\text{o}} \rightarrow 4s5s\ ^3S_1$ transition.

5.2 Nuclear Spin Determination

The ground state spins of the odd-A isotopes $^{63-71}$Zn and the isomeric spins of ^{69,71}Zn have already been confirmed in previous studies. The remaining odd-A isotopes, $^{73-79}$Zn, have tentative spin assignments for both their ground and isomeric states prior to this work. Confirming the nuclear spins of these isotopes will be the primary focus of the initial χ^2-minimisation fitting tests with Racah relative peak intensities. Since the ground and isomeric state structures are fitted simultaneously in this process, the spin of one state (ground or

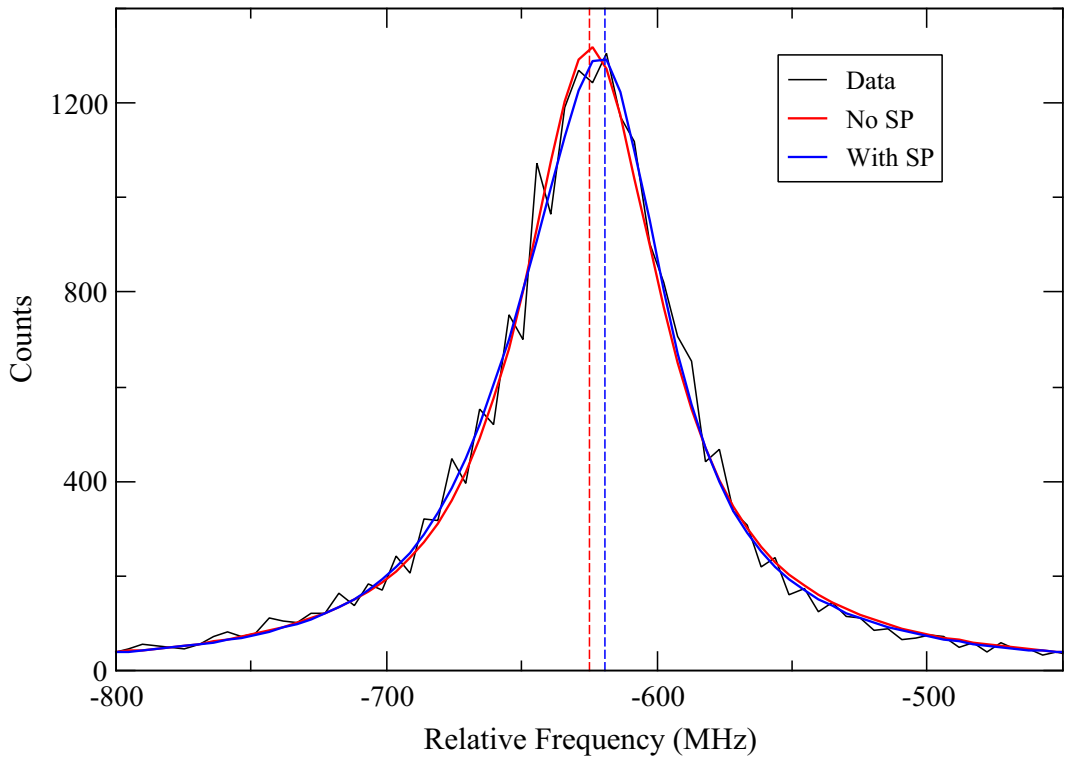

Figure 5.1: χ^2-minimisation fits with satellite peaks (blue) and without satellite peaks (red) included compared to the measured spectrum of ^{68}Zn. The blue and red dashed lines represent the respective peak centroids from the two fits with $\Delta\nu_0 \approx 6$ MHz.

isomer) will be kept constant (at the tentative spin assignment) whilst the other is varied between the tentative assignment and the neighbouring spin values (i.e. $I \pm 1$). The fitted spectra will be assessed (in order of applicability) on their ability to reproduce the number of measured resonance peaks and their relative spacing, the hyperfine A coefficient ratio ($R_{\text{exp}} = 0.4197(3)$ for the 481.1873 nm line in Zn)[2], and the Racah relative peak intensities (see Section 2.3.1 for more details). The χ^2_r value that reflects the statistical *goodness of fit* between the fitted spectrum and data can also be used, although this quantity is not particularly reliable unless there are drastic changes between the χ^2_r values of different spins. For instance, if a small fitting peak is visibly offset from a measured peak, the difference in χ^2_r will not necessarily be significant, even though the fitted structure clearly does not match

[2]Reference values of $A_{\text{l}} = +531.987(5)$ MHz and $A_{\text{u}} = +1267.5(1.0)$ MHz for the stable isotope ^{67}Zn are taken from Refs. [89] and [90] and used to calculate the expected ratio (R_{exp}) of $A(^3P_2)/A(^3S_1) = 0.4197(3)$ for the Zn isotope chain.

to the experimental structure.

Results of the χ^2-minimisation fitting for tentative ground and isomeric state spins and their neighbouring spin values for $^{73-79}$Zn are given in the following section. The fitted hyperfine structures for each nuclear spin are shown against experimental spectra in figures, with the ground and isomeric state peaks labelled g and m respectively or numbered to simplify discussion when the state is under investigation. The state to which individual resonance peaks are assigned to are initially determined by superimposing a model hyperfine spectrum with the tentative ground or isomeric spin over the measured spectrum. The fitting parameters $A(^3P_2)$, $A(^3S_1)$, $B(^3P_2)$, R_{exp} and χ^2_r corresponding to each spin value are given in tables, with values corresponding to the correct spin assignment displayed in bold text. $B(^3S_1)$ is not used henceforth as fitted values are ~ 0 and $\Delta B(^3S_1) \leq B(^3S_1)$ for all isotopes. The results for the previously confirmed spins of $^{63-71}$Zn are given in Appendix A for validation of our analysis process.

5.2.1 ^{73}Zn ($N = 43$)

The ground state of ^{73}Zn has a tentatively assigned spin of $I = 1/2$. The same spin assignment has been confirmed for the ground state of ^{69,71}Zn. The existence of a 13 ms isomeric state was first proposed in [15] from the β-decay of a ^{73}Cu beam, with the state initially being assigned a tentative spin of $I^\pi = 5/2^+$. Experimental evidence of a higher-spin second isomeric state has been proposed [91] with $t_{1/2} = 5.8$ s but was not observed in other work [15], and hence its existence is unconfirmed as of yet. The hyperfine spectrum of ^{73}Zn therefore presents the opportunity to determine the spin of the 13 ms isomer and the existence of the 5.8 s isomer.

In Figure 5.2, the χ^2-minimisation fits of the $I = 1/2$ and $3/2$ ground state spins are shown with the experimental spectrum. The experimental spectrum of the ground state ($t_{1/2} = 23.5$ s) is measured with an ISCOOL accumulation and release cycle of 4×100 ms per proton bunch. This proves to be too long for a measurable amount of the 13 ms isomer to remain as the hyperfine structure of the isomer is indistinguishable from background.

To increase the intensity of the isomer peaks relative to the background we put protons

directly on to the target to increase the yield of the ion beam [69]. At this mass number the beam contamination from proton-rich isobars, namely ^{73}Rb, will have a minimal effect due to their short lifetime of < 30 ns. As a result, the proton-neutron converter is not required to suppress rubidium isotopes. In addition, a shorter ISCOOL accumulation and release cycle of 2×10 ms following proton bunch is used to limit the photon counting window to a couple of isomeric state half-lives. The combination of these measures will work to maximise the statistics of the isomeric spectrum for the χ^2-minimisation fitting, the results of which are shown in Figure 5.3. It is therefore worth noting that the data for ^{73}Zn and ^{73m}Zn shown in Figures 5.2 and 5.3, respectively, are not from the same experimental run.

Ground State Spin

The measured hyperfine spectrum is rather conclusive regarding the spin of the ground state. Three observable peaks and their intensity distribution can only correspond to a spin-1/2 state for a $2 \rightarrow 1$ atomic transition, a fact that is also reflected by the output values from the χ^2-minimisation fitting shown in Table 5.2. As expected the additional resonance peaks associated with a spin-3/2 structure do not align with experimentally measured peaks, and the χ^2-minimisation fitting subsequently produces poor statistical fit ($\chi^2_r = 15.21$ and $A(^3P_2)/A(^3S_1) = 0.4166(8)$) when compared to $I = 1/2$. The ground state spin of ^{73}Zn is therefore confirmed as $I = 1/2$.

The duration of the 4×100 ms ISCOOL cycle should be more than sufficient for the measurement of the proposed 5.8 s isomeric state in ^{73}Zn. Beyond the peaks attributed to the $I = 1/2$ ground state, no others are observed to signal the presence of an isomeric state with a lifetime of the order of seconds. Therefore we conclude that the 5.8 s isomer either does not exist or is not populated by reactions within the target.

Isomeric State Spin

In addition to the three resonances of the $I = 1/2$ ground state, eight further resonance peaks are now observed in the spectrum and are attributed to the isomeric state. Based

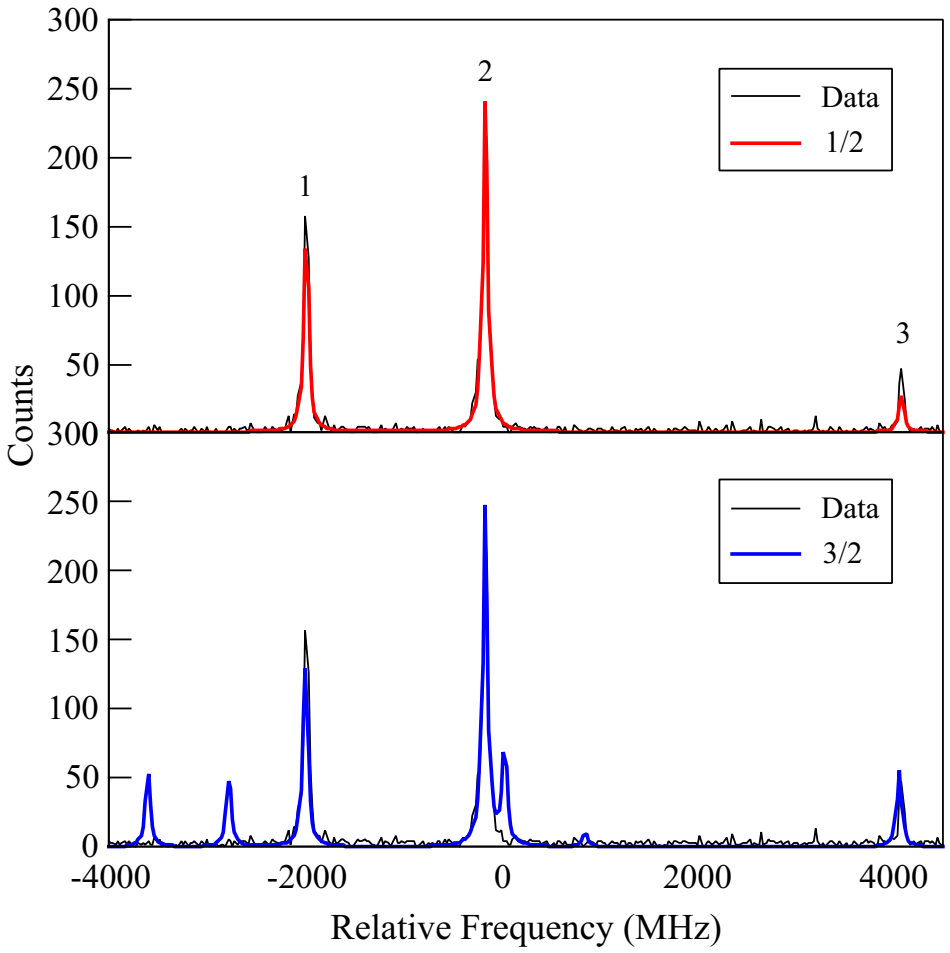

Figure 5.2: Plot of the fitted spectrum for different spin assignments of the ground state in ^{73}Zn.

Table 5.1: Results from the χ^2-minimisation fitting of the ground state structures for ^{73}Zn.

I	χ^2_r	$A(^3S_1)$ (MHz)	$A(^3P_2)$ (MHz)	$B(^3P_2)$ (MHz)	$A(^3P_2)/A(^3S_1)$
1/2	**1.10**	**+4041.4(3.9)**	**+1694.6(2.2)**	—	**0.4193(7)**
3/2	15.21	+2421.1(2.5)	+1008.7(1.6)	+786.9(4.2)	0.4166(8)

on the number of measured resonance peaks in the spectrum, the tentative spin assignment of $I = 5/2$ (nine peaks) and the two neighbouring spins $I = 3/2, 7/2$ (eight, nine peaks) could all reasonably reproduce the hyperfine structure of the isomer. The spin-5/2 structure represents the best statistical fit to the experimental data when compared to the neighbouring

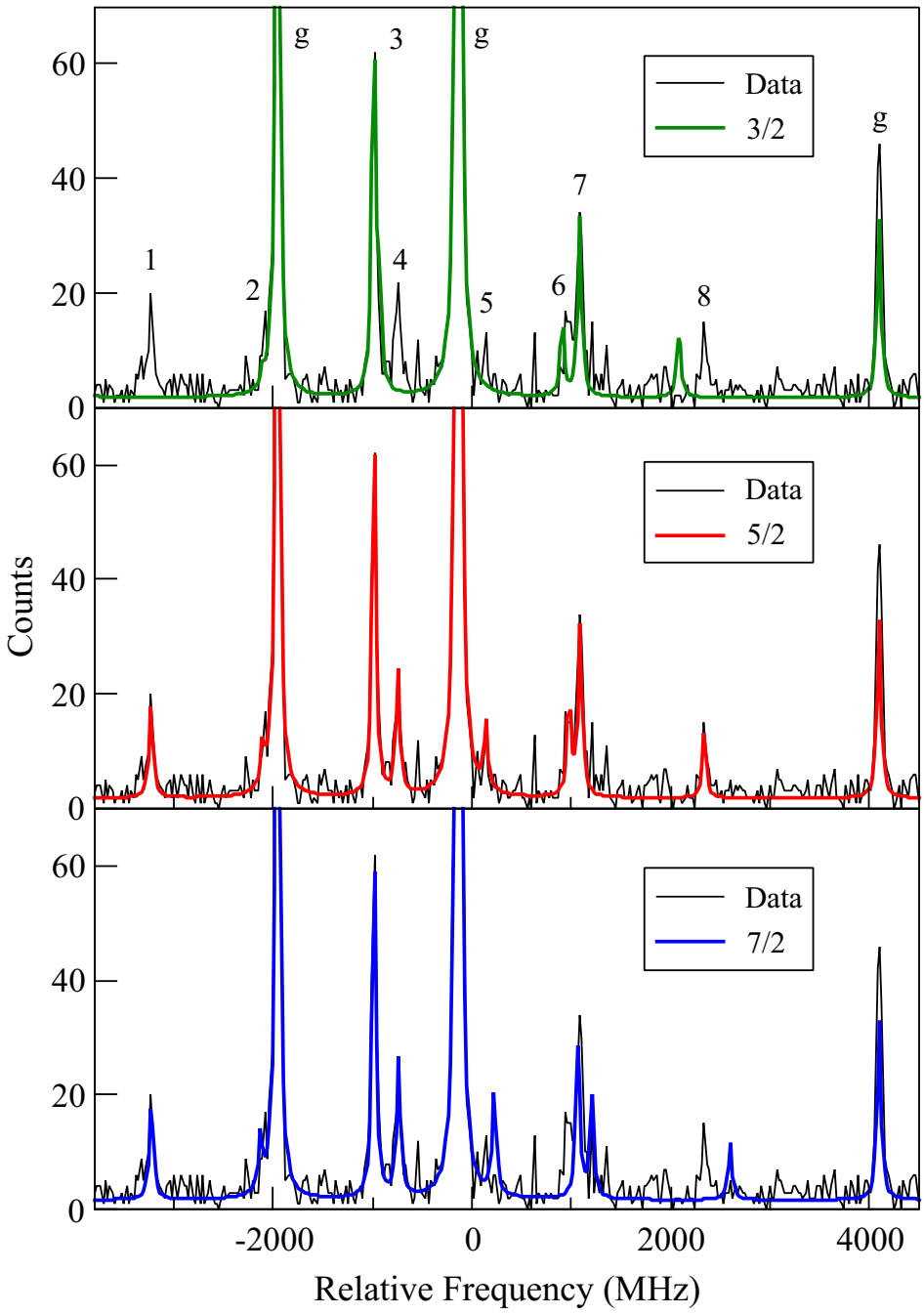

Figure 5.3: Plot of the fitted spectrum for different spin assignments of the isomeric state in ^{73}Zn.

spins ($\chi^2_r = 1.10$ compared to $\chi^2_r = 1.81, 1.61$), and hence the fitted spectrum matches to all eight resonance peaks (excluding one additional peak outside the scan range). Conversely

the spin-3/2 structure does not align with peaks 1, 2, 4, 5 and 8, with the majority of its fitting peaks not visible in the spectrum as they are likely masked by aligning to ground state resonances. The spin-7/2 is unable to match with peaks 2, 6 and 8. Visible differences between the intensity distributions of each χ^2-minimisation fit are minimal due to the generally low intensity of peaks in the isomeric structure, and hence they are not used here to determine the spin assignment. The neighbouring spins $I = 3/2$ and 7/2 present $A(^3P_2)/A(^3S_1)$ values (0.4105(10) and 0.4216(10) respectively) that are outside errors of R_{exp}, although these A ratios correspond to fits that do not reproduce all measured transition peaks. However, the A ratio for the spin-5/2 structure (0.4199(11)) lies within the fitting error of the known value of 0.4197(3) and reproduces all peaks in the measured spectrum. These results therefore confirm the nuclear spin of the isomeric state in ^{73}Zn as $I = 5/2$.

We can estimate the lifetime of the $I = 5/2$ isomer by changing the duration of the measurement cycle after protons hit the target and comparing the intensity of the isomeric structure peaks. The intensity of the isomeric structure in Figure 5.3 with a 20 ms measurement cycle (2×10 ms ISCOOL cycle) is $5\times$ greater than the intensity seen with a 10×10 ms cycle (shown in Figure 1b of Ref. [37] from this work). This provides confirmation that isomeric peaks are from a state with half-life the order of 10 ms (in agreement with the $t_{1/2} = 13$ ms from Ref. [15]). Further support for the half-life proposed in Ref. [15] was provided after this work in Ref. [92], where γ-decay spectroscopy measurements lead to a more precise value of $t_{1/2} = 13.1 \pm 1.8$ ms.

Table 5.2: Results from the χ^2-minimisation fitting of the isomeric state structures for ^{73}Zn.

I	χ^2_r	$A(^3S_1)$ (MHz)	$A(^3P_2)$ (MHz)	$B(^3P_2)$ (MHz)	$A(^3P_2)/A(^3S_1)$
3/2	1.81	−2012.5(2.6)	−826.1(1.7)	−72.7(5.4)	0.4105(10)
5/2	**1.11**	**−1234.9(1.9)**	**−518.6(1.1)**	**+130.5(5.6)**	**0.4199(11)**
7/2	1.61	−954.9(1.3)	−402.6(0.8)	−48.1(6.1)	0.4216(10)

5.2.2 ^{75}Zn ($N = 45$)

The ground and isomeric state spins in ^{75}Zn are tentatively assigned as $I = 7/2$ and $I = 1/2$, respectively. The ground state nuclear spin is determined from β- and γ-coincidence measurements of ^{77}Zn, from which conclusions can be drawn about the level arrangement in ^{75}Zn due to the similarities in the gross structure of their decay schemes [16]. This spin assignment is not in agreement with the expected spin of a single-neutron in the $\nu g_{9/2}$ orbit. This ground state spin has been observed in other even-Z, $N = 45$ isotones with three neutrons in $\nu 1g_{9/2}$, and occurs as a result of a three-quasiparticle ground state [17]. The results of the fitting process for the ground state with $I = 5/2, 7/2$ and $9/2$ are shown below in Figure 5.4.

The $I = 1/2$ isomeric spin assignment in ^{75}Zn [17] signals a deviation from the trend observed in $^{69-73}$Zn, where the spin-1/2 is assigned to the ground state as opposed to the isomeric state. Confirmation of this isomeric spin will signal the inversion of the $\nu 2p_{1/2}$ and $\nu 1g_{9/2}$ levels that would be expected to already occur in ^{71}Zn in a non-interacting shell model picture. The results of this fitting process for the isomeric state are shown below in Figure 5.5.

Ground State Spin

The experimental spectrum of ^{75}Zn is seen to consist of 12 resonance peaks (only the edge of peak 1 is measured at ≈ -4200 MHz), which, based on the tentative spin assignments suggests that the ground state has $I \geq 5/2$ (nine peaks) and the isomer $I = 1/2$ (three peaks). The χ^2_r values produced by the fitting process are fairly conclusive with regards to the ground state spin. The tentative spin assignment $I = 7/2$ gives the best statistical fit to the experimental data ($\chi^2_r = 1.29$). The spin-7/2 fitted structure aligns with all nine observed resonances and the Racah relative intensities closely reproduce the measured intensity distribution too. This is a marked improvement over the fit for spin-5/2 ($\chi^2_r = 3.10$) where the peaks 1, 2 and 9 are not reproduced, while for spin-9/2 ($\chi^2_r = 4.19$) the structure is unable to align with peak 9 in particular and does not reproduce the intensities of peak 7 and 8. The A ratio of

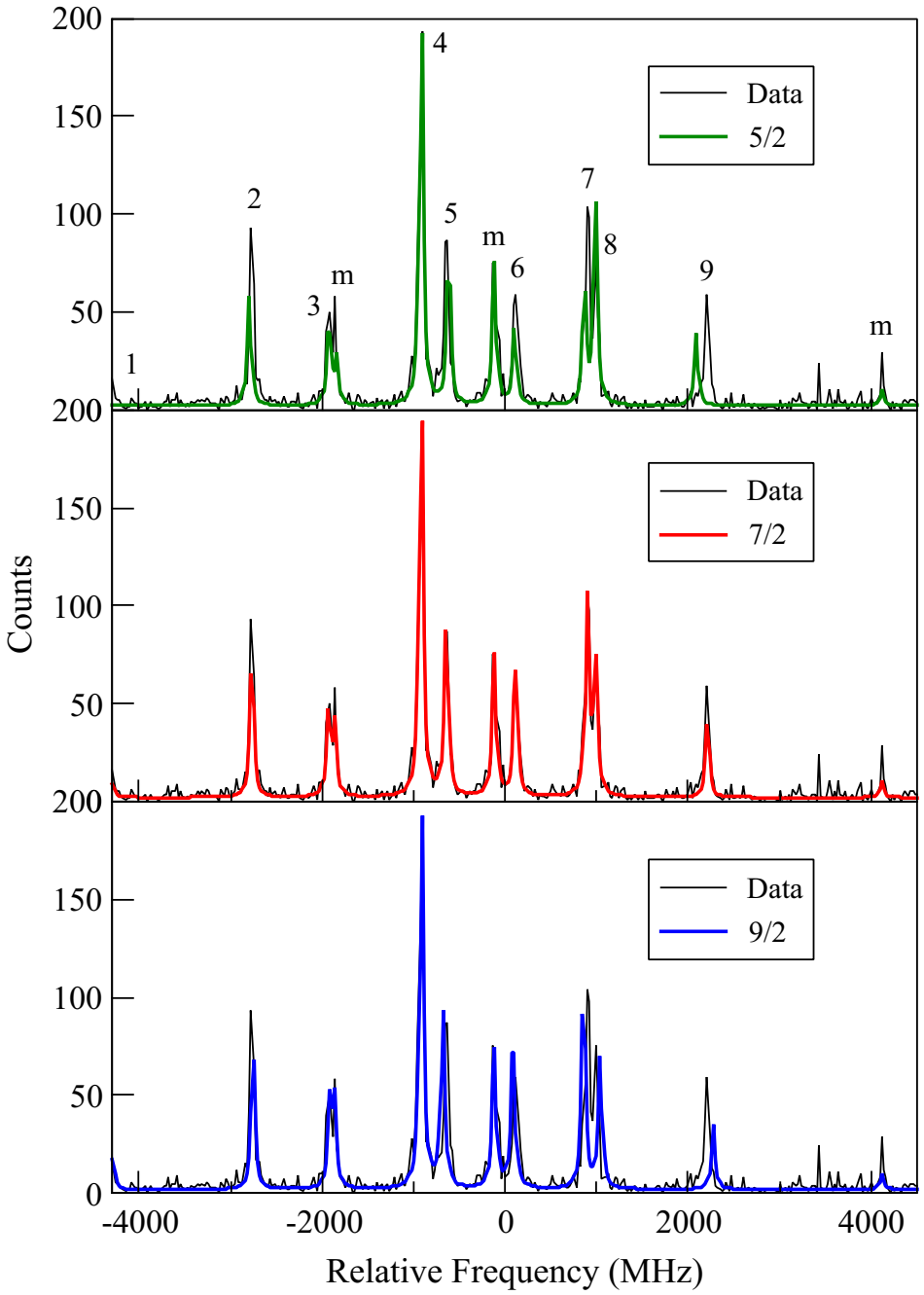

Figure 5.4: Plot of the fitted spectrum for different spin assignments of the ground state of ^{75}Zn.

spin-7/2 structure ($A(^3P_2)/A(^3S_1) = 0.4199(6)$) is an improvement over those for spin-5/2 and 9/2, and lies within errors of R_{exp}, and therefore confirms the ground state spin of ^{75}Zn as $I = 7/2$.

Table 5.3: Results from the χ^2-minimisation fitting of the ground state structures for ^{75}Zn.

I	χ^2_r	$A(^3S_1)$ (MHz)	$A(^3P_2)$ (MHz)	$B(^3P_2)$ (MHz)	$A(^3P_2)/A(^3S_1)$
5/2	3.10	−1082.4(1.2)	−448.9(0.8)	+200.8(4.6)	0.4147(9)
7/2	**1.29**	**−815.5(0.7)**	**−342.5(0.4)**	**+51.2(3.0)**	**0.4199(6)**
9/2	4.19	−656.5(0.8)	−278.9(0.5)	−55.4(4.9)	0.4248(8)

Isomeric State Spin

The three resonance peaks assigned to the isomeric state appear to best suit the tentative $I = 1/2$ spin assignment. The fitted $I = 3/2$ structure only appears to have unmatched peaks at ~ 3000 MHz and ~ 1500 MHz, with the remaining peaks associated with a spin-3/2 structure (eight in total) instead aligning to peaks already accounted for by the ground state, as shown in Figure 5.5. As a result the spin-1/2 structure produces the best statistical fit to the data ($\chi^2_r = 1.29$) and an A ratio of 0.4204(16) that is within errors of R_{exp}. These values are a notable improvement over those for $I = 3/2$ from the χ^2-minimisation fitting ($\chi^2_r = 2.57$, $A(^3P_2)/A(^3S_1) = 0.4160(12)$) and confirms the isomeric state spin of ^{75}Zn as $I = 1/2$.

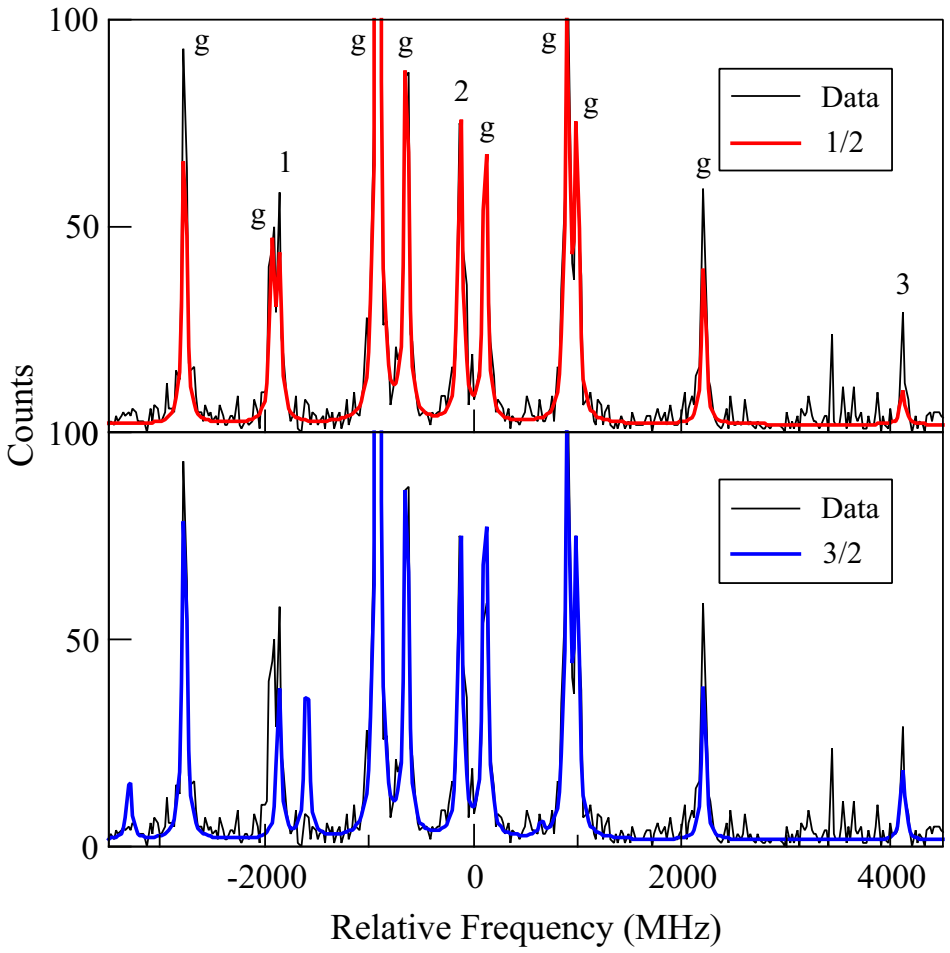

Figure 5.5: Plot of the fitted spectrum for different spin assignments of the isomeric state in ^{75}Zn.

Table 5.4: Results from the χ^2-minimisation fitting of the isomeric state structures for ^{75}Zn.

I	χ^2_r	$A(^3S_1)$ (MHz)	$A(^3P_2)$ (MHz)	$B(^3P_2)$ (MHz)	$A(^3P_2)/A(^3S_1)$
1/2	**1.29**	**+4032.7(9.2)**	**+1695.3(5.3)**	—	**0.4204(16)**
3/2	2.57	+2287.1(3.4)	+951.6(2.2)	+1039.6(5.1)	0.4160(12)

5.2.3 ^{77}Zn ($N = 47$)

The similarities in decay schemes and low-lying level structure of ^{75}Zn and ^{77}Zn mean that their ground and isomeric states both have the same tentative spin assignments of $I = 7/2$ and $1/2$, respectively. The results from β- and γ-coincidence measurements [18] and the reasons explained above for ^{75}Zn provide the basis for the tentative assignments. The results for the tentative ground state spin and $I = 5/2, 9/2$ are shown in Figure 5.6.

The combined ground and isomeric state hyperfine spectrum of ^{77}Zn is broader than that observed for lighter isotopes and subsequently extends beyond the scanning voltage range of the COLLAPS beam line. This means that, for the tentatively assigned spin-1/2 isomer, only two of the expected three peaks are measured in the scan range. A rough location of the 3$^{\text{rd}}$ peak is determined by superimposing a model hyperfine structure to the first two isomer peaks and constraining the A ratio to R_{exp}. This same process is also performed for the spin-3/2 structure. These locations are then measured experimentally by changing the Fluke voltage (that dictates the centre of the scanning range) and reducing the voltage range scanned. If the isomer is spin-1/2, the measurement of all three peaks is necessary as the hyperfine $A(^3P_2)$ and $A(^3S_1)$ coefficients cannot be accurately determined from only two peaks. The χ^2-minimisation fitting for the isomeric spins is performed on the full hyperfine spectrum plus the focused scan, the intensity of which is normalised to the number of scans taken over the full V_{scan} range in order to perform the fitting with Racah intensities. The results for the $I = 1/2$ and $3/2$ spins are shown below in Figure 5.7.

Ground State Spin

The 11 measured resonance peaks within the voltage scanning range (plus one isomer peak beyond V_{scan}) means that ground state spin assignments of $I \geq 5/2$ along with a tentatively assigned $I = 1/2$ isomer cannot be ruled out based on the number of peaks. The focused scan for the additional isomer peak is not included in these ground state spin tests. The $I = 7/2$ fitting produces the best statistical fit to the data ($\chi^2_r = 0.84$) of the three spins tested,

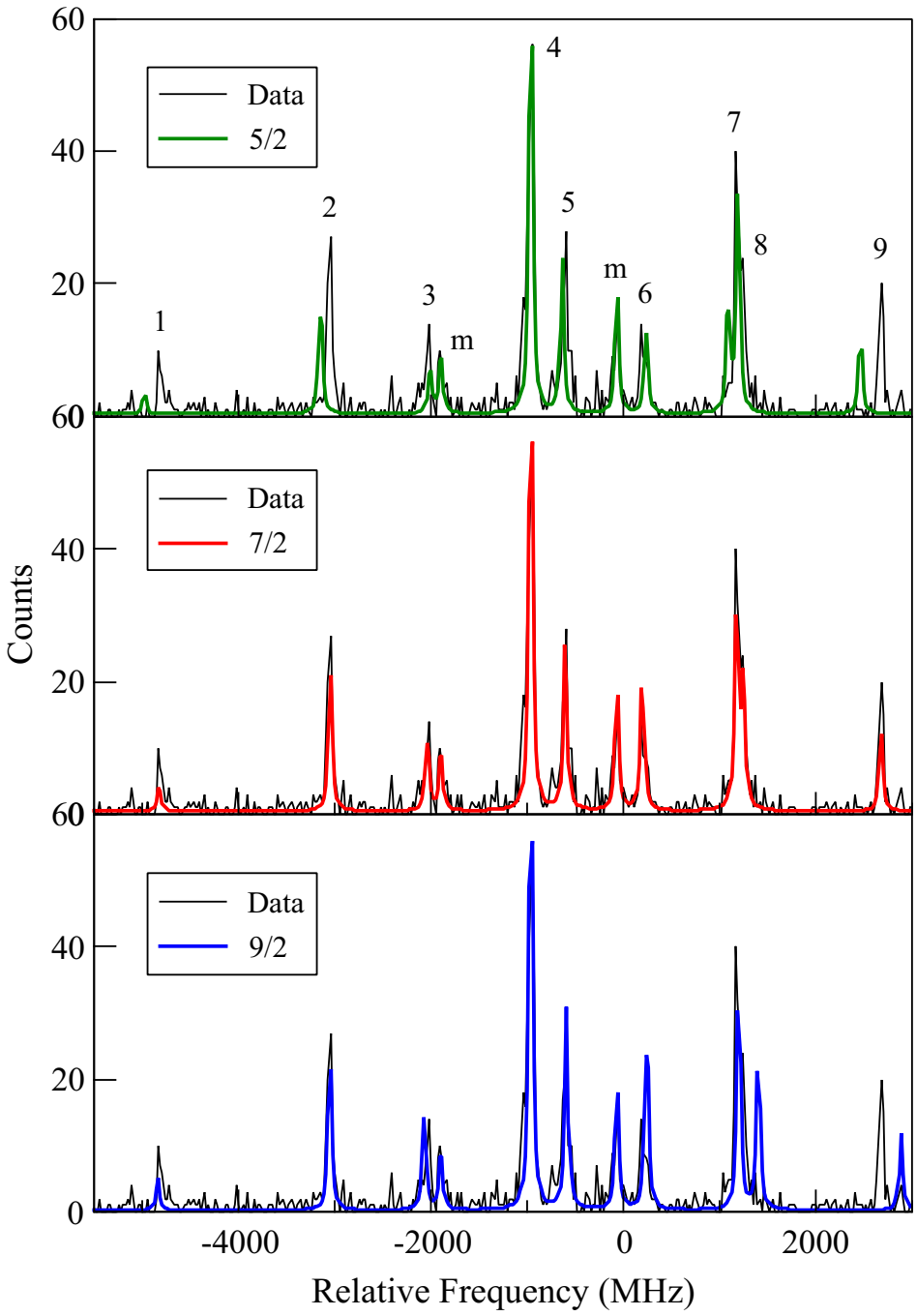

Figure 5.6: Plot of the fitted spectrum for different spin assignments of the ground state of ^{77}Zn.

with the spin-7/2 structure matching closely to the nine labelled peaks in the spectrum in both intensity and frequency. On the other hand, the $I = 5/2$ fitting does not reproduce

the measured peak intensity distribution, most notably at peaks 1 and 2, and is unable to align with resonance peaks 1, 2, 8 and 9. The spin-9/2 structure meanwhile does not match to peaks 8 and 9 in the spectrum. Both the spin-5/2 and 9/2 structures produce A ratios outside errors of R_{exp} ($A(^3P_2)/A(^3S_1) = 0.4139(7)$ and 0.4213(8), respectively), which, in addition to the peak misalignment, rule them out as the ground state spin. The A ratio of 0.4201(7) for $I = 7/2$ is in agreement with R_{exp}, meaning the spin is therefore confirmed as the ground state assignment for ^{77}Zn.

Table 5.5: Results from the χ^2-minimisation fitting of the ground state structures for ^{77}Zn.

I	χ^2_r	$A(^3S_1)$ (MHz)	$A(^3P_2)$ (MHz)	$B(^3P_2)$ (MHz)	$A(^3P_2)/A(^3S_1)$
5/2	1.84	−1239.6(1.1)	−513.1(0.8)	+182.0(4.8)	0.4139(7)
7/2	**0.76**	**−938.0(0.9)**	**−394.1(0.5)**	**+145.1(3.8)**	**0.4201(7)**
9/2	2.04	−772.5(0.8)	−325.4(0.5)	+51.3(5.5)	0.4213(8)

Isomeric State Spin

With the addition of the resonance peak from the focused scan, the overall hyperfine spectrum is now seen to contain twelve resonance peaks and thus supports the $I = 1/2$ isomeric state spin assignment (three isomer peaks plus nine from the ground state). The spin-3/2 structure aligns with resonance peaks 1 and 2, although the structure does not reproduce the peak in the focused scan. The additional resonance peaks associated with a spin-3/2 state are visible in the spectrum and do not align with any measured peaks. The spin-1/2 structure aligns with three measured peaks in the spectrum, including that from the focused scan. Both fits produce relatively large errors on their $A(^3P_2)/A(^3S_1)$ values although this is attributed to the uncertainties introduced by the focused scan fitting. The better agreement between the A ratio of 0.4200(29) for $I = 1/2$ and R_{exp} than is seen for the $I = 3/2$ fitting (0.4221(14)) is further confirmation of $I = 1/2$ as the isomeric state spin of ^{77}Zn.

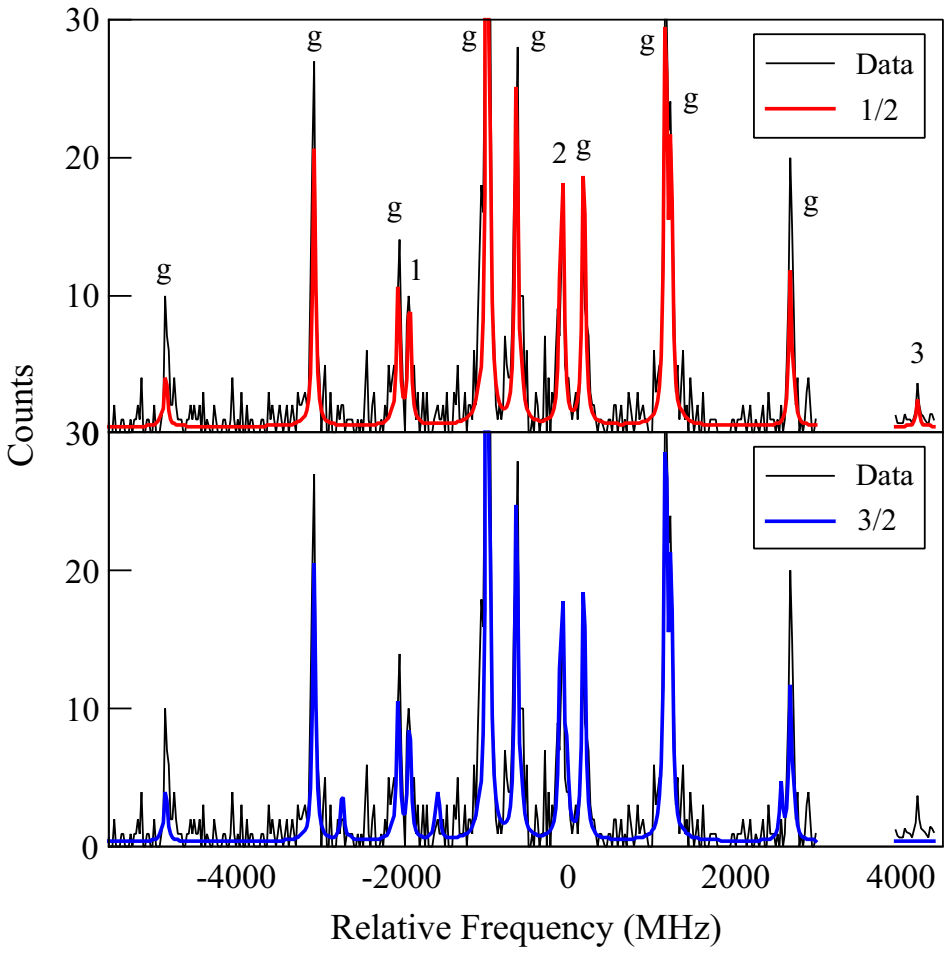

Figure 5.7: Plot of the fitted spectrum for different spin assignments of the isomeric state in ^{77}Zn.

Table 5.6: Results from the χ^2-minimisation fitting of the isomeric state structures for ^{77}Zn.

I	χ^2_r	$A(^3S_1)$ (MHz)	$A(^3P_2)$ (MHz)	$B(^3P_2)$ (MHz)	$A(^3P_2)/A(^3S_1)$
1/2	**0.73**	**+4061.9(16.0)**	**+1705.8(9.4)**	—	**0.4200(29)**
3/2	0.82	+1785.2(3.4)	+753.5(2.0)	−1.16(5.7)	0.4221(14)

5.2.4 ^{79}Zn ($N = 49$)

The heaviest odd-A isotope measured in this study, ^{79}Zn, has a tentative ground state spin assignment of $I = 9/2$ based on results from β-decay measurements of this isotope [93]. The

ground state of ^{79}Zn is expected to be dominated by a single-neutron hole in $\nu g_{9/2}$ just beneath the $N = 50$ shell closure. However the preceding isotopes ^{75,77}Zn have confirmed ground state spins of $I = 7/2$ from this work, meaning ^{79}Zn would be the first odd-A isotope measured here with a 9/2 ground state spin in the process of filling $\nu g_{9/2}$. The χ^2-minimisation fitting is therefore performed for the ground state spins $I = 7/2$ and 9/2, the results of which are given in Figure 5.8.

An isomeric state has recently been suggested in this isotope from γ-proton coincidences in a neutron transfer reaction experiment at REX-ISOLDE, with their analysis providing a tentative spin-parity assignment of $I^\pi = 1/2^+$ [19]. Confirmation of this spin-parity would exclude the $(\nu p_{1/2})^1$ led configuration seen in ^{75m,77m}Zn ($I^\pi = 1/2^-$) for ^{79m}Zn, instead suggesting the state is formed by a cross $N = 50$ shell closure excitation to a higher-lying orbital. For completeness, the neighbouring spin assignment of $I = 3/2$ will also be tested for the isomeric state.

As for the isomer in ^{77}Zn, a focused scan is required to locate the final peak of the tentatively assigned $I = 1/2$ isomeric state in ^{79}Zn. An initial estimate of this is again obtained by fitting a spin-1/2 structure to the two non-ground state peaks observed in the spectrum and fixing the A ratio to R_{exp}, with the region then scanned for resonances. The same process is followed for the spin-3/2 structure. The inset image in Figure 5.9 displays the 3$^{\text{rd}}$ isomer peak with intensity normalised to the full hyperfine spectrum. The results of the χ^2-minimisation fitting for the full scanning range and the additional focused scan is shown in Figure 5.9.

Ground State Spin

The measured hyperfine spectrum within the V_{scan} region contains 10 resonance peaks. Superimposed model ground state structures with $I = 7/2$ and 9/2 show that the lowest intensity transition peak lies outside the spectrum ($\sim 2\%$ of Racah relative intensities). This peak is not needed for the fitting process to determine the spin or hyperfine coefficients. The χ^2_r value for the spin-9/2 structure ($\chi^2_r = 1.03$) exhibits a much better statistical fit to the data

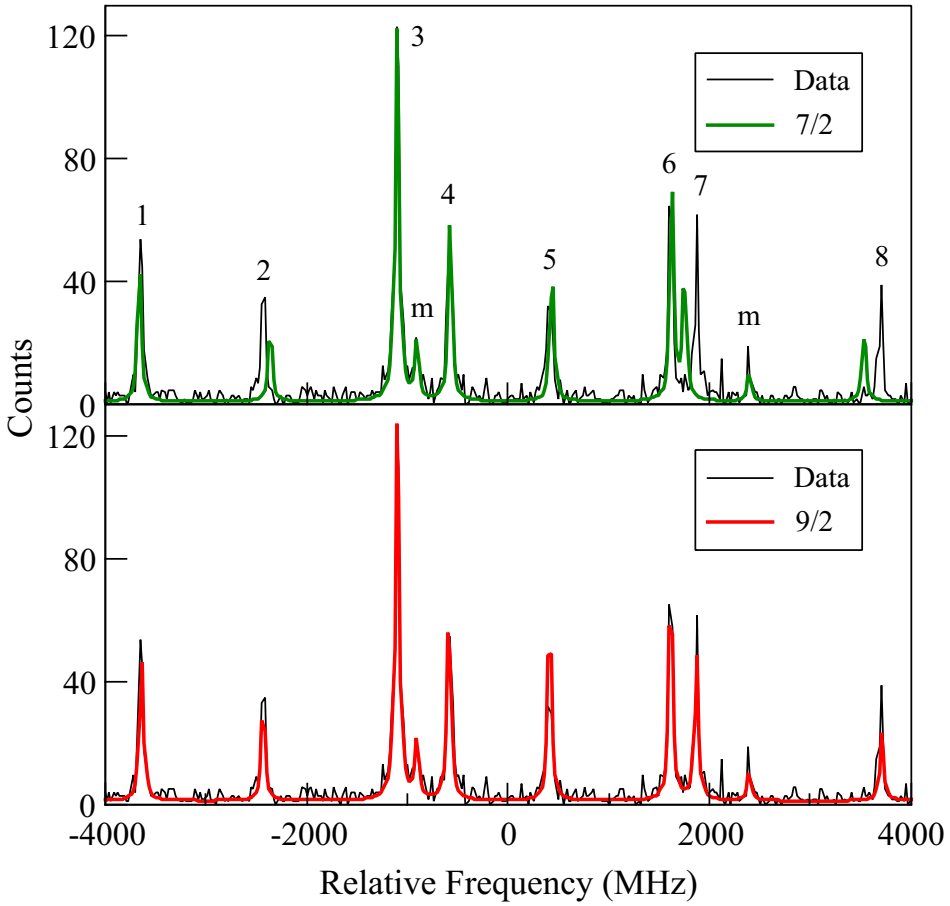

Figure 5.8: Plot of the fitted spectrum for different spin assignments of the ground state of ^{79}Zn.

than the spin-7/2 structure ($\chi^2_r = 3.29$). This can be seen clearly in the two spectra since the spin-9/2 structure aligns with all measured peaks and matches the intensity distribution more closely than spin-7/2, with visible improvements at peaks 2 and 7. Conversely, the spin-7/2 structure is unable to align with resonance peaks 2, 7 and 8. As a result, the hyperfine A

Table 5.7: Results from the χ^2-minimisation fitting of the ground state structures for ^{79}Zn.

I	χ^2_r	$A(^3S_1)$ (MHz)	$A(^3P_2)$ (MHz)	$B(^3P_2)$ (MHz)	$A(^3P_2)/A(^3S_1)$
7/2	3.29	−1174.5(0.9)	−487.3(0.5)	+210.7(5.0)	0.4149(5)
9/2	**1.03**	**−955.0(0.5)**	**−400.6(0.3)**	**+122.2(2.9)**	**0.4194(4)**

ratio for $I = 9/2$ (0.4194(4)) lies within errors of R_{exp} while the same value for $I = 7/2$ (0.4149(5)) does not. Therefore, we conclude that the ground state spin of ^{79}Zn is $I = 9/2$.

Isomeric State Spin

The discovery of a 3$^{\text{rd}}$ isomer peak from the focused scan strongly suggests an $I = 1/2$ assignment for ^{79m}Zn. Focused scans were also performed at the expected locations of spin-3/2 structure peaks based on the two isomer peaks already measured, although this revealed

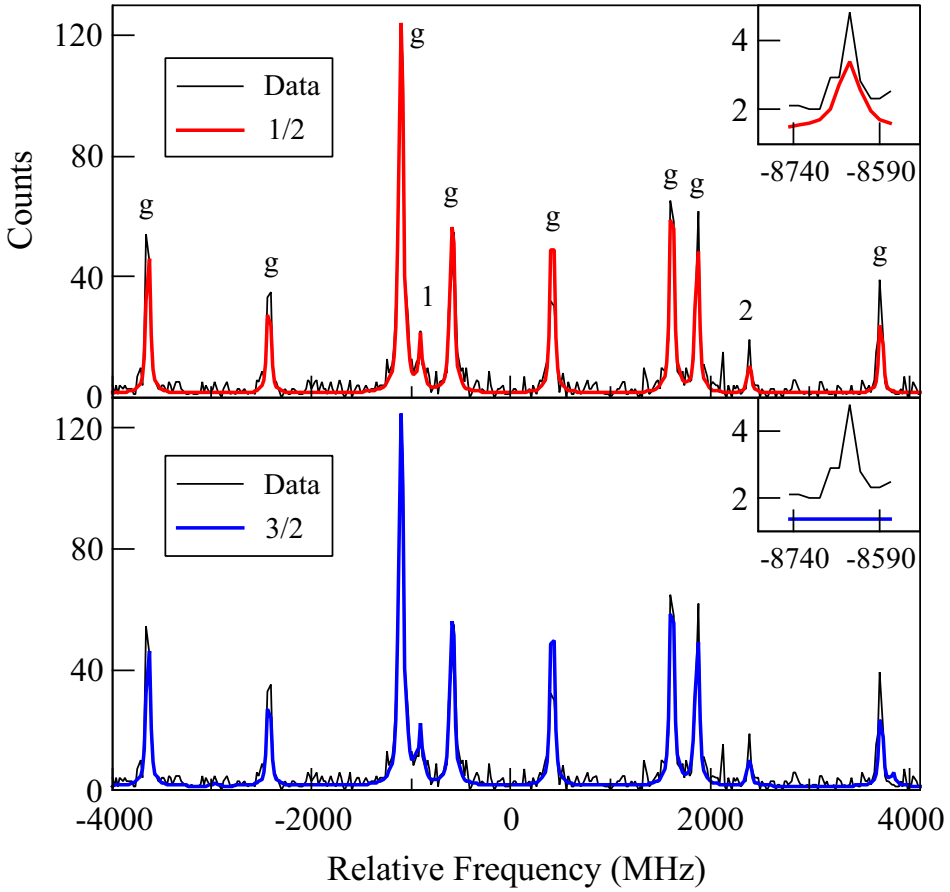

Figure 5.9: χ^2-minimisation fits to the measured spectrum of ^{79}Zn with the $I = 1/2$ (top) and 3/2 (bottom) isomeric state spin assignments. The inset graphs show the fits to the 3$^{\text{rd}}$ isomer peak measured in a focused scan away from the main structure. In order to observe the 3$^{\text{rd}}$ isomer peak, a greater number of scans was required than for the main structure. Thus the intensity of the third peak is normalised to the number of scans performed across the main structure.

no additional resonances. Both the spin-1/2 and spin-3/2 structures match to peaks 1 and 2 in the main spectrum in Figure 5.9, however the inset graphs show that only the spin-1/2 structure is able to match to the final isomer peak from the focused scan. The additional peaks associated with a spin-3/2 structure (eight in total) are likely masked by the ground state resonances as they are not visible in Figure 5.9. Both the $I = 1/2$ and 3/2 structures seem to produce "ideal " statistical fits to the data ($\chi^2_r = 1$ and 1.04 respectively), although this is misleading as the χ^2_r of the overall spectrum is dominated by the intense ground state structure. Therefore, based on the prior criteria, the spin assignment of the newly discovered isomer in ^{79}Zn is confirmed as $I = 1/2$.

Table 5.8: Results from the χ^2-minimisation fitting of the isomeric state structures for ^{79}Zn.

I	χ^2_r	$A(^3S_1)$ (MHz)	$A(^3P_2)$ (MHz)	$B(^3P_2)$ (MHz)	$A(^3P_2)/A(^3S_1)$
1/2	**1.00**	**−7358.1(16.4)**	**−3094.1(9.7)**	—	**0.4205(16)**
3/2	1.04	−3193.0(14.3)	−1339.0(8.2)	+1.21(13.3)	0.4194(32)

5.3 Collated Fitting Results

Once the nuclear spin assignment of a state is unambiguously confirmed, the fitting process for the correct spin is repeated with peak intensities as free parameters. The subsequent $A(^3S_1)$, $A(^3P_2)$ and $B(^3P_2)$ values will be used in combination with those from a complementary χ^2-minimisation analysis by X. F. Yang (COLLAPS collaborator, from KU Leuven at the time of experiment) to calculate the magnetic dipole moment and spectroscopic quadrupole moments. The two analyses are in agreement on the nuclear spins assigned to $^{73-79g,m}$Zn in this work.

Final values of the hyperfine parameters A and B are calculated by taking the simple average of A and B obtained from this work and from that of X. F. Yang. Errors are calculated by the addition of fitting errors in quadrature

Table 5.9: Final values of I, $A(^3S_1)$, $A(^3P_2)$ and $B(^3P_2)$ obtained from the χ^2-minimisation fitting in this work and by X. F. Yang. The moments μ_{expt} and $Q_{\text{s,expt}}$ are calculated from the hyperfine coefficients shown and the reference isotope ^{67}Zn with reference values of $A(^3P_2) = +531.987(5)$ MHz and $B(^3P_2) = +35.806(5)$ MHz from [89], $\mu = +0.875479(9)\mu_N$ from [14] and $Q_s = +0.122(10)$ b from this work and [94].

A	N	I	$A(^3S_1)$ (MHz)	$A(^3P_2{}^{\circ})$ (MHz)	$B(^3P_2{}^{\circ})$ (MHz)	$\mu_{\text{expt}}(\mu_N)$	$Q_{\text{s,expt}}$(b)
63	33	3/2	−676.9(8)	−286.0(13)	+60(4)	−0.281(2)	+0.25(33)
65	35	5/2	+1114.0(23)	+467.6(10)	−7(6)	+0.7695(16)	−0.030(24)
67	37	5/2	+1266.5(18)	+531.2(11)	+41(7)	+0.874(2)	+0.171(35)
69	39	1/2	+4033(9)	+1691(5)	—	+0.557(2)	
69^m	39	9/2	−933.7(4)	−392.1(2)	−113(4)	−1.1613(7)	−0.47(5)
71	41	1/2	+3987(5)	+1675(3)	—	+0.551(1)	
71^m	41	9/2	−844.5(9)	−354.3(3)	−76(5)	−1.049(1)	−0.32(4)
73	43	1/2	+4044.0(27)	+1696.9(16)	—	+0.5585(5)	
73^m	43	5/2	−1233.9(14)	−518.2(9)	+125(6)	−0.8527(14)	+0.52(6)
75	45	7/2	−815.4(6)	−342.3(4)	+48(4)	−0.7887(9)	+0.20(3)
75^m	45	1/2	+4034(6)	+1695.5(29)	—	+0.5580(9)	
77	47	7/2	−938.1(7)	−393.8(4)	+141(5)	−0.907(1)	+0.59(6)
77^m	47	1/2	+4063(10)	+1708(5)	—	+0.562(2)	
79	49	9/2	−955.0(6)	−400.6(3)	+116(5)	−1.1866(10)	+0.49(5)
79^m	49	1/2	−7362(6)	−3093(4)	—	−1.018(1)	

$$\Delta x_{\text{avg}} = \sqrt{(\Delta x_{\text{n,large}})^2 + (\Delta x_{\text{n-avg}})^2}, \tag{5.7}$$

where $\Delta x_{\text{n,large}}$ is the larger error of the two fits and $\Delta x_{\text{n-avg}}$ is the difference between a fit parameter and the average value. The resulting values of $A(^3S_1)$, $A(^3P_2)$ and $B(^3P_2)$ and their errors from this combined analysis are given in Table 5.9, along with the magnetic dipole moments and spectroscopic quadrupole moments calculated from these values using Equations 2.24 and 2.25. The ratio of the final upper and lower state hyperfine A coefficients, $A(^3P_2)/A(^3S_1)$, are compared to the expected ratio from literature, $R_{\text{exp}} = 0.4197(3)$ in Figure 5.10. For the ground and isomeric states of each Zn isotope (excluding the ground state of ^{63}Zn, which has a large statistical error), the hyperfine A ratio is seen to lie within fitting errors of the R_{exp}.

The reference isotope ^{67}Zn is selected to calibrate the nuclear moments across the iso-

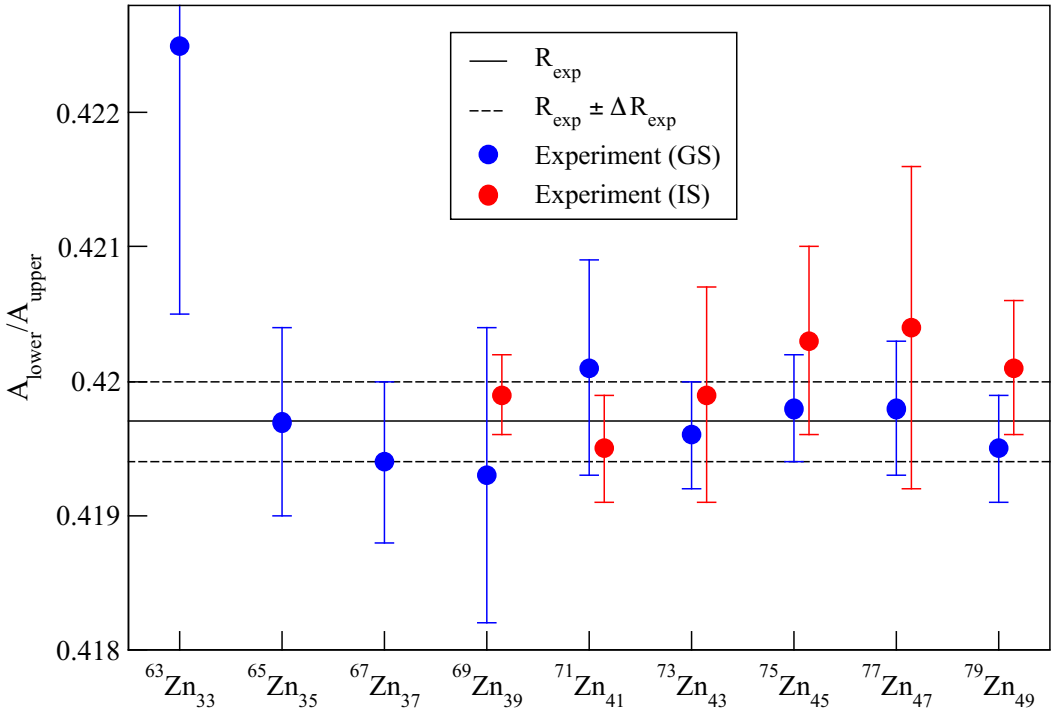

Figure 5.10: Ratio of the hyperfine A coefficients of Zn isotopes for the upper and lower states, $A(^3P_2)/A(^3S_1)$, of the atomic transition $4s4p\ ^3P_2^o \rightarrow 4s5s\ ^3S_1$ measured in this work are shown with fitting errors. Values are compared to the expected ratio, $R_{\text{exp}} = 0.4197(3)$, obtained from the literature values $A(^3P_2) = +531.987(5)$ [89] MHz and $A(^3S_1) = +1267.5(1.0)$ MHz [90].

tope chain. Reference values for the hyperfine coefficients $A(^3P_2) = +531.987(5)$ MHz and $B(^3P_2) = +35.806(5)$ MHz are taken from [89] and the reference moment $\mu = +0.875479(9)\mu_N$ is taken from [14]. An updated value for the quadrupole moment of the ^{67}Zn ground state has been determined especially for this work based on new calculations of the electric field gradient (EFG) for the $4s4p\ ^3P_{1,2}^o$ states [94]. The new reference quadrupole moment of $Q_s = +0.122(10)$ b is used to calculate Q_s across the isotope chain, and presents a rather drastic change from the previous value of $Q_s = +0.150(15)$ b [95] for ^{67}Zn.

Chapter 6

Discussion

The evolution of nuclear structure across an isotope chain is best understood through the measurement and interpretation of nuclear properties. From the hyperfine spectra obtained through collinear laser spectroscopy experiments, the low-lying state spins I, nuclear magnetic dipole moments μ and spectroscopic quadrupole moments Q_{s} that describe this structure evolution can be quantified. The nuclear properties of odd-A Zn isotopes measured in this experiment are discussed in the following sections.

6.1 Comparison to Shell Model Interactions

The measured electromagnetic moments and spins of low-lying energy levels of odd-A Zn across the isotope chain provide information on single-particle structure and the development of collectivity and deformation. In order to further probe how and why these elements of nuclear structure develop, large-scale shell-model interactions are employed. Isotope chains in the mass region of Zn provide a relatively unique opportunity to probe multiple shell closures, with isotopes stretching across $N = 28, 50$, and also lying in close proximity to $Z = 28$. Therefore, the experimental results of Zn outlined in this work will test the ability of shell-model interactions to predict neutron-dominated nuclear structure around shell closures and in mid-shell regions, as well as the effects of adding two protons outside the $Z = 28$ shell

gap.

The ability or inability of an interaction to consistently reproduce measured trends can provide information regarding its suitability for isotopes in this region. When an interaction shows a good agreement with measured values, it can be used to predict properties within nuclei beyond the scope of experiment, such as wave function configurations and occupation numbers, whilst also increasing the validity of its predictions for unexplored isotopes in the same region. On the other hand, interactions that are unable to reproduce experimental results may be deemed insufficient for such predictions, with the interaction model space, its parametrisation and the stability of local shell closures subsequently being called into question.

The following sections will assess the measured nuclear properties of odd-A Zn isotopes and compare them to the predictions of shell-model interactions. Interactions will be introduced in three separate sections, with each section grouping together interactions based on similarities in their model space. The introduction of each interaction will outline their model spaces and parametrisation. Then, the experimentally measured values of low-lying energy levels, nuclear magnetic dipole moments (g-factors) and spectroscopic quadrupole moments will be discussed in relation to predictions from these interactions.

6.2 JUN45 and jj44b Interactions

The model space utilised for both the JUN45 [59] and jj44b [26] shell model interactions consists of the $1p_{3/2}$, $0f_{5/2}$, $1p_{1/2}$, and $0g_{9/2}$ orbits above a doubly magic ^{56}Ni core. Due to the similarities in their construction and of the interaction model spaces (outlined in more detail in Section 3.3.1) the same effective parameters are used for the JUN45 and jj44b interactions. Therefore the calculations for Zn will use the effective g-factors $g_s^{\text{eff}} = 0.7 g_s^{\text{free}}$ and $g_l^{\text{eff}} = g_l^{\text{free}} \pm 0$, and the effective charges $e_{\text{p}}^{\text{eff}} = 1.5e$ and $e_{\text{n}}^{\text{eff}} = 1.1e$.

6.2.1 Energy Level Systematics

The trend of low-lying energy levels in odd-A Zn isotopes provides information on nuclear structure change in nuclei with changing neutron number N. Using the ground and isomeric state spins determined in Chapter 5 and level energies from decay spectroscopy experiments, the evolution of spin states across the Zn isotope chain has been confirmed. For Zn, the region beyond $N = 40$ where the $\nu g_{9/2}$ orbit is filled is of particular interest with regards to the evolution of nuclear structure [96, 25, 26, 97, 19], and also includes the isotopes ($N = 43 - 49$) with ground and isomeric state spins unambiguously confirmed in this work for the first time. Therefore the energies of the low-lying spins states for $N = 41 - 49$ are shown in Figure 6.1 and compared to the lowest lying energy levels from the JUN45 and jj44b interactions. The following section will firstly discuss the ground and isomeric state spins determined in Chapter 5 before comparing the energies of these states to the predictions from the JUN45 and jj44b interactions.

The ground state spins of odd-A Zn isotopes from $N = 41 - 49$ are expected to be $9/2^+$, providing that single unpaired neutron configurations are dominant beyond $N = 40$ as the $\nu g_{9/2}$ orbit is filled. However the experimental results reveal a very different picture, as the only isotope with this expected ground state spin is ^{79}Zn. The lower mass Zn isotopes in this range therefore deviate from this, starting with ^{71,73}Zn, where the tentatively assigned ground state spin-parity of $1/2^-$ in [15] is confirmed. The expected ground state of $9/2^+$ is instead isomeric in ^{71}Zn, although it has not yet been measured in ^{73}Zn. The measured isomeric spin of $5/2^+$ in ^{73}Zn [17] and the $7/2^+$ ground state spin of ^{75,77}Zn are rather more anomalous spin assignments around the mid-point of $\nu g_{9/2}$ filling, with $7/2^+$ state being formed by a $(\nu g_{9/2})^3$ three quasi-particle configuration [16]. The $1/2^-$ level, previously the ground state in ^{71,73}Zn, increases in energy with increasing N and is now isomeric in ^{75,77}Zn. The $9/2^+$ ground state spin of the final isotope in this range, ^{79}Zn, is representative of a single neutron-hole in the $\nu g_{9/2}$ orbit, and is the only ground state from $N = 41 - 49$ to exhibit single-particle behaviour. The ground state spin of ^{79}Zn and the increase in energy of

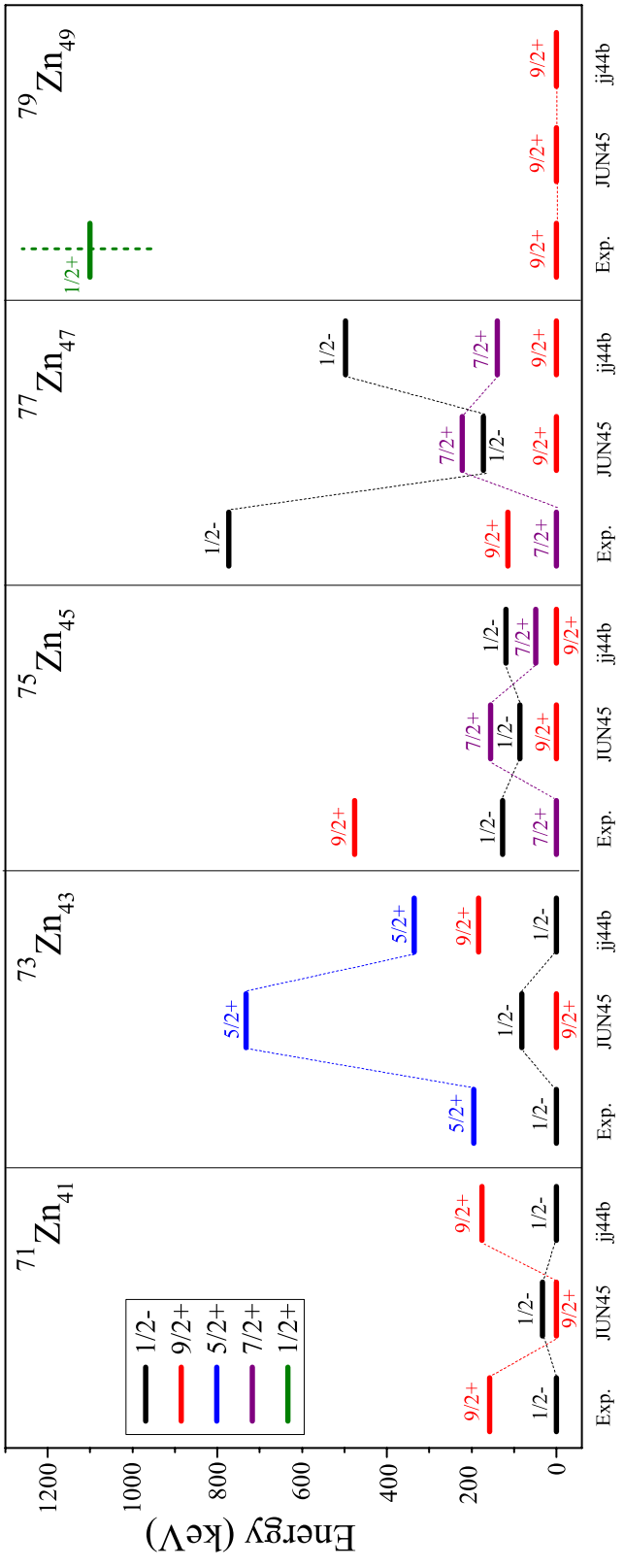

Figure 6.1: Measured low-energy spectra of Zn isotopes from $N = 41 - 49$ are compared to predictions from the JUN45 and jj44b shell-model interactions. Dotted lines represent the change in energy of the ground and isomeric states, while the vertical dashed line at ^{79}Zn shows the error on the measured energy.

the next low-lying states relative to other isotopes suggest the $N = 50$ shell closure persists with increasing N. The inconsistent spins of isotopes from $N = 41 - 47$ meanwhile indicate significant correlations. The long-lived $1/2^+$ isomeric state in ^{79}Zn has been observed in this work, but has not been measured in any of the lighter Zn isotopes. The spin-parity of this isomer does not align with that of any SP orbits in the region below $N = 50$, and could signal the presence of cross $N = 50$ excitations.

It is immediately noted that neither interaction is able to consistently reproduce both the ground and isomeric spins of $^{71-79}$Zn. The JUN45 interaction assigns a ground state spin of $9/2^+$ to all isotopes in this range. This assignment is incorrect for the ground state spins of $^{71-77}$Zn, although the correct spin states are within typical shell-model uncertainties (a few 100 keV) of the ground state. On the other hand, the jj44b interaction is able to replicate the $1/2^-$ ground state spin of ^{71,73}Zn as well as the energies of their $9/2^+$ and $5/2^+$ isomeric states, respectively. Conversely, JUN45 places the $5/2^+$ isomeric state of ^{73}Zn $\approx$500 keV above the measured energy. The inclusion of experimental data for $Z = 28 - 30$ isotopes in the jj44b interaction could explain the improvement in its predictions over JUN45 (uses data from $Z = 30 - 33$ nuclei) in $N > 40$ nuclei. The addition of neutrons beyond $N = 40$ induces the attractive $\pi f_{5/2}$-$\nu g_{9/2}$ monopole interaction that works to reduce the $N = 40$ subshell gap and the the repulsive $\pi f_{7/2}$-$\nu g_{9/2}$ monopole interaction that reduces the $Z = 28$ shell gap, both of which facilitate the development of collectivity [98]. This increases the relevance of data from $Z \sim 28$ nuclei for predicting level systematics in $N > 40$ nuclei due to the consideration of cross $N = 40$ and $Z = 28$ excitations.

Neither the JUN45 or jj44b interaction assigns the $7/2^+$ energy level as the ground state of ^{75,77}Zn, although both place the level at no more than 250 keV. Instead the interactions assign the $9/2^+$ level as the ground state as $N = 50$ is approached. The nature of the $7/2^+$ level in Zn remains uncertain, as the only SP orbit able to reproduce the spin-parity of the state, $\nu g_{7/2}$, lies beyond the $N = 50$ shell closure, meaning excitations to this state are unlikely to dominate the wave function. This will be investigated further in the following via the magnetic dipole moments. The energy of the now isomeric $1/2^-$ level in ^{75,77}Zn is

reproduced fairly accurately by both interactions, with the exception of the JUN45 interaction for ^{77}Zn. The general trend of the $1/2^-$ level from $N = 41 - 47$ is accurately reproduced by jj44b, but only relatively well reproduced by JUN45. For ^{79}Zn, the $9/2^+$ level is assigned as the ground state spin by both interactions. The agreement of this with the measured ground state spin assignment along with the lack of other low-lying levels in ^{79}Zn provides further evidence of the $N = 50$ shell closure persistence, as the f_5pg_9 model space does not consider excitations beyond $N = 50$. The recently discovered $1/2^+$ isomeric state in ^{79}Zn however is not predicted by either interaction. Since ^{79}Zn has 49 neutrons and the spin-parity of the isomer cannot be satisfied by any orbital with the f_5pg_9 model space, the state must be formed by an excitation to a spin-1/2 orbital beyond $N = 50$.

Overall, the general trend of low-lying energy level systematics is not reproduced consistently by either interaction, although predictions from the jj44b interaction do exhibit a noticeable improvement over those from JUN45. In order to draw more definitive conclusions over the validity of the f_5pg_9 model space for the purpose of predicting energy levels trends in Zn, and further investigate the isomer in ^{79}Zn, experimental results must be compared to other large-scale shell-model interactions with different model spaces (see Section 6.3.1).

6.2.2 Magnetic Dipole Moments

The nuclear magnetic dipole moment, μ, provides a sensitive probe of the orbital that is occupied by valence particles (or holes). Using the ground and isomeric state spins determined in Chapter 5, the g-factor (μ/I) can be obtained from the magnetic dipole moment to provide a dimensionless quantity that is very sensitive to orbits with unpaired particles and much less sensitive to those with paired particles (or holes). Measured g-factors from this experiment are compared to effective Schmidt g-factors, g_{eff}, for orbitals in this mass region. A close agreement suggests a rather pure $(\nu l_I)^1$ wave function configuration dominated by an unpaired neutron in the orbital whose effective g-factor it lies closest to, while any notable deviations can be indicative of mixing with configurations formed by np-mh excitations.

The JUN45 and jj44b interactions provide theoretical estimates for the magnetic dipole

moment, μ, and hence the g-factor across the Zn isotopic chain. In the event that a SM interaction reproduces the measured g-factor closely, its predicted wave function configurations and their relative contributions can be used to better understand the occupancy of each orbital within the interaction model space. For the JUN45 interaction, only the four most dominant configurations have been provided, while configurations totalling up to 100% have been made available for jj44b. The JUN45 calculations were performed by M. Honma and the jj44b calculations by X.F. Yang.

In this section the measured g-factors for the ground and isomeric states of $^{63-79}$Zn are compared to JUN45 and jj44b predictions. The results are shown in Table 6.1 and Figure 6.2.

Table 6.1: Nuclear magnetic dipole moments, μ (μ_N) calculated from experimental data are compared to JUN45 and jj44b shell-model calculations. †To calibrate across the isotope chain the magnetic dipole moment of ^{67}Zn is used as reference, with $\mu = +0.875479(9)$ μ_N taken from [14]. The precise hyperfine coefficient $A(^3P_2) = +531.987(5)$ MHz [89] is used as the reference for calculations.

A	I^π	μ_{expt}	μ_{JUN45}	μ_{jj44b}
63	$3/2^-$	$-0.282(1)$	-0.256	-0.305
65	$5/2^-$	$+0.7695(16)$	$+0.938$	$+0.647$
67	$5/2^-$	$+0.875479(9)^{\dagger}$	$+1.008$	$+0.695$
69	$1/2^-$	$+0.557(2)$	$+0.463$	$+0.436$
69^m	$9/2^+$	$-1.1613(7)$	-1.156	-0.981
71	$1/2^-$	$+0.551(1)$	$+0.456$	$+0.411$
71^m	$9/2^+$	$-1.049(1)$	-1.159	-0.976
73	$1/2^-$	$+0.5585(5)$	$+0.451$	$+0.425$
73^m	$5/2^+$	$-0.8527(14)$	-0.984	-0.628
75	$7/2^+$	$-0.7887(9)$	-0.915	-0.919
75^m	$1/2^-$	$+0.5580(9)$	$+0.445$	$+0.435$
77	$7/2^+$	$-0.9074(1)$	-0.876	-0.811
77^m	$1/2^-$	$+0.562(2)$	$+0.450$	$+0.445$
79	$9/2^+$	$-1.1866(10)$	-1.185	-1.173
79^m	$1/2^+$	$-1.018(1)$	—	—

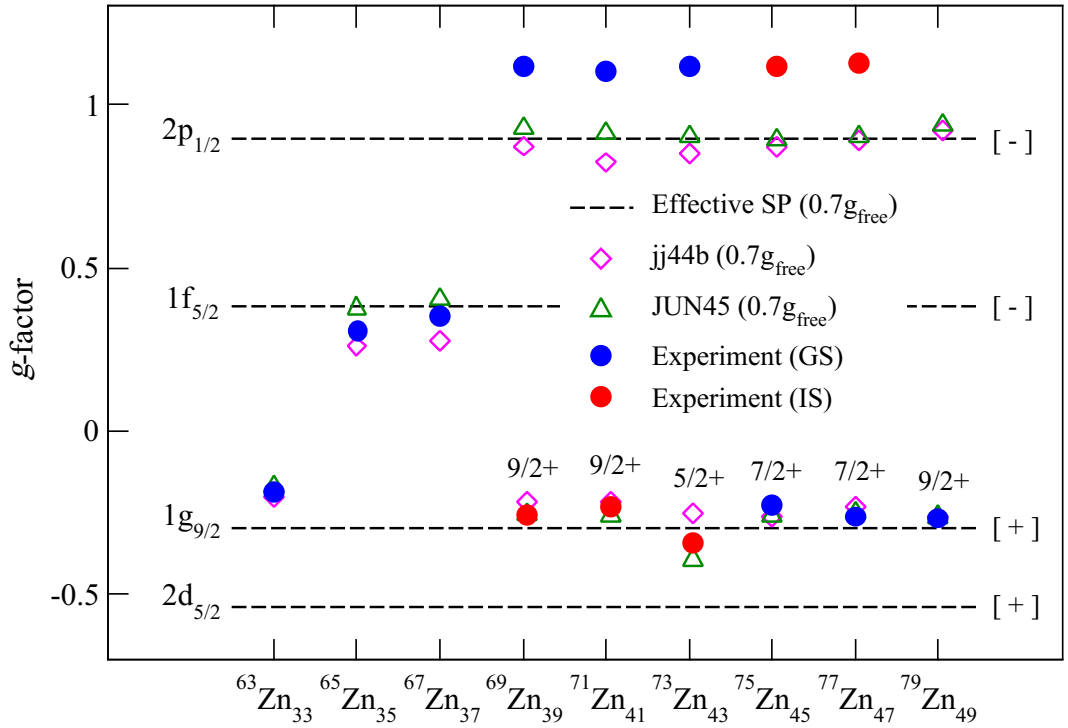

Figure 6.2: Experimental g-factors across the isotope chain in comparison to single-particle estimates and predictions from the JUN45 and jj44b interactions. The measured g-factor of ^{79m}Zn is not shown here due to scaling, as $g_{\text{expt}} = -2.036$. Errors on measured g-factors are smaller than the size of the symbols.

g-factors

Starting from the lowest mass Zn isotopes, a good agreement is seen between the measured and predicted g-factors in ^{63,65,67}Zn. The g-factor of ^{63}Zn is not in agreement with $g_{\text{eff}}(\nu p_{3/2})$ ($= -0.89$, thus beyond the scale of Figure 6.2) as would be expected due to its $3/2^-$ ground state spin. $(\nu p_{3/2})^3$ configurations are seen to dominate the wave function of ^{63}Zn, however, beyond the leading contribution of $\sim$ 25%, the remainder of the wave function is rather mixed with small contributions ($>$ 10% each) from configurations with an unpaired neutron in $\nu f_{5/2}$ and $\nu p_{1/2}$ that cause the measured g-factor to deviate from $g_{\text{eff}}(\nu p_{3/2})$ and towards that of $\nu f_{5/2}$ and $\nu p_{1/2}$. The g-factors of ^{65}Zn and ^{67}Zn lie close to the effective SP g-factor of $\nu f_{5/2}$, with the ground state wave functions of JUN45 and jj44b signalling that the $(\nu f_{5/2})^1$ odd-particle configuration are dominant. The JUN45 interaction incorrectly assigns the $1/2^-$

state (not measured in this work) as the ground state of ^{67}Zn, as opposed to the $5/2^-$ state which it predicts as the isomer, although these states are well within typical shell-model uncertainties (a few 100 keV) of each other.

The $1/2^-$ ground state of $^{69-73}$Zn and the $1/2^-$ isomer in ^{75,77}Zn are dominated by $(\nu p_{1/2})^1$ configurations ($> 50\%$ of the wave function), and therefore a good agreement between their measured g-factors and $g_{\text{eff}}(\nu p_{1/2})$ is expected. However, the measured g-factor is consistently greater than $g_{\text{eff}}(\nu p_{1/2})$, and in fact lies roughly halfway between the g_{eff} and g_{free} (beyond y-axis scale at +1.28). The JUN45 and jj44b interactions predict moments that are in agreement with $g_{\text{eff}}(\nu p_{1/2})$, and therefore systematically underestimate the measured g-factors of these $1/2^-$ states. One possible explanation is the fact that meson-exchange currents (MECs), that occur via nucleons interacting with one another, are unaccounted for in the JUN45 and jj44b interactions as the δg_l term is set to zero. The collaborators of this work call for more theoretical work in order to understand this.

The JUN45 and jj44b interactions predict low-lying spin-1/2 states in ^{79}Zn, although based on their g-factors and wave function configurations it is clear that these spin-1/2 states are not the isomeric $1/2^+$ state in question. The g-factors from both interactions are unable to provide a realistic estimate for the g-factor of ^{79m}Zn (not shown in Figure 6.2 due to scaling as $g_{\text{expt}} = -2.036$), and instead show a good agreement with $g_{\text{eff}}(\nu p_{1/2})$. The wave functions of these states confirm that they are dominated by a $(\nu p_{1/2})^1$ configuration, meaning these 1/2 states have negative parity. These results and the lack of a $1/2^+$ state in the JUN45 and jj44b low-lying spectra of ^{79}Zn confirm that the f_5pg_9 model space is insufficient for this isomer, and suggests the isomer instead occupies the positive parity $\nu s_{1/2}$ orbit beyond $N = 50$.

High-Spin State g-factors

The isomeric states of $^{69-73}$Zn and the ground state of $^{75-79}$Zn all align rather closely with the effective SP g-factor for the $\nu g_{9/2}$ orbital. As such, the wave function configurations of these isotopes are expected to be led by an unpaired neutron in this orbital. While this may be

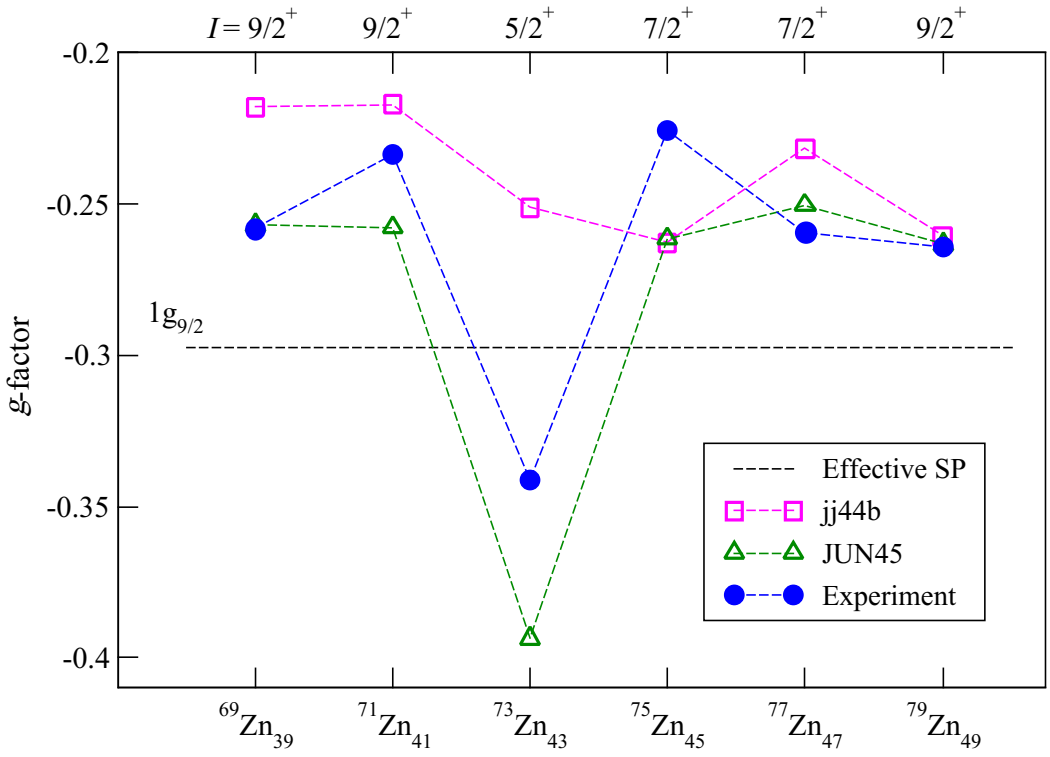

Figure 6.3: Comparison of measured high-spin state g-factors for isotopes from $N = 39 - 49$ and the predictions from the JUN45 and jj44b shell-model interactions.

the case, the spins of these states around the middle of the sub-shell beyond $N = 40$ suggest the configurations may be more complex. In Figure 6.2, both the shell-model interactions appear to reproduce the g-factors of these high-spin states fairly well, although a closer look at this in Figure 6.3 reveals a different story.

The isomeric $9/2^+$ states in ^{69,71}Zn are dominated by a single unpaired neutron in the $\nu g_{9/2}$ orbital, with the configuration accounting for >50% of the wave function in ^{69}Zn and >40% in ^{71}Zn. However, the contribution from this configuration reduces greatly for the $5/2^+$ isomeric state in ^{73}Zn, where the JUN45 and jj44b interactions predict very mixed wave functions (leading contributions $> 9\%$ and $> 14\%$, respectively). The measured g-factor of the anomalous $5/2^+$ spin isomer in ^{73}Zn produces a remarkable dip in the otherwise relatively linear trend from $N = 39-49$ in Figure 6.3. This dip is most accurately reproduced by JUN45, thus pointing to a great deal of configuration mixing in this state. It should be

noted that the $5/2^+$ isomer does not agree with the SP value of $g_{\text{expt}}(\nu d_{5/2})$, thus ruling out the possibility of the state being formed by an intruder isomer from excitations to $\nu d_{5/2}$. Despite this, the fact that the isomer lies below the SP value of $g_{\text{eff}}(\nu g_{9/2})$ means some admixture with such a configuration cannot be excluded.

The $(\nu g_{9/2})^1$ odd-particle configuration returns to dominate in the ground state of ^{75,77}Zn, although the ground state have anomalous spins of $7/2^+$. This means that, as suggested in Ref. [17], these states are likely to arise due to the coupling of an odd nucleon with a Coriolis-broken pair of nucleons, all in the $\nu g_{9/2}$ orbital, to form the anomalous $7/2^+$ spin. The exact nature of the $5/2^+$ isomer in ^{73}Zn and the $7/2^+$ ground state of ^{75,77}Zn will be discussed further in Section 6.2.3. The ground state wave functions of ^{75,77}Zn have leading contributions from $(\nu g_{9/2})^1$ odd-particle configuration of 45% and >75%, respectively, and this contribution increases in the $9/2^+$ ground state of ^{79}Zn where it accounts for >95% of the wave function in both interactions. The observed convergence of SM interaction g-factor predictions in the f_5pg_9 model space to experiment from $^{75-79}$Zn and the ∼100% contribution to the ground state wave function in ^{79}Zn from $(\nu g_{9/2})^{-1}$ configurations hint at the persistence of the $N = 50$ shell gap in neutron-rich nuclei. This conclusion will be tested in Section 6.3.2 where measured g-factors will be compared to SM interactions that consider cross $Z = 28$ and $N = 50$ excitations.

Occupation Numbers

Due to the accuracy of JUN45 predictions in matching the trend of experimental g-factors for the high spin states with $N = 39 - 49$, as shown in Figure 6.3, the interaction is selected to probe level systematics through its predicted occupation numbers. The occupation number describes the average number of nucleons within each orbital for a given isotope, with each orbital's occupancy based on its relative contribution to the overall wave function. Results for these high spin states are shown in Figure 6.4, with the displayed occupancies, n, normalised to the maximum orbital occupancy

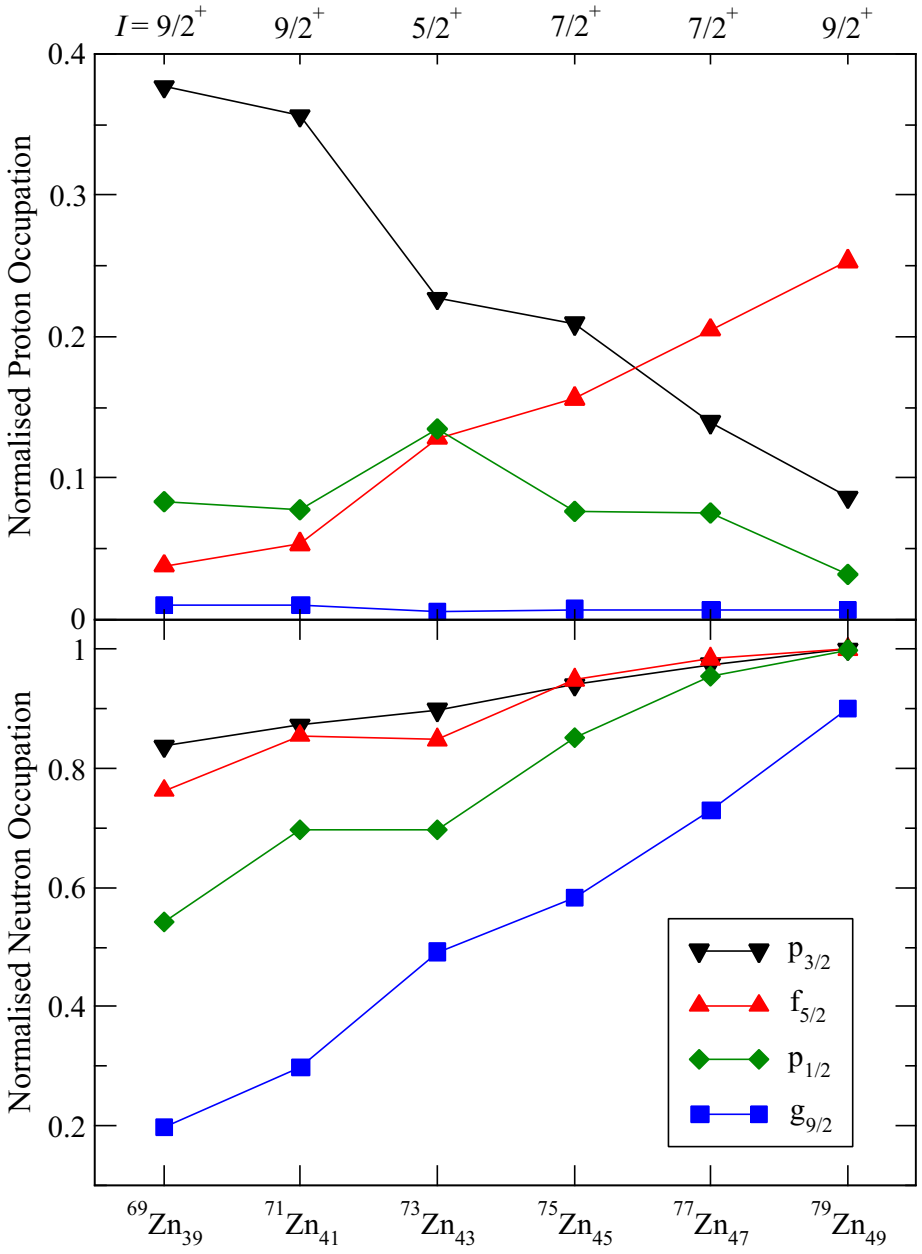

Figure 6.4: Proton (top) and neutron occupation (bottom) in the f_5pg_9 model space normalised to the maximum number of nucleons per orbital, as predicted by the JUN45 interaction.

$$n = \frac{n_j}{2j+1}, \tag{6.1}$$

where n_j is the calculated occupancy of an orbital with total angular momentum j and $2j+1$ the maximum occupancy of an orbital with j. Beyond $N = 40$, the increasing neutron number is expected to have an effect on level orientation, with one such example being the inversion of the $\pi f_{5/2}$ and $\pi p_{3/2}$ levels due to the attractive tensor interaction that lowers $\pi f_{5/2}$ as $\nu g_{9/2}$ is gradually filled [23]. This has been observed in odd-Z, even-N isotopes of Cu [25] and Ga [26] where, with one and three protons beyond $Z = 28$, respectively, this inversion manifests itself as a ground state spin change from $I = 3/2^-$ to $5/2^-$. The predictions of JUN45 therefore offer a unique glimpse into this behaviour in even-Z nuclei.

As expected in a non-interacting shell model picture, the two protons beyond the $Z = 28$ shell closure appear to occupy the $\pi p_{3/2}$ in ^{69m}Zn and ^{71m}Zn as the filling of the $\nu g_{9/2}$ begins. A notable drop in the proton occupation of this orbit is observed in the isomeric state of ^{73}Zn, with the occupancy of the $\pi f_{5/2}$ and $\pi p_{1/2}$ orbits offsetting this behaviour by increasing. A similar kink is observed here for most of the neutron levels, while the trend in occupancy with increasing neutron number appears to increase linearly for the other isotopes. The alignment of these kinks in the majority of f_5pg_9 proton and neutron levels provides more evidence of configuration mixing beyond $N = 40$ that peaks in the $5/2^+$ isomeric state of ^{73}Zn.

Beyond this point, occupancy of the $\pi f_{5/2}$ level continues to increase to the point where it becomes greater than that of $\pi p_{3/2}$ between $N = 45$ and $N = 47$, signalling an inversion of these orbitals. This point of inversion is in agreement with that observed in odd-Z Cu and Ga, where the ground state spin changes from $I = 3/2^-$ to $5/2^-$ occurs in Cu between $^{73}_{29}\mathrm{Cu}_{44}$ and $^{75}_{29}\mathrm{Cu}_{46}$ [25], and between $^{79}_{31}\mathrm{Ga}_{48}$ and $^{81}_{31}\mathrm{Ga}_{50}$ [26] in Ga. The influence of the attractive tensor interaction between $\nu g_{9/2}$ and $\pi f_{5/2}$ is therefore still observable, if only indirectly, in Zn. The tensor interaction persists into ^{79}Zn where the occupation of $\pi f_{5/2}$ continues to rise as $\pi p_{3/2}$ decreases further.

6.2.3 Spectroscopic Quadrupole Moments

The deviation of the nuclear shape from sphericity is understood quantitatively through the spectroscopic quadrupole moment, Q_s. The magnitude of the moment indicates the size of

Table 6.2: Spectroscopic quadrupole moments, Q_s (b), calculated from experimental data are compared to JUN45 and jj44b shell-model calculations. †To calibrate $Q_{s,expt}$ across the isotope chain, the quadrupole moment of ^{67}Zn is used as reference, with $Q_s = +0.122(10)$ b calculated for this work (details given in [94]). The precise hyperfine coefficient $B(^3P_2) = +35.806(5)$ MHz [89] is used as the reference in calculations.

A	I^{π}	$Q_{s,expt}$	$Q_{s,JUN45}$	$Q_{s,jj44b}$
63	$3/2^-$	+0.20(2)	+0.240	+0.264
65	$5/2^-$	−0.024(15)	−0.049	−0.038
67	$5/2^-$	+0.122(10)†	+0.128	+0.036
69^m	$9/2^+$	−0.39(3)	−0.410	−0.375
71^m	$9/2^+$	−0.26(3)	−0.284	−0.225
73^m	$5/2^+$	+0.43(4)	+0.281	+0.467
75	$7/2^+$	+0.16(2)	+0.070	+0.294
77	$7/2^+$	+0.48(4)	+0.421	+0.487
79	$9/2^+$	+0.40(4)	+0.356	+0.371

nuclear deformation, while the sign of the moment corresponds to the shape of the nucleus, with a positive moment meaning prolate deformation, negative meaning oblate deformation, and a zero moment being spherical. This quantity can be used to shed light on the evolution of charge distribution and collectivity with changing N. The quadrupole moments of low-lying states with $I > 1/2$ across the Zn isotope chain have been measured in the work, and are shown in Table 6.2. The values for $^{63-65g,69m}$Zn are updates to the moments previously stated in literature, while $^{71-73m,75-79g}$Zn are measured here for the first time. The quadrupole moment of ^{67}Zn has been calculated by atomic theorists especially for this work (more details in [94]) and is used as the reference isotope.

Quadrupole moment predictions from the JUN45 and jj44b interactions are used to probe which orbitals in this mass region required for describing quadrupole collectivity. This is due to the fact that the orbitals immediately before and after these f_5pg_9 model space may favour quadrupole correlations since they have $\Delta l = 2$: with $\pi f_{7/2}$ and $\pi p_{3/2}$ spanning $Z = 28$, and $\nu g_{9/2}$ and $\nu d_{5/2}$ spanning $N = 50$ [20]. Therefore, the agreement or disagreement of JUN45 and jj44b predictions with measured values will highlight how important the $\pi f_{7/2}$ and $\nu d_{5/2}$

orbitals are. Quadrupole collectivity has already been reported in the neighbouring element Ga [26] around the mid-point of the $N = 40$ sub-shell as $\nu g_{9/2}$ is filled. For this reason, the comparison of f_5pg_9 predictions to measured quadrupole moments will focus on isotopes where $(\nu g_{9/2})^1$ odd-particle configurations are dominant ($N = 39 - 49$). The results of this are shown in Figure 6.5.

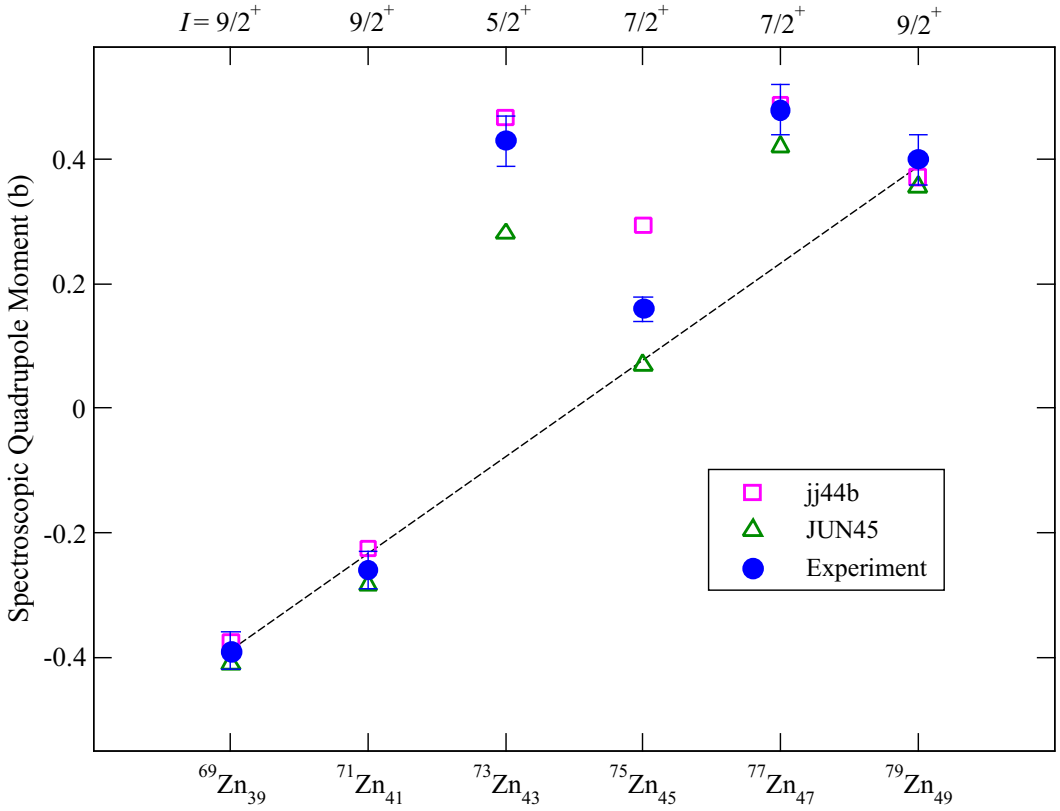

Figure 6.5: Spectroscopic quadrupole moments, Q_s, of $^{69-79}$Zn measured in this work compared to predictions from the JUN45 and jj44b shell model interactions.

The alignment of measured g-factors of $^{69-73m,75-79g}$Zn with the effective g-factor of $\nu g_{9/2}$ (Figure 6.2) indicates that their wave functions are dominated by $(\nu g_{9/2})^1$ odd-particle configurations. In the event that these are single-particle configurations, their quadrupole moments would exhibit a linear progression from $^{69-79}$Zn that crosses zero at $N = 44$. This line is representative of the seniority-1 $(\nu g_{9/2})^1_{9/2^+}$ moments. The opposite and equal moments of ^{69m}Zn ($Q_s = -0.39$ b) and ^{79}Zn ($Q_s = +0.40$ b) are representative of the single

$\nu g_{9/2}$ particle and the single $\nu g_{9/2}$ hole configurations, respectively. The moment of ^{71m}Zn is also in agreement with this trend. The moments predicted by JUN45 and jj44b for these seniority-1 $(\nu g_{9/2})^1_{9/2^+}$ states are in excellent agreement with the measured values.

For the remaining isotopes in this range, the Q_s values and confirmed spins of $^{73m,75-77g}$Zn exhibit a clear deviation from the linear trend. This is most notable at the $5/2^+$ isomer in ^{73}Zn, where the sudden change from a small oblate deformation ($Q_s = -0.32(6)$) in ^{71m}Zn to a large prolate deformation ($Q_s = +0.52(6)$)) in ^{73m}Zn points to a sudden onset of collectivity. The study of Zn isotopes at REX-ISOLDE by low-energy Coulomb excitation provides further verification of collectivity in this region. The sudden lowering of 2^+ states at $N = 40$ and an increase in B(E2$\downarrow$) strength towards $N = 44$ was associated with an increase in collectivity due to proton-neutron correlations and a weakening of the $N = 40$ sub-shell closure [99, 98], with the the maximum of collectivity being placed at $N = 42$ in even-even nuclei beyond $Z = 28$ (Zn, Ge, Se) [100, 101, 102, 103]. While both interactions reproduce this jump, JUN45 underestimates the quadrupole moment of the $5/2^+$ isomer by $\sim$25%. The following two states, ground state of ^{75,77}Zn, have spin-7/2, meaning both lie off the expected line for SP $9/2^+$ states. The former is not reproduced accurately by either interaction, while the latter is reproduced by both. The inability of the JUN45 and jj44b interactions to consistently reproduce the the quadrupole moments from $^{73-77}$Zn suggests they are unsuited for predicting quadrupole collectivity in Zn. The experimental results will later be compared to different shell-model interactions that include $f_{7/2}$ and $d_{5/2}$, orbitals that have previously highlighted as being key for describing collectivity, in order to see if there is any improvement over f_5pg_9 interactions.

Seniority States

To investigate these discrepancies around mid-point of the $\nu g_{9/2}$ filling, the measured quadrupole moments are compared to those from seniority-3 configurations, where all but three particles are coupled to $I = 0$. Figure 6.6 outlines the expected quadrupole moment values based on Equation 3.12 from Section 3.2.3 for the seniority-3 $I = 7/2^+$ and $I = 5/2^+$ $(\nu g_{9/2})^3$ states.

The quadrupole moments of the ^{75,77}Zn ground state are seen to be in agreement with the predictions for seniority-3 $(\nu g_{9/2})^3_{7/2^+}$ states, thus explaining their deviation from the linear progression of seniority-1 states. More interestingly, the $5/2^+$ isomeric state in ^{73}Zn does not align with the predictions for a $(\nu g_{9/2})^3_{5/2^+}$ configuration. This deviation is interpreted as further evidence of an onset in collectivity, and indicates the presence of substantial deformation in the isomer. Conclusions from beta-decay studies [15] and transfer reaction experiments [104] corroborate this result, where the low-energy states in ^{73}Zn are seen to be consistent with a moderate prolate deformation ($\beta_2 \approx +0.2$), although our results suggest a slightly stronger deformation ($\beta_2 = +0.236$). Collectivity has also been observed in odd-A Ga ($Z = 31$) isotopes beyond $N = 40$ [26] via their quadrupole moments, although the development of collectivity in Cu ($Z = 29$) isotones has not been observed [25]. An increase in collectivity with proton number is also observed through the $B(E2)$ values of even-even Ni ($Z = 28$), Zn ($Z = 30$) and Ge ($Z = 32$) nuclei, with a $B(E2)$ minimum at $N = 40$ in Ni and an increase in $B(E2)$ beyond $N = 40$ in Zn and Ge [105]. These observations, coupled with the increase in configuration mixing in ^{73m}Zn, strongly suggests that Zn isotopes are centred in a transitional region for nuclear shape between the spherical nuclei of Ni and the deformed nuclei of Ge [105].

6.3 Modified LNPS and A3DA Interactions

The model spaces of the LNPS and A3DA interactions both extend beyond the f_5pg_9 space used in the JUN45 and jj44b calculations. The LNPS interaction uses the full pf-shell for protons and includes the $\nu d_{5/2}$ on top of f_5pg_9 for neutrons, resulting in a valence space above a ^{48}Ca core that contains all the physical degrees of freedom required to describe low-lying properties of Zn isotopes [61]. Calculations in this space therefore use free spin g-factors. The effective neutron charge reduces from that in [61] to $e_{\mathrm{n}}^{\mathrm{eff}} = 0.46e$ due to $\nu d_{5/2}$, while the effective charge for protons is $e_{\mathrm{p}}^{\mathrm{eff}} = 1.31e$ [106]. The LNPS-m calculations for this work have been performed by F. Nowacki.

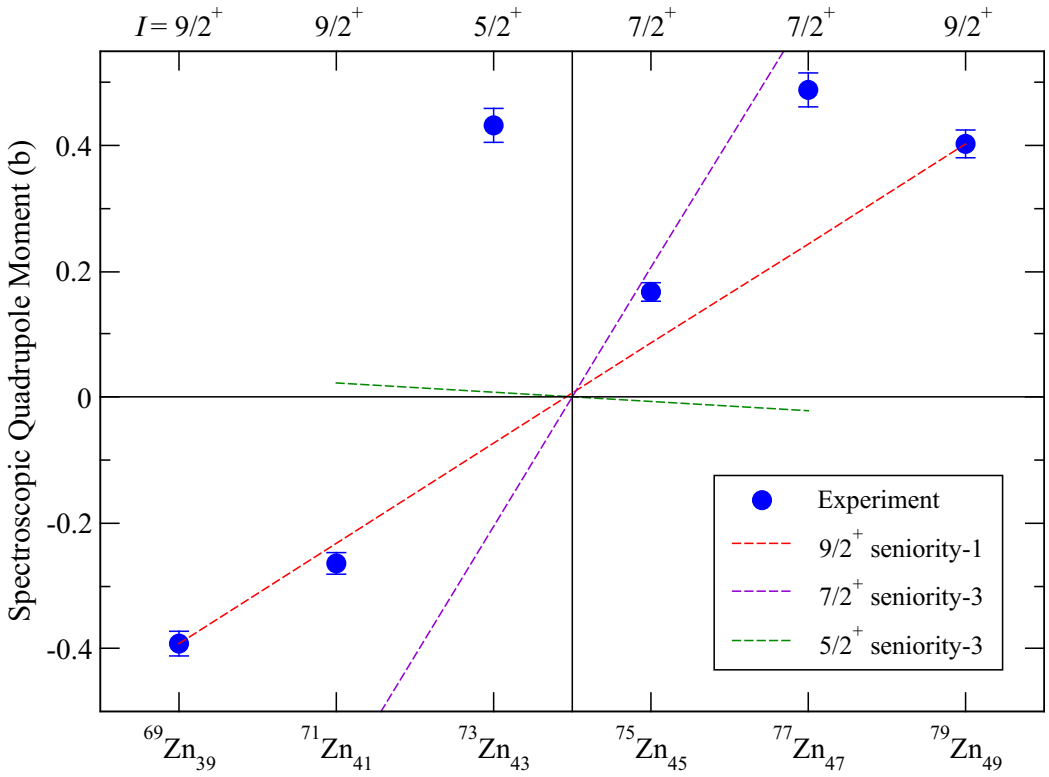

Figure 6.6: Proton and neutron occupation in the f_5pg_9 model space normalised to the maximum number of nucleons per orbital, as predicted by the JUN45 interaction.

The A3DA interaction model space extends again beyond that of LNPS to include the full pf-shell along with the $g_{9/2}$ and $d_{5/2}$ orbits for both protons and neutrons. The $\nu f_{7/2}$ orbit is however effectively frozen in A3DA calculations due to Pauli blocking effects that greatly limit excitations from the orbit in neutron-rich isotopes $N > 38$. The inert core for these calculations is now ^{48}Ca instead of ^{40}Ca. The shell model interaction parameters stated above for LNPS are also used for A3DA calculations given in this work, but are somewhat different from those listed in [62]. The A3DA-m calculations for this work have been performed by T. Otsuka and Y. Tsunoda.

6.3.1 Energy Level Systematics

As was shown in Section 6.2.1, the f_5pg_9 model space adopted in the JUN45 and jj44b interactions proved insufficient for describing the progression of energy levels in odd-A Zn

isotopes beyond $N = 40$. One such way to test this conclusion is to compare the same nuclear property to shell-model interactions with a different model space and see if there is any improvement. The A3DA-m and LNPS-m interactions provide an opportunity to do this, as their model spaces extend beyond f_5pg_9 by including the $\pi f_{7/2}$ orbit below $Z = 28$ and the $\nu d_{5/2}$ orbit above $N = 50$. The influence of these orbitals on the relative spacing of energy levels should therefore become clear from their predictions. The A3DA-m and LNPS-m results for low-lying energy levels in Zn isotopes from $N = 41 - 49$ are compared to those from experiment in Figure 6.7, with any noticeable differences from the predictions by JUN45 and jj44b also addressed.

It is immediately noted that, relative to the spin assignments from JUN45 and jj44b, the A3DA-m and LNPS-m interactions much less frequently assign the $9/2^+$ level as the ground state spin. Other than for the ground states of ^{71,79}Zn, the predicted ground state spins are not $9/2^+$, and are in fact rather varied. For ^{71}Zn, the LNPS-m interaction rather accurately replicates the energies of the ground and isomeric state spins $1/2^-$ and $9/2^+$ respectively, while A3DA-m assignments are reversed. The trend of the $1/2^-$ level from this point on is rather consistent between the two interactions and experiment, with the three never deviating by more than ≈200 keV. The lowering of the $5/2^+$ level, measured as an isomeric state in ^{73}Zn, is more extreme in A3DA-m and LNPS-m than in the f_5pg_9 interactions. The $5/2^+$ level lowers to the ground state here in LNPS-m, and is almost degenerate with the $1/2^-$ ground state in A3DA-m. The increase in density of low-lying levels in ^{73}Zn, measured experimentally and predicted by theory, can signal the development of collectivity. Such behaviour has already been highlighted by an increase in B(E2↓) strength towards $N = 44$ in Zn ($N = 43$ for ^{73}Zn), and the addition of the $\pi f_{7/2}$ and $\nu d_{5/2}$ orbits in the interaction model spaces means that A3DA-m and LNPS-m are better suited for predicting the development of collectivity [59].

The lowering of the $7/2^+$ level is reproduced well by the A3DA-m interaction in ^{75,77}Zn and by LNPS-m in ^{77}Zn, with the sole exception in these isotopes being the LNPS-m interaction placing the level at ≈800 keV in ^{75}Zn. In particular, the agreement between measured

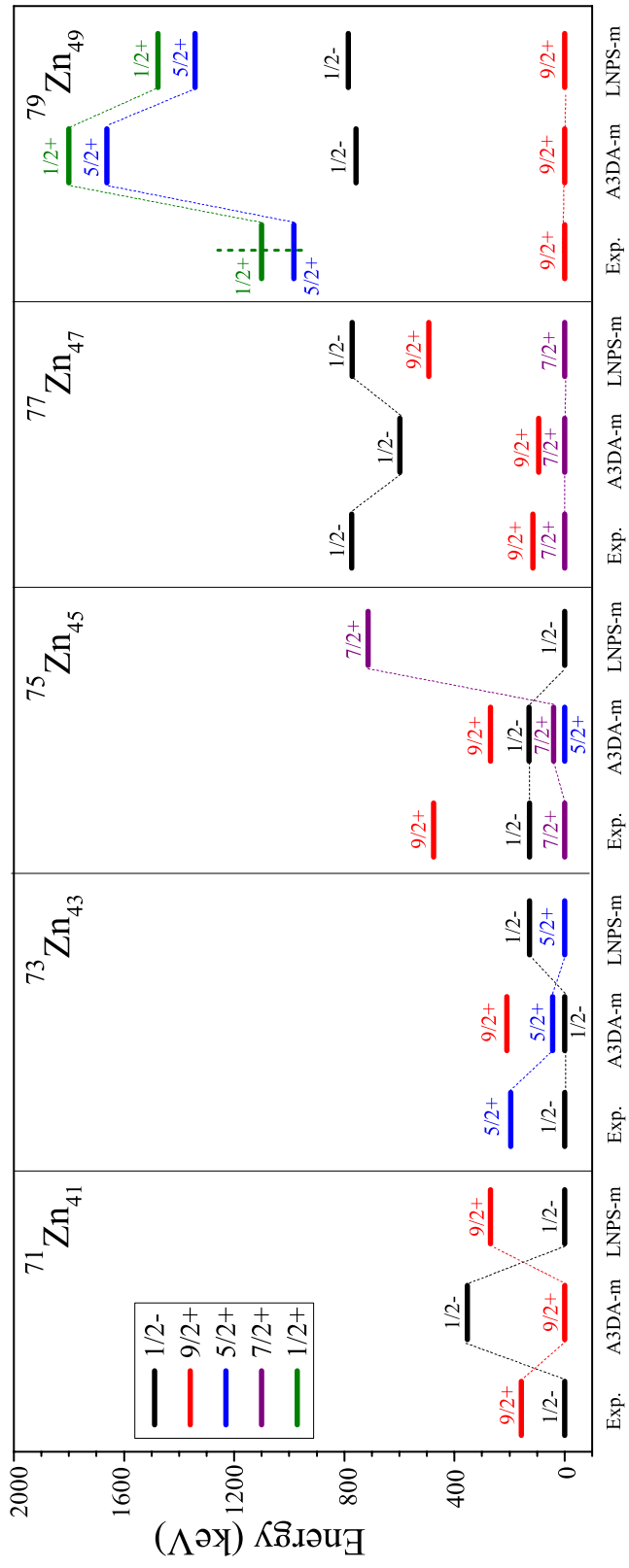

Figure 6.7: Measured low-energy spectra of Zn isotopes from $N = 41 - 49$ are compared to predictions from the A3DA-m and LNPS-m shell-model interactions. Dotted lines represent the change in energy of the ground and isomeric states, while the vertical dashed line at ^{79}Zn shows the error on the measured energy.

low-lying level energies and the shell-model predictions in ^{77}Zn is excellent. These predictions exhibit a noticeable improvement over those from JUN45 and jj44b, suggesting that excitations involving orbitals in the extended model space are important in characterising the energy of the $7/2^+$ level. The systematics of the low-lying $9/2^+$ level from $^{75-77}$Zn are most accurately reproduced by the A3DA-m interaction, although both interactions correctly predict the ground state spin inversion of $7/2^+$ to $9/2^+$ from ^{77}Zn to ^{79}Zn.

The isomeric state in ^{79}Zn was earlier shown to occupy an orbital beyond the $N = 50$ shell closure in the discussion of the f_5pg_9 interactions, hence preventing the interactions from predicting the energy of the $1/2^+$ level. The level energies from the A3DA-m and LNPS-m interactions for ^{79}Zn can provide an idea of the importance of the $\nu d_{5/2}$ orbit in characterising the isomer. A3DA-m and LNPS-m do in fact predict a positive-parity $1/2^+$ level among the low-lying states of ^{79}Zn, although in both interactions the level appears at higher energy (1.8 and 1.5 MeV) than has been measured (1.10(15) MeV). The accompanying $5/2^+$ intruder level is also elevated in terms of energy from experiment by both interactions. The spin-parity of this state suggests that the level is formed by the excitation of an unpaired neutron across $N = 50$ to the $d_{5/2}$ orbit. Despite the fact that A3DA-m and LNPS-m predict these levels in the low-lying level spectrum of ^{79}Zn, the overestimation of their energy means that the extended model spaces of these interactions are still insufficient to describe the isomer.

6.3.2 Magnetic Dipole Moments

The discussion of shell-model predictions in the f_5pg_9 model space have proved fairly accurate in reproducing experimental observables across the Zn isotope chain. By comparing these predictions to those from the LNPS-m and A3DA-m interactions, it can be seen how important the roles of orbitals beyond the $Z = 28$ and $N = 50$ shell gaps are in understanding the nuclear structure development in Zn. Due to the similarities in their model spaces, the comparison of the LNPS-m and A3DA-m interactions to experimental results will be given simultaneously in this section. The experimentally measured g-factors and predictions from the LNPS-m and A3DA-m interactions are shown in Table 6.3 and Figure 6.8 across the Zn

isotope chain from $N = 33 - 49$.

Table 6.3: Nuclear magnetic dipole moments, μ (μ_N) calculated from experimental data are compared to A3DA-m and LNPS-m shell-model calculations. †To calibrate across the isotope chain the magnetic dipole moment of ^{67}Zn is used as reference, with μ taken from [14]. The precise hyperfine coefficient $A(^3P_2) = +531.987(5)$ MHz [89] is used.

A	I^π	μ_{expt}	$\mu_{\text{LNPS-m}}$	$\mu_{\text{A3DA-m}}$
63	$3/2^-$	$-0.282(1)$	-0.18	$+0.110$
65	$5/2^-$	$+0.7695(16)$	$+0.77$	$+1.027$
67	$5/2^-$	$+0.875479(9)^\dagger$	$+1.31$	$+1.309$
69	$1/2^-$	$+0.557(2)$	$+0.47$	$+0.404$
69^m	$9/2^+$	$-1.1613(7)$	-1.27	-1.306
71	$1/2^-$	$+0.551(1)$	$+0.48$	$+0.482$
71^m	$9/2^+$	$-1.049(1)$	-1.10	-1.434
73	$1/2^-$	$+0.5585(5)$	$+0.50$	$+0.521$
73^m	$5/2^+$	$-0.8527(14)$	-0.81	-0.543
75	$7/2^+$	$-0.7887(9)$	-0.88	-0.614
75^m	$1/2^-$	$+0.5580(9)$	$+0.51$	$+0.509$
77	$7/2^+$	$-0.9074(1)$	-1.04	-0.964
77^m	$1/2^-$	$+0.562(2)$	$+0.50$	$+0.537$
79	$9/2^+$	$-1.1866(10)$	-1.49	-1.508
79^m	$1/2^+$	$-1.018(1)$	-0.741	-0.603

g-factors

A3DA-m and LNPS-m are unable to reproduce the g-factors of low mass Zn isotopes as accurately as JUN45 and jj44b, except for the LNPS-m prediction for the ground state of ^{65}Zn. For ^{67}Zn, both interactions predict a deviation from the effective SP g-factor of $\nu f_{5/2}$ towards that of $\nu p_{1/2}$, suggesting the incorrect prediction of some mixing between configurations with unpaired neutrons in each orbital.

The lowest lying $1/2^-$ states in $^{69-77}$Zn are once again underestimated by the shell-model interactions, although in comparison to the predictions of the JUN45 and jj44b interactions, A3DA-m and LNPS-m are much closer to the experimental values. The predicted g-factors for the $1/2^-$ states gradually moves away from the effective SP value for $\nu p_{1/2}$ and converge to the

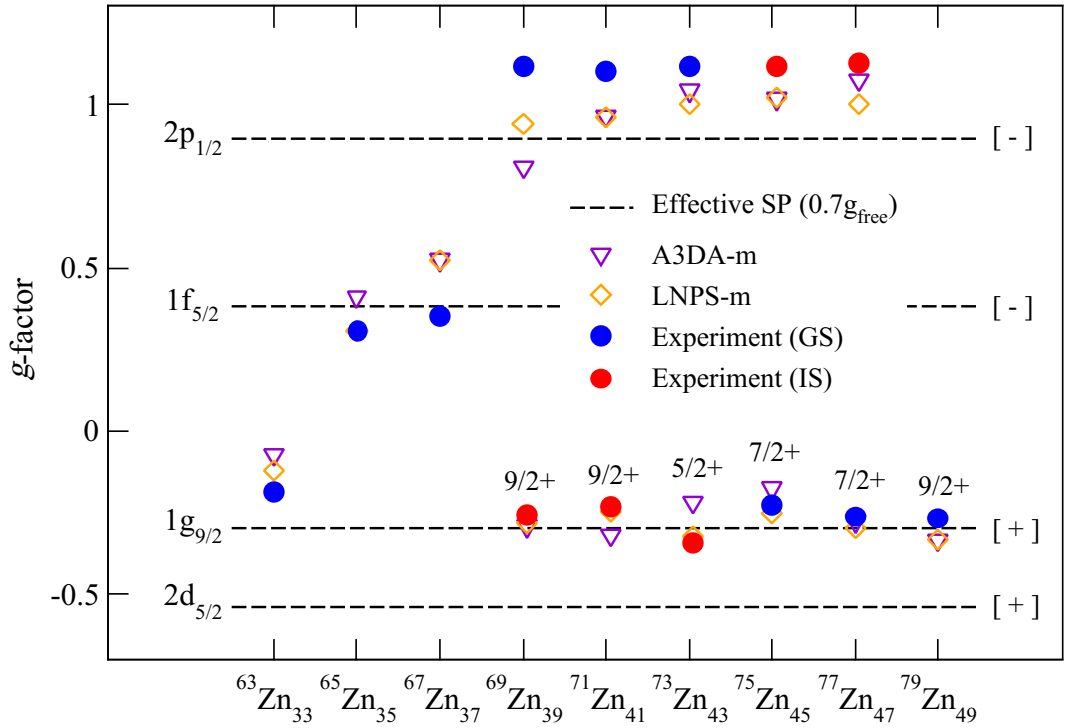

Figure 6.8: Experimental g-factors across the isotope chain in comparison to single-particle estimates and predictions from the A3DA-m and LNPS-m interactions. The measured g-factor of ^{79m}Zn and predictions from the interactions are not shown here due to scaling, as $g_{\text{expt}} = -2.036$, $g_{\text{LNPS-m}} = -1.48$ and $g_{\text{A3DA-m}} = -1.21$. Errors on measured g-factors are smaller than the size of the symbols.

measured values up to ^{77}Zn, after which the next spin-1/2 state is the positive parity isomer in ^{79}Zn. A3DA-m and LNPS-m interaction predictions for this state again show an improvement over those from the f_5pg_9 model space due to their extended model spaces that consider excitations across $N = 50$, although their model spaces still fall short of $\nu 3s_{1/2}$, the orbital expected to be occupied in the isomer based on its spin-parity $1/2^+$. The measured g-factor of ^{79m}Zn ($g_{\text{expt}} = -2.036$) is therefore not reproduced by either interaction ($g_{\text{A3DA-m/LNPS-m}} = -1.21/-1.48$), although both do at least reproduce the expected $1/2^+$ spin-parity of the state. These results exhibit a marked improvement over those from JUN45 and jj44b, which are unable to assign the correct spin-parity to the isomer. In order to fully describe the nature of the isomeric wave function, an interaction with an even more extended neutron model space is required. This newly developed shell-model interaction will be introduced in

Section 6.4.

High-Spin State g-factors

For the high-spin states from $N = 39 - 49$, there is an obvious difference in the accuracy of predictions from the LNPS-m and A3DA-m interactions. Even in the broad view of all measured g-factors shown in Figure 6.8, an obvious discrepancy can be seen between A3DA-m and experiment across this range, with the largest difference seen at the $5/2^+$ isomer in ^{73m}Zn. Conversely, LNPS-m much more accurately reproduces the measured values. In spite of some inaccuracies, all predictions are still representative of a $(\nu g_{9/2})^1$ odd-particle configuration due to their proximity to the effective SP value for $\nu g_{9/2}$. To investigate this further, a view of the high-spin g-factors on a smaller scale is shown in Figure 6.9, as was done earlier for JUN45 and jj44b.

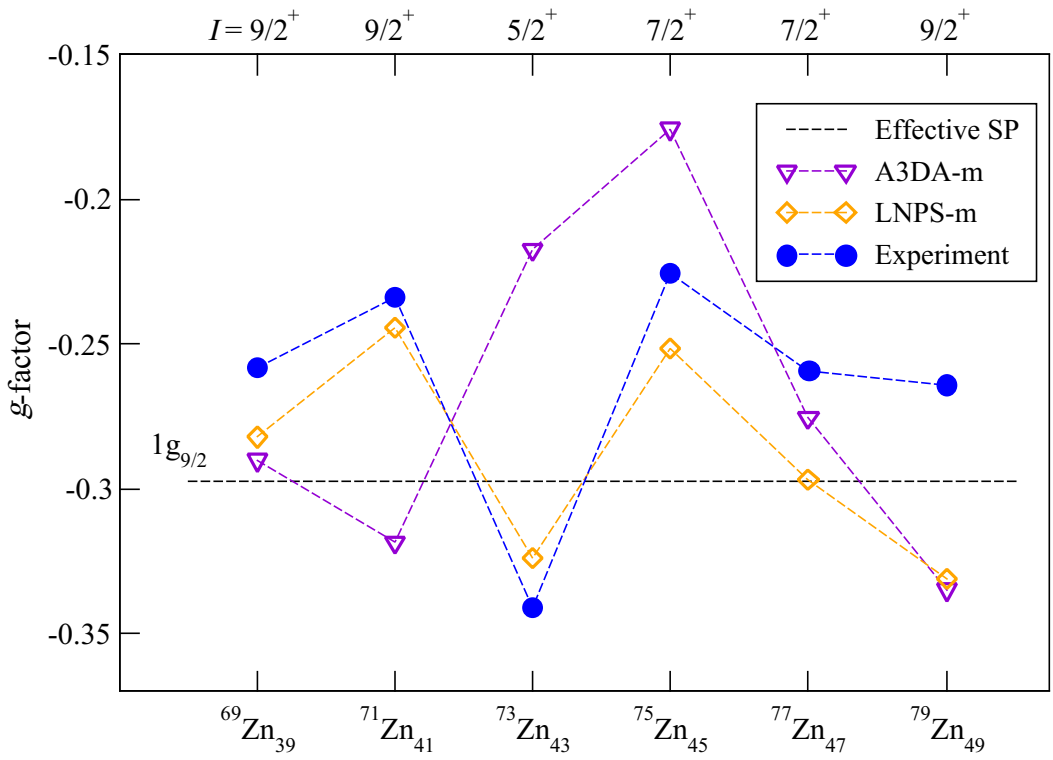

Figure 6.9: Comparison of measured high-spin state g-factors for isotopes from $N = 39 - 49$ and the predictions from the LNPS-m and A3DA-m shell-model interactions.

The LNPS-m interaction is able to reproduce the general trend of the experimental values rather well, with its prediction for the key feature in this range, the dip at ^{73m}Zn, being even more accurate than that of JUN45. On the other hand, A3DA-m struggles to reproduce the trend of g-factors beyond $N = 40$. The predictions from A3DA-m are seen to differ greatly from those of experiment and LNPS-m, especially from $N = 41 - 45$, suggesting that the interaction is perhaps not suited for predicting neutron configurations in this region of increased configuration mixing. The occupation numbers from the A3DA-m interaction, shown in Figure 6.10, can be used in an attempt to explain why experiment and theory are so far apart here. For the $5/2^+$ isomer in ^{73}Zn, where the difference between A3DA-m and experiment is greatest, the occupancies of both protons and neutrons seem to be roughly comparable to those from JUN45, which is able to reproduce the observed dip in g-factor. One such difference between the interactions is an increase in neutron excitations to the $d_{5/2}$ orbital in A3DA-m. The increased occupation of this orbital, while only minor, would be expected to shift the g-factor towards the effective SP value for $\nu d_{5/2}$ and hence closer to reproducing the dip. However, the opposite is seen, and the difference is attributed to a small increase relative to JUN45 in the occupancy of $\pi p_{1/2}$ and $\pi f_{5/2}$. Excitations to the $\nu d_{5/2}$ orbital from $\nu g_{9/2}$ will be discussed later in this section with the quadrupole moments.

Returning to the high-spin g-factors, another interesting feature is observed in the heavier Zn isotopes, whereby LNPS-m predictions begin to deviate from measured values from ^{75}Zn up to ^{79}Zn. While the A3DA-m interaction has been shown not to reproduce results from experiment or LNPS-m, its predictions begin to converge with those from LNPS-m towards ^{79}Zn, therefore also diverging from experiment. Their predicted g-factors for the $9/2^+$ ground state of ^{79}Zn drop below the effective SP value for $\nu g_{9/2}$ and in the direction of the effective SP value for $\nu d_{5/2}$, the latter of which has a non-zero occupation according to the A3DA-m interaction (seen in Figure 6.10). These results are in stark contrast to those of JUN45 and jj44b, as their predictions for the same isotopes (seen in Figure 6.3) converge on the measured values as $N = 50$ is approached. The exclusion of the $\nu d_{5/2}$ orbit from the f_5pg_9 model space and the accuracy of JUN45 and jj44b predictions over A3DA-m and LNPS-m suggests that

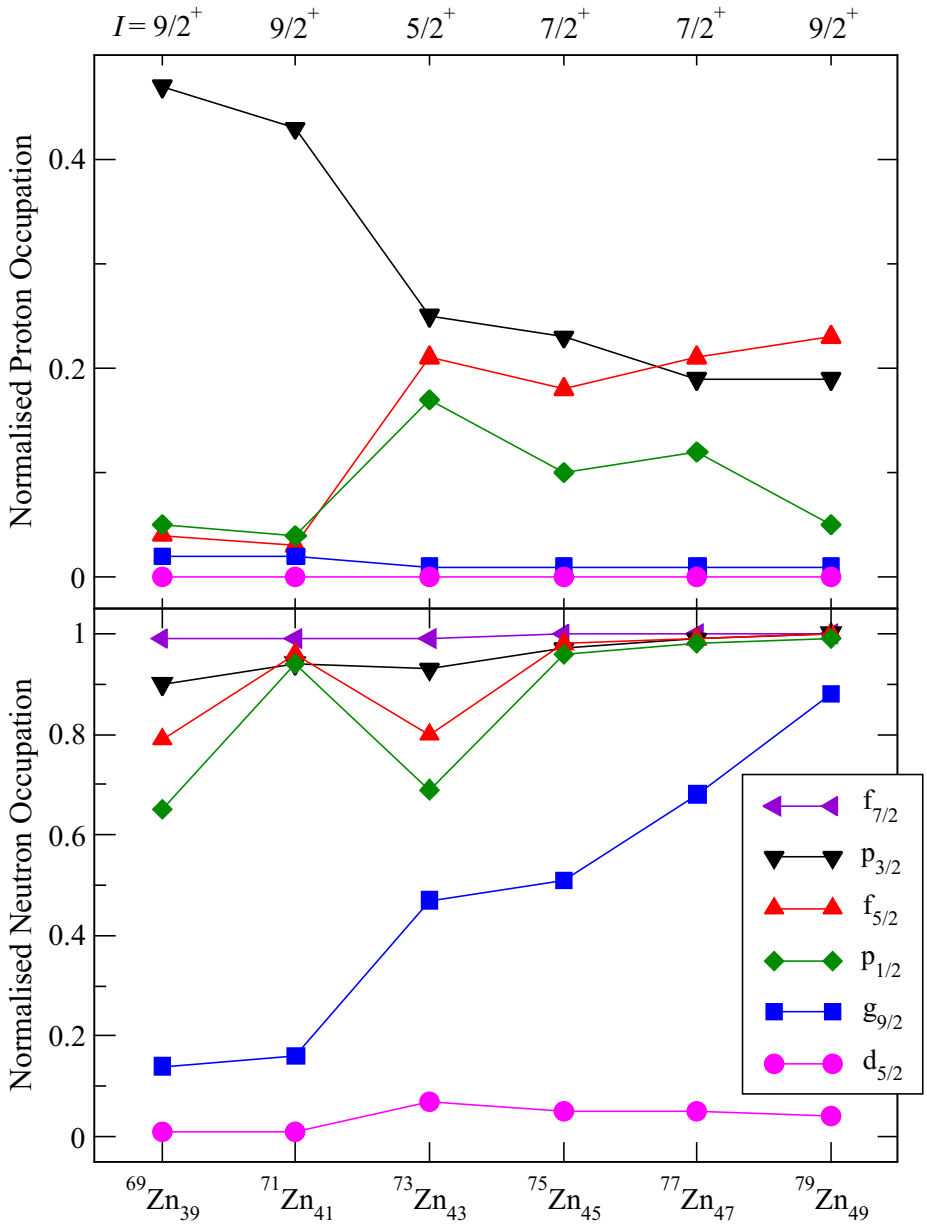

Figure 6.10: Proton and neutron occupation from $N = 39 - 49$ in the fpg_9d_5 model space normalised to the maximum number of nucleons per orbital, as predicted by the A3DA-m interaction. Data for the $\pi f_{7/2}$ orbital are not shown here to focus on the systematics of higher lying levels, as the normalised occupancy remains at ≈1 across the range.

excitations to this orbit are not influential in the ground state of ^{79}Zn, and hence gives further indication towards the stability of the $Z = 28$ and $N = 50$ shell gaps with increasing neutron number.

Table 6.4: Spectroscopic quadrupole moments, Q_s (b), calculated from experimental data are compared to A3DA-m and LNPS-m shell-model calculations. †To calibrate across the isotope chain the quadrupole moment of ^{67}Zn is used as reference, with $Q_s = +0.122(10)$ b calculated for this work (details given in [94]). The precise hyperfine coefficient $B(^3P_2) = +35.806(5)$ MHz [89] is used as the reference in calculations.

A	I^{π}	$Q_{s,expt}$	$Q_{s,LNPS-m}$	$Q_{s,A3DA-m}$
63	$3/2^-$	+0.20(2)	+0.19	+0.209
65	$5/2^-$	−0.024(15)	−0.036	+0.013
67	$5/2^-$	+0.122(10)†	+0.10	+0.219
69^m	$9/2^+$	−0.39(3)	−0.40	−0.435
71^m	$9/2^+$	−0.26(3)	−0.22	−0.264
73^m	$5/2^+$	+0.43(4)	+0.48	+0.420
75	$7/2^+$	+0.16(2)	+0.20	+0.055
77	$7/2^+$	+0.48(4)	+0.60	+0.487
79	$9/2^+$	+0.40(4)	+0.546	+0.367

6.3.3 Spectroscopic Quadrupole Moments

As stated in Section 6.2.3, quadrupole moments beyond $N = 40$ in the mass region of Zn are expected to be sensitive to the influence of $\pi f_{7/2}$ and $\nu d_{5/2}$ due to excitations involving $\pi p_{3/2}$ and $\nu g_{9/2}$, respectively. Due to the inclusion of the former two orbits in the A3DA-m and LNPS-m model spaces, any notable improvement in the predictions of the A3DA-m and LNPS-m interactions over those of JUN45 and jj44b will provide a clear indication of their contribution to quadrupole collectivity in the mid-shell. By also using the occupation numbers from A3DA-m, given previously in Figure 6.10, the importance of the $\pi f_{7/2}$ and $\nu d_{5/2}$ orbitals can be probed individually. The measured values of Q_s are shown in Table 6.3 and, as for JUN45 and jj44b, the moments Zn isotopes where $N = 39 - 49$ are given in comparison to the LNPS-m and A3DA-m predictions in Figure 6.11.

The general trend of the quadrupole moment appears to be best reproduced across this range by the A3DA-m interaction, with its only deviation from experiment occurring at the $7/2^+$ ground state of ^{75}Zn. The $5/2^+$ isomeric state in ^{73}Zn was highlighted in the previous section for the sudden onset of deformation due to its large deviation from the expected Q_s of

a seniority-3 $(\nu g_{9/2})^3_{5/2^+}$ state. The measured moment ($Q_{\mathrm{s,expt}} = +0.43(4)$) of the isomer is predicted within experimental errors by A3DA-m ($Q_{\mathrm{s,A3DA-m}} = +0.42$) and is therefore more accurate than any of the other interactions described here. Here the occupation of $\nu d_{5/2}$ (in Figure 6.10) peaks at the $5/2^+$ isomer in the A3DA-m interaction. Therefore, the increased occupation of $\nu d_{5/2}$ (while only minor) at the point of maximum quadrupole deformation coupled with the excellent agreement between A3DA-m predictions of Q_{s} and experiment for isotopes from $N = 39-49$, points to the strong influence of $\nu d_{5/2}$ in characterising quadrupole collectivity beyond $N = 40$. This is in agreement with the conclusion from Ref. [59] that quadrupole collectivity beyond $N = 40$ cannot develop sufficiently within the f_5pg_9 due to the missing $\nu d_{5/2}$ and $\pi f_{7/2}$ single-particle orbits. However, the occupation of $\pi f_{7/2}$ remains constant at ~ 1 across the isotope chain, meaning there are no quadrupole excitations from

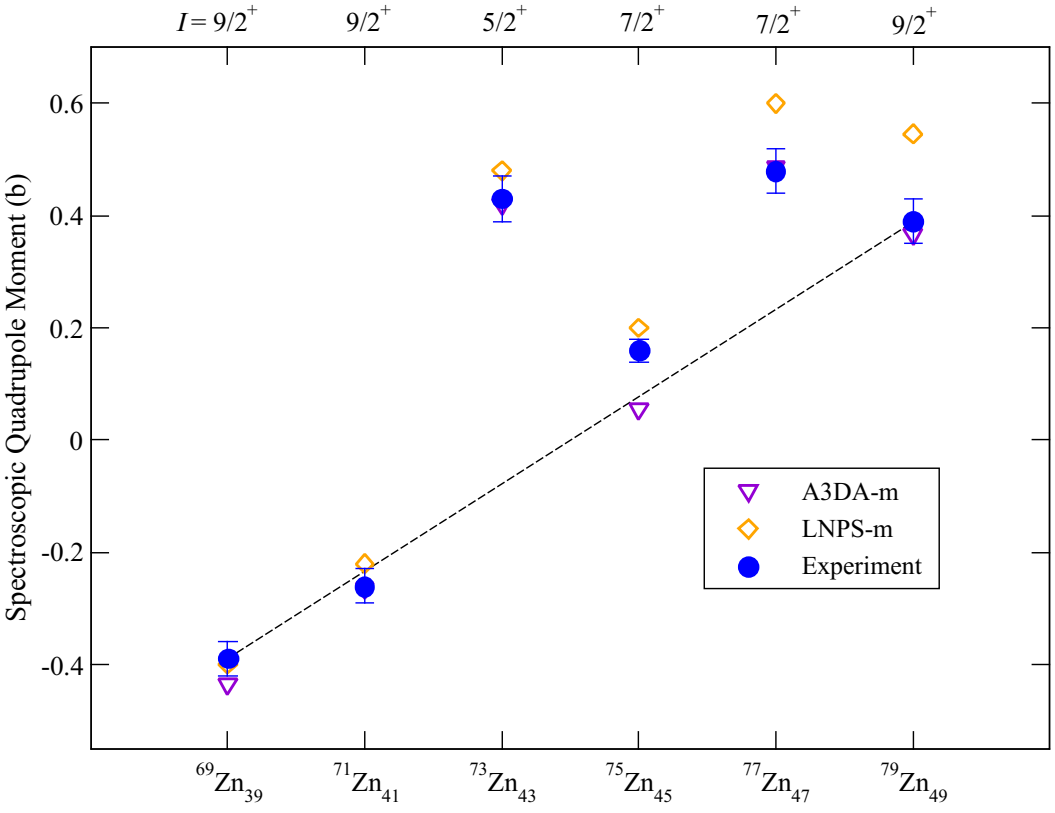

Figure 6.11: Spectroscopic quadrupole moments, Q_{s}, of $^{69-79}$Zn measured in this work compared to predictions from the A3DA-m and LNPS-m shell model interactions.

this orbital across $Z = 28$. Therefore, the onset of collectivity beyond $N = 40$ in Zn is attributed to the influence of $E2$ excitations from $\nu g_{9/2}$ to $\nu d_{5/2}$. Results from Ref. [30] also support this, where the removal of $\nu d_{5/2}$ from the A3DA model space leads to a deviation between measured Q_{s} values in neutron-rich Cu ($Z = 29$) isotopes and A3DA estimates.

6.4 PFSDG-U Interaction

6.4.1 Model Space and Parameters

The shell-model interactions used thus far have been unable to reproduce the magnetic dipole moment of the isomeric state in ^{79}Zn, and as such the f_5pg_9 and pfg_9d_5 model spaces are deemed inadequate for characterising the isomer. Based on the tentatively assigned spin of $1/2^+$ and its proximity to the effective SP g-factor of a $\nu s_{1/2}$ orbit, the wave function is expected to have a strong contribution from an unpaired neutron in the nearest $s_{1/2}$ orbit, which in this instance is $\nu 3s_{1/2}$ across the $N = 50$ shell closure. As such, a new interaction and model space are required to characterise this state. The PFSDG-U shell-model interaction [28] has been developed in-line with this work, and is therefore used to further investigate the nature of ^{79m}Zn. The model space utilises a full pf-shell for protons and a full sdg-shell for neutrons, as shown in Figure 6.12, allowing both the $Z = 28$ and $N = 50$ shell closures to be probed simultaneously in neutron-rich isotopes. The inclusion of all spin-orbit partners within both the proton and neutron valence spaces mean that free g-factors are used for the calculation of the magnetic dipole moments. The quadrupole moments are calculated with the effective nucleon charges $e_{\mathrm{p}}^{\mathrm{eff}} = 1.31e$ and $e_{\mathrm{n}}^{\mathrm{eff}} = 0.46e$, as for LNPS-m and A3DA-m.

The original motivation for the creation of the PFSDG-U interaction was to investigate the possible existence of a new island of inversion (IOI) at $N = 50$. Neutron-rich regions of the nuclear chart have proved to be fruitful in such investigations due to the development of shape coexistence near semi-magic and doubly magic nuclei. Here, deformed intruder bands appear at lower energies than spherical ones [28]. Previous theoretical work by the group behind this interaction signalled towards an IOI around $N = 40$ through the LNPS

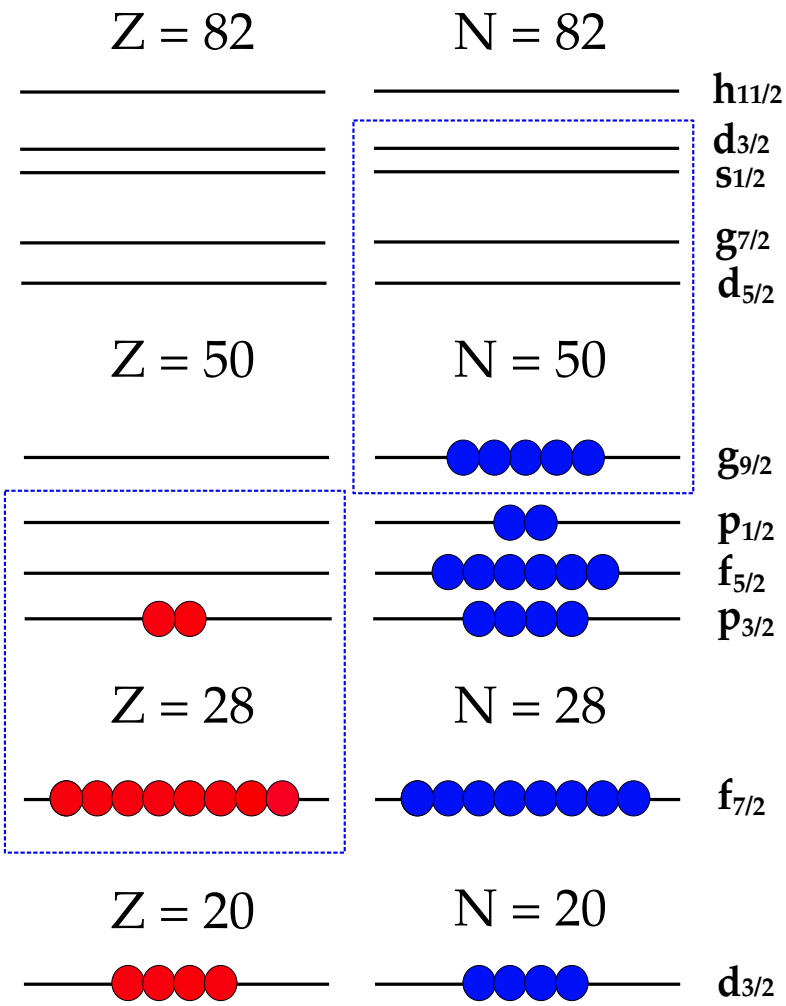

Figure 6.12: The nucleon configuration of ^{75}Zn with the model space of the PFSDG-U interaction. The valence space consists of a full pf-shell for protons and sdg-shell for neutrons on top of a virtual ^{60}Ca core.

interaction. $N = 50$ was suggested as the next such IOI, in an analogy to the case of IOIs $N = 20$ and $N = 28$ [107], although the LNPS model space is insufficient for such work. The proton pf and neutron sdg valence spaces adopted in PFSDG-U allow the interaction to probe level systematics in nuclei across the $Z = 28$ and $N = 50$ shell gaps. β-delayed conversion spectroscopy of ^{80}Ge [108] has provided some of the first experimental evidence of shape coexistence around $N = 50$. More recently, the occupation numbers of ^{78,79}Cu ($N = 49, 50$) predicted by PFSDG-U indicate a reduction in cross $Z = 28$ and $N = 50$

excitations, while exhibiting an excellent agreement with the measured moments in neutron-rich Cu isotopes [30]. The application of the PFSDG-U interaction to this study, and more specifically ^{79}Zn, will shed further light on the nature of the $Z = 28$ and $N = 50$ shell gaps in this region, and hence the potentially doubly magic nature of the neutron-rich nucleus ^{78}Ni.

The PFSDG-U model space places limitations on which Zn isotopes the interaction can be applied to without compromising the validity of its predictions. As neutron number decreases from $N = 50$ to $N = 40$, the role of orbitals in the neutron pf-shell (namely $\nu p_{1/2}$) begin to take over from the orbits in the *sdg*-shell, with the crossover point being located at $N \sim 46$ [28], hence rendering the neutron valence space ineffective for Zn isotopes with $N < 46$. Additionally, due to the $1/2^-$ isomeric state in ^{77}Zn formed by a single neutron in the $p_{1/2}$ orbital below the *sdg*-space, the application of PFSDG-U is limited to low-lying states in just one odd-A Zn isotope measured in this work, ^{79}Zn ($N = 49$). The PFSDG-U calculations given in this work have been performed by F. Nowacki.

6.4.2 Energy Level Systematics in $N = 49$ Isotones

In the region of nuclear shell gaps, the relative spacing of energy levels can provide an indication of gap stability as nucleon number varies. For the two sets of interactions discussed previously, energy level systematics have been shown in terms of increasing neutron number as the Zn isotope chain is crossed. The specialist nature of the PFSDG-U interaction in the Zn chain restricts its application to ^{79}Zn, and so its predictions for low-lying level energies will be compared the measured values of the even Z, $N = 49$ isotones $^{77}_{28}$Ni, $^{79}_{30}$Zn [19], $^{81}_{32}$Ge, $^{83}_{34}$Se and $^{85}_{36}$Kr (others adapted from Refs. [109, 110]). The experimental and predicted level energies shown in Figure 6.13 are the lowest-lying $9/2^+$, $1/2^+$ and $5/2^+$ states, representing the ground state and positive-parity intruder states in these isotopes.

The assignment of $9/2^+$ to the ground state of each isotope is correctly reproduced by the PFSDG-U interaction, as would be expected in a non-interacting shell-model picture with a single neutron hole in $g_{9/2}$. This has yet to be determined for $^{77}_{28}$Ni, although this is strongly expected to be the case for its ground state too since it has no protons beyond the $Z = 28$

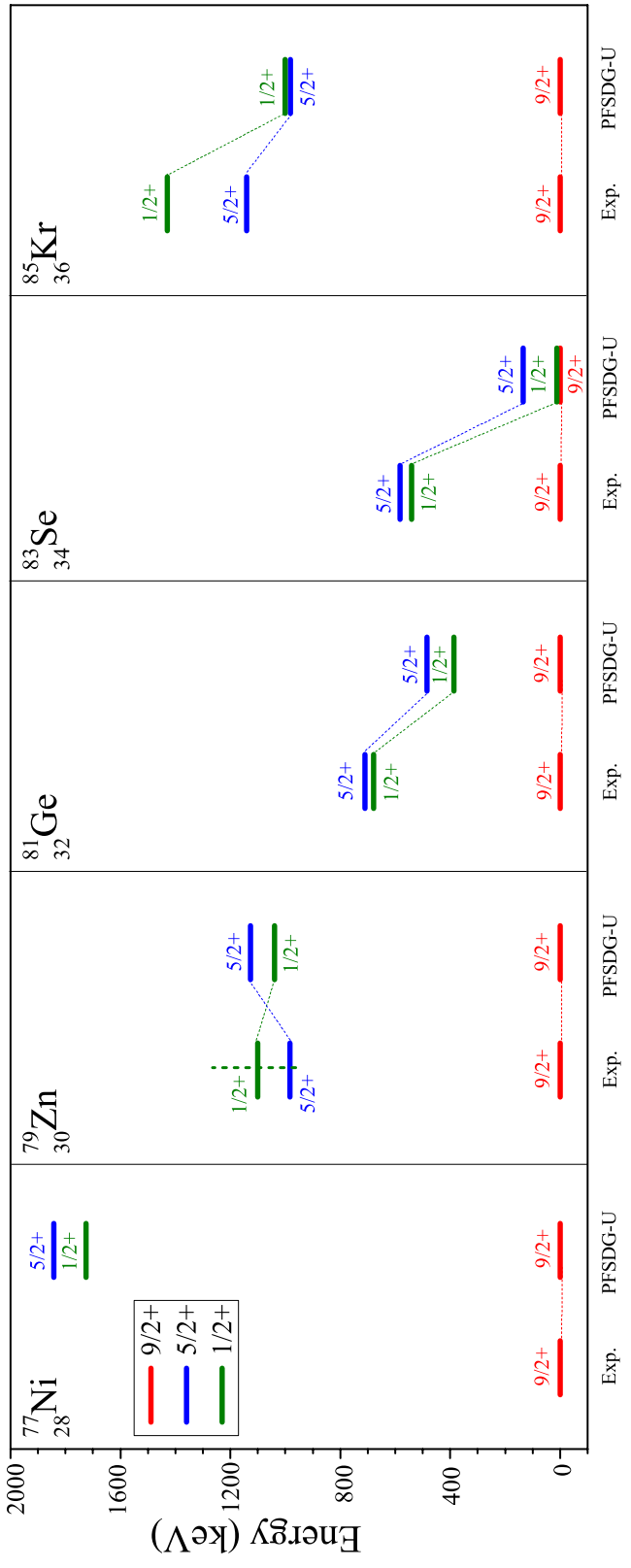

Figure 6.13: Measured low energy spectra of $N = 49$ isotones are compared to predictions from the PFSDG-U shell-model interaction (values for ^{79}Zn from [19], other isotopes adapted from [109, 110]). Dotted lines represent the change in energy for low-lying states while the vertical dashed line at ^{79}Zn shows the error on the measured energy.

shell closure and 49 neutrons.

For ^{79}Zn, the energies of the $1/2^+$ and $5/2^+$ intruder states predicted by PFSDG-U (1.040 and 1.127 MeV, respectively) are in good agreement with the measured energies (1.10(15) and 0.983 MeV respectively). While the ordering of the levels appears to be incorrect, the large uncertainty on the $1/2^+$ state energy means it could be lower than that of the $5/2^+$ state and therefore be in agreement with the ordering measured in $^{81}_{32}$Ge, $^{83}_{34}$Se and also the ordering predicted by the interaction. As proton number increases away from Zn an increase in the deviation between PFSDG-U energies and experiment is noted, with the predicted energies systematically underestimating those measured by $200 - 500$ keV. The exact reason for this is currently unknown, and so requires further investigation to be explained.

For the lightest isotope shown in 6.13, $^{77}_{28}$Ni, the $1/2^+$ and $5/2^+$ intruder levels are predicted at energies approaching 2 MeV. This energy is indicative of a rather good doubly magic nature in ^{78}Ni, with the PFSDG-U interaction predicting the first 2p-2h intruder state in ^{78}Ni at 3 MeV [28]. Contrary to this conclusion, the increase of the $1/2^+$ and $5/2^+$ intruder level energies from a minimum at $^{83}_{34}$Se to ~ 1 MeV in $^{79}_{30}$Zn is rather slow compared to the increase from the minimum to $^{85}_{36}$Kr, and thus questions the suggested doubly magic nature of ^{78}Ni. Experimental measurements of $1/2^+$ and $5/2^+$ in $^{77}_{28}$Ni are therefore needed in order to clarify the energy increase of these intruder levels towards $Z = 28$, and hence the suitability of the PFSDG-U interaction for neutron-rich even-Z nuclei close to $Z = 28$.

6.4.3 Magnetic Dipole Moment of ^{79g,m}Zn

PFSDG-U predictions for the magnetic dipole moments μ of the $9/2^+$, $1/2^+$ and $5/2^+$ states in ^{79}Zn and its isotone ^{81}Ge are given in Table 6.5. The PFSDG-U g-factors for the $9/2^+$ ground state and $1/2^+$ isomer in ^{79}Zn are compared to those of the A3DA-m and LNPS-m interactions and experiment in Figure 6.14. Predictions from the PFSDG-U interaction are given in two forms, one with free g-factors (labelled "bare") and the other with spin quenched g-factors ($0.75g_{\text{free}}$).

Firstly, the PFSDG-U interaction predictions show an excellent agreement with the $9/2^+$

Table 6.5: Calculated magnetic dipole moments μ for low-lying states in ^{79}Zn and ^{81}Ge from the PFSDG-U interaction.

^{A}Z	I^{π}	$\mu_{\rm expt}(\mu_N)$	$\mu_{\rm bare}/\mu_{\rm quenched}(\mu_N)$
^{79}Zn	$9/2^+$	-1.1866	$-1.03/-1.10$
	$5/2^+$	—	$-0.84/-0.67$
	$1/2^+$	-1.018	$-1.14/-0.91$
^{81}Ge	$9/2^+$	—	$-0.90/-0.95$
	$5/2^+$	—	$-0.77/-0.61$
	$1/2^+$	—	$-1.15/-0.94$

ground state in ^{79}Zn. The interaction shows good agreement with the experimental g-factor ($g_{\rm expt} = -0.264$) for both the bare and effective g-factors ($g_{\rm bare}/g_{\rm eff} = -0.229/-0.244$). The single neutron hole configuration in $g_{9/2}$, $(\nu g_{9/2})^{-1}$, leads the wave function with >60% of all contributions, although its g-factor deviates from experiment more than JUN45 and jj44b ($g_{\rm JUN45}/g_{\rm jj44b} = -0.263/-0.261$). This, coupled with the fact that the JUN45 and

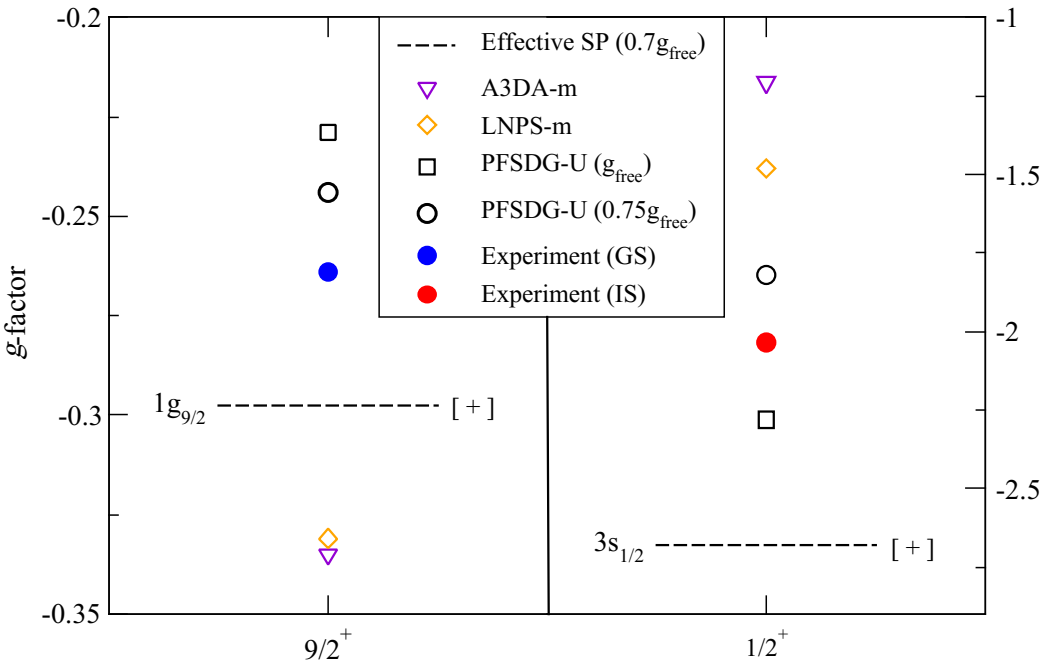

Figure 6.14: Experimental g-factors of the $9/2^+$ ground and isomeric $1/2^+$ states of ^{79}Zn in comparison to single-particle estimates and predictions from the A3DA-m, LNPS-m and PFSDG-U interactions.

jj44b interactions both predict >95% ground state wave function contribution from $(\nu g_{9/2})^{-1}$ configurations in ^{79}Zn, once again points to the stability of the $N = 50$ shell closure in neutron-rich nuclei.

The $1/2^+$ isomeric state in ^{79}Zn is quite clearly reproduced more accurately by the PFSDG-U interaction than any of the other interactions. The predictions with bare and effective g-factors ($g_{\text{bare}}/g_{\text{eff}} = -2.28/-1.82$) appear to be roughly equidistant from the measured value of $g_{\text{expt}} = -2.036$, while also approaching the effective SP g-factor of $\nu s_{1/2}$. The single unpaired neutron in the isomer is expected to occupy the $\nu 3s_{1/2}$ orbital based on its spin-parity. These results exhibit a clear improvement over those from the LNPS-m and A3DA-m interactions, as shown in Figure 6.14, due to the extension of the neutron valence space to account for the full *sdg*-shell. The occupation of neutron orbits in the *sdg*-shell for the isomeric state are compared to the occupancy of the ground state in Figure 6.15, where

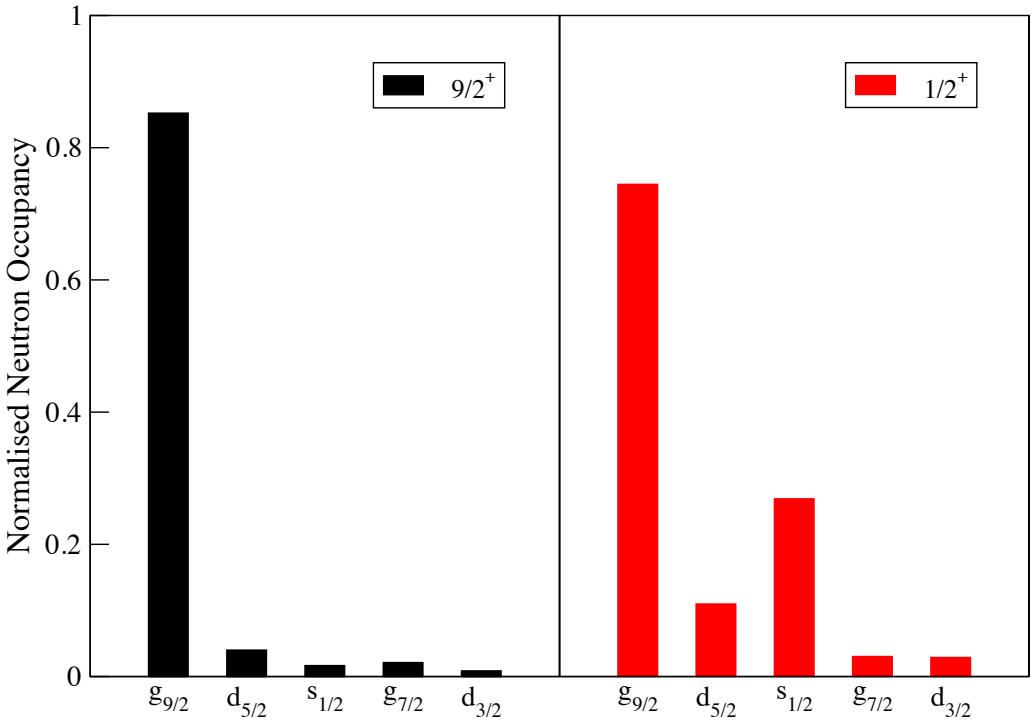

Figure 6.15: Normalised neutron occupancies for orbitals in the *sdg*-shell for the ground and isomeric states in ^{79}Zn as predicted by the PFSDG-U interaction. Occupancies are normalised to the maximum number of neutrons in the orbital.

they are normalised to the maximum number of nucleons in each orbital. A clear increase in the occupation of all orbits beyond $N = 50$ is observed in the $1/2^+$ isomeric state, with larger increases seen in the $\nu d_{5/2}$ and $\nu s_{1/2}$ orbits relative to the others. The deviation from the effective SP value of $\nu s_{1/2}$ seen in Figure 6.14 is expected to be induced by some mixing of $(\nu s_{1/2})^1$ and $(\nu d_{5/2})^1$ led configurations, an argument that is supported by the predicted increase in the occupancy of these two states for the isomer. The PFSDG-U wave function confirms this, with $\nu(1g_{9/2}^{-2}3s_{1/2}^1)$ and $\nu(1g_{9/2}^{-2}2d_{5/2}^1)$ configurations forming ≈30% and ≈20% of the isomeric wave function, respectively. This result confirms the mixed 1p-2h intruder nature of the isomeric state.

6.4.4 Spectroscopic Quadrupole Moment of ^{79}Zn

The quadrupole moment prediction for the $9/2^+$ ground state in ^{79}Zn is shown in Table 6.2. The model spaces outlined in previous sections have proved to be sufficient for reproducing the measured quadrupole moment of ^{79}Zn, with all interactions other than LNPS-m showing a good agreement with experiment. The different model space in PFSDG-U means its prediction can highlight the importance of excitations to the *sdg*-shell in characterising the nuclear shape.

The PFSDG-U prediction for the quadrupole moment of ^{79}Zn ($Q_\mathrm{s} = +0.42$) lies within errors of the value measured in this work (+0.40(4)), in fact exhibiting a marginal improvement

Table 6.6: Calculated energies (MeV) and quadrupole moments Q_s for low-lying levels in ^{79}Zn and ^{81}Ge from the PFSDG-U interaction.

^AZ	I^π	$Q_{\mathrm{s,expt}}$(b)	Q_s(b)
^{79}Zn	$9/2^+$	+0.40(4)	+0.42
	$5/2^+$	—	−0.36
	$1/2^+$	—	—
^{81}Ge	$9/2^+$	—	+0.60
	$5/2^+$	—	−0.41
	$1/2^+$	—	—

over the JUN45, jj44b and A3DA-m predictions (+0.356, +0.371 and +0.367, respectively). While there is no change noted in the occupancy of $\nu d_{5/2}$, the influential orbital in describing quadrupole deformation in this region, between A3DA-m and PFSDG-U, a small decrease is observed in the occupancy of $\nu g_{9/2}$ in PFSDG-U compared to all interactions. This is offset by an increase in the neutron $s_{1/2}$, $d_{3/2}$ and $g_{7/2}$ orbits, which could account for the accuracy of the PFSDG-U prediction for Q_{s} in ^{79}Zn. In order to further test the suitability of PFSDG-U for determining the nuclear deformation of neutron-rich isotopes around $N = 50$, further quadrupole moment measurements of odd-A nuclei in this region, including heavier Zn isotopes and ^{81}Ge (isobar of ^{79}Zn) are required.

Chapter 7

Conclusion

In this work, collinear laser spectroscopy has been used to obtain the nuclear spins and electromagnetic moments of odd-A Zn isotopes from $^{63-79}$Zn ($N = 33-49$) via their hyperfine structure. Zn isotopes were produced at ISOLDE, CERN, and delivered to the COLLAPS beam line in ion bunches by the ISCOOL ion cooler and buncher. The temporal coordination of ion bunches and photon gating on PMTs in the detection region reduced background contributions by a factor of $\sim 4 \times 10^4$. This greatly improved the clarity of the hyperfine spectra and allowed the measurement of exotic isotopes and relatively short-lived isomeric states. The 4s4p $^3P_2^o \rightarrow$ 4s5s $^3S_1$ atomic transition was selected for Zn. The 4s4p $^3P_J^o$ triplet is populated by quasi-resonant charge exchange with Na atoms in the CEC, with the $J = 2$ level selected in part due to its greater sensitivity to the nuclear spin I than the $J = 0, 1$ levels.

Using the χ^2-minimisation process, a hyperfine structure was fitted to experimental spectra in order to determine the nuclear spin, as well as the hyperfine A and B coefficients. The hyperfine coefficients were used to calculated the magnetic dipole moments μ and spectroscopic quadrupole moments Q_s of Zn isotopes. This was achieved by using a reference isotope, ^{67}Zn, to calibrate the moments across the isotope chain. In this work, the reference values of $A(^3P_2) = +531.987(5)$ MHz [89] and $\mu = +0.875479(9)\mu_N$ [14] were used to calculate the magnetic dipole moments, while $B(^3P_2) = +35.806(5)$ MHz [89] and $Q_s = +0.122(10)$ b [94]

were used for the spectroscopic quadrupole moments. The ground and isomeric state nuclear spins I of the neutron-rich nuclei $^{73-79}$Zn were unambiguously confirmed in this work, and the electromagnetic moments of the same nuclei were measured for the first time. The moments of $^{63-71}$Zn were determined in earlier studies, although these results have since updated the values for these isotopes given in literature [14]. All nuclear spins and electromagnetic moments determined in this work have now been published in *Phys. Lett. B* [111].

The nuclear properties of Zn isotopes are compared to a number of large-scale shell model interactions with different model spaces. The JUN45 and jj44b interactions both adopt the f_5pg_9 model space, and hence do not consider excitations across the $N, Z = 28, 50$ shell closures, although they differ somewhat in their construction. However, the A3DA-m and LNPS-m interactions extend beyond the f_5pg_9 model space to include $\pi f_{7/2}$ (immediately below $Z = 28$) and $\nu d_{5/2}$ (immediately after $N = 50$). The comparison of our results to the predictions of these sets of interactions therefore provided an opportunity to probe the influence of the $\pi f_{7/2}$ and $\nu d_{5/2}$ orbits across the Zn isotope chain, and also the stability of the $Z = 28$ and $N = 50$ shell closures as N changes.

The magnetic dipole moments (g-factors) of ground and isomeric states in Zn are generally reproduced well by all the large-scale shell model interactions used in this thesis. However, the exclusion of cross $Z = 28$ and $N = 50$ excitations in the JUN45 model space means the interaction reproduces the observed trend more accurately than the A3DA-m and LNPS-m interactions. This is most notable for the high-spin states as $N = 50$ is approached. Here, g-factors predicted by the JUN45 and jj44b interactions gradually converge towards measured g-factors, with their predictions for ^{79}Zn ($> 95\%$ w.f. contribution from $(\nu g_{9/2})^{-1}$, $g_{\mathrm{JUN45/jj44b}} = -0.263/-0.261$) almost identical to the measured value ($g_{\mathrm{expt}} = -0.264$). Conversely the A3DA-m and LNPS-m predictions for the same states gradually diverge from measured values, with the difference largest at ^{79}Zn ($g_{\mathrm{A3DA-m/LNPS-m}} = -0.335/-0.331$) where the A3DA-m interaction predicts a non-zero occupation of $\nu d_{5/2}$. All these factors strongly point to the persistence of the $N = 50$ shell closure in neutron-rich nuclei, and therefore provide evidence for the doubly magic nature of ^{78}Ni.

Due to its accuracy for magnetic dipole moments, occupation numbers from the JUN45 interaction are used to investigate level systematics of high-spin states more closely. For the anomalous isomeric state spin of $5/2^+$ in ^{73}Zn, kinks are observed in the neutron occupancies of the $f_{5/2}$, $p_{1/2}$ and $g_{9/2}$ orbitals, and also in the $p_{3/2}$, $f_{5/2}$ and $p_{1/2}$ proton orbitals. At the same point, a large dip from the otherwise linear g-factor trend of high-spin states in also seen. This is representative of configuration mixing, and is confirmed by the JUN45 wave function in which no single configuration contributes more than 10% to the total wave function. Proton occupation numbers also reveal a reordering of the $\pi f_{5/2}$ and $\pi p_{3/2}$ orbitals, which occurs as $\nu g_{9/2}$ is filled due to the tensor interaction. In Zn, JUN45 places the point of inversion between ^{75}Zn$_{45}$ and ^{77}Zn$_{47}$ (it is worth noting this is also predicted by A3DA-m). This is in agreement with the results seen in the neighbouring elements Cu ($Z = 29$) and Ga ($Z = 31$), where the inversion is seen as a ground state spin change from $3/2^-$ to $5/2^-$ between $N = 44 - 46$ and $N = 48 - 50$, respectively. The Z-dependence of this effect is therefore pinpointed for the isotopes beyond $Z = 28$, with future measurements of Ge extending this range further.

The quadrupole moments of Zn isotopes (with $I \geq 1/2$) have been determined across the isotope chain. The high-spin states from $^{69-79}$Zn represent isotopes formed by odd-particle configurations in $\nu g_{9/2}$, and are of particular interest here. The quadrupole moments across this range are reproduced most accurately by the A3DA-m interaction. The improvement of A3DA-m over the JUN45 and jj44b interactions is most obvious around the mid-point of the $\nu g_{9/2}$ subshell, where a sudden change from a small oblate deformation ($Q_\mathrm{s} = -0.32(6)$ b) in ^{71m}Zn ($N = 41$) to a large prolate deformation ($Q_\mathrm{s} = +0.52(6)$ b) in ^{73m}Zn ($N = 43$) is observed. Such a large and sudden change in nuclear shape is indicative of an onset of collectivity. An increase in the occupation of the $\nu d_{5/2}$ orbital is predicted by A3DA-m, which, coupled with the lack of $\nu d_{5/2}$ in the f_5pg_9 model space, confirms the strong influence of this orbital in this region for characterising quadrupole collectivity.

Quadrupole moments are also used to investigate the presence of multi-particle configurations. From $N = 39-49$, the $9/2^+$ states of ^{69m,71m,79g}Zn follow the linear trend of quadrupole

moments for a SP in $\nu g_{9/2}$ that starts at Q_{particle} and ends at Q_{hole}, i.e. seniority-1 $(\nu g_{9/2})^1_{9/2^+}$ states. However the $5/2^+$ isomer in ^{73}Zn and the $7/2^+$ ground state of ^{75,77}Zn deviate from this trend, as is expected based on their anomalous spins. The ground state of ^{75,77}Zn instead show a good agreement with the expected quadrupole moments for seniority-3 $(\nu g_{9/2})^3_{7/2^+}$ states (calculated from Q_{particle}), meaning they are formed by three neutrons in $\nu g_{9/2}$ coupled to $I^\pi = 7/2^+$. For ^{73}Zn, the expected value of a seniority-3 $(\nu g_{9/2})^3_{5/2^+}$ state ($Q \approx 0$) drastically underestimates the measured moment of the $5/2^+$ isomer ($Q_{\text{s}} = +0.52(6)$ b). This is interpreted as substantial deformation in the isomer ($\beta_2 = +0.236$) and also as further evidence of mid-subshell collectivity. These results for Zn tie into previous investigations into collectivity in this region, including $B(E2)$ values of Ni ($Z = 28$), Zn ($Z = 30$) and Ge ($Z = 32$), as well as quadrupole moments of Cu ($Z = 29$) and Ga ($Z = 31$). This leads to the overall conclusion that Zn lies within a transitional region of nuclear structure from spherical Ni nuclei to deformed Ge nuclei.

In short, it has been shown that collectivity measured beyond $N = 40$ is best described by the A3DA-m interaction due to cross-shell excitations from $\nu g_{9/2}$ to $\nu d_{5/2}$. The latter orbital is included in the model space of A3DA-m, but not in the f_5pg_9 model space used in JUN45 and jj44b. However, as $N = 50$ is approached, the JUN45 interaction best reproduces the trend of the measured moments, thus suggesting that the magicity of ^{78}Ni is restored. This is in agreement with the results from collinear laser spectroscopy of $^{73-79}$Cu ($Z = 29$) [30]. Here the excellent agreement of measured magnetic dipole moments with A3DA-m and PFSDG-U predictions coupled with the sudden drop in occupation of the $\nu 1f_{7/2}$ and $\nu 1d_{5/2}$ orbitals in ^{78,79}Cu points to the restoration of $Z = 28$ and $N = 50$ shell closures only one proton away from ^{78}Ni.

The hyperfine structure of the newly discovered isomeric state in ^{79}Zn has been measured for the first time in this work. As a result, the spin-parity of the state has now been confirmed as $I^\pi = 1/2^+$. This spin-parity strongly suggests the isomer is formed by an np-mh excitation across the $N = 50$ shell closure. The g-factor of ^{79m}Zn ($g_{\text{expt}} = -2.036$) is not close to the effective SP g-factor of any orbital within the previously available model spaces, meaning the

JUN45, jj44b, A3DA-m and LNPS-m are all insufficient for describing this state. Instead the measured g-factor is closest to the effective SP g-factor of $\nu s_{1/2}$ ($g_{\text{eff}}(\nu s_{1/2}) = -2.678$), the spin-parity of which is in agreement with that measured. In order to understand the nature of this isomer, an interaction that extends beyond the model spaces of the aforementioned interactions was required. The newly developed PFSDG-U interaction was therefore utilised, and considers a full pf-shell for protons and a full sdg-shell for protons. The PFSDG-U predictions for ^{79m}Zn with effective and bare g-factors ($g_{\text{bare}}/g_{\text{eff}} = -2.28/-1.82$) are in good agreement with the experimental value $g_{\text{expt}} = -2.036$, and exhibit a clear improvement over the A3DA-m and LNPS-m interactions ($g_{\text{A3DA-m/LNPS-m}} = -1.21/-1.48$). The PFSDG-U occupancy of the $\nu 3s_{1/2}$ and $\nu 2d_{5/2}$ orbitals show a sharp increase from the $9/2^+$ ground state to the $1/2^+$ isomer. This corresponds to an isomeric wave function with ≈30% and ≈20% contributions from $\nu(1g_{9/2}^{-2}3s_{1/2}^{1})$ and $\nu(1g_{9/2}^{-2}2d_{5/2}^{1})$ configurations, respectively. The notable contribution from an unpaired neutron in $\nu 2d_{5/2}$ to the wave function explains why the measured g-factor deviates from the effective SP value of $\nu s_{1/2}$. Therefore the $1/2^+$ isomer in ^{79}Zn is confirmed to be a rather mixed 1p-2h intruder state.

The $1/2^+$ isomeric state in ^{79}Zn has also been the subject of a *Phys. Rev. Lett.* publication [112] based on this work. By studying the isomer shift, it was determined that the mean square charge radius of the intruder isomer is much larger than that of the ground state due to an increase in deformation (moments are not sensitive to the deformation of $I = 1/2$ states). This result is interpreted as one of the first signatures of shape coexistence in the region around ^{78}Ni, with Ref. [108] providing evidence of shape coexistence in ^{80}Ge ($Z = 32$) around the same time. These results challenge the magicity of ^{78}Ni, although more measurements in this region are required in order to support this conclusion.

The PFSDG-U interaction is also used to predict the energy of the lowest-lying $9/2^+$, $1/2^+$ and $5/2^+$ levels in ^{79}Zn and its isotones $^{77}_{28}$Ni (energies of $1/2^+$ and $5/2^+$ not measured yet), $^{81}_{32}$Ge, $^{83}_{34}$Se and $^{85}_{36}$Kr. The experimental energies of the $1/2^+$ and $5/2^+$ intruder levels in ^{79}Zn (1.10(15) and 0.983 MeV, respectively [19]) are in good agreement with the predicted energies (1.040 and 1.127 MeV), although, while the ordering is different, the error on the

$1/2^+$ level means it could in fact be lower than the $5/2^+$. In the heavier isotones, the PFSDG-U predictions are consistently $200-500$ MeV lower than the measured energies of the intruder states. This systematic deviation requires further investigation. For ^{77}Ni, the intruder levels are predicted to approach ≈ 2 MeV, which suggests a rather good doubly magic nature in ^{78}Ni. However, the rise in intruder level energy from its measured minimum in $^{83}_{34}$Se to $^{85}_{36}$Kr is quicker than the rise from the minimum to ~ 1 MeV in ^{79}Zn. While this result may question the doubly magic nature of ^{78}Ni, the evidence presented thus far has more strongly pointed to the contrary. Regardless, measurements of the $1/2^+$ and $5/2^+$ level energies in ^{77}Ni would help to clarify the stability of the $Z = 28$ and $N = 50$ shell gaps in neutron-rich nuclei.

7.1 Recommendations for Future Work

The results obtained for Zn in this work could be supported by the further studies of nearby isotopes and elements. The two neighbouring even-Z elements, Ni ($Z = 28$) and Ge ($Z = 32$), are obvious candidates for future collinear laser spectroscopy studies. By comparing the Zn results in this work to the spins, electromagnetic moments and mean square charge-radii of odd-A Ni and Ge isotopes, the evolution of nuclear structure as we move away from the $Z = 28$ shell closure can be understood. By extending the measured range to neutron-rich nuclei, we can probe the stability of the $Z = 28$ and $N = 50$ shell closures as N increases more thoroughly, and hence strengthen our conclusion regarding the doubly magic nature of ^{78}Ni. Recent COLLAPS experiments have measured the nuclear properties of Ni [113] and Ge [114] around $N = 40$, while a proposal for laser spectroscopy of neutron-rich Ge has also been submitted [115].

While our results generally support the doubly magic nature of the neutron-rich nucleus ^{78}Ni, more experimental measurements in the region are required in order to reach a more well-informed conclusion. Recent measurements of ^{78,79}Cu ($Z = 29$) [30] have highlighted the magicity of the $Z = 28$ and $N = 50$ shell closures only one proton away from ^{78}Ni. However, β-delayed conversion spectroscopy of ^{80}Ge ($Z = 32$) [108] points to the presence of shape

coexistence in neutron-rich nuclei that corresponds to a reduction of the $N = 50$ shell gap. This result is also observed in the low-lying states of ^{79}Zn [112]. In order to further probe the existence of shape coexistence close to ^{78}Ni, measurement of the $1/2^+$ isomeric state in ^{81}Ge and the low-lying level properties in ^{77}Ni are required. The authors of Ref. [108] acknowledge the lack of mass measurements in this region as an issue that prevents the precise assessment of the $N = 50$ shell gap. Thus it is hard to reach a concrete conclusion regarding the magicity of ^{78}Ni at this time. Continued experimental and theoretical efforts in the neutron-rich region close to $Z = 28$ and $N = 50$ are therefore strongly encouraged.

Bibliography

[1] J. J. Thomson. XL. Cathode Rays. *Philos. Mag.*, 44(269):293–316, 1897.

[2] J. J. Thomson. XXIV. On the structure of the atom: an investigation of the stability and periods of oscillation of a number of corpuscles arranged at equal intervals around the circumference of a circle; with application of the results to the theory of atomic structure. *Philos. Mag.*, 7(39):237–265, 1904.

[3] H. Geiger and E. Marsden. On a diffuse reflection of the α-particles. *Proc. Roy. Soc.*

[4] N. Bohr. I. On the constitution of atoms and molecules. *Philos. Mag.*, 26(151):1–25, 1913.

[5] M. Orme. XXIV. The constitution of atoms. *Philos. Mag.*, 41(242):281–285, 1921.

[6] J. Chadwick. Possible Existence of a Neutron. *Nature*, 129:312, feb 1932.

[7] J. Franck and G. Hertz. On the collisions between electrons and molecules of mercury vapor and the ionization potential of the same. *Verhandlungen der Deutschen Physikalischen Gesellschaft*, 16:457–467, 1914.

[8] J. Franck and G. Hertz. On the excitation of mercury resonance lines at 253.6 nm by electron collisions. *Verhandlungen der Deutschen Physikalischen Gesellschaft*, 16:512–517, 1914.

[9] R. S. Shankland. Michelson and his interferometer. *Phys. Tod.*, 27:37–43, April 1974.

[10] W. Pauli. Zur Frage der theoretischen Deutung der Satelliten einiger Spektrallinien und ihrer Beeinflussung durch magnetische Felder. *Naturwiss.*, 12:741–743, sep 1924.

[11] E. Fermi. Über die magnetischen Momente der Atomkerne. *Z. Phys.*, 60(5):320–333, May 1930.

[12] E. Mané et al. An ion cooler-buncher for high-sensitivity collinear laser spectroscopy at ISOLDE. *Eur. Phys. J. A*, 42(3):503–507, Dec 2009.

[13] B. Cheal and K. T. Flanagan. Progress in laser spectroscopy at radioactive ion beam facilities. *J. Phys. G*, 37(11):113101, 2010.

[14] N. J. Stone. *INDC International Nuclear Data Committee*, 0658, 2014.

[15] M. Huhta, P. F. Mantica, et al. New evidence for deformation in ^{73}Zn. *Phys. Rev. C*, 58:3187–3194, Dec 1998.

[16] B. Ekström, B. Fogelberg, P. Hoff, E. Lund, and A. Sangariyavanish. Decay Properties of $^{75-80}$Zn and $Q_\beta-$values of Neutron-Rich Zn and Ga Isotopes. *Phys. Scr., T*, 34(6A):614, 1986.

[17] S. V. Ilyushkin, J. A. Winger, K. P. Rykaczewski, et al. β studies of the transitional nucleus ^{75}Cu and the structure of ^{75}Zn. *Phys. Rev. C*, 83:014322, Jan 2011.

[18] S. V. Ilyushkin, J. A. Winger, C. J. Gross, et al. β decay of the $\pi f_{5/2}$ ground state of ^{77}Cu studied with 225 MeV and 0.2 MeV purified radioactive beams. *Phys. Rev. C*, 80:054304, Nov 2009.

[19] R. Orlandi, D. Mücher, R. Raabe, et al. Single-neutron orbits near ^{78}Ni : Spectroscopy of the N = 49 isotope ^{79}Zn. *Phys. Lett. B*, 740:298–302, 2015.

[20] M.-G. Porquet and O. Sorlin. Evolution of the $N = 50$ gap from $Z = 30$ to $Z = 38$ and extrapolation toward ^{78}Ni. *Phys. Rev. C*, 85:014307, Jan 2012.

[21] K. Sieja and F. Nowacki. Three-body forces and persistence of spin-orbit shell gaps in medium-mass nuclei: Toward the doubly magic ^{78}Ni. *Phys. Rev. C*, 85:051301, May 2012.

[22] H. Schatz, P. T. Hosmer, et al. The half-life of the doubly-magic r-process nucleus ^{78}Ni. *Eur. Phys. J. A*, 25(1):639–642, Sep 2005.

[23] T. Otsuka, T. Suzuki, et al. Evolution of Nuclear Shells due to the Tensor Force. *Phys. Rev. Lett.*, 95:232502, Nov 2005.

[24] K. T. Flanagan, P. Vingerhoets, et al. Nuclear Spins and Magnetic Moments of ^{71,73,75}Cu: Inversion of $\pi 2p_{3/2}$ and $\pi 1f_{5/2}$ Levels in ^{75}Cu. *Phys. Rev. Lett.*, 103:142501, Oct 2009.

[25] P. Vingerhoets, K. T. Flanagan, et al. Nuclear spins, magnetic moments, and quadrupole moments of Cu isotopes from $N = 28$ to $N = 46$: Probes for core polarization effects. *Phys. Rev. C*, 82(6):064311, 2010.

[26] B. Cheal, E. Mané, et al. Nuclear Spins and Moments of Ga Isotopes Reveal Sudden Structural Changes between $N = 40$ and $N = 50$. *Phys. Rev. Lett.*, 104:252502, Jun 2010.

[27] R. A. Meyer, O. G. Lien, and E. A. Henry. Coexisting intruder bands in ^{83}Se and evidence for the role of proton subshell closure in inhibiting formation of odd-neutron intruder bands. *Phys. Rev. C*, 25:682–685, Jan 1982.

[28] F. Nowacki, A. Poves, E. Caurier, and B. Bounthong. Shape coexistence in ^{78}Ni as the portal to the fifth island of inversion. *Phys. Rev. Lett.*, 117:272501, Dec 2016.

[29] Y. Shiga, K. Yoneda, D. Steppenbeck, et al. Investigating nuclear shell structure in the vicinity of ^{78}Ni: Low-lying excited states in the neutron-rich isotopes ^{80,82}Zn. *Phys. Rev. C*, 93:024320, Feb 2016.

[30] R. P. de Groote et al. Dipole and quadrupole moments of $^{73\text{-}78}$Cu as a test of the robustness of the $Z = 28$ shell closure near ^{78}Ni. *Phys. Rev. C*, 96:041302, Oct 2017.

[31] J. Hakala, S. Rahaman, V.-V. Elomaa, et al. Evolution of the $N = 50$ Shell Gap Energy towards ^{78}Ni. *Phys. Rev. Lett.*, 101:052502, Jul 2008.

[32] P. L. Smith, C. Heise, J. R. Esmond, and R. L. Kurucz. Atomic spectral line database from CD-ROM 23 of R. L. Kurucz., 2017. `https://www.cfa.harvard.edu/amp/ampdata/kurucz23/sekur.html`.

[33] National Institute of Standards and Technology (NIST). Basic Atomic Spectroscopic Data: Periodic Table of Elements. `https://physics.nist.gov/PhysRefData/Handbook/periodictable.htm`.

[34] K. S. Krane. *Introductory Nuclear Physics*. Wiley, 72, 1987.

[35] J. Billowes and Campbell. P. High-resolution laser spectroscopy for the study of nuclear sizes and shapes. *J. Phys. G*, 21(6):707, 1995.

[36] I. Angeli. A consistent set of nuclear rms charge radii: properties of the radius surface R(N,Z). *At. Data Nucl. Data Tables*, 87(2):185 – 206, 2004.

[37] X. F. Yang, Y. Tsunoda, et al. Investigating the large deformation of the $5/2^+$ isomeric state in ^{73}Zn: An indicator for triaxiality. *Phys. Rev. C*, 97:044324, Apr 2018.

[38] M. G. Mayer. On Closed Shells in Nuclei. *Phys. Rev.*, 74:235–239, Aug 1948.

[39] C. E. Moore. *Atomic Energy Levels*. Number v. 1. National Bureau of Standards, 1949.

[40] A. Bohr and B. R. Mottelson. *Nuclear Structure*. Number v. 1 in Nuclear Structure. World Scientific, 1998.

[41] J. H. E. Mattauch, W. Thiele, and A. H. Wapstra. Consistent set of Q-values. *Nuclear Physics*, 67(1):32–72, 1965.

[42] M. Ismail, A. Y. Ellithi, A. Adel, and H. Anwer. On magic numbers for super- and ultraheavy systems and hypothetical spherical double-magic nuclei. *J. Phys. G*, 43(1):015101, 2016.

[43] V. I. Zagrebaev and W. Greiner. Cross sections for the production of superheavy nuclei. *Nucl. Phys. A*, 944:257 – 307, 2015. Special Issue on Superheavy Elements.

[44] M. G. Mayer. Nuclear Configurations in the Spin-Orbit Coupling Model. I. Empirical Evidence. *Phys. Rev.*, 78:16–21, Apr 1950.

[45] M. G. Mayer. Nuclear Configurations in the Spin-Orbit Coupling Model. II. Theoretical Considerations. *Phys. Rev.*, 78:22–23, Apr 1950.

[46] O. Haxel, J. H. D. Jensen, and H. E. Suess. On the Magic Numbers in Nuclear Structure. *Phys. Rev.*, 75:1766–1766, Jun 1949.

[47] S. Bacca. Structure models: From shell model to ab initio methods. *Eur. Phys. J. P*, 131(4):107, Apr 2016.

[48] G. Neyens. Nuclear magnetic and quadrupole moments for nuclear structure research on exotic nuclei. *Rep. Prog. Phys.*, 66(4):633, 2003.

[49] B. F. Bayman and A. Lande. Tables of identical-particle fractional parentage coefficients. *Nucl. Phys.*, 77(1):1 – 80, 1966.

[50] A. de Shalit and I. Talmi. *Nuclear Shell Theory.* Elsevier, 1963.

[51] D. T. Yordanov et al. Spins, electromagnetic moments, and isomers of $^{107-129}$Cd. *Phys. Rev. Lett.*, 110:192501, May 2013.

[52] G. Klotz et al. Beta decay of ^{31,32}Na and ^{31}Mg: Study of the N=20 shell closure. *Phys. Rev. C*, 47:2502–2516, Jun 1993.

[53] O. Tarasov et al. Search for ^{28}O and study of neutron-rich nuclei near the $N = 20$ shell closure. *Phys. Lett. B*, 409(1):64 – 70, 1997.

[54] T. Otsuka, R. Fujimoto, Y. Utsuno, et al. Magic Numbers in Exotic Nuclei and Spin-Isospin Properties of the *NN* Interaction. *Phys. Rev. Lett.*, 87:082502, Aug 2001.

[55] T. Otsuka, Y. Utsuno, R. Fujimoto, et al. Frontiers and challenges of the nuclear shell model. *Eur. Phys. J. A*, 13(1):69–74, Jan 2002.

[56] I. Tanihata, H. Hamagaki, O. Hashimoto, et al. Measurements of Interaction Cross Sections and Nuclear Radii in the Light *p*-Shell Region. *Phys. Rev. Lett.*, 55:2676–2679, Dec 1985.

[57] T. Otsuka. *The Euroschool Lectures on Physics with Exotic Beams, Vol. III, Chapter Shell Structure of Exotic Nuclei.* Lecture Notes in Physics. Springer-Verlag Berlin Heidelberg, 1 edition, 2009.

[58] T. Otsuka. Monte Carlo shell model. *Nucl. Phys. A*, 693(1):383 – 393, 2001. Radioactive Nuclear Beams.

[59] M. Honma, T. Otsuka, T. Mizusaki, and M. Hjorth-Jensen. New effective interaction for f_5pg_9-shell nuclei. *Phys. Rev. C*, 80:064323, Dec 2009.

[60] T. Otsuka, M. Honma, and T. Mizusaki. Structure of the $N = Z = 28$ closed shell studied by monte carlo shell model calculation. *Phys. Rev. Lett.*, 81:1588–1591, Aug 1998.

[61] S. M. Lenzi, F. Nowacki, A. Poves, and K. Sieja. Island of inversion around ^{64}Cr. *Phys. Rev. C*, 82:054301, Nov 2010.

[62] Y. Tsunoda, T. Otsuka, N. Shimizu, M. Honma, and Y. Utsuno. Novel shape evolution in exotic Ni isotopes and configuration-dependent shell structure. *Phys. Rev. C*, 89:031301, Mar 2014.

[63] N. Shimizu, T. Abe, Y. Tsunoda, et al. New Generation of the Monte Carlo Shell Model for the K Computer Era.

[64] B. A. Marsh et al. RILIS applications at CERN/ISOLDE. *Hyperfine Interact.*, 227(1):101–111, Jun 2014.

[65] T. J. Giles et al. The high resolution spectrometer at ISOLDE.

[66] C. Babcock and T. Giles. Upgrade of the radio frequency quadrupole cooler and buncher for the hie-isolde project. *Nucl. Instrum. Methods Phys. Res., Sect. B*, 317:484 – 487, 2013. XVIth International Conference on ElectroMagnetic Isotope Separators and Techniques Related to their Applications, December 27, 2012 at Matsue, Japan.

[67] ISOLDE: The Radioactive Ion Beam Facility. ISOLDE Logos, Layouts and Templates. `http://isolde.web.cern.ch/isolde-logos-layouts-and-templates`.

[68] A. Gottberg. Target materials for exotic ISOL beams. *Nucl. Instrum. Methods Phys. Res., Sect. B*, 376:8 – 15, 2016.

[69] R. Catherall, J. Lettry, S. Gilardoni, and U. Köster. Radioactive ion beams produced by neutron-induced fission at ISOLDE. *Nucl. Instrum. Methods Phys. Res., Sect. B*, 204:235–239, 2003.

[70] A. Gottberg et al. Experimental tests of an advanced proton-to-neutron converter at ISOLDE-CERN. *Nucl. Instrum. Methods Phys. Res., Sect. B*, 336:143 – 148, 2014.

[71] B. A. Marsh et al. The ISOLDE RILIS pump laser upgrade and the LARIS Laboratory. *Hyperfine Interact.*, 196(1):129–141, Feb 2010.

[72] S. Rothe et al. Laser ion beam production at CERN-ISOLDE: New features - More possibilities. *Nucl. Instrum. Methods Phys. Res., Sect. B*, 376:91 – 96, 2016.

[73] E. Kugler et al. The new CERN-ISOLDE on-line mass-separator facility at the PS-Booster. *Nucl. Instrum. Methods Phys. Res., Sect. B*, 70(1):41 – 49, 1992.

[74] A. Jokinen, M. Lindroos, E. Molin, and M. Petersson. RFQ-cooler for low-energy radioactive ions at ISOLDE. *Nucl. Instrum. Methods Phys. Res., Sect. B*, 204:86 – 89, 2003.

[75] W. H. Wing, G. A. Ruff, W. E. Lamb, and J. J. Spezeski. Observation of the Infrared Spectrum of the Hydrogen Molecular Ion HD^+. *Phys. Rev. Lett.*, 36(25):1488, 1976.

[76] S. L. Kaufman. High-resolution laser spectroscopy in fast beams. *Opt. Commun.*, 17(3):309, 1976.

[77] C. J. Foot. *Atomic Physics*. Oxford University Press, 2005.

[78] W. Demtröder. *Laser Spectroscopy: Basic Principles*. Springer, 5 edition, 2013.

[79] J. Papuga, M. L. Bissell, K. Kreim, et al. Shell structure of potassium isotopes deduced from their magnetic moments. *Phys. Rev. C*, 90:034321, Sep 2014.

[80] A. Klose, K. Minamisono, et al. Tests of atomic charge-exchange cells for collinear laser spectroscopy. *Nucl. Instrum. Methods Phys. Res., Sect. A*, 678:114 – 121, 2012.

[81] A. C. Mueller, F. Buchinger, W. Klempt, et al. Spins, moments and charge radii of barium isotopes in the range $^{122-146}$Ba determined by collinear fast-beam laser spectroscopy. *Nucl. Phys. A*, 403(2):234 – 262, 1983.

[82] N. Bendali, H. T. Duong, P. Juncar, J. M. Saint Jalm, and J. L. Vialle. Na^+ -Na charge exchange processes studied by collinear laser spectroscopy. *J. Phys. B*, 19(2):233, 1986.

[83] National Institute of Standards and Technology (NIST). Basic Atomic Spectroscopic Data: Zinc (Zn). `https://physics.nist.gov/PhysRefData/Handbook/Tables/zinctable1.htm`.

[84] National Institute of Standards and Technology (NIST). Basic Atomic Spectroscopic Data: Sodium (Na). `https://physics.nist.gov/PhysRefData/Handbook/Tables/sodiumtable1.htm`.

[85] P. Campbell. *Nuclear Ground State Properties of Stable and Radioactive Isotopes by Ultraviolet Laser Spectroscopy.* PhD Thesis, University of Manchester, 1994.

[86] U. Köster et al. ISOLDE beams of neutron-rich zinc isotopes: yields, release, decay spectroscopy. *AIP Conf. Proc.*, 798(1):315–326, 2005.

[87] L. Xie, X. F. Yang, C. Wraith, et al. to be published. 2018.

[88] G. Racah. Theory of complex spectra. ii. *Phys. Rev.*, 62:438–462, Nov 1942.

[89] A. Lurio. Hyperfine Structure of the ^3P States of Zn^{67} and Mg^{25}. *Phys. Rev.*, 126:1768–1773, Jun 1962.

[90] P. Campbell, J. Billowes, and I. S. Grant. The specific mass shift of the zinc atomic ground state. *J. Phys. B*, 30(10):2351, 1997.

[91] E. Runte et al. Decay studies of neutron-rich isotopes of manganese, iron, cobalt, nickel, copper and zinc. *Nucl. Phys. A*, 441(2):237 – 260, 1985.

[92] V. Vedia, V. Paziy, L. M. Fraile, et al. Search for the ^{73}Ga ground-state doublet splitting in the β decay of ^{73}Zn. *Phys. Rev. C*, 96:034311, Sep 2017.

[93] A. Korgul, K. P. Rykaczewski, J. A. Winger, et al. β-γ and β-delayed neutron-γ decay of neutron-rich copper isotopes. *Phys. Rev. C*, 86:024307, Aug 2012.

[94] J. Bieroń et al. Ab initio calculations of the hyperfine structure of zinc and evaluation of the nuclear quadrupole moment $Q(^{67}\mathrm{Zn})$. *Phys. Rev. A*, 97:062505, Jun 2018.

[95] N. S. Laulainen and M. N. McDermott. Spin and Nuclear Moments of the Zn^{63} Ground State. *Phys. Rev.*, 177:1606–1615, Jan 1969.

[96] M. L. Bissell, T. Carette, K. T. Flanagan, et al. Cu charge radii reveal a weak sub-shell effect at $N = 40$. *Phys. Rev. C*, 93:064318, Jun 2016.

[97] C. Santamaria, C. Louchart, A. Obertelli, et al. Extension of the $N = 40$ Island of Inversion towards $N = 50$: Spectroscopy of ^{66}Cr, ^{70,72}Fe. *Phys. Rev. Lett.*, 115:192501, Nov 2015.

[98] O. Perru, O. Sorlin, S. Franchoo, et al. Enhanced core polarization in ^{70}Ni and ^{74}Zn. *Phys. Rev. Lett.*, 96:232501, Jun 2006.

[99] J. Van de Walle et al. Low-energy coulomb excitation of neutron-rich zinc isotopes. *Phys. Rev. C*, 79:014309, Jan 2009.

[100] N. Aoi, S. Kanno, S. Takeuchi, et al. Enhanced collectivity in ^{74}Ni. *Phys. Lett. B*, 692(5).

[101] C. J. Chiara, W. B. Walters, I. Stefanescu, et al. Seniority, collectivity, and $B(E2)$ enhancement in ^{72}Ni. *Phys. Rev. C*, 84:037304, Sep 2011.

[102] C. Louchart, A. Obertelli, A. Görgen, et al. Collective nature of low-lying excitations in ^{70,72,74}Zn from lifetime measurements using the AGATA spectrometer demonstrator. *Phys. Rev. C*, 87:054302, May 2013.

[103] M. Niikura, B. Mouginot, S. Franchoo, et al. First direct lifetime measurement of the 2_1^+ state in ^{72,74}Zn: New evidence for a shape transition between $N = 40$ and $N = 42$ close to $Z = 28$. *Phys. Rev. C*, 85:054321, May 2012.

[104] M. Bernas et al. Mass and excited levels of the neutron-rich nuclei ^{73}Zn and ^{74}Zn studied with the ^{76}Ge(^{14}C, ^{17}O) and (^{14}C, ^{16}O) reactions. *Nucl. Phys. A*, 413(2):363 – 374, 1984.

[105] S. Leenhardt, O. Sorlin, M.-G. Porquet, et al. Coulomb excitation of $^{72}_{30}$Zn$_{42}$. *Eur. Phys. J. A*, 14, May 2002.

[106] M. Dufour and A. P. Zuker. Realistic collective nuclear Hamiltonian. *Phys. Rev. C*, 54:1641–1660, Oct 1996.

[107] E. Caurier, F. Nowacki, and A. Poves. Merging of the islands of inversion at $N = 20$ and $N = 28$. *Phys. Rev. C*, 90:014302, Jul 2014.

[108] A. Gottardo, D. Verney, C. Delafosse, et al. First Evidence of Shape Coexistence in the ^{78}Ni Region: Intruder 0_2^+ State in ^{80}Ge. *Phys. Rev. Lett.*, 116:182501, May 2016.

[109] P. Hoff and B. Fogelberg. Properties of strongly neutron-rich isotopes of germanium and arsenic. *Nucl. Phys. A*, 368(2):210 – 236, 1981.

[110] K. Heyde, P. Van Isacker, M. Waroquier, J. L. Wood, and R. A. Meyer. Coexistence in odd-mass nuclei. *Phys. Rep.*, 102(5):291 – 393, 1983.

[111] C. Wraith, X. F. Yang, L. Xie, et al. Evolution of nuclear structure in neutron-rich odd-Zn isotopes and isomers. *Phys. Lett. B*, 771:385 – 391, 2017.

[112] X. F. Yang, C. Wraith, L. Xie, et al. Isomer Shift and Magnetic Moment of the Long-Lived $1/2^+$ Isomer in $^{79}_{30}Zn_{49}$: Signature of Shape Coexistence near ^{78}Ni. *Phys. Rev. Lett.*, 116:182502, May 2016.

[113] B. Cheal et al. CERN-INTC-2013-007: High-resolution laser spectroscopy of nickel isotopes. 2013.

[114] M. L. Bissell, X. F. Yang, et al. CERN-INTC-2016-035: Ground and isomeric state spins, moments and radii of Ge isotopes across the $N = 40$ subshell closure via laser spectroscopy at COLLAPS. 2013.

[115] M. L. Bissell, X. F. Yang, et al. CERN-INTC-2016-036: Laser spectroscopy measurements on neutron-rich $^{77?83}$Ge isotopes across $N = 50$ and establishing shape coexistence in ^{81}Ge via laser spectroscopy (COLLAPS). 2013.

[116] E. Ikonen, J. Hietaniemi, and T. Katila. Influence of alternating magnetic fields on ^{67}Zn Mössbauer resonance in ZnO. 38:6380–6391, Oct 1988.

Appendix A

Spin Assignments of $^{63-71g,69-71m}$Zn

Prior to this work the ground and isomeric state nuclear spins for a number of odd-A Zn isotopes had already been confirmed. These states include the ground state of $^{63-71}$Zn and the isomeric states of ^{69,71}Zn. The χ^2-minimisation process outlined in Chapter 5 is also applied to the hyperfine spectra of long-lived states in these isotopes. Fits with the confirmed nuclear spin I and also the neighbouring spin assignments ($I \pm 1$) are compared to experimental spectra, with spin assignments judged on their ability to reproduce all measured transition peaks (most definitive), produce an A coefficient ratio within errors of $R_{\text{exp}} = 0.4197$ and match to the intensity distribution of the spectrum. The agreement of fitted structures with the previously determined spin assignments signals a proof of method for the χ^2-minimisation fitting applied to $^{73-79g,m}$Zn (full results shown in Chapter 5) where the nuclear spins were previously tentatively assigned. The hyperfine A and B coefficients of the correct spin assignment are given in bold text in the following tables.

A.1 ^{63}Zn ($N = 33$)

The ground state of ^{63}Zn has five neutrons beyond the $N = 28$ shell closure, which in a non-interacting shell model picture would correspond to a single-neutron in the $\nu f_{5/2}$ orbit and a spin assignment of $I = 5/2$. However, the confirmed spin of $I^\pi = 3/2^-$ suggests that

the ground state wave function configuration is led by a single-neutron in $\nu p_{3/2}$ instead. Here a χ^2-minimisation fitting is performed for the known spin, as well as the neighbouring spin assignments $I = 1/2, 5/2$. The three fitted spectra for these spins are shown in Figure A.1.

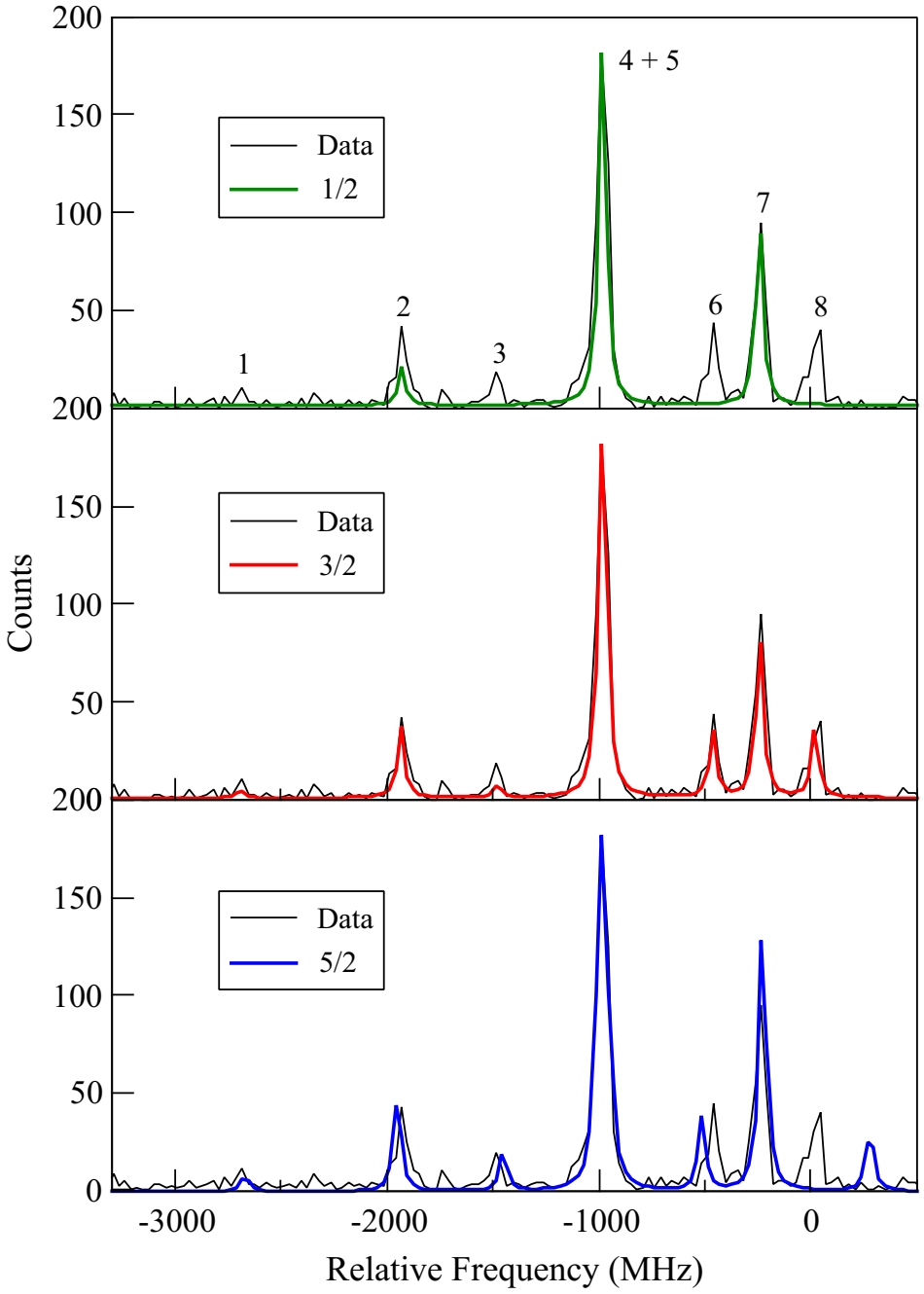

Figure A.1: Plot of the fitted spectrum for different spin assignments of the ground state in ^{63}Zn. The corresponding χ^2_r are displayed in Table A.1, along with the hyperfine coefficients.

Based on the eight resonance peaks in the measured spectrum, we can immediately rule out the $I = 1/2$ assignment as a structure with this spin corresponds to only three peaks for a $2 \rightarrow 1$ atomic transition and there is no known isomeric state to account for the additional peaks. The $I = 5/2$ structure (nine transition peaks) is not able to fit to all resonance peaks simultaneously, with the fit failing to match to peaks 6 and 8 despite the good agreement with the observed intensity distribution. This results in a hyperfine A coefficient ratio of 0.4216(24) that only lies within errors of $R_{\text{exp}} = 0.4197(3)$ due to its relatively large error. We therefore eliminate $I = 5/2$ as the ground state spin. The spin-3/2 structure has eight transition peaks that align with those measured experimentally, although its hyperfine A coefficient ratio of 0.4247(25) is outside errors of R_{exp}. However, since the alignment with transition peaks is the most definitive test, we agree with the known ground state spin assignment of $I = 3/2$.

Table A.1: Results from the χ^2-minimisation fitting of the ground state structures for ^{63}Zn.

I	χ^2_r	$A(^3S_1)$ (MHz)	$A(^3P_2)$ (MHz)	$B(^3P_2)$ (MHz)	$A(^3P_2)/A(^3S_1)$
1/2	3.28	−1125.3(11.4)	−379.2(6.8)	—	0.3369(70)
3/2	**1.95**	**−677.6(2.4)**	**−288.8(1.4)**	**+57.3(3.5)**	**0.4247(25)**
5/2	13.62	−491.8(1.4)	−207.3(1.1)	−34.9(7.1)	0.4216(24)

A.2 ^{65}Zn ($N = 35$)

The ground state of ^{65}Zn has a confirmed spin of $I = 5/2$. This assignment is in agreement with the non-interacting shell model picture that places an unpaired neutron in the $\nu f_{5/2}$ orbit. The χ^2-minimisation fitting is performed for the known ground state spin as well as the neighbouring spin assignments $I = 3/2, 7/2$. The three resulting χ^2-minimisation fits are shown in Figure A.2.

Based on the eight observable resonance peaks in Figure A.2, none of the three spin assignments can be ruled out. For the $2 \rightarrow 1$ atomic transition used in this work, the spin-3/2 structure corresponds to eight transition peaks while spin-5/2 and 7/2 structures

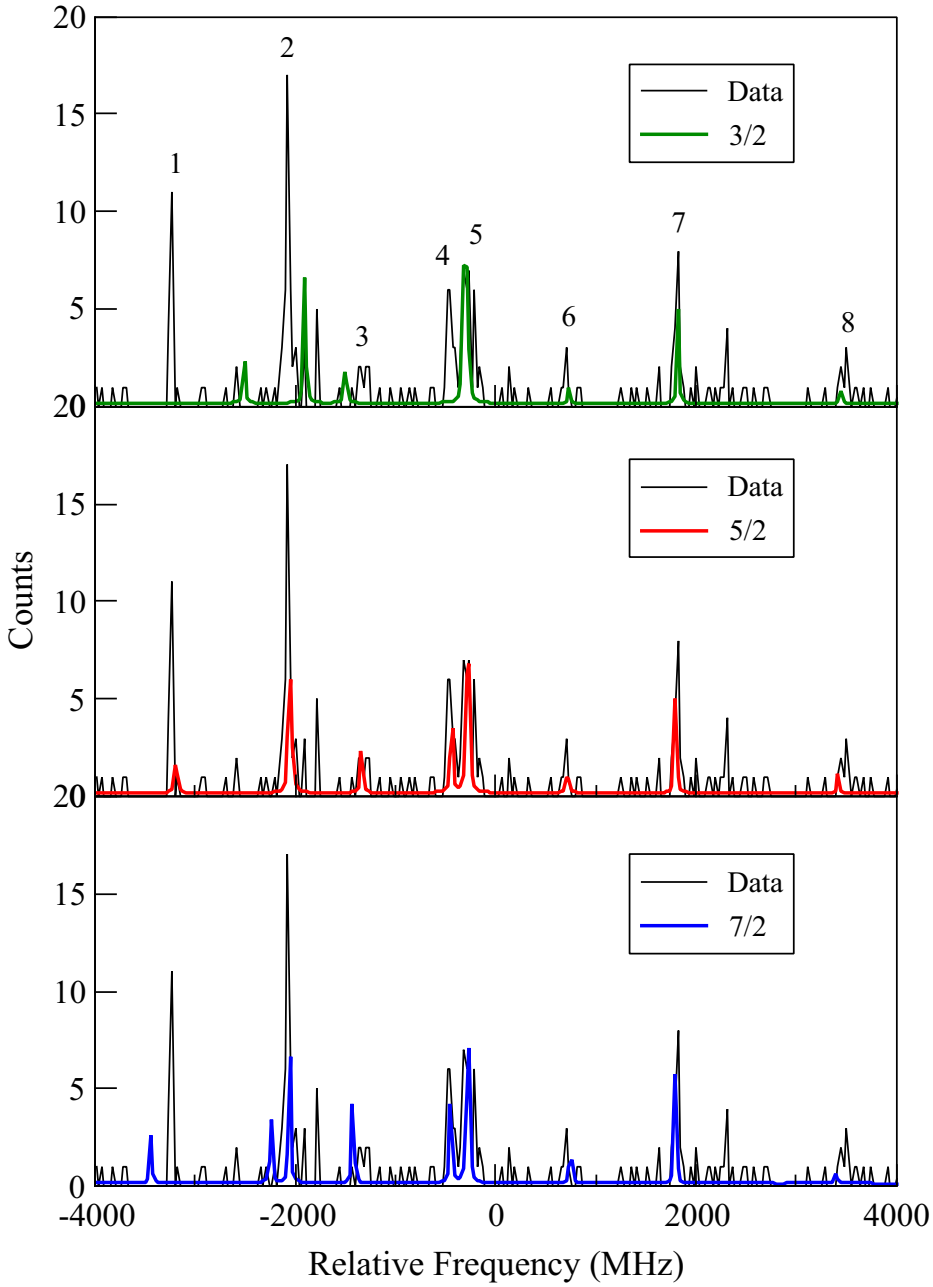

Figure A.2: Plot of the fitted spectrum for different spin assignments of the ground state in ^{65}Zn.

correspond to nine peaks. Despite this fact, clear differences can be seen between the quality of the three fits. This can clearly be observed across the hyperfine spectrum as the spin-3/2 structure fails to match to any transition peaks other than 5 and 7, leading to a hyperfine A

coefficient ratio of 0.4223(8) that is far from R_{exp}. The spin-7/2 structure also matches poorly to the data and fails to align with observed peaks 1, 6 and 8, but does produce a hyperfine A coefficient ratio of 0.4200(4) that is within errors of R_{exp}, although this is trivial given the erroneous fit. In comparison the spin-5/2 structure aligns with all observed resonances, with two transition peaks aligning to form a single peak around -2100 MHz, thus explaining why only eight peaks are observed instead of the nine typically seen for $I = 5/2$. The match between each fitted structure and the measured intensity distribution is generally poor for all spin values, and so is not used as a deciding factor between spins for this isotope. The hyperfine A coefficient ratio for $I = 5/2$ ($A(^3P_2)/A(^3S_1) = 0.4198(5)$) lies within errors of R_{exp}, and while the same is true for $I = 7/2$, its poor alignment with the measured peaks points to $I = 5/2$ as the ground state spin assignment.

Table A.2: Results from the χ^2-minimisation fitting of the ground state structures for ^{65}Zn.

I	χ^2_r	$A(^3S_1)$ (MHz)	$A(^3P_2)$ (MHz)	$B(^3P_2)$ (MHz)	$A(^3P_2)/A(^3S_1)$
3/2	0.46	+1489.8(1.6)	+629.1(1.0)	−84.0(1.9)	0.4223(8)
5/2	**0.36**	**+1101.1(0.8)**	**+462.3(0.5)**	**−6.8(2.7)**	**0.4198(5)**
7/2	0.47	+855.1(0.5)	+359.2(0.3)	+165.0(2.5)	0.4200(4)

A.3 ^{67}Zn ($N = 37$)

The only stable odd-A isotope of zinc, ^{67}Zn, has a confirmed ground state spin of $I = 5/2$. As for ^{67}Zn, the non-interacting shell model picture of the ground state consists of an unpaired neutron in $\nu f_{5/2}$. The χ^2-minimisation fitting is performed for the known ground state spin as well as the neighbouring spin assignments $I = 3/2, 7/2$. There is also a $1/2^-$ isomeric state in ^{67}Zn [116], although its half-life of $t_{1/2} = 9.07\mu s$ is too short for its hyperfine structure to be measured with the setup at COLLAPS. Therefore, only the fitting to the ground state is discussed here. The three fits to the ground state are shown in Figure A.3.

As for ^{65}Zn, the hyperfine spectrum of ^{67}Zn has eight observable resonance peaks. The

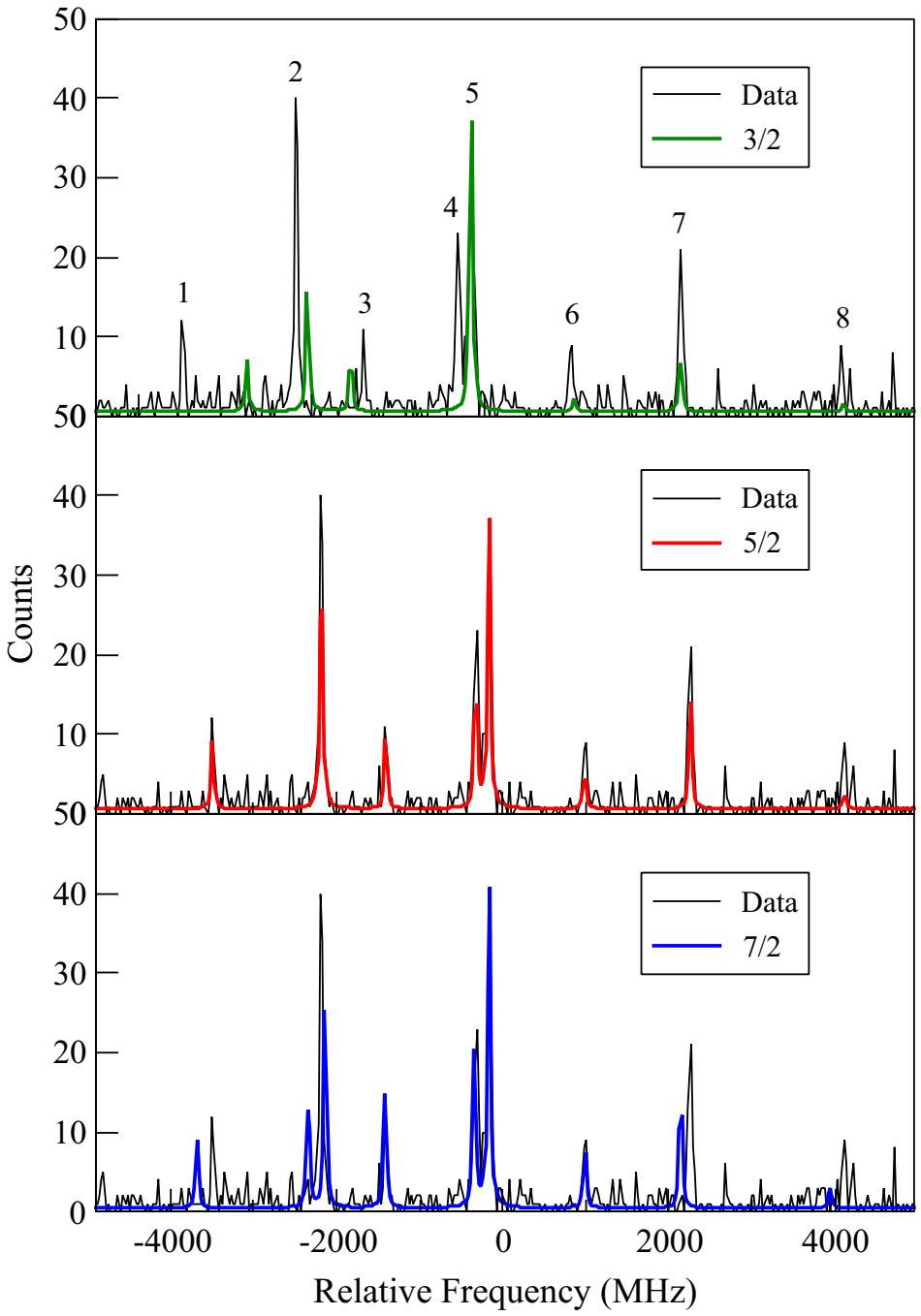

Figure A.3: Plot of the fitted spectrum for different spin assignments of the ground state in ^{67}Zn.

spin-3/2 structure, like the measured spectrum, consists of eight peaks for the $2 \rightarrow 1$ atomic transition, but is only able to align with transition peaks 5 and 7. As a result, the fact that

its $A(^3P_2)/A(^3S_1)$ value of 0.4193(20) is close to R_{exp} is trivial. For $I = 7/2$, the fitting does not match to peaks 1, 7 and 8, with the ninth peak of the spin-7/2 structure lying on the shoulder of peak 2. This leads to an A ratio of 0.4209(5) that is outside errors of R_{exp}. The spin-5/2 structure is seen to match to all measured peaks in the spectrum of ^{67}Zn. As for the spin-5/2 structure in ^{65}Zn, two peaks in the structure are found to align to form peak 2, hence explaining why only eight peaks are measured instead of nine. The visible peak matching along with the excellent agreement of the $I = 7/2$ A ratio of 0.4198(8) with R_{exp} means the χ^2-minimisation fitting reproduces the known ground state spin of $I = 5/2$.

Table A.3: Results from the χ^2-minimisation fitting of the ground state structures for ^{67}Zn.

I	χ^2_r	$A(^3S_1)$ (MHz)	$A(^3P_2)$ (MHz)	$B(^3P_2)$ (MHz)	$A(^3P_2)/A(^3S_1)$
3/2	1.55	+1722.3(4.3)	+722.2(2.9)	−129.4(4.0)	0.4193(20)
5/2	**0.65**	**+1268.9(1.5)**	**+532.6(0.9)**	**+42.8(5.2)**	**0.4198(8)**
7/2	1.58	+951.9(0.6)	+400.7(0.4)	+178.8(4.0)	0.4209(5)

A.4 ^{69}Zn ($N = 39$)

As we move across the zinc isotope chain, ^{69}Zn is the first unstable odd-A isotope on the neutron-rich side of the nuclear chart. Here the ground and isomeric state spins are confirmed as $I = 1/2$ and 9/2 respectively. With 11 neutrons beyond the $N = 28$ shell closure, this corresponds to a ground state with a single-neutron in $\nu p_{1/2}$ and an isomer formed by a neutron excitation to $\nu g_{9/2}$ in the non-interacting shell model. The χ^2-minimisation fits are shown below in Figure A.4 for the known spin $I = 1/2$ and the neighbouring ground state spin assignment $I = 3/2$. The results for the isomeric state spins of $I = 7/2$ and 9/2 are also shown in Figure A.5.

A.4.1 Ground State Spin

Based on the 11 observed resonance peaks and the tentative spin assignment of $I = 9/2$ to the isomer (corresponding to nine hyperfine transitions for $2 \rightarrow 1$), three peaks are attributed to the ground state if we assume that one $I = 9/2$ lies outside the scan range. The ground state peaks (labelled in Figure A.4) are therefore most suited to the $I = 1/2$ assignment. This is reflected by all the spin-1/2 structure peaks matching to those in the spectrum and the proximity of the A ratio of 0.4198(14) to the known ratio. The spin-3/2 structure (eight transition peaks) is only able to align with the measured transition peaks 2 and 3, and the

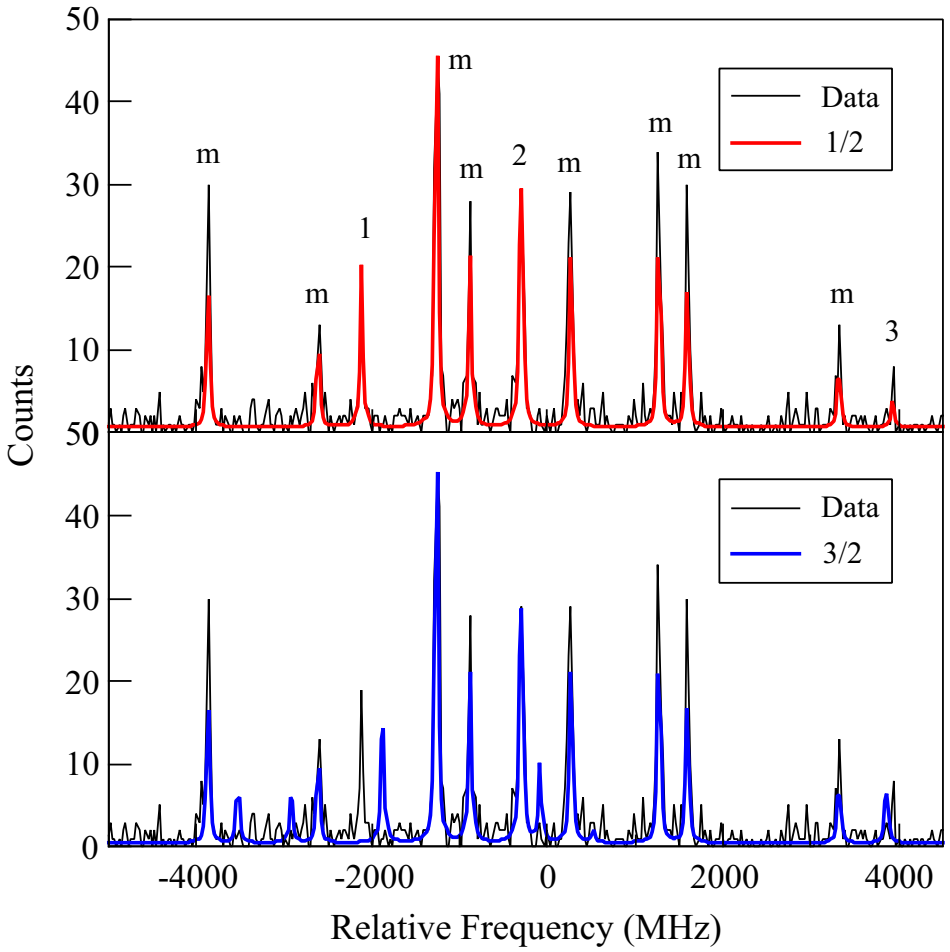

Figure A.4: Plot of the fitted spectrum for different spin assignments of the ground state in ^{69}Zn.

additional peaks associated with a spin-3/2 state with Racah relative intensities appear in regions of background. The fitting is therefore in agreement with the known ground state spin of $I = 1/2$.

Table A.4: Results from the χ^2-minimisation fitting of the ground state structures for ^{69}Zn.

I	χ^2_r	$A(^3S_1)$ (MHz)	$A(^3P_2)$ (MHz)	$B(^3P_2)$ (MHz)	$A(^3P_2)/A(^3S_1)$
1/2	**0.78**	**+4033.3(8.2)**	**+1693.2(4.7)**	—	**0.4198(14)**
3/2	1.56	+2295.2(2.3)	+953.5(1.4)	+941.8(3.1)	0.4154(7)

A.4.2 Isomeric State Spin

Both the $I = 7/2$ and 9/2 spin assignments have statistical fits of comparable quality based on their χ^2_r values. Clear differences arise though when visually comparing the fits to the eight transition peaks attributed to the isomeric state (one additional peak outside the scan range at < 5000 MHz, estimated by superimposing a model hyperfine structure on the spectrum). The spin-7/2 structure is unable to align with peaks 7 and 8, and, although the fit produces a hyperfine A coefficient ratio of 0.4198(18) that is close to the expected value, the fact it is for an erroneous fit negates its agreement with R_{exp}. The A ratio of the spin-9/2 structure (0.4192(7)) is also within errors of R_{exp} and is seen to align with all observed isomeric transition peaks. Therefore the fitting is in agreement with the confirmed isomeric state spin of $I = 9/2$.

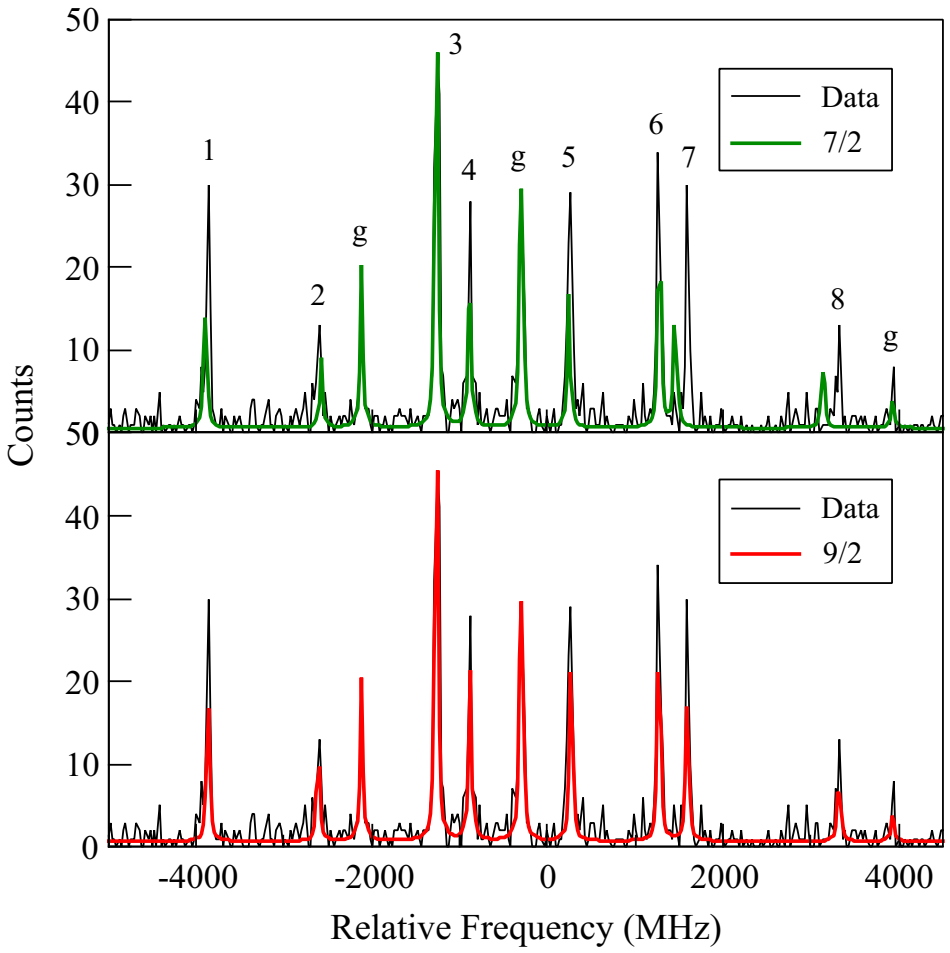

Figure A.5: Plot of the fitted spectrum for different spin assignments of the isomeric state in ^{69}Zn. The first hyperfine transition peak of the isomeric state lies outside the scan range shown here.

Table A.5: Results from the χ^2-minimisation fitting of the isomeric state structures for ^{69}Zn.

I	χ^2_r	$A(^3S_1)$ (MHz)	$A(^3P_2)$ (MHz)	$B(^3P_2)$ (MHz)	$A(^3P_2)/A(^3S_1)$
7/2	1.22	−1150.5(1.0)	−480.9(0.7)	+10.4(6.2)	0.4198(18)
9/2	**0.78**	**−933.8(0.9)**	**−391.5(0.5)**	**−106.8(6.2)**	**0.4192(7)**

A.5 ^{71}Zn ($N = 41$)

^{71}Zn is the heaviest odd-A isotope of Zn with previously confirmed ground and isomeric state spins of $I = 1/2$ and $9/2$ respectively. The confirmed spins are contrary to those expected in the non-interacting shell model where the unpaired neutron would be expected to occupy $\nu g_{9/2}$ in the ground state and $\nu p_{1/2}$ in the isomer, thus indicating that the $\nu g_{9/2}$ orbit has not yet lowered in energy to below $\nu p_{1/2}$. Confirmation of the nuclear spin for heavier odd-A Zn isotopes will determine the point at which these orbitals invert in terms of energy. The known nuclear spins are tested against the neighbouring ground and isomeric state spin assignments of $I = 3/2$ and $7/2$ respectively, the results of which are shown below in Figures A.6 and A.7.

A.5.1 Ground State Spin

As for the ground and isomeric states of ^{69}Zn, the 11 observed transition peaks indicate the presence of an $I = 1/2$ (three peaks) states and an $I \geq 3/2$ state (eight or nine peaks). The spin-3/2 structure (corresponding to eight peaks) does not align with peak 1 of the isomeric structure in the spectrum, and its additional peaks are clearly seen to not align with any counts corresponding to a hyperfine transition. On the other hand, the spin-1/2 structure is clearly able to align with all measured transition peaks in the spectrum which leads to an improved statistical fitting ($\chi^2_r = 0.84$) over that for $I = 3/2$ ($\chi^2_r = 1.68$). The A ratios of the two fits are fairly similar, although the obviously erroneous fit for the spin-3/2 structure means its A ratio is trivial. Therefore, the χ^2-minimisation fitting agrees with the known ground state spin of $I = 1/2$.

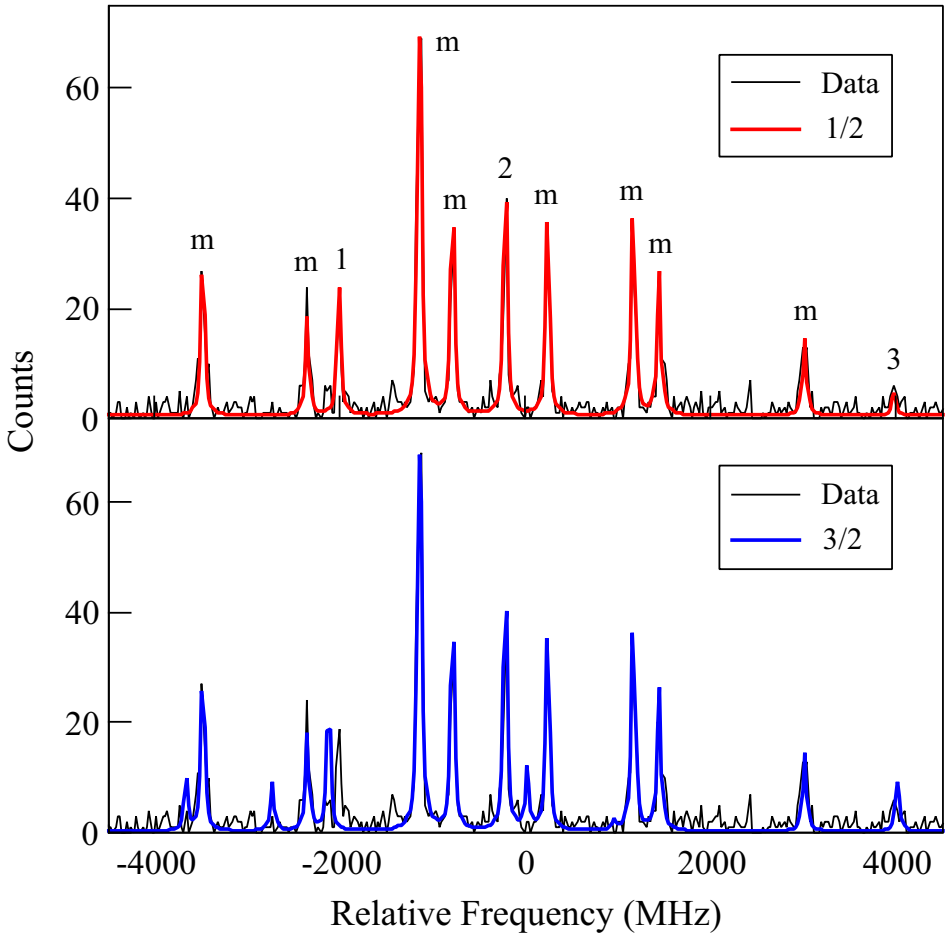

Figure A.6: Plot of the fitted spectrum for different spin assignments of the ground state in ^{71}Zn.

Table A.6: Results from the χ^2-minimisation fitting of the ground state structures for ^{71}Zn.

I	χ^2_r	$A(^3S_1)$ (MHz)	$A(^3P_2)$ (MHz)	$B(^3P_2)$ (MHz)	$A(^3P_2)/A(^3S_1)$
1/2	**0.84**	**+3990.5(8.6)**	**+1677.1(5.0)**	—	**0.4203(15)**
3/2	1.68	+2455.9(2.4)	+1033.5(1.4)	+705.1(3.6)	0.4208(7)

A.5.2 Isomeric State Spin

The χ^2-minimisation fitting for the spin-9/2 structure produces a more statistically ideal fit to the data ($\chi^2_r = 0.84$) than the spin-7/2 structure ($\chi^2_r = 2.09$). This is reflected in the spectra

shown in Figure A.7 where the spin-7/2 structure does not align with transition peaks 1, 2, 7 and 8. The spin-9/2 structure is able to align with all eight measured transition peaks and subsequently has an $A(^3P_2)/A(^3S_1)$ value of 0.4195(5) that is within errors of R_{exp}. This fitting is therefore in agreement that the ground state spin assignment of $I = 9/2$.

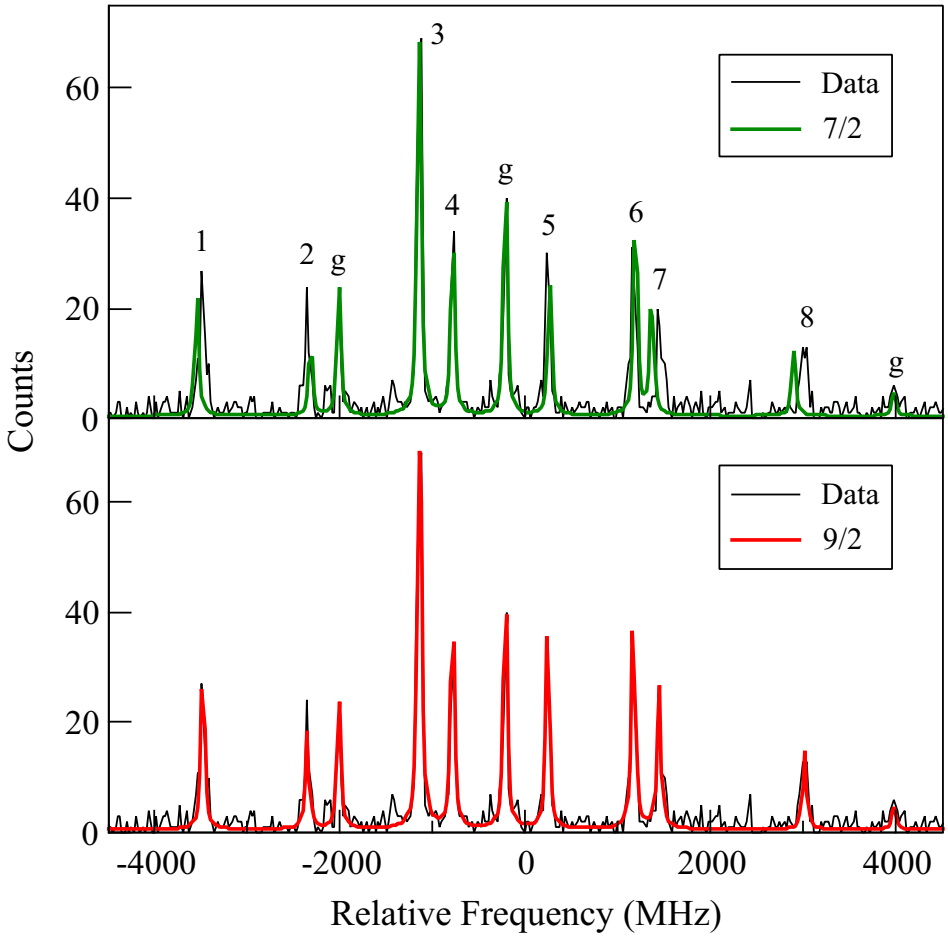

Figure A.7: Plot of the fitted spectrum for different spin assignments of the isomeric state in ^{71}Zn.

Table A.7: Results from the χ^2-minimisation fitting of the isomeric state structures for ^{71}Zn.

I	χ^2_r	$A(^3S_1)$ (MHz)	$A(^3P_2)$ (MHz)	$B(^3P_2)$ (MHz)	$A(^3P_2)/A(^3S_1)$
7/2	2.09	−1051.5(1.0)	−437.7(0.6)	+7.2(5.5)	0.4163(7)
9/2	**0.84**	**−844.2(0.6)**	**−354.2(0.4)**	**−77.2(3.8)**	**0.4195(5)**

Appendix B

χ^2-minimisation Fit Parameters with Free Intensities

A complementary χ^2-minimisation analysis has been performed by X. F. Yang on Zn isotopes from $N = 33 - 49$. This analysis follows the same principles as the one outlined in Chapter 5 with a non-normalised Lorentzian line shape with free intensities and a series of satellite peaks with fixed energy offset and Poisson intensities (but a fixed Poisson parameter, b, and a free n parameter in Equation 5.5) to replicate the skewed Lorentzian peaks. The results from these two analyses for I, $A(^3P_2)$, $A(^3S_1)$ and $B(^3P_2)$ are given in Table B.1 below. The final values of $A(^3P_2)$ and $B(^3P_2)$ used to calculate the nuclear moments are obtained by taking a simple average of values from the two analyses.

Table B.1: The hyperfine structure coefficients $A(^3P_2)$, $A(^3S_1)$ and $B(^3P_2)$ and their errors from the χ^2-minimisation fitting process in this work (details in Chapter 5) and from the complementary analysis by X. F. Yang. The simple average of these values provides the final hfs coefficients used to calculate magnetic dipole moments, μ, and electric quadrupole moments, Q_s, by means of a reference isotope. The commonly agreed upon nuclear spins, I, are also shown.

			This Work			Complementary Analysis		
A	N	I	$A(^3S_1)$ (MHz)	$A(^3P_2^o)$ (MHz)	$B(^3P_2^o)$ (MHz)	$A(^3S_1)$ (MHz)	$A(^3P_2^o)$ (MHz)	$B(^3P_2^o)$ (MHz)
63	33	3/2	−676.88(0.43)	−285.81(1.64)	+58.50(4.30)	−677.0(1.1)	−286.2(1.0)	+60.8(3.5)
65	35	5/2	+1115.01(0.48)	+467.97(0.20)	−7.00(2.99)	+1113.00(2.12)	+467.16(0.89)	−7.30(5.69)
67	37	5/2	+1266.75(0.67)	+530.67(0.36)	+39.53(2.76)	+1266.15(1.75)	+531.75(0.93)	+42.28(7.08)
69	39	1/2	+4035.91(8.20)	+1690.91(4.86)	—	+4029.82(4.33)	+1691.05(2.65)	—
69^m	39	9/2	−933.53(0.43)	−391.99(0.23)	−115.26(3.56)	−933.77(0.33)	−392.11(0.21)	−110.80(3.55)
71	41	1/2	+3986.72(5.16)	+1675.28(3.03)	—	+3987.23(4.47)	+1674.56(2.34)	—
71^m	41	9/2	−845.18(0.51)	−354.43(0.29)	−77.20(3.96)	−843.74(0.54)	−354.07(0.28)	−75.17(4.45)
73	43	1/2	+4043.94(2.08)	+1696.82(1.16)	—	+4044.14(2.70)	+1696.88(1.56)	—
73^m	43	5/2	−1233.96(1.41)	−518.21(0.84)	+124.79(6.31)	−1233.87(1.40)	−518.09(0.88)	+124.99(6.12)
75	45	7/2	−815.56(0.56)	−342.48(0.33)	+49.42(3.40)	−815.23(0.40)	−342.14(0.25)	+47.07(2.59)
75^m	45	1/2	+4031.93(5.09)	+1695.05(2.82)	—	+4035.86(3.05)	+1695.91(1.71)	—
77	47	7/2	−938.08(0.72)	−393.88(0.41)	+140.86(4.93)	−938.10(0.70)	−393.78(0.41)	+141.47(4.91)
77^m	47	1/2	+4058.61(6.00)	+1706.84(2.41)	—	+4067.12(8.72)	+1709.22(5.07)	—
79	49	9/2	−954.76(0.56)	−400.44(0.32)	+116.82(4.73)	−955.23(0.39)	−400.72(0.26)	+115.65(4.92)
79^m	49	1/2	−7361.42(6.04)	−3095.19(2.78)	—	−7362.82(5.01)	−3090.93(2.92)	—